A STUDY OF ADVANCED MAGNESIUM-BASED HYDRIDE AND DEVELOPMENT OF A METAL HYDRIDE THERMAL BATTERY SYSTEM

by

Chengshang Zhou

A dissertation submitted to the faculty of
The University of Utah
in partial fulfillment of the requirements for the degree of

Doctor of Philosophy

Department of Metallurgical Engineering

The University of Utah

May 2015

The University of Utah Graduate School

STATEMENT OF DISSERTATION APPROVAL

The dissertation of **Chengshang Zhou**

has been approved by the following supervisory committee members:

Zhigang Zak Fang	, Chair	February 2, 2015 Date Approved
Hong Yong Sohn	, Member	February 2, 2015 Date Approved
Sivaraman Guruswamy	, Member	February 2, 2015 Date Approved
Kent Udell	, Member	February 2, 2015 Date Approved
Robert Bowman	, Member	February 2, 2015 Date Approved

and by **Manoranjan Misra** , Chair/Dean of

the Department of **Metallurgical Engineering**

and by David B. Kieda, Dean of The Graduate School.

ABSTRACT

Metal hydrides are a group of important materials known as energy carriers for renewable energy and thermal energy storage. A concept of thermal battery based on advanced metal hydrides is studied for heating and cooling of cabins in electric vehicles. The system utilizes a pair of thermodynamically matched metal hydrides as energy storage media. The hot hydride that is identified and developed is catalyzed MgH_2 due to its high energy density and enhanced kinetics. $TiV_{0.62}Mn_{1.5}$, $TiMn_2$, and $LaNi_5$ alloys are selected as the matching cold hydride.

A systematic experimental survey is carried out in this study to compare a wide range of additives including transitions metals, transition metal oxides, hydrides, intermetallic compounds, and carbon materials, with respect to their effects on dehydrogenation properties of MgH_2. The results show that additives such as Ti and V-based metals, hydride, and certain intermetallic compounds have strong catalytic effects.

Solid solution alloys of magnesium are exploited as a way to destabilize magnesium hydride thermodynamically. Various elements are alloyed with magnesium to form solid solutions, including indium and aluminum. Thermodynamic properties of the reactions between the magnesium solid solution alloys and hydrogen are investigated, showing that all the solid solution alloys that are investigated in this work have higher equilibrium hydrogen pressures than that of pure magnesium.

Cyclic stability of catalyzed MgH_2 is characterized and analyzed using a PCT Sievert-

type apparatus. Three systems, including MgH_2-TiH_2, MgH_2-$TiMn_2$, and MgH_2-VTiCr, are examined. The hydrogenating and dehydrogenating kinetics at 300 °C are stable after 100 cycles. However, the low temperature (25 °C to 150 °C) hydrogenation kinetics suffer a severe degradation during hydrogen cycling. Further experiments confirm that the low temperature kinetic degradation can be mainly related the extended hydrogenation-dehydrogenation reactions.

Proof-of-concept prototypes are built and tested, demonstrating the potential of the system as HVAC for transportation vehicles. The performance of the concept-demonstration-unit show both high heating/cooling power and high energy densities. An extended cycling test shows degradation on the performance of the system. To solve this problem, a metal hydride hydrogen compressor is proposed for aiding the recharge process of the system.

This dissertation is dedicated to Jing and Lotus.

TABLE OF CONTENTS

LIST OF TABLES

ACKNOWLEDGEMENTS

I would like to express my sincere thanks to all the people who made it possible for me to successfully complete my graduate study.

I thank Professor Zhigang Zak Fang, my supervisor, for the opportunity to work on this project, and for his expert guidance, supporting, instructions, and encouragement.

I would also like to acknowledge my committee members, Dr. Robert C. Bowman, Professor Kent Udell, Professor Hong Yong Sohn, and Professor Sivaraman Guruswamy, for their insightful suggestions, discussion, and supervising my dissertation.

My gratitude also goes to Dr. Peng Fan. Our endless discussion has indeed helped me throughout the research project.

I would like to take this opportunity to show my appreciation for the fruitful collaboration from every member of the Fang Group. Important contributions to my research work and the thermal battery project were provided by Ms. Jingzhu (April) Li and Dr. Chai Ren, to whom I want to give appreciations. In addition, I want to especially thank Dr. Pei Sun, for his patience in the training course of my graduate study. I have to express my gratitude to Dr. Yang Xia, who offered support for TEM characterization in many ways. Special acknowledgement is extended to Dr. Mark Koopman for proofreading my manuscript and constructive suggestions.

I am greatly indebted to Dr. John J. Vajo from HRL Laboratories, for his valuable discussion, suggestion, and assistance during the study of metal hydride.

I am also grateful for the assistance given from the colleagues in the Udell group, Dr. Bidzina Kekelia and Mr. Gareth D. Whatcott, and the researcher in the Vajo group, Dr. Justin J. Purewal.

Special appreciation must go to Dr. Jun Lu, Dr. Yang Ren, and Dr. Xiaoyi Zhang from the Argonne National Laboratory, for their valuable help on XRD analysis. A great deal of assistance for fulfilling the XRD work was made by Dr. Xiangyi Luo, to whom I also truly give thanks.

Finally, I would like to acknowledge the financial support from the National Science Foundation (Grant No. 0933778) and the U.S. Department of Energy (DOE) under contract number DE-AR0000173.

CHAPTER 1

INTRODUCTION

1.1 Electric Vehicle (EV)

In a world that is facing an energy crisis and environmental pollution, the development of an electric vehicle (EV) as zero-emission, energy-efficiency mode of transportation has taken on an accelerated pace.[1] After 1990s, most of major automotive manufacturers have launched aggressive programs to develop new-generation EVs, and some economical EVs have been commercialized. Moreover, market forecasting has suggested that Hybrid Electric Vehicles (HEVs), Plug-in Hybrid Electric Vehicles (PHEVs), and Electric Vehicles (EV), will be a growing component of the US vehicle fleets in the near future.[2]

By supplying power to EV, a rechargeable electric battery is one of the most crucial components in EV. However, the capacity and cost of an electric battery represent the highest barriers to wide scale adoption of electric vehicles as the large and expensive batteries needed to provide significant driving range can result in unattractive vehicle design and price-points. In addition to the electric energy that has been used in powertrain, a key drain on the electrical battery system of an EV is needed to serve cabin heating and cooling loads. In general, cabin climate conditioning can significantly reduce the electric range of plug-in and full electric vehicles, by as much as 40% in extreme cases,[3] or inversely and can increase the battery size and cost by a comparable amount for the same

range. Therefore, significant reduction in the size/cost of EV batteries or a significant increase in driving range can be enabled by eliminating the need for cabin climate load to draw on the electrical battery system.

1.2 Thermal Battery Technology

Today's EVs generally use the capacity of the electric battery for highly inefficient resistive heating as opposed to internal-combustion vehicles, which simply route waste engine heat to the cabin. Considering the fact that capacities of current electric batteries are very limited, there is significant interest in developing a novel thermal battery technology that can provide both cooling and heating to the vehicle cabin, freeing critical electrical battery capacity for driving loads.

In the ideal case, the design of the thermal battery as a heating and air conditioning (HVAC) system for electric vehicle must be compact and modular and have high-energy density, high efficiency, and low cost. The requirements include

(1) The space occupied by the thermal battery for heating and cooling would be equivalent to the total space saved by eliminating the existing vapor compression cooling system and the existing heating system in PHEVs and EVs;

(2) The energy density of the thermal battery would be higher than the energy density of an electric battery (e.g., Li-ion battery);

(3) In many cases, the cooling and heating provided from the thermal battery system would be equivalent or better than the existing air conditioning system;

(4) The cost of the overall thermal battery system would be lower than the total cost saved by eliminating the existing air conditioning system and downsizing the

electric battery pack;

(5) In the typical use case, such a thermal battery would simply be charged upon plug-in, in tandem with the electrical battery being charged.

This work is based on a concept that employs metal hydride materials as energy storage materials to build a new generation thermal battery with sufficient energy density to meet the above requirements. The proposed technology is a thermochemical energy storage technique based on hydrogenation and dehydrogenation reactions of metal hydrides. Typically, dehydrogenation of a metal hydride is endothermic, and the reverse reaction of hydrogenation is exothermic. As shown in Figure 1-1, the thermal battery will consist of two hydride beds – a hot hydride bed and a cold hydride bed.

The hot hydride bed contains material with low vapor pressure for hydrogen. And the cold hydride bed contains metal hydride with high vapor pressure for hydrogen. When the valve between the two hydride beds is opened the system seeks equilibrium, and hydrogen naturally moves from the cold bed toward the hot bed. The hydride in the hot bed will absorb hydrogen via an exothermic reaction that releases heat to the environment. In the meantime the hydride in the cold bed will release hydrogen causing an endothermic reaction that absorbs heat from the environment. This process generates a heating or cooling effect that can be used to warm or chill air for the passenger cabin.

To make the thermal battery practical, a recharge ability will be necessary. The recharge process is required to achieve using plug-in electric power, just like a rechargeable electric battery. Given that the equilibrium pressure of hydride is increased when increasing the temperature, recharging can be performed by heating the hot hydride beds to a certain temperature until the vapor pressure of the hot hydride is higher than that of cold hydride

at ambient temperature, so the hydrogen will desorb from hot hydride and can be absorbed by the cold hydride (H_2 flows from hot bed to cold bed). The principle of the recharge mode is illustrated in Figure 1-2.

1.3 Metal Hydrides

Because of the intrinsic thermodynamic properties of metal hydrides, the hydrogenation and dehydrogenation are reversible at moderate conditions, which makes it at least in principle feasible to harness the heating or cooling effect of the reactions. In reality, however, using metal hydride for heating/cooling of a vehicle faces many material and engineering challenges.

Each metal hydride selected for the system must meet the following requirements:

(1) High energy density both gravimetrically and volumetrically;

(2) Fast kinetic rate during both dehydrogenation and hydrogenation;

(3) Cycle stability / durability;

(4) Low cost.

Besides, as shown in Figure 1-1, a pair of metal hydrides is used for the proposed thermal battery system: one of the pair is named the hot hydride because it serves as a heating source, and its equilibrium pressure is low; the other is named cold hydride because it serves as a cooling source, and its equilibrium pressure is high. More specifically, the pair of hydrides must meet the following requirements:

(1) Hydrogenation of hot hydrides and dehydrogenation of cold hydrides are kinetically feasible at working temperature and pressure during discharging;

(2) During discharging, the hot hydride bed temperature is in a range between 100 °C

and 200 °C, and the hot hydride bed temperature is in a range between 10 °C and -10 °C;

(3) Dehydrogenation of hot hydrides and hydrogenation of cold hydrides are kinetically feasible at working temperature and pressure during charging;

(4) During discharging, the temperature of the cold hydride bed is at ambient temperature (0 °C to 40 °C). The hot hydride bed must be heated to a high temperature that can supply enough hydrogen pressure for the cold hydride bed, while the temperature of the hot hydride bed should be lower than 400 °C regarding the potential engineering and safety problem under high temperature and pressure.

1.4 Selection of Working Hydride Pair

The selection of the two hydride materials must have complementary thermodynamic properties to enable discharging and charging of the thermal battery in desired temperature ranges. Specifically, for discharging the thermal battery, the equilibrium pressure of the cold hydride must be high enough at the ambient temperature (e.g., -10 to 35 °C) so that the hot hydride metal can be hydrogenated at temperatures above the ambient temperature. For charging of the thermal battery, the equilibrium pressure of the hot hydride at an elevated temperature (e.g., 200 °C to 350 °C) must be high enough to hydrogenate the cold hydride metal at ambient temperature. To identify a working pair(s) of hydride materials, a screening of a large number of hydride materials was conducted based on thermodynamics properties.

1.4.1 Hot Hydride

Figure 1-3 is the van't Hoff plots of selected hydrides. Hot hydride is on the left of the diagram, while cold hydrides are on the right. It shows that there are few options for hot hydride considering that the temperature for recharging of the thermal battery should not be more than 400 °C for practical reasons. Catalyzed nanosized MgH_2 is thus selected as a candidate hot hydride material. Because of a high usable hydrogen capacity up to 7.0 wt% and a high reaction enthalpy of 75 kJ/mol H_2, MgH_2 has high gravimetric energy density. Relevant properties of MgH_2 and other comparable hot hydride candidates are summarized in Table 1-1. It can be seen that gravimetric energy density and volumetric energy density of Mg/MgH_2 are 2831 kJ/kg and 4020 kJ/L, respectively.

1.4.2 Cold Hydride

Once the hot hydride is determined, candidates for cold hydride are selected from the shaded square in Figure 1-3. First of all, to hydrogenate magnesium during the discharging mode, it was expected that at least 1-bar hydrogen pressure is needed from cold hydride. Second, to recharge the system in relatively warm climate conditions (e.g., summer in the southern US), equilibrium pressure of cold hydride at 40 °C must be low enough so that hydrogen can flow back from the heated hot hydride and hydrogenate the cold bed. On the basis of above criteria, the shaded area in Figure 1-3 shows the range of van't Hoff plots of any suitable cold hydride candidates must have their van't Hoff plots fall inside the area. It can be found that there are several cold hydride candidates including 75V-5Ti-20Cr, $TiMn_{1.5}V_{0.62}$ (denoted as TiMnV), $(V_{0.9}Ti_{0.1})_{0.95}Fe_{0.05}$, $Ti_{0.98}Zr_{0.02}V_{0.43}Fe_{0.09}Cr_{0.05}Mn_{1.5}$ (denoted as $TiMn_2$), $TiMn_{1.5}$, and $LaNi_5$, and their relevant properties are provided in Table

1-1.

It has to be pointed out that although the various cold hydrides in Figure 1-3 could be considered as candidates to pair with MgH_2, the selection of a different cold hydride may result in significant impacts on the performance of a thermal battery system. For example, hydrides with van't Hoff lines on the right side in Figure 1-3, i.e., $TiMn_2$, $TiMn_{1.5}$, can provide relatively higher pressures to hydrogenate Mg, leading to enhanced cooling and heating system performance due to the large difference between the equilibrium pressures of the hot bed and the cold bed. However, using the high-pressure cold hydrides may cause difficulties during recharging of the system because higher temperature would be required to heat the hot bed to provide sufficiently high pressure for recharging the cold bed. The overheating of MgH_2 should, however, be avoided due to the potential risk of its degradation.[4] In comparison, hydrides such as $(V_{0.9}Ti_{0.1})_{0.95}Fe_{0.05}$, $LaNi_5$, and $LaNi_{4.7}Sn_{0.3}$ can be easily rehydrogenated under relatively low pressure. The problem of using the lower pressure cold hydrides lies in the potential of decreasing system performance since the kinetic of hydrogenating Mg will be slower at lower pressures.

1.5 Scopes and Objectives

The concept of using metal hydride for TES and heat pump is known and has been mentioned in previous researchle,[5] and a detailed review of this field will be in the next chapter. However the specific concept of "thermal battery" for an HVAC system of EV that stores electric (or external) energy during "recharging" and then converts it to thermal energy during "discharging" service has not been widely investigated. Besides, the potential of adopting Mg-based hydride for thermal energy storage offers attractive energy

density, but to date its research and application are still very limited.

In the research of the present dissertation, the concept of a high-energy-density thermal battery based on advanced metal hydrides including Mg-based hydrides and intermetallic alloys will be explored. The present research focused on a specified on-board application to develop a novel HVAC system for EV. However, the methodology of the thermal battery could be extended to a much broader range of applications, including other transportation vehicles such as long haul trucks, stationary HVAC, solar thermal energy storage systems, and waste heat recovery and storage systems.

The thermal battery is intended to achieve a high energy density TES system by taking advantage of newly developed hydride system (catalyzed nano MgH_2). Needless to say, the properties (hydrogen storage properties) of MgH_2 materials are one of the crucial factors that determines the performance of the thermal battery system. Despite a lot of research previously devoted to improve MgH_2 in the field of hydrogen storage, an optimum Mg-based hydride material is required to have fast kinetics, tunable thermodynamics, good cycle life, and sufficient hydrogen capacity for the application of the thermal battery. Further, the fundamental mechanisms of additives on hydrogen storage properties of MgH_2 in terms of catalytic effect, thermodynamic destabilization, and cyclic stability, still remain unclear.

To develop a workable metal hydride based thermal battery system for an air conditioning system of EV, the research of this dissertation has two major directions – the study and optimization of advanced magnesium-based hydride and the development and testing of metal hydride thermal battery prototype. The main parts of present research are listed as follows:

(1) Kinetics improvement of magnesium hydride by catalytic doping;

(2) Thermodynamic destabilization of magnesium hydride by formation of a Mg solid solution;

(3) Cyclic stability of catalyzed magnesium hydride;

(4) The development and testing thermal battery prototypes;

(5) Performance of thermal battery with a metal hydride hydrogen compressor.

1.6 References

1. Chan, C. C. An Overview of Electric Vehicle Technology. *Proc. IEEE* **1993**, *81*, 1202−1213.

2. Al-Alawi, B. M.; Bradley, T. H., Review of Hybrid, Plug-in Hybrid, and Electric Vehicle Market Modeling Studies. *Renewable Sustainable Energy Rev.* **2013**, *21*, 190−203.

3. Barnitt, R. A.; Brooker, A. D.; Ramroth, L.; Rugh, J.; Smith, K. A., Analysis of Off-Board Powered Thermal Preconditioning in Electric Drive Vehicles. *National Renewable Energy Laboratory,* Golden, CO **2010**.

4. Bogdanović, B.; Ritter, A.; Spliethoff, B., Active Mgh_2-Mg Systems for Reversible Chemical Energy Storage. *Angew. Chem. Int. Edit.* **1990**, *29*, 223−234.

5. Muthukumar, P.; Groll, M., Erratum to "Metal Hydride Based Heating and Cooling Systems: A Review" [International Journal of Hydrogen Energy (2010) 35: 3817–3831]. *Int. J. Hydrogen Energy* **2010**, *35*, 8816−8829.

6. Sandrock, G.; Thomas, G., The Iea/Doe/Snl on-Line Hydride Databases. *Appl. Phys. A* **2001**, *72*, 153−155.

Table 1-1. Properties of hydride candidates.[6]

	Materials	H-capacity, wt.%	ΔH, kJ/mol H_2	Density, kg/L	T for 1 bar, °C	P @ 25 °C, Bar	Energy density	
							Gravimetric, kJ/kg	Volumetric, kJ/L
Hot hydrides	Mg	7.6 *	74.5	1.42	279	0.00001	2831.0	4020
	Mg_2Ni	3.3	64.5	2.75	255	0.0001	1064.3	2927
	$LaNi_{4.25}Al_{0.75}$	1.13	44.1	7.0	104	0.024	249.2	1744
Cold hydrides	75V-5Ti-Cr	2.6 **	33	5.5	-30	8	429.0	2360
	$TiV_{0.62}Mn_{1.5}$	2.15	28.6	5.45	-6	3.8	307.5	1676
	$(V_{0.9}Ti_{0.1})_{0.95}Fe_{0.05}$	1.95 **	43.2	5.65	36	0.5	421.2	2380
	$TiMn_2$	1.9	27.4	6.0	-28	11	260.3	1562
	$TiMn_{1.5}$	1.86	28.7	6.4	-21	8.4	266.9	1708
	$LaNi_5$	1.49	30.8	7.8	12	1.8	229.5	1790
	$LaNi_{4.7}Sn_{0.3}$	1.37	37	7.7	66	0.3	253.5	1952

* For catalyzed MgH_2, a hydrogen capacity > 6.0 wt.% can be achieved.
** The V based alloys have theoretical H capacities over 3.5 wt.%; however, only a portion of the hydrogen is available under practical conditions.

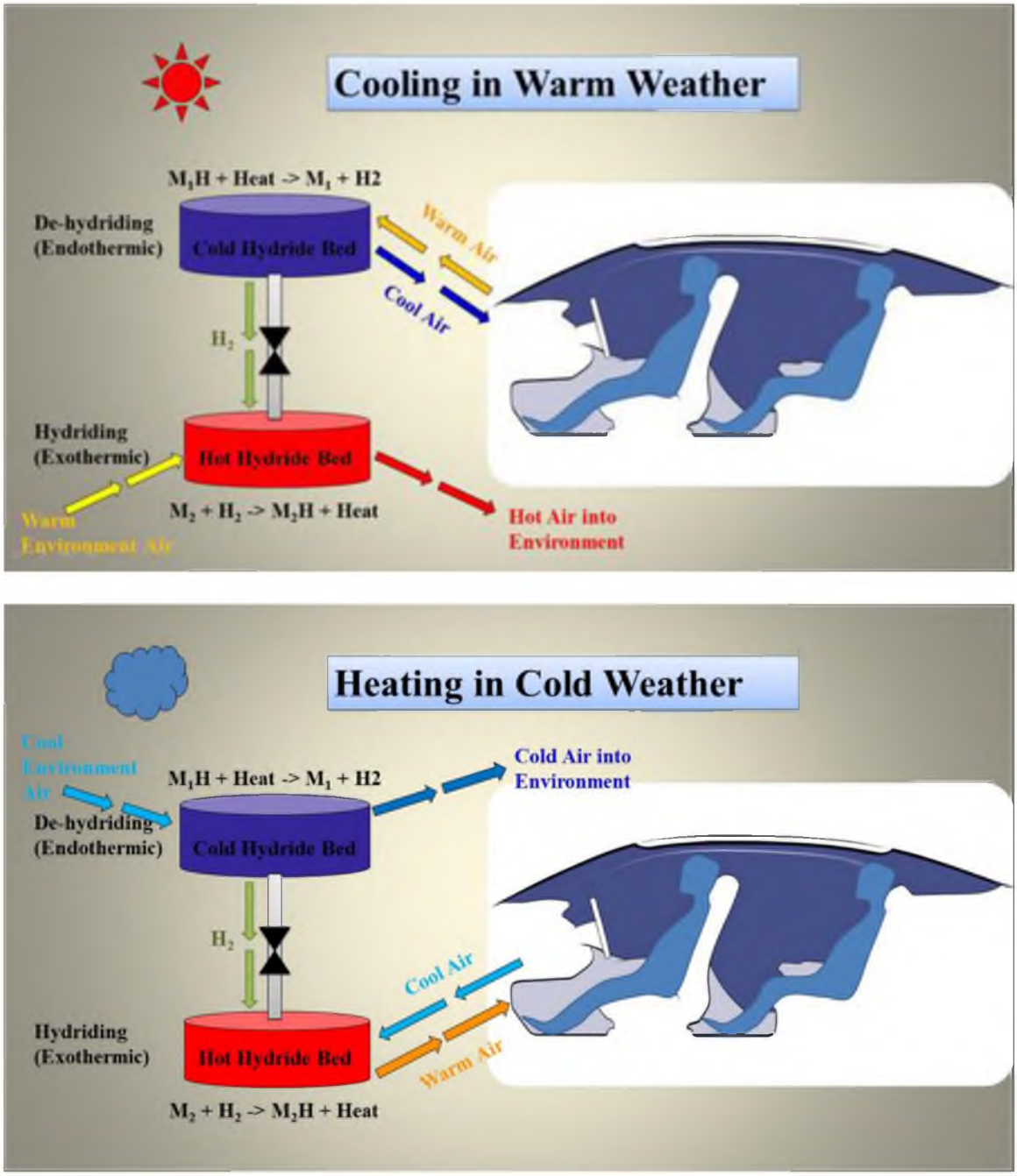

Figure 1-1. Principle of the proposed metal hydride based thermal battery system to produce cooling and heating.

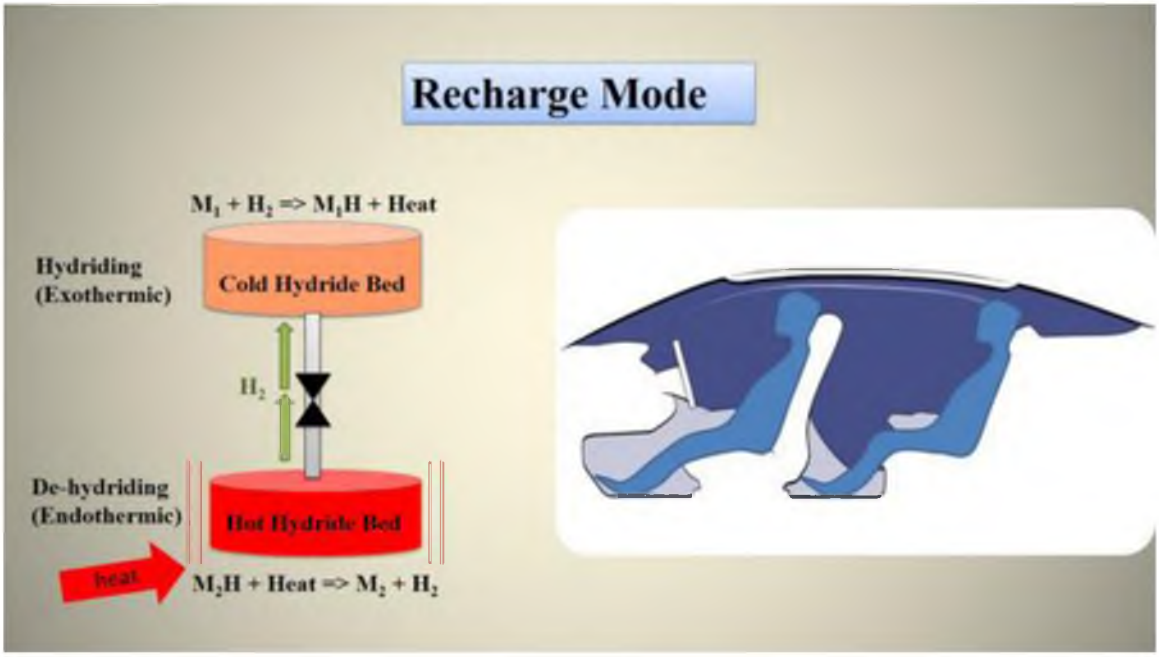

Figure 1-2. Principle of the recharge mode of the proposed metal hydride based thermal battery system.

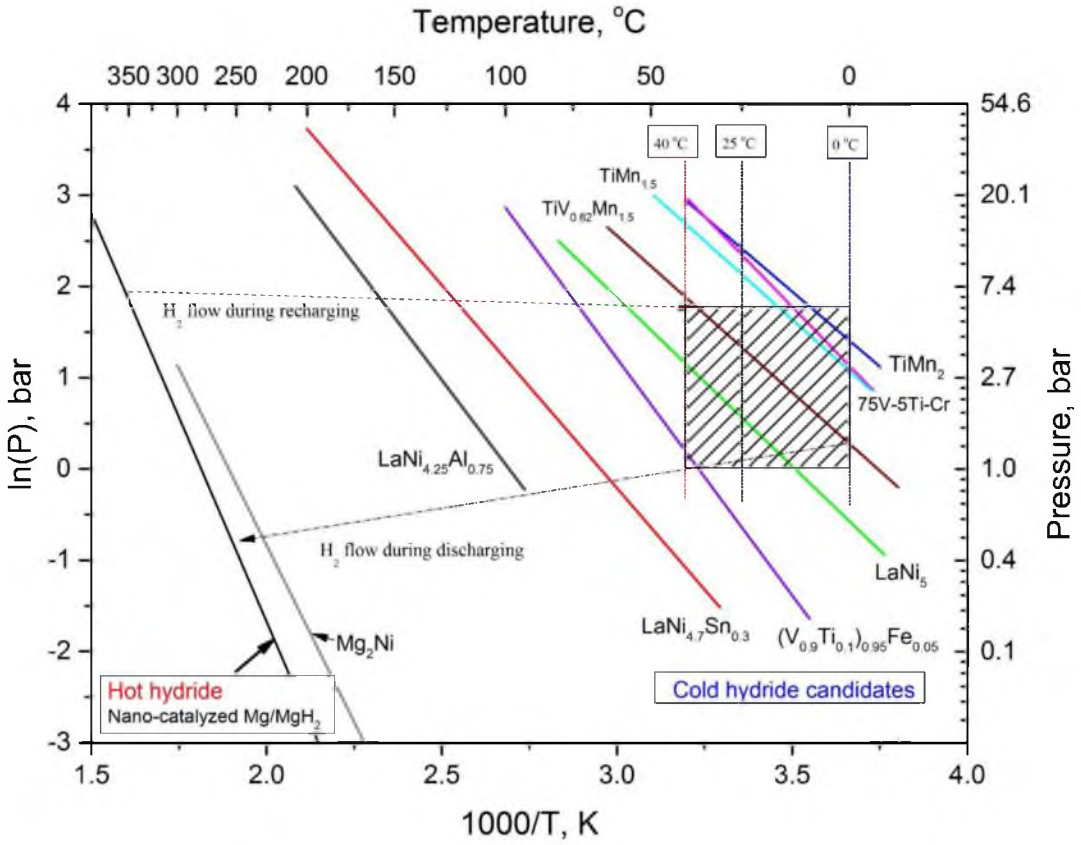

Figure 1-3. Selection of a working pair of hydride materials.

CHAPTER 2

LITERATURE REVIEW

2.1 Metal Hydride Materials

Metal hydrides refer to a group of compounds that contain hydrogen bonded to metals. In fact, this group of materials received a tremendous amount of interest in the past decades as promising candidates for hydrogen storage. In chemistry, metal hydrides can be categorized as light metal hydrides (such as MgH_2, LiH, NaH, and AlH_3); complex hydrides, including alanates, nitrides, and borohydrides, etc.; and intermetallic compounds. In the interest of the proposed thermal battery application, these families of hydrides are reviewed in the next three sections.

2.1.1 Magnesium-based Hydride

Magnesium hydride is the chemical compound MgH_2. The crystalline structure of α-MgH_2 is a rutile type under normal condition.[1] Stempfer et al.[2] determined the thermodynamic data of MgH_2, showing an enthalpy (ΔH) of 74.4 ± 0.3 kJ/mol H_2 and an entropy (ΔS) of 135.1 ± 1.9 J/mol $H_2 \cdot K$.

MgH_2 is considered a promising candidate material for both hydrogen storage and thermal energy storage owing to its high theoretical H capacity (7.6 wt%), reversibility, and low cost. Although MgH_2 meets many criteria for a hydrogen storage material, there

are two major limitations preventing it from being used in practical applications. (1) MgH_2 is thermodynamically too stable. The dehydrogenation reaction requires a high temperature of 350–400 °C.[3] A temperature of 288 °C is required to reach a dissociation hydrogen pressure of 1 bar.[2] (2) The Mg-H_2 reaction has poor kinetics. Hydrogenation of Mg without additives is usually very sluggish and typically requires a temperature higher than 300 °C and pressure more than 20 bar. Dehydrogenation of MgH_2 generally requires a temperature above 350 °C.

2.1.1.1 Kinetics

In the past 2 decades, many efforts were directed to improve the hydrogen storage properties of Mg. A very effective technique is to use mechanical ball milling to create fresh surface areas and reduce crystallite size to nanoscales.[4] Another widely-used pathway to enhance the kinetics is to use catalysts or additives that could enable magnesium to absorb and release hydrogen at relatively low temperatures. Effective additives reported in literatures can be categorized in three different groups: transition metals (TM),[5–7] transition metal oxides,[8–11] and intermetallic compounds.[12–17] These additives can also be classified as catalytic additives or alloying additives depending on their interactions with Mg. Although the effects of different materials on MgH_2 are not all well understood, we can generally refer to those as "catalysts" that are effective in increasing the rate, but do not participate in the de/hydrogenation reactions. Further, usually only a small amount are added as "catalysts." In contrast, those that are added to MgH_2 in relatively large percentages are regarded as alloying additives, which may form alloys with Mg or participate in the reactions. As examples of catalytic additive, Liang et al.[5] reported that

the hydrogen storage properties of MgH_2 can be improved by adding transition metals (Ti, V, Mn, Fe, and Ni). Among these elements, it was found that V and Ti have superior catalytic effects on desorption and absorption properties, respectively.

Lu[18, 19] and Choi[20–22] reported the catalytic effects of titanium hydride. It was demonstrated that the nanosized Mg-Ti-H system prepared by using a custom-made ultra high-energy-high-pressure (UHEHP) planetary ball milling facilitated both the hydrogenation and the dehydrogenation reaction for MgH_2. The results showed that the presence of TiH_2 decreases the enthalpy ΔH and also the entropy ΔS[18] of the dehydrogenation of MgH_2. Moreover, the system can absorb a significant amount of hydrogen at room temperature.[19] The effect of TiH_2 is attributed to the presence of Ti element, which raises the issue of whether other Ti-based alloys and intermetallic compounds could be more effective than TiH_2.

Another widely-studied catalyst is Nb_2O_5. It was shown that adding just 1 mol. % Nb_2O_5 can lead to a rapid room temperature absorption of hydrogen and desorption at temperature as low as 200 °C.[23] Nickel is also known as an effective catalyst for MgH_2. Borgdanivic et al.[24] reported a systematic study of Ni-doped Mg powder on its kinetics, H capacity, and cycling stability, which demonstrated the effectiveness of Ni-doping. Other additives, such as non-transition-metal elements,[25–28] hydride,[18, 19] nitrides,[29, 30] carbides,[29, 31, 32] halides,[33–38] and carbon,[39–42] also showed positive effects, as reported in the literature.

2.1.1.2 Thermodynamics

The general consensus is that the kinetic rate of hydrogenation of Mg is adequate when Mg is reduced to nanoscale by various mechanical ball milling methods and when it is

doped with catalytic additives, such as transition metal intermetallic compounds.[18, 43, 44] Although the kinetics of dehydrogenation of MgH_2 can also be significantly improved by using catalytic additives and nanosized particles, it is far from being satisfactory from the standpoint of practical applications because the thermodynamic properties of MgH_2 remain essentially unchanged by the addition of catalysts.[45, 46] For instance, it has been reported that catalyzed MgH_2 is able to desorb hydrogen in a temperature range as low as 150–250 °C[6, 20] and the rehydrogenation could occur even at room temperature.[5, 19, 23] There is little evidence, however, that the catalysts affect the thermodynamics.[5] Based on the published data,[2] the dissociation equilibrium pressure of MgH_2 is approximately 1.0×10^{-4} bar at 120 °C, which is grossly inadequate for practical applications such as PEM fuel cells, which have a maximum working temperature of 120 °C.

It is not impossible, however, to alter the thermodynamics of magnesium hydride. For example, theoretical calculations have suggested that a reduction in grain/particle size can lead to thermodynamic destabilization of MgH_2.[47–49] A study focusing on the quantum chemistry of the system predicted that MgH_2 clusters with a size of 0.9 nm have a desorption enthalpy of -63 kJ/mol H_2.[49] This effect of size on enthalpy was later demonstrated experimentally by Paskevicius et al.[46] who employed a mechano-chemical method to reduce MgH_2 size to 7 nm, resulting in a decrease of H by 2.83 kJ/mol H_2. Their study, however, also pointed out that the destabilization effect was less than expected from theoretical studies due to the simultaneous decrease of entropy (ΔS) that acts to partially counteract the desired effect from changes in ΔH. Moreover, it was also pointed out that a further reduction in particle size would be very challenging, and that even if particle sizes could be further reduced, it is unlikely that the nanocrystals would be sufficiently stable to

maintain the nanoscale particle size during thermal cycling.[50–52]

An alternative route for tuning the thermodynamic properties of MgH_2 is to alloy Mg with other elements such as Ni, Cu, Al, and Zn to form magnesium intermetallic compounds.[28, 53–56] One well-known hydride of this type is Mg_2NiH_4, which has a reaction enthalpy of 64.9 kJ/mol H_2. However, the hydrogen storage capacity of Mg_2NiH_4 is only 3.6 wt.% – less than half that of MgH_2. Similarly, a number of other elements can also form intermetallic compounds and reversibly store hydrogen, such as Mg_2Cu, $Mg_{17}Al_{12}$, and Mg_5Zn_2. Although the reaction enthalpies of these intermetallic compounds with hydrogen are all lower than that of Mg, they all suffer a significant penalty in terms of the loss of hydrogen storage capacity.

Recently, the use of Mg-based solid solution alloys was found to be a promising approach for altering the thermodynamics of MgH_2. Liang et al.[26, 45] reported that the plateau pressure of hydrogenation/dehydrogenation could be increased by mechanically alloying Mg with Zn, Al, Ag, Ga, Cd, and In. They concluded that cadmium and indium were most effective among within this group. Later, Zhong et al.[57] confirmed that a Mg-In solid solution had a lower reaction enthalpy than that of pure Mg.

2.1.1.3 Cyclic Stability

Although the kinetics barrier has been overcome, one of the crucial characteristics for the practical use of MgH_2 is its long-term cyclic stability. Dehouche et al.[51] investigated the effect of long-term cycling on the hydrogenating and dehydrogenating properties of MgH_2-V nanocomposite. Their result exhibited a good reversibility and only a slight deterioration in desorption rate over 2000 cycles holding at 300 °C constantly. The Mitlin

group reported a series of hydrogen cycling tests for Mg-Cr-V,[52] Mg-Nb-V,[58] Mg-Fe-Ti,[59-62] Mg-Al-Ti,[62, 63] and Mg-Cr-Ti[64] thin film nanocomposites, which were synthesized by the physical vapor deposition (PVD) method. In particular, one of their studies focused on binary Mg-Nb and ternary Mg-V-Nb systems,[58] suggesting that the cycling induced microstructure evolution in terms of Mg/MgH_2 grain size, catalyst crystalline size, and distribution of catalyst has a key influence to the hydrogenation behavior. Given the fact that the Mg/MgH_2 grain tends to coarsen and the catalyst is likely to agglomerate during the hydrogenation and dehydrogenation cycling, here rises a rational concern of the long-term stability of nanocatalyzed Mg/MgH_2. However, most of the cycling reports to date were carried out using isothermal conditions typically above 200 °C and with fairly high driving forces (large hydrogen pressure differentiation). Therefore, a comprehensive study is needed to evaluate low temperature and low hydrogen pressure differentiation kinetic behavior cycling, which is believed to be important properties for the practical usage of MgH_2.

2.1.2 Intermetallic Compound Hydrides

Research on hydrogen storage in intermetallic compounds could be traced back to the 1950's. The discovery of the hydrogen storage capability of intermetallic compounds, including $ZrNi_2$,[65] $LaNi_5$,[66] and FeTi[67] etc., opened plenty of new possibilities for industrial developments. In the past decades, thousands of intermetallic compounds hydrides were developed. Classified on the basis of their crystal structure, they are known as AB_5, AB_3, AB_2 (Laves phase), AB, and BCC (solid solution).[4] The hydrogen storage properties of some typical intermetallic compounds were summarized in Table 2-1.[68] Fast kinetics of

hydrogenation/dehydrogenation reactions were usually observed for this group of hydrides. Their thermodynamic properties vary significantly with their compositions. However, gravimetric hydrogen densities of intermetallic compounds are generally less than 3.0 wt.%.[4]

2.1.3 Complex Hydrides

Complex hydrides, as another class of hydride materials such as alanates $[AlH_4]^-$, amides $[NH_2]^-$, borohydrides $[BH_4]^-$, and so on, attracted intense interest in the field of hydrogen storage in the course of the past 2 decades.[69] The hydrides of this category often are known for their high hydrogen-storage capacity. For example, the hydrogen content is as high as 18 wt.% for $LiBH_4$. Among various complex hydrides, sodium aluminum hydride, $NaAlH_4$, would seem to be close to application as an on-board hydrogen storage material. Bogdanovic et al. demonstrated that with proper titanium compounds doping, the dehydrogenation of $NaAlH_4$ could be kinetically enhanced and maintain reversibility under moderate conditions. However, practical use of complex hydrides for hydrogen storage, to date, remains quite challenging because of their irreversibility and poor kinetics.

2.2 Thermal Energy Applications Based on Metal Hydride

Energy in thermal form plays a very important role in energy technologies. More than 60% of all primary energy consumption nowadays is wasted in the form of thermal energy.[70] In a world that is increasingly keen for renewable energy and energy efficiency, thermal energy storage (TES) is one of the most important approaches for harnessing and utilizing thermal energies such as solar energy and industrial waste heat.

The basic idea of using metal hydrides for thermal engineering applications was originated in the 1970s. It was recognized that the substantial heat of the reaction associated with hydrogenation (exothermic) and dehydrogenation (endothermic) reactions can be utilized for various practical purposes such as heat storage and heating and cooling systems. Based on this unique characteristic of metal hydrides, energy can be stored through the heat of the reaction (ΔH) where energy is released or absorbed through the following reversible metal-hydrogen chemical reaction:

$$MH_x + \Delta H \leftrightarrow M + \frac{x}{2} H_2 \quad (2\text{-}1)$$

A comprehensive review of the potential applications of metal hydrides was given by Sandrock, Suda, and Schlapbach.[71] A more recent review by Muthukumar and Groll is also available.[72] The applications of metal hydrides include thermal energy storage, temperature or heat upgrading, heat pump, or refrigeration.

To establish the background for the proposed technology, we discuss briefly in the next sections based on the use of metal hydrides for heat storage and heat pumps/refrigeration.

2.2.1 Thermal Energy Storage

TES is generally classified by different forms of storing heat, such as sensible heat, latent heat, and chemical energy.[73] Of all these forms, thermochemical energies have received growing interests due to their intrinsic high energy-density.[74] In particular, a metal hydride based TES system is very promising due to the fact that there are a large amount of metals and alloys that can combine with hydrogen to form metal hydrides under favorable temperatures and hydrogen pressure.

In 1974, Libowitz suggested that hydrogenation/dehydrogenation could be used for

thermal storage.[75, 76] Recently, there are considerable renewed interests in the use of metal hydride for, in particular, solar energy storage. Examples include the reports by Ono,[77] Yonezu et al.[78] and Bogdanovic et al.[79] A recent review by Harris et al.[74] covered the field of the use of metal hydride for concentrating solar thermal heat storage.

The principle of solar heat storage is schematically illustrated in Figure 2-1. Sunlight may be used to heat and dissociate a first metal hydride, generating hydrogen gas that can be stored in a gas tank, or more preferably in a second metal hydride from the point of view of maximizing volumetric energy density. The first metal hydride that dissociates at higher temperatures than the second metal hydride is referred to as the high temperature (HT) (or "hot") hydride, while the second is referred to the low temperature (LT) (or "cold") hydride. When sun light is not available, the HT hydride can be rehydrogenated exothermically by H_2 from the gas tank (or the LT hydride), generating heat, thus recovering the solar heat that was stored. Compared to conventional heat storage systems that rely on sensible heat and latent heat, heat storage systems using metal hydride require substantially less volume.[71, 80, 81]

2.2.2 Heat Pump

Metal hydride heat pumps and refrigerators, including those for air-conditioning of automobiles, also attracted considerable R&D interest since the 1970s. Similar to the principles of heat storage, a metal hydride heat pump (or refrigerator) usually consists of two coupled beds of metal hydrides: one contains a high temperature (HT) metal hydride, and the other contains a low temperature (LT) metal hydride. By transferring H_2 back and forth between the two beds in a closed system, the cyclic exothermic hydrogenation and

endothermic dehydrogenation can be used to produce heating or cooling.[71] The cycle can be driven by either mechanical energy (using mechanical compressor) or thermal energy (using waste heat, solar heat, etc.). A large number of patents for metal hydride heat pumps/refrigerators are available.[82–88] The thermodynamics of metal hydride heat pumps/refrigerators was reviewed by Dantzer et al.[89]

A common thread of the existing reported research that must be noted is that most of them, if not all, use metal hydrides that are the AB_5 type of intermetallic compounds of rare earth elements such as $LaNi_5$, $Ca_{0.4}Mm_{0.6}Ni_5$, and $MmNi_{4.5}Al_{0.5}$. Mm stands for misch metals, which are alloys of rare earth elements in various naturally occurring proportions. In addition to the issues of limited hydrogen capacity of those compounds, the costs of those materials are prohibitive. Original thermodynamic[16, 21–24] and economic analyses of metal hydride heat pumps/refrigerators suggested that they have some potential advantages over competing systems and thus chances for commercialization. However, for commercial reality to be achieved, the use of existing intermetallic hydrides remains a problem, especially with respect to cost and mass (low H-capacity) issues.[71]

2.2.2.1 Thermal-Driven Heat Pump (Refrigeration)

The thermodynamic principle of cooling can be illustrated using the lnP vs 1/T plot (van't Hoff plot) as shown in Figure 2-2 (a). At the beginning of a cooling cycle, the LT hydride bed is in the hydrogenated state, while the HT hydride in the dehydrogenated state. Opening the valve between the two hydride beds will allow hydrogen gas to flow from the LT hydride bed (with a relatively high pressure) towards the HT hydride bed, resulting in the cooling of LT hydride bed and the passing air due to the endothermic nature of the

dehydrogenation reaction, while the heat from the exothermic hydrogenation of the HT hydride will be rejected.

Ron designed, built, and tested a prototype of heat pump for air-conditioning of bus.[90] $MmNi_{4.15}Fe_{0.85}$ was used as the LT hydride and $LaNi_{4.7}Al_{0.3}$ as the HT hydride. The COP of the prototype air conditioner showed values between 0.22 and 0.35.

2.2.2.2 Mechanical-Driven Heat Pump

Contrasting to the waste heat driven systems, an example of mechanically driven systems was demonstrated by Magnetto et al. of Fiat and DaCosta et al of HERA USA Incorporate.[91] They developed a prototype of an air-conditioning system for automobile applications. The hydride used was a rare-earth-metal based alloy, which was not specified in their report. The authors claimed that the prototype was superior to conventional R-134a refrigerant cycles in terms of performance and maintenance. The Magnetto's system is a compressor driven system as shown in Figure 2-3. The two hydride beds use the same hydride. The compressor drives hydrogen gas to flow back and forth. At the beginning of the first half cycle, the metal hydride in Bed A is in a hydrogenated state, while the metal hydride in Bed B is in a dehydrogenated metallic state. When the valve is open, the metal hydride in Bed A dehydrogenates endothermically generating "cold." The released hydrogen from Bed A is pumped into Bed B where hydrogenation takes place, generating heat. When the hydrogen in Bed A is depleted and Bed B is hydrogenated, the system is switched to reverse the direction of hydrogen flow.

2.2.2.3 Heat Upgrading Heat Pump

The heat pump for heat upgrading was first suggested by Cottingham.[83] It is designed to use a high temperature heat source to pump heat from low temperature to a mediate temperature, which is identical to the refrigeration cycle (Figure 2-2 (b)). The output of the heat from this system at mediate temperature (T_M) can be approximately twice than the heat absorbed at high temperature (T_H). The concept of heat upgrading is believed to be useful for improving heat management of power plant and space heating.

2.2.2.4 Temperature Upgrading Heat Pump

A thermal-driven, temperature-upgrading hydride heat pump was first introduced by Terry[84] in 1976. To upgrade temperature for a heat source, two coupled hydrides are used, which is similar to the cycle of refrigeration and heat upgrading. However, the cycle direction is different, as shown in Figure 2-3. The cycle allows the system to apply heat at intermediate temperatures (T_M) and raises a part of the heat to a high temperature (T_h) while rejecting the rest of heat at a low temperature (T_L, usually ambient temperature).

2.2.2.5 Other Applications

Applying the thermochemical principles of metal hydrides, Buchner[92] developed a system for preheating of the engine and passenger compartment when the vehicle is cold in wintery climate. With the vehicle being cold, a valve is opened to release H_2 from a LT hydride bed into a previously dehydrogenated HT hydride bed thus providing instant heat. Once the vehicle is in operation, exhaust heat is used to drive the H_2 back to the low temperature hydride bed and the valve is closed. This stores heat for the next cold start.

As another example, Golben, DaCosta, and Sandrock[93] developed a prototype of a cold-start heater for automotive catalytic converters. The aim is to use the metal hydride heater to heat the catalyst instantly to its effective operating temperature, which greatly reduces the cold-start hydrocarbon emissions.

2.2.3 Hydrogen Compressor

Technically, hydride-based hydrogen compressor is not design for thermal energy application but for producing pressurized hydrogen. However, the concept of the hydrogen compressor can be easily integrated as a part of the hydride-based heat pump by providing pressurized hydrogen. Therefore, this section will describe the concept of the hydride-based hydrogen compressor.

A hydride-based hydrogen compressor has several merits in contrast to a conventional mechanical compressor. First, it is thermal-driven and utilizes low-grade waste heat instead of electricity. Second, the absence of moving parts allows the compressor to be simple to operate and maintain and also be reliable and safe.

The compressing cycle of this system is illustrated in Figure 2-4. A more detailed introduction can be found in a review paper by Lotoskyy et al.[94]

2.3 References

1. Manchester, F. D. *Phase Diagrams of Binary Hydrogen Alloys*; ASM International, 2000.

2. Stampfer, J. F.; Holley, C. E.; Suttle, J. F., The Magnesium-Hydrogen System. *J. Am. Chem. Soc.* **1960**, *82*, 3504−3508.

3. Jain, I. P.; Lal, C.; Jain, A., Hydrogen Storage in Mg: A Most Promising Material. *Int. J. Hydrogen Energy* **2010**, *35*, 5133−5144.

4. Sakintuna, B.; Lamari-Darkrim, F.; Hirscher, M., Metal Hydride Materials for Solid Hydrogen Storage: A Review. *Int. J. Hydrogen Energy* **2007**, *32*, 1121−1140.

5. Liang, G.; Huot, J.; Boily, S.; Van Neste, A.; Schulz, R., Catalytic Effect of Transition Metals on Hydrogen Sorption in Nanocrystalline Ball Milled MgH_2–Tm (Tm=Ti, V, Mn, Fe and Ni) Systems. *J. Alloys Compd.* **1999**, *292*, 247−252.

6. Hanada, N.; Ichikawa, T.; Fujii, H., Catalytic Effect of Nanoparticle 3d-Transition Metals on Hydrogen Storage Properties in Magnesium Hydride MgH_2 Prepared by Mechanical Milling. *J. Phys. Chem. B* **2005**, *109*, 7188−7194.

7. Shang, C. X.; Bououdina, M.; Song, Y.; Guo, Z. X., Mechanical Alloying and Electronic Simulations of (Mgh2+M) Systems (M=Al, Ti, Fe, Ni, Cu and Nb) for Hydrogen Storage. *Int. J. Hydrogen Energy* **2004**, *29*, 73−80.

8. Song, M.; Bobet, J.-L.; Darriet, B., Improvement in Hydrogen Sorption Properties of Mg by Reactive Mechanical Grinding with Cr_2O_3, Al_2O_3 and CeO_2. *J. Alloys Compd.* **2002**, *340*, 256−262.

9. Friedrichs, O.; Aguey-Zinsou, F.; Fernández, J. R. A.; Sánchez-López, J. C.; Justo, A.; Klassen, T.; Bormann, R.; Fernández, A., MgH_2 with Nb_2O_5 as Additive, for Hydrogen Storage: Chemical, Structural and Kinetic Behavior with Heating. *Acta Mater.* **2006**, *54*, 105−110.

10. Wang, P.; Wang, A. M.; Zhang, H. F.; Ding, B. Z.; Hu, Z. Q., Hydrogenation Characteristics of Mg–TiO_2 (Rutile) Composite. *J. Alloys Compd.* **2000**, *313*, 218−223.

11. Milošević, S.; Rašković-Lovre, Ž.; Kurko, S.; Vujasin, R.; Cvjetićanin, N.; Matović, L.; Grbović Novaković, J., Influence of VO_2 Nanostructured Ceramics on Hydrogen Desorption Properties from Magnesium Hydride. *Ceram. Int.* **2013**, *39*, 51−56.

12. Guoxian, L.; Erde, W.; Shoushi, F., Hydrogen Absorption and Desorption Characteristics of Mechanically Milled Mg-35wt.%$FeTi_{1.2}$ Powders. *J. Alloys Compd.* **1995**, *223*, 111−114.

13. Orimo, S.; Fujii, H.; Horie, S., Investigations of Interfacial Materials Design—the Effect of Interface Microstructures in $ZrCr_{1.8}Cu_{0.3}$/Mg on MgH_2 Formation as a Result of Hydrogen Interdiffusion. *J Alloys Compd.* **1995**, *231*, 766−772.

14. Liang, G.; Boily, S.; Huot, J.; Neste, A. V.; Schulz, R., Hydrogen Absorption Properties of a Mechanically Milled Mg–50 Wt.% $LaNi_5$ Composite. *J. Alloys Compd.* **1998**, *268*, 302−307.

15. Terzieva, M.; Khrussanova, M.; Peshev, P., Hydriding and Dehydriding Characteristics of Mg-$LaNi_5$ Composite Materials Prepared by Mechanical Alloying. *J. Alloys Compd.* **1998**, *267*, 235−239.

16. Wang, P.; Wang, A.; Zhang, H.; Ding, B.; Hu, Z., Hydriding Properties of a Mechanically Milled Mg–50 wt.% $ZrFe_{1.4}Cr_{0.6}$ Composite. *J. Alloys Compd.* **2000**, *297*, 240−245.

17. Fernández, J. F.; Bodega, J.; Sánchez, C. R., Hydriding/Dehydriding Properties of Magnesium–$ZrCr_2$ Composites. *J. Alloys Compd.* **2003**, *356-357*, 343−347.

18. Lu, J.; Choi, Y. J.; Fang, Z. Z.; Sohn, H. Y.; Rönnebro, E., Hydrogen Storage Properties of Nanosized MgH_2−$0.1TiH_2$ Prepared by Ultrahigh-Energy−High-Pressure Milling. *J. Am. Chem. Soc.* **2009**, *131*, 15843−15852.

19. Lu, J.; Choi, Y. J.; Fang, Z. Z.; Sohn, H. Y.; Rönnebro, E., Hydrogenation of Nanocrystalline Mg at Room Temperature in the Presence of TiH_2. *J. Am. Chem. Soc.* **2010**, *132*, 6616−6617.

20. Choi, Y. J.; Lu, J.; Sohn, H. Y.; Fang, Z. Z., Hydrogen Storage Properties of the Mg–Ti–H System Prepared by High-Energy–High-Pressure Reactive Milling. *J. Power Sources* **2008**, *180*, 491−497.

21. Choi, Y. J.; Choi, J. W.; Sohn, H. Y.; Ryu, T.; Hwang, K. S.; Fang, Z. Z., Chemical Vapor Synthesis of Mg–Ti Nanopowder Mixture as a Hydrogen Storage Material. *Int. J. Hydrogen Energy* **2009**, *34*, 7700−7706.

22. Choi, Y. J.; Lu, J.; Sohn, H. Y.; Fang, Z. Z.; Rönnebro, E., Effect of Milling Parameters on the Dehydrogenation Properties of the Mg−Ti−H System. *J. Phys. Chem. C* **2009**, *113*, 19344−19350.

23. Hanada, N.; Ichikawa, T.; Fujii, H., Hydrogen Absorption Kinetics of the Catalyzed MgH_2 by Niobium Oxide. *J Alloys Compd.* **2007**, *446-447*, 67−71.

24. Bogdanović, B.; Hartwig, T. H.; Spliethoff, B., The Development, Testing and Optimization of Energy Storage Materials Based on the MgH_2–Mg System. *Int. J. Hydrogen Energy* **1993**, *18*, 575−589.

25. Andreasen, A.; Sørensen, M. B.; Burkarl, R.; Møller, B.; Molenbroek, A. M.; Pedersen, A. S.; Andreasen, J. W.; Nielsen, M. M.; Jensen, T. R., Interaction of Hydrogen with an Mg–Al Alloy. *J. Alloys Compd.* **2005**, *404–406*, 323−326.

26. Liang, G.; Schulz, R., The Reaction of Hydrogen with Mg-Cd Alloys Prepared by Mechanical Alloying. *J. Mater. Sci.* **2004**, *39*, 1557−1562.

27. Imamura, H.; Yoshihara, K.; Yoo, M.; Kitazawa, I.; Sakata, Y.; Ooshima, S., Dehydriding of Nanocomposite Formed by Ball Milling of with Sn. *Int. J. Hydrogen Energy* **2007**, *32*, 4191−4194.

28. Vajo, J. J.; Mertens, F.; Ahn, C. C.; Bowman, R. C.; Fultz, B., Altering Hydrogen Storage Properties by Hydride Destabilization through Alloy Formation: LiH and MgH_2 Destabilized with Si. *J. Phys. Chem. B* **2004**, *108*, 13977−13983.

29. Oelerich, W.; Klassen, T.; Bormann, R., Comparison of the Catalytic Effects of V, V_2O_5, VN, and VC on the Hydrogen Sorption of Nanocrystalline Mg. *J. Alloys Compd.* **2001**, *322*, L5−L9.

30. Wang, Y.; Li, L.; An, C.; Wang, Y.; Chen, C.; Jiao, L.; Yuan, H., Facile Synthesis of Tin Decorated Graphene and Its Enhanced Catalytic Effects on Dehydrogenation Performance of Magnesium Hydride. *Nanoscale* **2014**, *6*, 6684−6691.

31. Milanović, I.; Milošević, S.; Rašković-Lovre, Ž.; Novaković, N.; Vujasin, R.; Matović, L.; Francisco Fernández, J.; Sánchez, C.; Grbović Novaković, J., Microstructure and Hydrogen Storage Properties of MgH_2–TiB_2–SiC Composites. *Ceram. Int.* **2013**, *39*, 4399−4405.

32. da Conceição, M. O. T.; Brum, M. C.; dos Santos, D. S., The Effect of V, VCl_3 and VC Catalysts on the MgH_2 Hydrogen Sorption Properties. *J. Alloys Compd.* **2014**, *586, Supplement 1*, S101−S104.

33. Malka, I. E.; Czujko, T.; Bystrzycki, J., Catalytic Effect of Halide Additives Ball Milled with Magnesium Hydride. *Int. J. Hydrogen Energy* **2010**, *35*, 1706−1712.

34. Grzech, A.; Lafont, U.; Magusin, P. C. M. M.; Mulder, F. M., Microscopic Study of TiF_3 as Hydrogen Storage Catalyst for MgH_2. *J. Phys. Chem. C* **2012**, 116, 26027−26035.

35. Danaie, M.; Mitlin, D., Tem Analysis of the Microstructure in TiF_3-Catalyzed and Pure MgH_2 During the Hydrogen Storage Cycling. *Acta Mater.* **2012**, *60*, 6441−6456.

36. Luo, Y.; Wang, P.; Ma, L.-P.; Cheng, H.-M., Hydrogen Sorption Kinetics of MgH_2 Catalyzed with NbF_5. *J. Alloys Compd.* **2008**, *453*, 138−142.

37. Shahi, R. R.; Bhatnagar, A.; Pandey, S. K.; Dixit, V.; Srivastava, O. N., Effects of Ti-Based Catalysts and Synergistic Effect of SWCNTs-TiF_3 on Hydrogen Uptake and Release from MgH_2. *Int. J. Hydrogen Energy* **2014**, 39, 14255−14261.

38. da Conceição, M. O. T.; dos Santos, D. S., Catalytic Effect of Chlorides Compounds on Hydrogen Sorption Properties of Magnesium Hydride. *J. Alloys Compd.* **2014**, 615, Supplement 1, S715−S718.

39. Yao, X.; Wu, C.; Du, A.; Zou, J.; Zhu, Z.; Wang, P.; Cheng, H.; Smith, S.; Lu, G., Metallic and Carbon Nanotube-Catalyzed Coupling of Hydrogenation in Magnesium. *J. Am. Chem. Soc.* **2007**, *129*, 15650−15654.

40. Lillo-Ródenas, M. A.; Guo, Z. X.; Aguey-Zinsou, K. F.; Cazorla-Amorós, D.; Linares-Solano, A., Effects of Different Carbon Materials on MgH_2 Decomposition. *Carbon* **2008**, *46*, 126−137.

41. Amirkhiz, B. S.; Danaie, M.; Mitlin, D., The Influence of SWCNT–Metallic

Nanoparticle Mixtures on the Desorption Properties of Milled MgH_2 Powders. *Nanotech.* **2009**, *20*, 204016.

42. Amirkhiz, B. S.; Danaie, M.; Barnes, M.; Simard, B.; Mitlin, D., Hydrogen Sorption Cycling Kinetic Stability and Microstructure of Single-Walled Carbon Nanotube (SWCNT) Magnesium Hydride (MgH_2) Nanocomposites. *J. Phys. Chem. C* **2010**, *114*, 3265−3275.

43. Bogdanović, B.; Bohmhammel, K.; Christ, B.; Reiser, A.; Schlichte, K.; Vehlen, R.; Wolf, U., Thermodynamic Investigation of the Magnesium–Hydrogen System. *J. Alloys Compd.* **1999**, *282*, 84−92.

44. Schimmel, H. G.; Huot, J.; Chapon, L. C.; Tichelaar, F. D.; Mulder, F. M., Hydrogen Cycling of Niobium and Vanadium Catalyzed Nanostructured Magnesium. *J. Am. Chem. Soc.* **2005**, *127*, 14348−14354.

45. Liang, G., Synthesis and Hydrogen Storage Properties of Mg-Based Alloys. *J. Alloys Compd.* **2004**, *370*, 123−128.

46. Paskevicius, M.; Sheppard, D. A.; Buckley, C. E., Thermodynamic Changes in Mechanochemically Synthesized Magnesium Hydride Nanoparticles. *J. Am. Chem. Soc.* **2010**, *132*, 5077−5083.

47. Berube, V.; Chen, G.; Dresselhaus, M. S., Impact of Nanostructuring on the Enthalpy of Formation of Metal Hydrides. *Int. J. Hydrogen Energy* **2008**, *33*, 4122−4131.

48. Berube, V.; Dresselhaus, M. S.; Chen, G., Temperature Dependence of the Enthalpy of Formation of Metal Hydrides Characterized by an Excess Volume. *Int. J. Hydrogen Energy* **2008**, *33*, 5617−5628.

49. Wagemans, R. W. P.; van Lenthe, J. H.; de Jongh, P. E.; van Dillen, A. J.; de Jong, K. P., Hydrogen Storage in Magnesium Clusters: Quantum Chemical Study. *J. Am. Chem. Soc.* **2005**, *127*, 16675−16680.

50. Manivasagam, T. G.; Magusin, P. C. M. M.; Srinivasan, S.; Krishnan, G.; Kooi, B. J.; Notten, P. H. L., Electrochemical Deuteration of Metastable MgTi Alloys: An Effective Way to Inhibit Phase Segregation. *Adv. Energ. Mater.* **2013**, 4, 1300590.

51. Dehouche, Z.; Djaozandry, R.; Huot, J.; Boily, S.; Goyette, J.; Bose, T. K.; Schulz, R., Influence of Cycling on the Thermodynamic and Structure Properties of Nanocrystalline Magnesium Based Hydride. *J. Alloys Compd.* **2000**, *305*, 264−271.

52. Zahiri, B.; Danaie, M.; Tan, X.; Amirkhiz, B. S.; Botton, G. A.; Mitlin, D., Stable Hydrogen Storage Cycling in Magnesium Hydride, in the Range of Room Temperature to 300 °C, Achieved Using a New Bimetallic Cr-V Nanoscale Catalyst. *J. Phys. Chem. C* **2011**, *116*, 3188−3199.

53. Reilly, J. J.; Wiswall, R. H., Reaction of Hydrogen with Alloys of Magnesium and Copper. *Inorg. Chem.* **1967**, *6*, 2220−2223.

54. Reilly, J. J.; Wiswall, R. H., Reaction of Hydrogen with Alloys of Magnesium and Nickel and the Formation of Mg_2NiH_4. *Inorg. Chem.* **1968**, *7*, 2254−2256.

55. Bruzzone, G.; Costa, G.; Ferretti, M.; Olcese, G. L., Hydrogen Storage in $Mg_{51}Zn_{20}$. *Int. J. Hydrogen Energy* **1983**, *8*, 459−461.

56. Walker, G. S.; Abbas, M.; Grant, D. M.; Udeh, C., Destabilisation of Magnesium Hydride by Germanium as a New Potential Multicomponent Hydrogen Storage System. *Chem. Commun.* **2011**, *47*, 8001−8003.

57. Zhong, H. C.; Wang, H.; Liu, J. W.; Sun, D. L.; Zhu, M., Altered Desorption Enthalpy of MgH_2 by the Reversible Formation of Mg(In) Solid Solution. *Scripta Mater.* **2011**, *65*, 285−287.

58. Tan, X.; Zahiri, B.; Holt, C. M. B.; Kubis, A.; Mitlin, D., A Tem Based Study of the Microstructure During Room Temperature and Low Temperature Hydrogen Storage Cycling in MgH_2 Promoted by Nb–V. *Acta Mater.* **2012**, *60*, 5646−5661.

59. Kalisvaart, W. P.; Kubis, A.; Danaie, M.; Amirkhiz, B. S.; Mitlin, D., Microstructural Evolution During Hydrogen Sorption Cycling of Mg–FeTi Nanolayered Composites. *Acta Mater.* **2011**, *59*, 2083−2095.

60. Amirkhiz, B. S.; Zahiri, B.; Kalisvaart, P.; Mitlin, D., Synergy of Elemental Fe and Ti Promoting Low Temperature Hydrogen Sorption Cycling of Magnesium. *Int. J. Hydrogen Energy* **2011**, *36*, 6711−6722.

61. Zahiri, B.; Harrower, C. T.; Amirkhiz, B. S.; Mitlin, D., Rapid and Reversible Hydrogen Sorption in Mg−Fe−Ti Thin Films. *Appl. Phys. Lett.* **2009**, *95*, 103114−3.

62. Kalisvaart, W. P.; Harrower, C. T.; Haagsma, J.; Zahiri, B.; Luber, E. J.; Ophus, C.; Poirier, E.; Fritzsche, H.; Mitlin, D., Hydrogen Storage in Binary and Ternary Mg-Based Alloys: A Comprehensive Experimental Study. *Int. J. Hydrogen Energy* **2010**, *35*, 2091−2103.

63. Zahiri, R.; Zahiri, B.; Kubis, A.; Kalisvaart, P.; Shalchi Amirkhiz, B.; Mitlin, D., Microstructural Evolution During Low Temperature Sorption Cycling of Mg-AlTi Multilayer Nanocomposites. *Int. J. Hydrogen Energy* **2012**, *37*, 4215−4226.

64. Zahiri, B.; Amirkhiz, B. S.; Mitlin, D., Hydrogen Storage Cycling of MgH_2 Thin Film Nanocomposites Catalyzed by Bimetallic Cr−Ti. *Appl. Phys. Lett.* **2010**, *97*, 083106−3.

65. Libowitz, G. G.; Hayes, H. F.; Gibb, T. R. P., The System Zirconium–Nickel and Hydrogen. *J. Phys. Chem.* **1958**, *62*, 76−79.

66. Van Mal, H. H.; Buschow, K. H. J.; Miedema, A. R., Hydrogen Absorption in $LaNi_5$ and Related Compounds: Experimental Observations and Their Explanation. *J. Less Common Met.* **1974**, *35*, 65−76.

67. Reilly, J. J.; Wiswall, R. H., Formation and Properties of Iron Titanium Hydride. *Inorg. Chem.* **1974**, *13*, 218−222.

68. Chen, P.; Zhu, M., Recent Progress in Hydrogen Storage. *Mater. Today* **2008**, *11*, 36−43.

69. Orimo, S.-i.; Nakamori, Y.; Eliseo, J. R.; Züttel, A.; Jensen, C. M., Complex Hydrides for Hydrogen Storage. *Chem. Rev.* **2007**, *107*, 4111−4132.

70. Cot-Gores, J.; Castell, A.; Cabeza, L. F., Thermochemical Energy Storage and Conversion: A-State-of-the-Art Review of the Experimental Research under Practical Conditions. *Renew. Sus. Energ. Rev.* **2012**, *16*, 5207−5224.

71. Sandrock, G.; Suda, S.; Schlapbach, L., *Hydrogen in Intermetallic Compounds II*, 2 ed.; Springer-Verlag, 1992; Vol. 67, p 328.

72. Muthukumar, P.; Groll, M., Erratum to "Metal Hydride Based Heating and Cooling Systems: A Review" [International Journal of Hydrogen Energy (2010) 35: 3817–3831]. *Int. J. Hydrogen Energy* **2010**, *35*, 8816−8829.

73. Zalba, B.; Marín, J. M.; Cabeza, L. F.; Mehling, H., Review on Thermal Energy Storage with Phase Change: Materials, Heat Transfer Analysis and Applications. *Appl. Therm. Eng.* **2003**, *23*, 251−283.

74. Harries, D. N.; Paskevicius, M.; Sheppard, D. A.; Price, T. E. C.; Buckley, C. E., Concentrating Solar Thermal Heat Storage Using Metal Hydrides. *Proc. IEEE* **2012**, *100*, 539−549.

75. Libowitz, G. In *Metal Hydrides for Thermal Energy Storage*, 9th Intersociety Energy Conversion Engineering Conference, **1974**; pp 322−325.

76. Libowitz, G.; Blank, Z. In *An Evaluation of the Use of Metal Hydrides for Solar Thermal Energy Storage*, 11th Intersociety Energy Conversion Engineering Conference, **1976**; pp 673−680.

77. Ono, S.; Yamaguchi, M.; Ohta, T., Solar Energy Storage by Metal Hydride. In *Solar-Hydrogen Energy Systems* Pergamon Press, Oxford and New York, **1979**, *1*, 193−224.

78. Yonezu, I.; Nasako, K.; Honda, N.; Sakai, T., Development of Thermal Energy Storage Technology Using Metal Hydrides. *J. Less Common Met.* **1983**, *89*, 351−358.

79. Bogdanović, B.; Ritter, A.; Spliethoff, B., Active MgH_2-Mg Systems for Reversible

Chemical Energy Storage. *Angew. Chem. Int. Ed.* **1990**, *29*, 223−234.

80. Felderhoff, M.; Bogdanović, B., High Temperature Metal Hydrides as Heat Storage Materials for Solar and Related Applications. *Int. J. Mol. Sci.* **2009**, *10*, 325−344.

81. Wenzl, H., Properties and Applications of Metal Hydrides in Energy Conversion Systems. *Int. Mater. Rev.* **1982**, *27*, 140−168.

82. McClaine, A. W. C., Ventura Method and Apparatus for Heat Transfer, Using Metal Hydrides. US4039023 A, Aug. 2, 1977.

83. Cottingham, J. G. Hydride Heat Pump. US4044819 A, Aug. 30, 1977.

84. Terry, L. E. Hydrogen-Hydride Absorption Systems and Methods for Refrigeration and Heat Pump Cycles. US4055962 A, Nov. 1, 1977.

85. Ferguson, E. T.; Van Mal, H. H. Cyclic Desorption Refrigerator and Heat Pump, Respectively. US4111002 A, Sep. 5, 1978.

86. Bowman, W. H.; Sirovich, B. E. Moving Bed Hydride/Dehydride Systems. US4178987 A, Dec. 18, 1979.

87. Sirovich, B. E. Hydride Heat Pump. US4200144 A, Apr. 29, 1980.

88. Fields, P. R.; Gruen, D. M. System for Thermal Energy Storage, Space Heating and Cooling and Power Conversion. US4262739 A, 1981.

89. Dantzer, P.; Orgaz, E., Thermodynamics of Hydride Chemical Heat Pump—II. How to Select a Pair of Alloys. *Int. J. Hydrogen Energy* **1986**, *11*, 797−806.

90. Ron, M., A Hydrogen Heat Pump as a Bus Air Conditioner. *J. Less Common Met.* **1984**, *104*, 259−278.

91. Magnetto, D.; Mola, S.; Dacosta, D. H.; Golben, M., A Metal Hydride Mobile Air Conditioning System. SAE Technical Paper 2006-01-1235, **2006**, doi:10.4271/2006-01-1235..

92. Buchner, H.; Saufferer, H. Parking Heater and Method Using Hydrides in Motor Vehicles Powered by Hydrogen. US4214699 A, Jul. 29, 1980.

93. Golben, P. M.; DaCosta, D.; Sandrock, G., Hydride-Based Cold-Start Heater for Automotive Catalyst. *J. Alloys Compd.* **1997**, *253–254*, 686−688.

94. Lototskyy, M. V.; Yartys, V. A.; Pollet, B. G.; Bowman, R. C., Metal Hydride Hydrogen Compressors: A Review. *Int. J. Hydrogen Energy* **2014**, *39*, 5818−5851.

Table 2-1. Crystal structure and hydrogen storage properties of typical intermetallic compound hydrides.

Type	Metal	Hydrides	Crystal structure	Mass%	P_{eq} @ T
AB_5	$LaNi_5$	$LaNi_5H_6$	Hexagonal	1.4	2 bar, 298 K
AB_3	$CaNi_3$	$CaNi_3H_{4.4}$	Hexagonal	1.8	0.5 bar, 298 K
AB_2	ZrV_2	$ZrV_2H_{5.5}$	Hexagonal	3.0	10^{-8} bar, 323 K
AB	TiFe	$TiFeH_{1.8}$	Cubic	1.9	5 bar, 303 K
Solid solution	Ti-V-based	Ti-V-H_4	Cubic	2.6	1 bar, 298 K

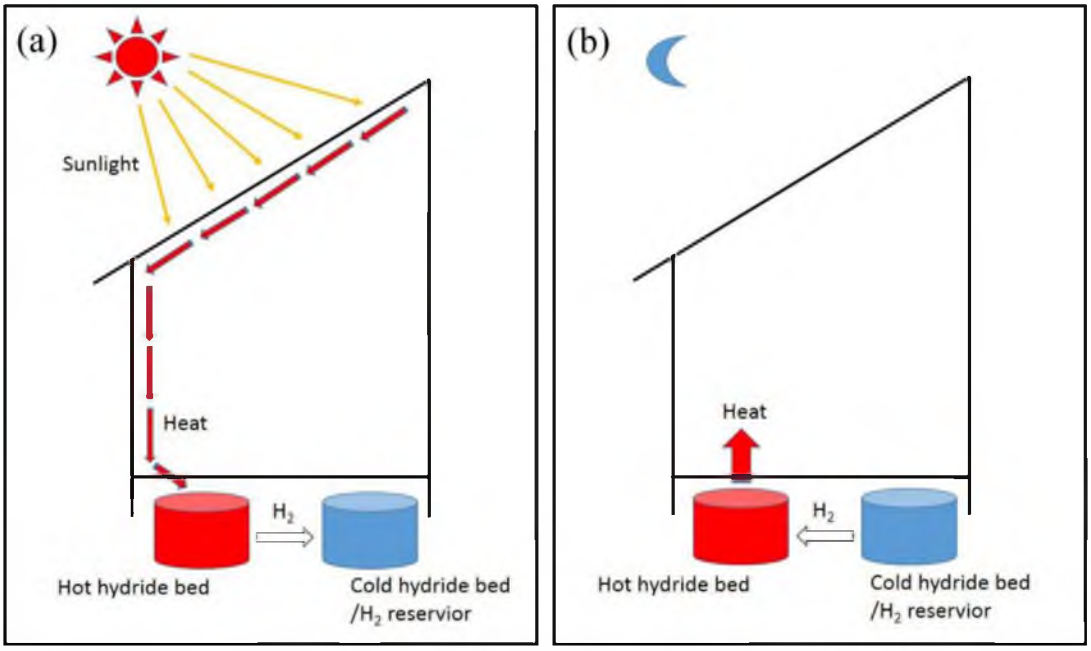

Figure 2-1. Principle of metal hydride heat storage system for solar energy storage. (a) Heat is absorbed at daytime, (b) Heat is released at nighttime.

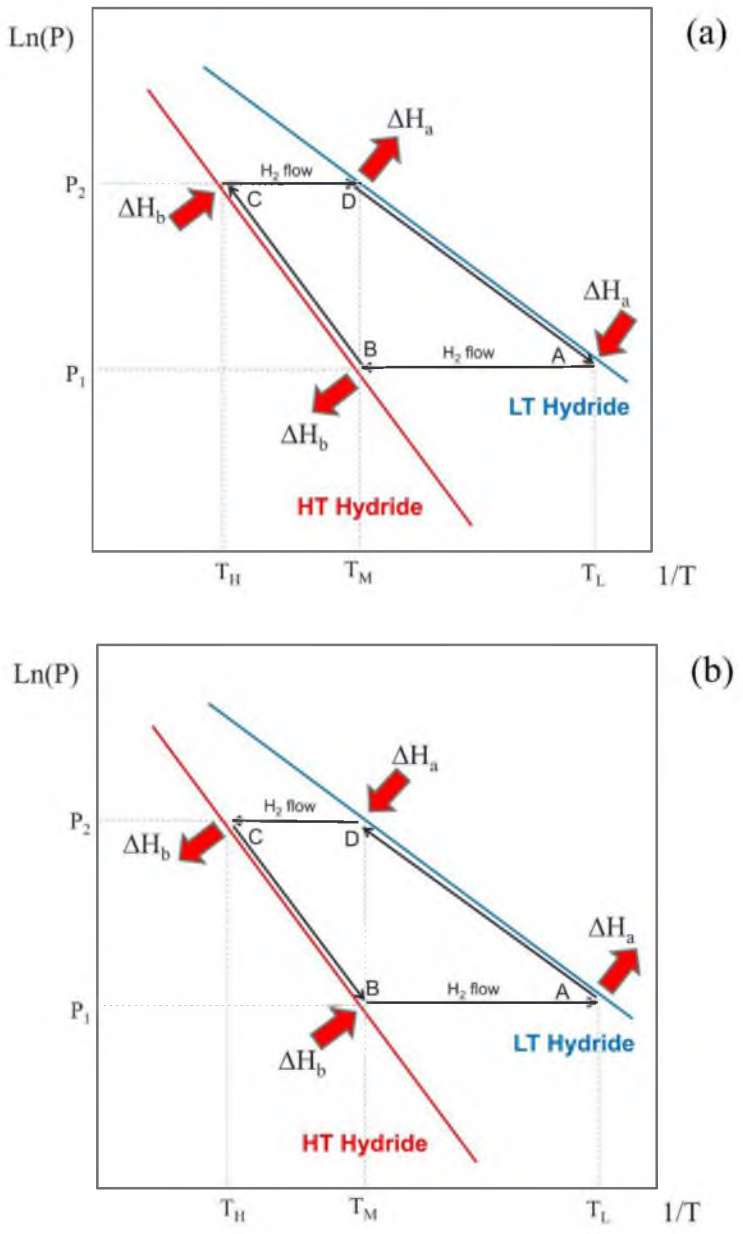

Figure 2-2. Thermodynamic principle of metal hydride based heat pumps. (a) Waste-heat-driven air conditioner using a pair of metal hydrides, where T_H is the temperature of the heat source, T_M generally refers to ambient temperature, and T_L is the cooling temperature; (b) the temperature upgrading device, where T_H is the heating temperature, T_M is the temperature of the heat source, and T_L refers to ambient temperature.

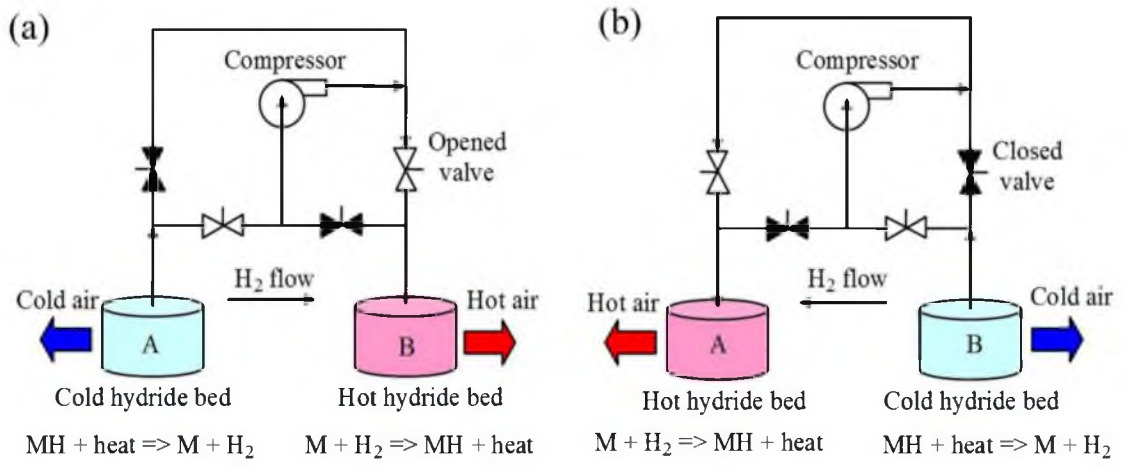

Figure 2-3. Principle of mechanically driven heat pump/refrigerator based on metal hydride. (a) First half cycle; (b) Second half cycle.

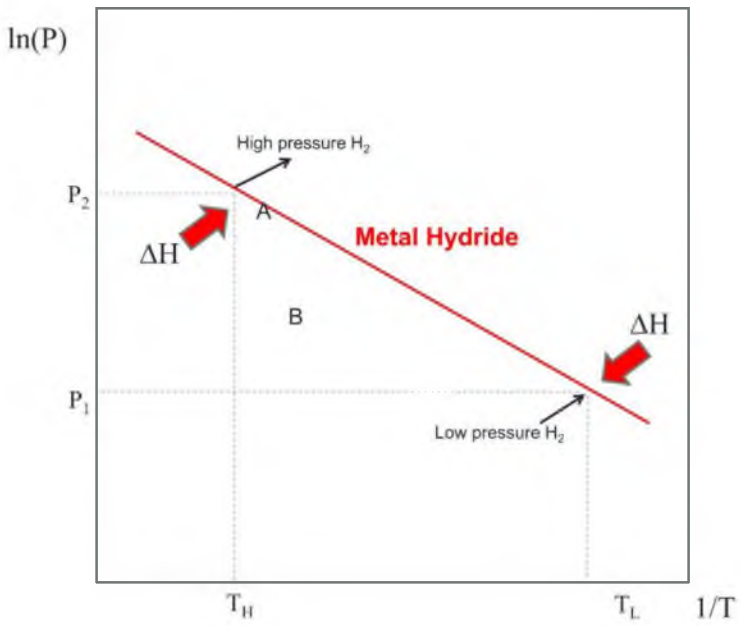

Figure 2-4. Principle of hydrogen compressor based on metal hydride.

CHAPTER 3

EXPERIMENTAL METHODS

3.1 Materials and Material Handling

All the starting materials involved in the current research, such as magnesium hydride (MgH_2), titanium hydride (TiH_2), titanium-manganese alloy ($TiMn_2$), etc., were purchased from Sigma-Aldrich and Alfa-Aesar. Some other additives were custom made by arc-melting technique or powder metallurgy process in our laboratory. There are some materials used in the present research were provided by other laboratory. All this information is listed in Table 3-1.

In order to prevent samples and raw materials from undergoing oxidation and/or hydroxide formation and/or other contamination, all the material handling was carried out in a glove-box filled with circulating purified argon (99.999%), which contains less than 1 ppm water vapor and oxygen, respectively. All the air-sensitive sample were sealed inside the glove-box before being taken out.

3.2 Ultra High Energy High Pressure (UHEHP) Ball Milling

A custom design of the planetary mill was used for synthesis of nanosized MgH_2 particles. This dual-drive planetary mill can achieve ultra high grinding rates and an enhanced milling effect compared to common mills. By creating a very high centrifugal

field, the custom made planetary milling machine is able to efficiently confine the particles to nanoscale and reducing the "dead zone" effect.[1]

Before each milling batch, the mixtures of MgH_2 and additive(s) with a various molar ratio were weighed and handled in the glove box. Mixture and ¼ inch stainless steel balls (ca. 330 g) were sealed in a stainless steel milling canister (Parr instrument) inside the glove box. Then, the canister filled with the MgH_2+A (A stands for additive) mixture was pressurized by hydrogen gas up to 150 bar and evacuated 3−4 times for purification. The ultra high energy high pressure (UHEHP) milling proceeded for a certain amount of time using the custom-made planetary ball milling machine. During the milling operation, to restrict the temperature rise of the canister, there was an intermittent time of 0.5 hour after 2 hours continuous milling. After UHEHP milling, the high pressure hydrogen remaining in the canister was evacuated. Then the canister was transfer into the glove-box.

3.3 Characterization Methods

3.3.1 Pressure-Composition-Isothermal (PCI) Measurement

The pressure-composition-isothermal (PCI) measurement, known as the "Sieverts method," is a volumetric technique that is most widely used to characterize solid-gas sorption/desorption reaction.[2] The Sieverts method is a volumetric measurement technique that was commonly used to measure the de/sorption of gaseous hydrogen by materials.[3] A detailed description of this measurement method can be found in the literature.[4, 5] The amount of hydrogen absorbed by a sample is calculated using the real gas law:

$$PV = nZRT \tag{3-1}$$

where P is the pressure, V is the volume, n is the value of moles, Z is the gas

compressibility, R is the universal gas constant, and T is the temperature.

The isothermal hydrogenation, dehydrogenation, and equilibrium pressure measurement in the current research was performed by using a commercial Sieverts type apparatus (Hy-Energy LLC., PCTPro-2000). The PCTPro-2000 used an ultra high purity (UHP) hydrogen supply with 99.999% purity. Hydrogen pressure was measured by a Teledyne Taber model 206 piezoelectric transducer, 0–200 bar, with a resolution of 10^{-3} bar. 0.1–0.3 g of hydride powder was packed in a small stainless steel sample holder, which was then sealed in a PCT high-pressure-high-temperature sample vessel. Before each kinetic test, the volume of the PCT sample vessel was calibrated using helium gas. Also the whole PCT system as well as the sample vessel was required to pass a pressurizing leak test before starting an experiment. During the experiments, the sample was heated by a Watlow band heater, and the temperature of sample was held constant by a PID controller (Watlow, PID Controller SD). The amount of hydrogen release-uptake was calculated based on the changes of pressures in calibrated volumes.

3.3.2 Thermal Gravimetric Analysis (TGA)

Thermogravimetric analysis (TGA) is a gravimetric technique to characterize the hydrogen releasing of hydrides at profiled temperature or isothermal. The dehydrogenation experiments were conducted by the use of a thermal gravimetric analyzer (Shimadzu, TGA50) in which about 15 mg samples were heated using a heating rate of 5 °C under 50 ml/min flowing ultra high purity argon. The TGA instrument was placed inside the glove box at all time. TA60 (version 2.00) software was used to analyze the obtained TGA curves.

3.3.3 X-Ray Diffraction (XRD)

X-ray diffraction is a useful tool to determine the crystalline structure of materials. In this work, the identification of phase composition was carried out using a high energy synchrotron X-ray diffraction (HE-XRD).

The *in situ* HE-XRD measurements were carried out at the 11-ID-C beam-line and the 11-ID-D beam-line of the Advanced Photon Source (APS), Argonne National Laboratory. The *ex situ* HE-XRD measurements were also conducted at the same beam-lines. The X-ray wave length used in the 11-ID-D beam-line was 0.774901 Å, and the X-ray wave length used in the 11-ID-C beam-line was 0.108040 Å. The XRD patterns were collected in the transmission mode using a Perkin Elmer large area detector. The collected 2D patterns were then integrated into conventional 1D patterns (intensity vs. 2θ) for final data analysis using the Fit2d software. Rehydrogenated samples were also characterized by the same technique. All samples were completely covered with kapton tape as a protective film in the glove box to avoid undesired reactions with ambient atmosphere.

3.3.4 Scanning Electron Microscopy (SEM)

The morphological and microstructural characterization of the materials was performed using scanning electron microscopy (SEM) for imaging. The SEM used for the current work is FEI NovaNano 630, which are high-resolution field emission gun SEMs.

3.3.5 Transmission Electron Microscopy (TEM)

The microstructure characterization of the materials was also carried out using transmission electron microscopy (TEM). TEM images and Energy-Dispersive X-ray

Spectroscopy (EDS) spectra were collected using a JEOL 2800 Scanning Transmission Electron Microscope, operated at 200 kV with a 1.0 nm probe size. The EDS spectra and spectral maps were acquired using a dual SDD detector system.

3.4 References

1. Butler, B. G.; Lu, J.; Fang, Z. Z.; Rajamani, R. K., Production and Characteristics of Nanocrystalline Tungsten Carbide Powder Using a High Energy Dual-Drive Planetary Mill. *Int. J. Powder Metallurgy* **2007**, *43*, 35.

2. Broom, D., Hydrogen Sorption Properties of Materials. In *Hydrogen Storage Materials*, Springer London: 2011; pp 61−115.

3. Broom, D., Gas Sorption Measurement Techniques. In *Hydrogen Storage Materials*, Springer London: 2011; pp 117−139.

4. Lee, Y.-W.; Clemens, B. M.; Gross, K. J., Novel Sieverts' Type Volumetric Measurements of Hydrogen Storage Properties for Very Small Sample Quantities. *J. Alloys Compd.* **2008**, *452*, 410−413.

5. Gross, K. J. Method and Apparatus for Measuring Gas Sorption and Desorption Properties of Materials. US patent, US7429358B1, Sep. 30, 2008.

Table 3-1. Raw materials for this study.

Materials	Supplier (Part No.)	Remarks
MgH_2	Sigma-Aldrich (683043)	
$Ti_{0.98}Zr_{0.02}V_{0.43}Fe_{0.09}Cr_{0.05}Mn_{1.5}$ alloy	Sigma-Aldrich (685941)	Pulverized by hydrogenating-dehydrogenating cycle, denoted as $TiMn_2$
$TiNb_{0.2}$ alloy	Custom making	Sintered
TiFe alloy	Alfa Aesar (43500)	
TiAl alloy	Alfa Aesar (88393)	
Ti_3Al alloy	Alfa Aesar (43101)	
$TiMn_{1.5}V_{0.62}$ alloy	GfE, Hydralloy C	Pulverized by hydrogenating-dehydrogenating cycle, denoted as TiMnV
TiNi alloy	Alfa Aesar (88384)	
75V-5Ti-20Cr alloy	HRL Lab (prepared at Ames Lab, ISU)	Arc-melted, pulverized by hydrogenating, 75 at.% V, 5 at.% Ti, 20 at.% Cr
80V-8Ti-12Cr alloy	HRL Lab (prepared at Ames Lab, ISU)	Arc-melted, pulverized by hydrogenating, 80 at.% V, 8 at.% Ti, 12 at.% Cr
80V-20Ti alloy	Custom prepared (UU)	Arc-melted, pulverized by hydrogenating, 80 at.% V, 20 at.% Ti
80V-20Cr alloy	Custom prepared (UU)	Arc-melted, pulverized by hydrogenating, 80 at.% V, 20 at.% Cr
$LaNi_5$ alloy	Sigma-Aldrich (685933)	
$LaNi_{4.7}Sn_{0.3}$ alloy	Custom prepared (UU)	Arc-melted, pulverized by hydrogenating
AlLi alloy	Sigma-Aldrich (426490)	
LiH	Alfa Aesar (41596)	
Y	Sigma-Aldrich (261327)	
Y_2O_5	Sigma-Aldrich (205168)	
Ti	Sigma-Aldrich (268496)	
TiH_2	Sigma-Aldrich (209279)	
Zr	Alfa Aesar (00847)	
ZrH_2	Alfa Aesar (89484)	
ZrO_2	Sigma-Aldrich (544760)	
V	Alfa Aesar (12234)	
$VH_{0.7}$	Custom prepared (UU)	Hydrogenated V metal powder
V_2O_3	Alfa Aesar (43377)	
Nb	Sigma-Aldrich (262722)	
$NbH_{0.8}$	Custom prepared (UU)	Hydrogenated Nb metal powder
Nb_2O_5	Sigma-Aldrich (203920)	
Ta	Sigma-Aldrich (262846)	
Ta_2O_5	Sigma-Aldrich (204536)	
Cr	Alfa Aesar (10148)	
Mo	Alfa Aesar (10030)	
MoO_2	Sigma-Aldrich (234761)	
MoO_3	Sigma-Aldrich (711209)	
WO_3	Sigma-Aldrich (550086)	
Mn	Sigma-Aldrich (266132)	
Fe	Alfa Aesar (10214)	
Co	Alfa Aesar (10453)	
Ni	Alfa Aesar (43214)	

Table 3-1. Continued.

Materials	Supplier (Part No.)	Remarks
Al	Alfa Aesar (43891)	
Ge	Alfa Aesar (10190)	
In	Alfa Aesar (11024)	
Sn	Alfa Aesar (10397)	
Si	Alfa Aesar (12681)	
Pb	Alfa Aesar (10223)	
Sb	Alfa Aesar (10099)	
Graphite	Alfa Aesar (40798)	
Carbon nanotube	Alfa Aesar (44945)	
Mesoporous Carbon	Sigma-Aldrich (699624)	

CHAPTER 4

KINETICS IMPROVEMENT OF MAGNESIUM HYDRIDE BY CATALYTIC DOPING

In this chapter, the research was designed to investigate the effects of different catalysts on the hydrogen adsorption and desorption properties of MgH_2. Catalytic doping has been known as an important method for improving the hydrogen storage properties of MgH_2. There is a lack of a standard methodology, however, that can be used to select or compare the effectiveness of different additives. A systematic experimental survey was carried out in this study to compare a wide range of additives, including transitions metals, transition metal oxides, hydrides, intermetallic compounds, and carbon materials, with respect to their effects on dehydrogenation properties of MgH_2.

The experimental survey restricted catalyst selection of a relatively small range to Ti, V, and Nb compounds and alloys. The following works focused on evaluation of Ti and V-based intermetallic alloys as dopant to MgH_2 and hydrogen storage properties of the doped systems. The results demonstrate that all the selected Ti-based intermetallic catalysts have significant catalytic effects on the hydrogen storage properties of magnesium hydride.

4.1 Catalyst Candidates Screening

Although considerable research has been reported in recent decades on using additives to improve the hydrogen storage properties of MgH_2,[1–3] to date, it is still difficult to assess and compare the effectiveness of different additives because there are considerable discrepancies among different previous research reports, which may be attributed to different methodologies in terms of material preparation and characterization. Forty-nine MgH_2-additive materials were synthesized and characterized to compare the effect of those additives on the dehydrogenation properties of MgH_2. The additives were selected from a wide range of materials including transition metal or other elemental materials, transition metal oxides, transition metal hydrides, transition metal intermetallics, and carbon materials. Since the preparation process and the characterization were maintained throughout these experiments, the results of this work provide analogous data for guiding both experimental and mechanism studies of MgH_2 with additives.

In order to quantitatively characterize the dehydrogenation behavior, TGA analysis was utilized to test different MgH_2 systems with additives because the TGA dehydrogenation curve was considered as a prompt and efficient method to compare kinetics of MgH_2 system. Two temperature points, namely the calculated on-set dehydrogenation temperature ($T_{on\text{-}set}$) and the calculated end dehydrogenation temperature (T_{end}) were determined based on TGA curves. All the TGA experiments were carried out using a heating rate of 5 °C/min. As illustrated in Figure 4-1, the point of $T_{on\text{-}set}$ was determined by the intersection of the extension line of the high plateau (the horizontal part of the curve before the dehydrogenation reaction) and the tangent of the half-dehydrogenated point (the midpoint in Figure 4-1). The point of T_{end} was determined by the intersection of the

extension line of the low plateau (the horizontal part of the curve after the dehydrogenation reaction) and the tangent of the half-dehydrogenating point.

Figure 4-2 summarizes the key results of all MgH_2-additive samples that were prepared and tested in this work. The additives were classified into groups as transition metals and their compounds (oxides and hydride), intermetallic compounds, III-B and IV-B group elements, and carbon materials. In addition, MgH_2 with LiH as an additive and three other compositions with binary-additives (combining two additives together), i.e., MgH_2-TiH_2-Ni, MgH_2-TiH_2-Nb_2O_5, and MgH_2-In-$TiMn_2$, were synthesized and characterized. The dehydrogenation temperatures of as-milled pure MgH_2 were also given as a baseline for comparison. The effectiveness of additives was evaluated by comparing their $T_{on\text{-}set}$ and T_{end} to those of the as-milled MgH_2 sample without any additives (see the lines in Figure 4-2).

4.1.1 Transition Metals and Their Hydrides and Oxides

The most effective additives in this study were found in the IV-A and V-A groups. The elements from the VII-A (Mn) and the VIII-A (Fe, Co, Ni) groups had moderate catalytic effects. For the VI A group, metal Cr presented a moderate improvement; however, Mo, Mo oxides, and W oxides seemed to have no effect. Yttrium (III-A group) and Yttrium oxide showed no improvement to the kinetics. For the catalysts in metallic form, Ti exhibited the lowest $T_{on\text{-}set}$, followed by V, Mn, Zr, Nb, Fe, Ni, Cr, and Co.

It was seen that the light elements such as Ti, V, and their compounds were more effective than heavier metals (Zr, Nb, Ta) in the same groups. Another interesting observation was that the metals of Ti, Zr, and V showed stronger catalytic effects than their

hydrides and oxides. However, for Nb and Ta metals and compounds, the oxides performed better than their hydrides or the pure metals.

4.1.2 Intermetallic Compounds

A set of intermetallic compounds as additives was also examined. It was found that the compounds containing Ti and/or V ($TiMn_2$, $TiNb_{0.2}$, TiFe, TiAl, Ti_3Al, TiVMn, TiNi, VTiCr) exhibited relatively low $T_{on\text{-}set}$ and T_{end}. It was noted that some of the compounds, such as $TiMn_2$, TiFe, TiVMn, and VTiCr, were themselves hydride-forming materials with very good reaction kinetics with hydrogen.[4] $LaNi_5$, which is another well-known alloy for hydrogen storage, showed moderate improvement on the dehydrogenation of MgH_2. However, the AlLi compound, which contains no transition metal, showed limited effect on the dehydrogenation.

4.1.3 III-B and IV-B Groups

The elements in the group of post-transition metals were generally less effective than the transition metals, with two notable exceptions. The addition of Sn significantly reduced the $T_{on\text{-}set}$ to 250.1 °C, and the addition of Al reduced the $T_{on\text{-}set}$ and the T_{end} by approximately 30 °C. It has been reported that the addition of III-B and IV-B group elements including Al, In, Si, and Sn can destabilize MgH_2 thermodynamically[5–9] The destabilization reaction can be given generally as $MgH_2 + xA \rightarrow MgA_x + H_2$. The results of this study suggest that the destabilizing of MgH_2 by these III-B and IV-B elements do not necessarily result in an improvement of the kinetics of the dehydrogenation of MgH_2. For example, the addition of indium was able to thermodynamically destabilize MgH_2

significantly, while significant reduction of the dehydrogenation temperature was only observed when indium was used in combination with another additive, such as $TiMn_2$.

4.1.4 Carbon and LiH

Carbon materials that were tested in this work, regardless of the form of those carbon materials (micrometer-sized graphite, nanometer-sized carbon nanotube carbon, or mesoporous graphite), showed no improvement to the dehydrogenation kinetics. These results are consistent with previous reports.[10–12] It should be pointed out, however, that there have been intense efforts recently of using carbon materials as additives for tailoring the hydrogen storage properties of MgH_2. It was reported that carbon could offer various advantages, including improving cyclic stability[10] and enhancing the thermal conductivity of the hydride[13–15], Moreover, LiH as a dopant was also tested in the present work; however, it showed no improvement on the dehydrogenation, which corresponded to a recent report for LiH doped MgH_2[16].

4.1.5 Binary Additives

The effects of binary-additives were studied by simultaneously milling MgH_2 with two additives. It can be seen that the addition of indium and $TiMn_2$ drastically decreased the $T_{on\text{-}set}$ and the T_{end} to 174.2 °C and 234.2 °C, respectively. This is because of a synergetic effect of indium that provided thermodynamic destabilization and $TiMn_2$ that has been proven as a strong kinetics enhancer. However, the binary additives, such as MgH_2-5%TiH_2-1%Nb_2O_5 and MgH_2-5%TiH_2-5%Ni, did not show significant improvements compared to those with similar monoadditives such as MgH_2-5%TiH_2, MgH_2-5%Ni, and

MgH_2-1%Nb_2O_5. It can be inferred that the catalytic mechanisms of various transition metals and transition metal compounds are very similar to each other, if not exactly the same. Therefore, adding another catalyst into the system is probably similar to increasing the amount of catalyst, which is discussed in the next section.

4.1.6 Content of Additives

In order to examine the effect of the relative content of additives on the dehydrogenation behavior of MgH_2, three samples with the addition of 1, 3, and 5 mol% of Nb_2O_5 were prepared, and their TGA weight loss analysis is shown in Figure 4-3. Figure 4-3 shows that the dehydrogenation reaction of MgH_2-5 mol% Nb_2O_5 occurred at a temperature that is approximately 10 °C lower compared to the sample with 1 mol% Nb_2O_5. As expected, the total weight loss (i.e. hydrogen capacity of the systems) decreased when more Nb_2O_5 additive was added to the MgH_2. Also, the result showed that the $T_{on\text{-}set}$ and the T_{end} decreased from 238.6 °C to 220.6 °C and 285.6 °C to 266.2 °C, respectively, as more Nb_2O_5 was added. It was found that the $T_{on\text{-}set}$, and particularly the T_{end}, were also affected by the amount of hydrogen that was released from the system. Despite that, the comparison of the pure MgH_2 (see Figure 4-1) and MgH_2-Nb_2O_5 systems showed that 1% of Nb_2O_5 doping caused a significant reduction of dehydrogenation temperature (e.g., $T_{on\text{-}set}$ is 323.5 °C for the as-milled MgH_2 and 238.6 °C for MgH_2-1 mol%Nb_2O_5). This result indicated that increasing the quantity of the additive from 1 to 5 mol% did not provide significant further benefits, while it significantly reduced the hydrogen capacity of the material. A similar trend was also reported by Choi et al.[17] in which the change of on-set dehydrogenation temperature of MgH_2-TiH_2 system was studied, varying the TiH_2 content

from 2 mol% to 20 mol%.

4.2 Ti-based Intermetallic Compound as Catalysts

4.2.1 Dehydrogenation Properties

A series of thermal gravimetric analysis (TGA) were performed using a heating rate of 5 °C/min for each as-milled MgH_2-M specimen, respectively. Figure 4-4 (a) compares the selected TGA curves of as-received, as-milled, TiH_2-doped, $TiMn_2$-doped, and TiAl-doped MgH_2 measured under a heating rate of 5 °C/min. The temperatures of dehydrogenation at a fractional conversion point ($\alpha = 0.4$) of all the undoped and the doped specimens are further given in Figure 4-4 (b). The dehydrogenation temperature of as-received MgH_2 is 414 °C for a heating rate of 5 °C/min, which is consistent with the temperature range of 350–450 °C as reported for undoped MgH_2 in the literature.[18] After UHEHP milling, the dehydrogenation temperature decreased to 333 °C, which is significantly lower than that of the as-received MgH_2. Compared to the as-milled undoped MgH_2, the doping of MgH_2 by TiH_2 further reduced the dehydrogenation temperature. The Ti-based intermetallic dopants all showed varying degrees of effectiveness in reducing the dehydrogenation temperature of MgH_2. For example, at the heating rate of 5 °C/min, the dehydrogenation temperature of MgH_2 doped with TiH_2 and MgH_2 doped with TiVMn are 244.6 °C and 216.7 °C, respectively, both significantly lower than that of undoped MgH_2. Note that the difference between the dehydrogenation temperature of as-milled MgH_2 and the as-milled MgH_2 doped with TiVMn is nearly 80 °C, clearly demonstrating the effect of the dopant.

In addition to the TGA measurements, isothermal dehydrogenation tests were carried out at temperature of 240 °C and 270 °C, respectively, with the back pressure set at 0.01 to

0.12 bar. Based on the TGA results, systems doped with TiH_2, $TiMn_2$, $TiVMn_2$, TiAl, TiNb, and TiFe were selected for measurement using the PCT machine. The data are plotted in Figure 4-5. At 240 ˚C, all selected doped MgH_2 specimens were able to fully dehydrogenate within 15 minutes, and at 270 ˚C, the rate of dehydrogenation became so rapid that the hydrides were fully dehydrogenated within 4 minutes. In particular, the TiVMn and TiNb doped systems completed the dehydrogenation reaction within 2 minutes. These results demonstrate again that the kinetics of the dehydrogenation of MgH_2 can be improved significantly by doping it with the Ti-based intermetallic alloys.

4.2.2 Hydrogenation Properties

Based on previous published research, nanosized MgH_2 with TiH_2 dopant can absorb a significant amount of hydrogen at room temperature[19]. This work investigated the effects of other Ti-based intermetallic alloys including TiAl, TiNb, TiFe, $TiMn_2$, and TiVMn on the kinetics of the hydrogenation of Mg and compared that to the effects of TiH_2. The hydrogenation experiments were performed using the PCT instrument under 1 bar pressure of hydrogen at 25, 60, and 100 ˚C, respectively. The results as shown in Figure 4-6, which clearly demonstrates that a relatively large amount of hydrogen can be absorbed by Mg under rather moderate kinetic conditions (room temperature and 1 bar pressure), suggesting that most of the Ti-based intermetallic alloys have strong effects that accelerate the hydrogenation of magnesium. For instance, the MgH_2-$TiMn_2$ absorbed 3.3 wt% of hydrogen under the condition described above. More specifically, the $TiMn_2$ and TiVMn doped Mg were able to absorb rapidly 1.5wt% hydrogen at room temperature within the first 5 minutes. The hydrogenation processes continued as time increased, although the

reactions became gradually slower. A total of ~3wt% of hydrogen was absorbed in 4 hours. Moreover, the results also showed that considerably faster rates of hydrogenation were readily achieved at moderately higher temperatures (60 and 100 ˚C). For instance, Mg-$TiMn_2$, Mg-TiNb, Mg-TiVMn, and Mg-TiFe systems could absorb up to 4 wt.% and more than 4.5 wt.% hydrogen at 60 and 100 ˚C within 240 minutes, respectively. Similar kinetic behaviors were also observed for $TiMn_2$, TiNb, TiFe, and TiVMn doped MgH_2 systems.

4.2.3 Pressure-Composition-Isothermal Measurements

Pressure-Composition-Isothermal (PCI) measurements were carried out to investigate the thermodynamic aspects of the doped Mg-H systems. As shown in Figure 4-7, the undoped MgH_2 has equilibrium pressures during hydrogenation of 0.85 and 2.0 bar at 270 and 300 ˚C, respectively. The equilibrium pressures of $TiMn_2$ doped MgH_2 were determined as 0.84 and 1.9 bar at 270 and 300 ˚C, respectively. It can be seen that the addition of $TiMn_2$ did not change the equilibrium pressure compared to the undoped Mg system. The corresponding van't Hoff plots were plotted in Figure 4-8. The equilibrium pressures and the van't Hoff plots indicate the thermodynamics of Mg-H reaction remain unchanged by the additions of the Ti-based intermetallic alloys studied in this work.

4.3 V-based BCC Alloys as Catalysts

4.3.1 Hydrogen Storage Properties

The ability of Mg with Ti-based additives to uptake a significant amount of hydrogen at relatively low hydrogen pressure and room temperature has been demonstrated in the last section. To characterize the effect of V-based additives on the hydrogenation kinetics

of Mg, a series of hydrogenation experiments were performed using the Sievert-type apparatus under 1 bar hydrogen pressure and at room temperature. Figure 4-9 (a) shows the comparison of room-temperature hydrogenation kinetic curves of MgH_2 with 75V-5Ti-20Cr, 80V-8Ti-12Cr, V, 80V-20Ti, and 80V-20Cr additives. On the basis of Figure 4-9 a, the sample of MgH_2-5 mol% 75V-5Ti-20Cr showed a rapid hydrogenation step at the beginning with 1.5 wt% hydrogen absorbed within the first 10 min. The hydrogen uptake of this sample increased with time and reached 3.5 wt% hydrogen absorbed in 200 min. By comparing the different kinds of V-based additives, it can be seen that the effectiveness of the additives on improving hydrogenation kinetics follows an order of 75V-5Ti-20Cr, V, 80V-8Ti-12Cr, 80V-20Cr, and 80V-20Ti from highest to lowest. The significant hydrogen absorption of MgH_2 with V-based additives at such a moderate condition (1 bar hydrogen pressure and room temperature) suggests a strong effect of V-based additives on the hydrogenation of Mg.

To further investigate the dehydrogenation kinetics, isothermal dehydrogenation tests were performed at 240 °C on MgH_2 with all five additives with a back pressure of 0.01 bar. The isothermal dehydrogenation curves are shown in Figure 4-9 (b). All of the samples were able to fully dehydrogenate within 10 min, and the samples with 75V-5Ti-20Cr, 80V-8Ti-12Cr, and pure V as additives were able to complete dehydrogenation within about 6 min.

4.3.2 Pressure-Composition-Isothermal Measurements

The thermodynamic behavior of MgH_2 with 75V-5Ti-20Cr was studied by performing the pressure-composition-isothermal (PCI) measurements using the Sievert-type apparatus.

Figure 4-10 compares the PCI curves of pure MgH_2 and the MgH_2-5% 75V-5Ti-20Cr samples measured at 300 °C. No significant differences in the equilibrium pressures can be observed between the MgH_2 with and without 75V-5Ti-20Cr additive. In other words, the V-based additives have strong effects on the kinetics of hydrogenation and dehydrogenation; they do not affect the thermodynamic stability of magnesium hydride.

4.4 Catalytic Effects

4.4.1 XRD Analysis

In order to understand the effect of the catalysts, x-ray diffraction (XRD) technique was used to characterize the phase compositions of the MgH_2 doped with catalysts ($TiMn_2$ and TiH_2) as an example. Figure 4-11 shows the high-resolution (synchrotron) XRD spectrum before and after the dehydrogenation of MgH_2-10 mol%$TiMn_2$. Figure 4-12 (a) and (b) further shows the high-resolution (synchrotron) XRD spectrum of as-milled, dehydrogenated, partially rehydrogenated, and fully rehydrogenated MgH_2-10 mol%TiH_2 samples. The partially rehydrogenated sample has approximately 3.5 wt% hydrogen. It can be seen that the $TiMn_2$ and TiH_2 catalyst phases appear to be stable during the dehydrogenation and rehydrogenation process, suggesting that the catalyst did not participate in the reaction of $MgH_2 = Mg + H_2$, nor did it participate in the hydrogenation reaction of $Mg + H_2 = MgH_2$. Further, it should be noted that the XRD measurements did not indicate the formation of any hydrides of $TiMn_2$, although $TiMn_2$ is a hydride forming material. This is understandable because the equilibrium pressure of $TiMn_2$ with hydrogen is much higher than the pressure that is used in these experiments. Therefore, the above results suggest that the $TiMn_2$ and TiH_2 dopants to MgH_2 played a role of catalyst during

both the hydrogenation and dehydrogenation process.

As it was mentioned earlier, the catalytic effects of transition metals (TM) such as Ti, V, Mn, Fe, Ni, and Nb[20–24] has been reported in multiple studies. Ti, V, Nb, and Ni were reported to have relatively more significant effects than other transition metal elements. The results shown above demonstrate that the intermetallic alloys of these elements have even more pronounced catalytic effects. It is not clear at the present time, however, why the intermetallic alloys would have more significant effects than their elemental counterparts. One observation is that these alloys form less stable hydrides than their corresponding elemental metals.

4.4.2 TEM Analysis

Transmission electron microscopy (TEM) analysis for as-milled MgH_2-TiH_2 sample was carried out. Figure 4-13 shows the combined bright field image of a representative MgH_2-TiH_2 powder sample. It can be seen that the dark parts inside of particles are TiH_2 catalysts, which have size in a range of a few nanometers to tens of nanometers. The grey region of the particles consists of MgH_2 grains with a size of about 10 to 20 nm. The result of TEM micrographs indicates that our milling technique produced a nanosized composite of MgH_2 and catalysts. The observed grain size of MgH_2 and the morphology of the particle are consistent with previous reports.[25, 26] The other important fact is a uniform distribution of the catalysts phase. As has been previously reported, such a nanostructure is considered to be a favorable feature for kinetics improvement.[2, 3]

4.4.3 Optimization of Catalyst

Additive doping has been proved as an efficient way to improve the kinetic properties of MgH_2. The fact that some additives are effective while others are not has challenged scientists for decades to understand the fundamental mechanism of the effects of additives. Understanding the mechanisms will help and guide the discovery of the ultimate additive that would dramatically improve kinetic as well as thermodynamic properties of MgH_2 and enable MgH_2 to be used for practical applications.

The experimental survey demonstrated (see Figure 4-2) that additives such as Ti and V-based metals, hydride, and certain intermetallic compounds have strong catalytic effects. A common thread of these effective catalysts is that they are hydride-forming materials. In other words, these catalysts are able to react with hydrogen. As suggested in previous literature, although not having been explicitly proved, a catalyst should act as a "hydrogen conduit" or "hydrogen pathway," which accelerates diffusion of the hydrogen atom in the catalyzed material. This means the hydrogen diffusion rate in the catalyst must be higher than that of the body of Mg or MgH_2. As we known, many transition metal based hydrides have excellent kinetics when reacting with hydrogen.[4] Therefore, they should be capable as catalysts for MgH_2.

However, it was found in Figure 4-2 that not all hydride materials can be effective. Take LiH for example, which has an ionic bond with a hydrogen atom. Contrasted to those interstitial hydrides that formed from transition metals, the hydrogen movement in the LiH lattice may be restricted, and as a result there is no catalytic effect. Moreover, a similar trend can be expected for other ionic hydrides such as KH, NaH, CaH_2, etc. And it can be supported via previous experimental research since the attempt to use ionic hydride as a

catalyst showed less positive effect.

Given the discussion above, a comprehensive survey of the hydrogen diffusion coefficient for a group of relevant materials was conducted, and the data are plotted in Figure 4-14.[27] It should be pointed out that the diffusion coefficient of hydrogen (D_H) is dependent to temperature and hydrogen pressure. It also should be pointed out that the data were collected from different reports using various experimental techniques according to the references.[27]

Generally, D_H increases with increases of temperature and hydrogen pressure. In Figure 4-14, the data of D_H are collected in the temperature range of 25 °C to 400 °C, and the pressure is generally referred as 1 atm (1 bar). Moreover, the set of data includes the diffusion data from samples with both dilute hydrogen (metal status) and a high concentration of hydrogen (hydride status). It indicates that a hydride with higher hydrogen content usually has lower D_H than that of a hydride with lower hydrogen content. For example, the D_H of $TiH_{1.71}$ are lower than those of $Ti_{1.66}$ and metallic α-Ti. However, considering the case of the hydrogenating/dehydrogenating reactions of MgH_2, $TiH_{1.71}$ is closer to the phase that existed as a catalyst in MgH_2.

First, it can be found that the D_H of MgH_2 is very low, which is in accord with the sluggish dehydrogenation kinetics. Second, the D_H of LiH is also very low – at the same level to that of MgH_2. Therefore, the addition of LiH is not able to provide improvement regarding the hydrogen diffusion rate. At last, it is important to note that most transition metals and their compounds own sufficiently high D_H compared to MgH_2.

However, problems arise when Figure 4-14 is used to assess the effectiveness of the catalyst candidates. For example, metals with excellent catalytic effects, such as Ti, V, and

$TiMn_2$, do not show higher D_H than those of materials with less effects, such as Fe, Al, Mo, and W. Moreover, it can be found that metallic Mg has a relatively high level of D_H, which is similar to those of Pt and $Mg_2NiH_{0.3}$, and even higher than those of $TiFeH_{1.03}$ and Mg_2NiH_4.

Herein, it must be realized that the D_H – the diffusion coefficient – does not represent the diffusive flux of hydrogen. According to Fick's first law[28], the diffusion flux is proportional to the concentration gradient through the expression

$$J = -D \frac{dC}{dx} \tag{4-1}$$

where D is expressed in square meters per second and C is the concentration. From Fick's first law, it is known that D is the concentration-independent constant. The diffusive flux is also dependent on the concentration gradient. Therefore, in this case, a factor can be introduced and known as hydrogen permeation P[29]:

$$P = D_H \times c_H \tag{4-2}$$

Hydrogen permeation (H permeability) is commonly expressed as an important factor in the field of hydrogen purification membranes, generally referring to the penetration of a permeate through a solid phase. Related to our case (catalyst), it can be assumed that the catalyst particle serves as a hydrogen membrane to convey the hydrogen atom in or out of the substrate (Mg or MgH_2) body. The feasibility that allows transportation of hydrogen though a catalyst represents the effectiveness of the catalytic effect that a catalyst can provide. Consequently, a high permeability for hydrogen is required for an effective catalyst. Furthermore, criteria for selection of the catalyst are (1) it should have a high D_H and (2) it should have a high hydrogen content to offer a sufficient concentration gradient.

Given this concept, Figure 4-15 provides hydrogen solubility of various metals. It

shows that elements such as Cr, Mo, Mn, Fe, Co, Ni, Zn, and Al have almost negligible hydrogen content at moderate temperatures and pressure condition. Although the D_H of these metals are relatively high, low hydrogen concentration prevents the mass diffusivity of hydrogen in their lattice. In contrast, elements in the IV-A and V-A groups (Ti, Zr, V, Nb, Ta) have significantly higher hydrogen solubility and high D_H. The features of these group of materials enable a feasible and quick hydrogen transportation and therefore make them good catalysts. The hydrides of LiH and MgH_2 are stoichiometric, but these ionic metal hydrides have very low D_H.

4.5 Summary

In conclusion, 49 MgH_2-additive compositions were examined based on the dehydrogenation temperature of MgH_2 through the use of TGA analysis. Additives with strong catalytic effects were found to be Ti-based, V-based metals, and hydride, as well as some intermetallic compounds. Elements such as Al, In, Ge, Sn, and Si did not show significant improvement of the kinetic rates of the dehydrogenation of MgH_2. Moreover, the dehydrogenation temperature was further reduced by combining $TiMn_2$, a kinetic additive, and indium, a thermodynamic destabilizer.

The Ti and V-based intermetallic alloys studied in this work have significant effects on improving the kinetics of dehydrogenation and hydrogenation of magnesium hydride. In particular, $TiMn_2$ doped MgH_2 exhibits drastically improved kinetics of hydrogenation at room temperature, significantly more effective than other catalytic materials as reported in the literature. The results also demonstrate that the effects of Ti intermetallic additives are primarily catalytic. $TiMn_2$ does participate in the dehydrogenation and hydrogenation

reactions under the experimental conditions of this work. Further, the Ti intermetallic catalyst does not affect the thermodynamic equilibrium pressure of MgH_2. TEM characterization shows a nanosized structure of MgH_2 together with TiH_2 catalysts. Further mechanistic analysis indicates that an optimum catalyst should have both a high hydrogen solubility and diffusion coefficient.

4.6 References

1. Sakintuna, B.; Lamari-Darkrim, F.; Hirscher, M., Metal Hydride Materials for Solid Hydrogen Storage: A Review. *Int. J. Hydrogen Energy* **2007**, *32*, 1121−1140.

2. Aguey-Zinsou, K.-F.; Ares-Fernandez, J.-R., Hydrogen in Magnesium: New Perspectives toward Functional Stores. *Energy Environ. Sci.* **2010**, *3*, 526−543.

3. Jain, I. P.; Lal, C.; Jain, A., Hydrogen Storage in Mg: A Most Promising Material. *Int. J. Hydrogen Energy* **2010**, *35*, 5133−5144.

4. Sandrock, G.; Thomas, G., The IEA/DOE/SNL On-Line Hydride Databases. *Appl. Phys. A* **2001**, *72*, 153−155.

5. Liang, G., Synthesis and Hydrogen Storage Properties of Mg-Based Alloys. *J. Alloys Compd.* **2004**, *370*, 123−128.

6. Zhong, H. C.; Wang, H.; Liu, J. W.; Sun, D. L.; Zhu, M., Altered Desorption Enthalpy of MgH_2 by the Reversible Formation of Mg(In) Solid Solution. *Scripta Mater.* **2011**, *65*, 285−287.

7. Vajo, J. J.; Mertens, F.; Ahn, C. C.; Bowman, R. C.; Fultz, B., Altering Hydrogen Storage Properties by Hydride Destabilization through Alloy Formation: LiH and MgH_2 Destabilized with Si. *J. Phys. Chem. B* **2004**, *108*, 13977−13983.

8. Andreasen, A., Hydrogenation Properties of Mg–Al Alloys. *Int. J. Hydrogen Energy* **2008**, *33*, 7489−7497.

9. Crivello, J. C.; Nobuki, T.; Kuji, T., Improvement of Mg–Al Alloys for Hydrogen Storage Applications. *Int. J. Hydrogen Energy* **2009**, *34*, 1937−1943.

10. Amirkhiz, B. S.; Danaie, M.; Barnes, M.; Simard, B.; Mitlin, D., Hydrogen Sorption Cycling Kinetic Stability and Microstructure of Single-Walled Carbon Nanotube (SWCNT) Magnesium Hydride (MgH_2) Nanocomposites. *J. Phys. Chem. C* **2010**, *114*, 3265−3275.

11. Shang, C. X.; Guo, Z. X., Effect of Carbon on Hydrogen Desorption and Absorption of Mechanically Milled MgH_2. *J. Power Sources* **2004**, *129*, 73−80.

12. Huang, Z. G.; Guo, Z. P.; Calka, A.; Wexler, D.; Liu, H. K., Effects of Carbon Black, Graphite and Carbon Nanotube Additives on Hydrogen Storage Properties of Magnesium. *J. Alloys Compd.* **2007**, *427*, 94−100.

13. Shim, J.-H.; Park, M.; Lee, Y. H.; Kim, S.; Im, Y. H.; Suh, J.-Y.; Cho, Y. W., Effective Thermal Conductivity of MgH_2 Compacts Containing Expanded Natural Graphite under a Hydrogen Atmosphere. *Int. J. Hydrogen Energy* **2014**, *39*, 349−355.

14. Chaise, A.; de Rango, P.; Marty, P.; Fruchart, D.; Miraglia, S.; Olivès, R.; Garrier, S., Enhancement of Hydrogen Sorption in Magnesium Hydride Using Expanded Natural Graphite. *Int. J. Hydrogen Energy* **2009**, *34*, 8589−8596.

15. Pohlmann, C.; Röntzsch, L.; Weißgärber, T.; Kieback, B., Heat and Gas Transport Properties in Pelletized Hydride–Graphite-Composites for Hydrogen Storage Applications. *Int. J. Hydrogen Energy* **2012**, *38*, 1685−1691.

16. Leng, H.; Pan, Y.; Li, Q.; Chou, K.-C., Effect of LiH on Hydrogen Storage Property of MgH_2. *Int. J. Hydrogen Energy* **2014**, *39*, 13622−13627.

17. Choi, Y. J.; Lu, J.; Sohn, H. Y.; Fang, Z. Z.; Rönnebro, E., Effect of Milling Parameters on the Dehydrogenation Properties of the Mg−Ti−H System. *J. Phys. Chem. C* **2009**, *113*, 19344−19350.

18. Choi, Y. J.; Choi, J. W.; Sohn, H. Y.; Ryu, T.; Hwang, K. S.; Fang, Z. Z., Chemical Vapor Synthesis of Mg–Ti Nanopowder Mixture as a Hydrogen Storage Material. *Int. J. Hydrogen Energy* **2009**, *34*, 7700−7706.

19. Lu, J.; Choi, Y. J.; Fang, Z. Z.; Sohn, H. Y.; Rönnebro, E., Hydrogenation of Nanocrystalline Mg at Room Temperature in the Presence of TiH_2. *J. Am. Chem. Soc.* **2010**, *132*, 6616−6617.

20. Liang, G.; Huot, J.; Boily, S.; Van Neste, A.; Schulz, R., Catalytic Effect of Transition Metals on Hydrogen Sorption in Nanocrystalline Ball Milled MgH_2–Tm (Tm=Ti, V, Mn, Fe and Ni) Systems. *J. Alloys Compd.* **1999**, *292*, 247−252.

21. Shang, C. X.; Bououdina, M.; Song, Y.; Guo, Z. X., Mechanical Alloying and Electronic Simulations of (MgH_2+M) Systems (M=Al, Ti, Fe, Ni, Cu and Nb) for Hydrogen Storage. *Int. J. Hydrogen Energy* **2004**, *29*, 73−80.

22. Friedlmeier, G.; Groll, M., Experimental Analysis and Modelling of the Hydriding Kinetics of Ni-Doped and Pure Mg. *J. Alloys Compd.* **1997**, *253-254*, 550−555.

23. Bobet, J. L.; Akiba, E.; Nakamura, Y.; Darriet, B., Study of Mg-M (M=Co, Ni and Fe) Mixture Elaborated by Reactive Mechanical Alloying — Hydrogen Sorption

Properties. *Int. J. Hydrogen Energy* **2000**, *25*, 987−996.

24. Pelletier, J. F.; Huot, J.; Sutton, M.; Schulz, R.; Sandy, A. R.; Lurio, L. B.; Mochrie, S. G. J., Hydrogen Desorption Mechanism in MgH_2-Nb Nanocomposites. *Phys. Rev. B* **2001**, *63*, 052103.

25. Lu, J.; Choi, Y. J.; Fang, Z. Z.; Sohn, H. Y.; Rönnebro, E., Hydrogen Storage Properties of Nanosized Mgh_2−$0.1TiH_2$ Prepared by Ultrahigh-Energy−High-Pressure Milling. *J. Am. Chem. Soc.* **2009**, *131*, 15843−15852.

26. Danaie, M.; Mitlin, D., Tem Analysis and Sorption Properties of High-Energy Milled MgH_2 Powders. *J. Alloys Compd.* **2009**, *476*, 590−598.

27. Fisher, D.J. *Hydrogen diffusion in metals -Data compilation-*. Trans Tech Publications, Durnten-Zurich, Switzerland, 2014.

28. Callister, W. D.; Rethwisch, D. G., *Materials Science and Engineering: An Introduction*; Wiley New York, 2007; Vol. 7.

29. Flanagan, T. B. In *The Role of the Thermodynamic Factor in Hydrogen Diffusion in Metal and Alloy Membranes*, Defect and Diffusion Forum, Trans Tech Publ: 2014; pp 1−23.

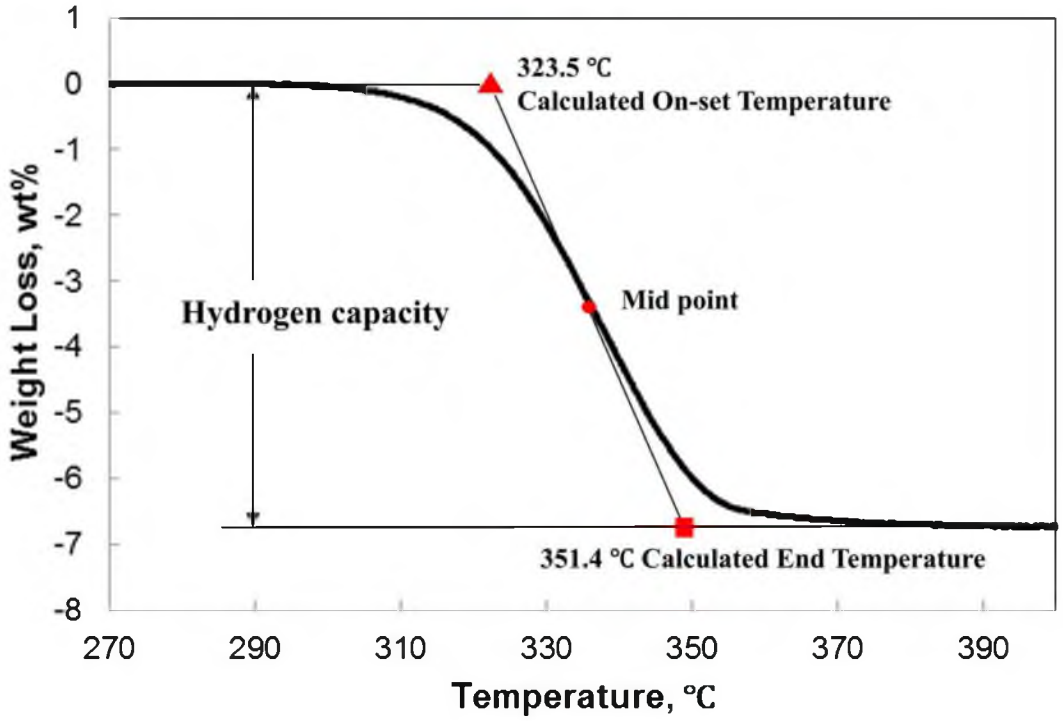

Figure 4-1. Determination of calculated on-set temperature ($T_{on\text{-}set}$) and calculated end temperature (T_{end}) based on TGA dehydrogenation curve of as-milled MgH_2.

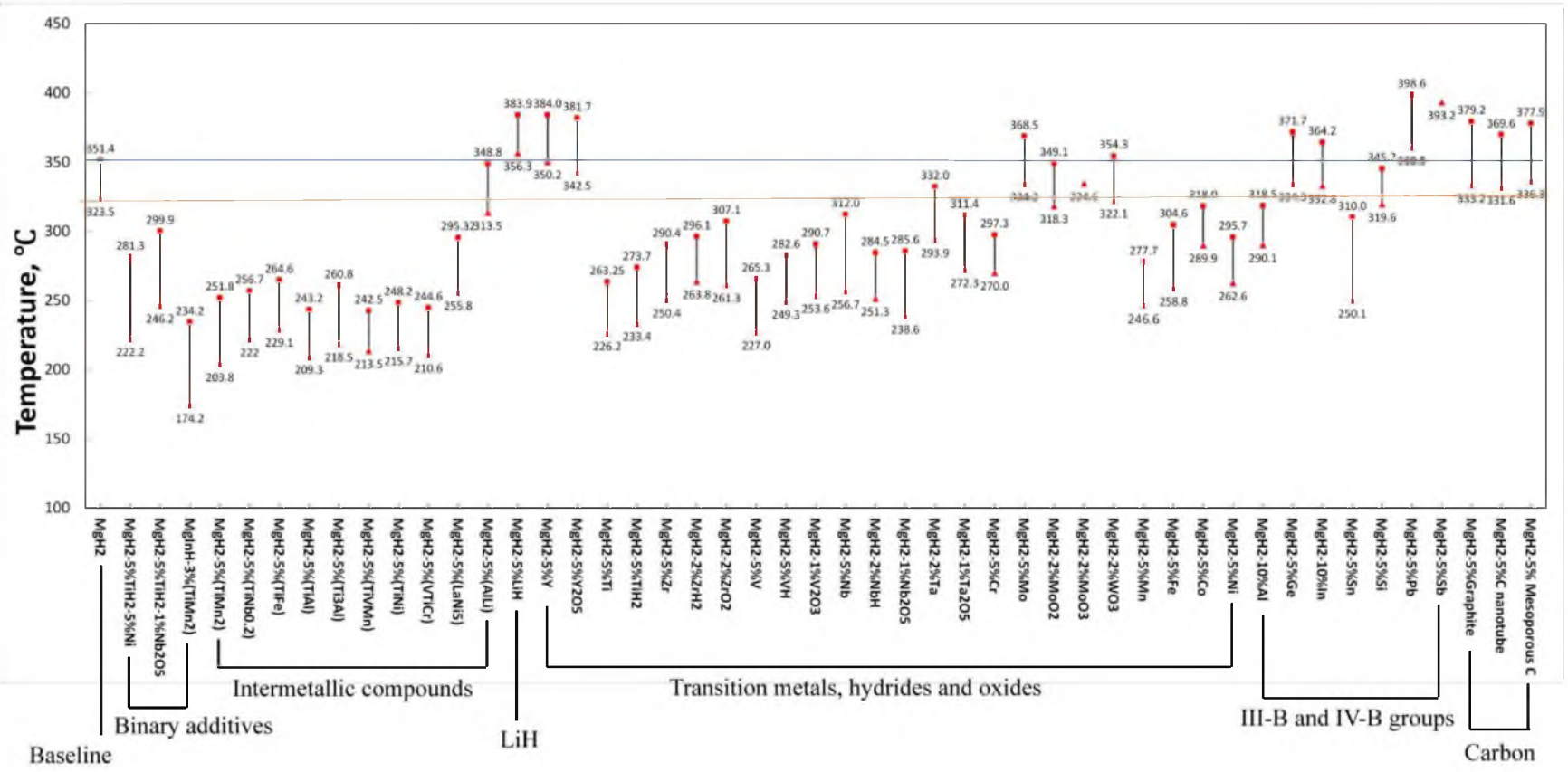

Figure 4-2. Effect of various additives on dehydrogenation temperature of MgH_2. Data of dehydrogenation temperature were collected based on TGA analysis. TGA experiments were performed using a heating rate of 5 °C/min.

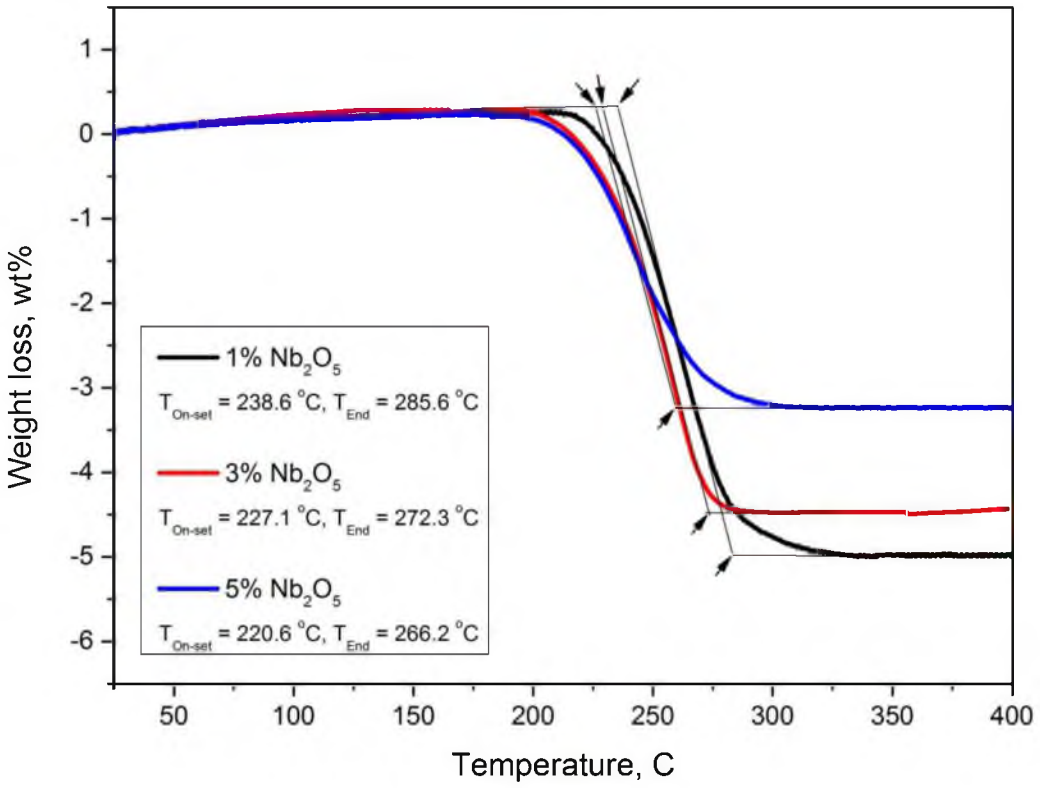

Figure 4-3. Effect of varying amounts of additive on the TGA dehydrogenation behavior of MgH_2. TGA experiments were performed using a heating rate of 5 °C/min.

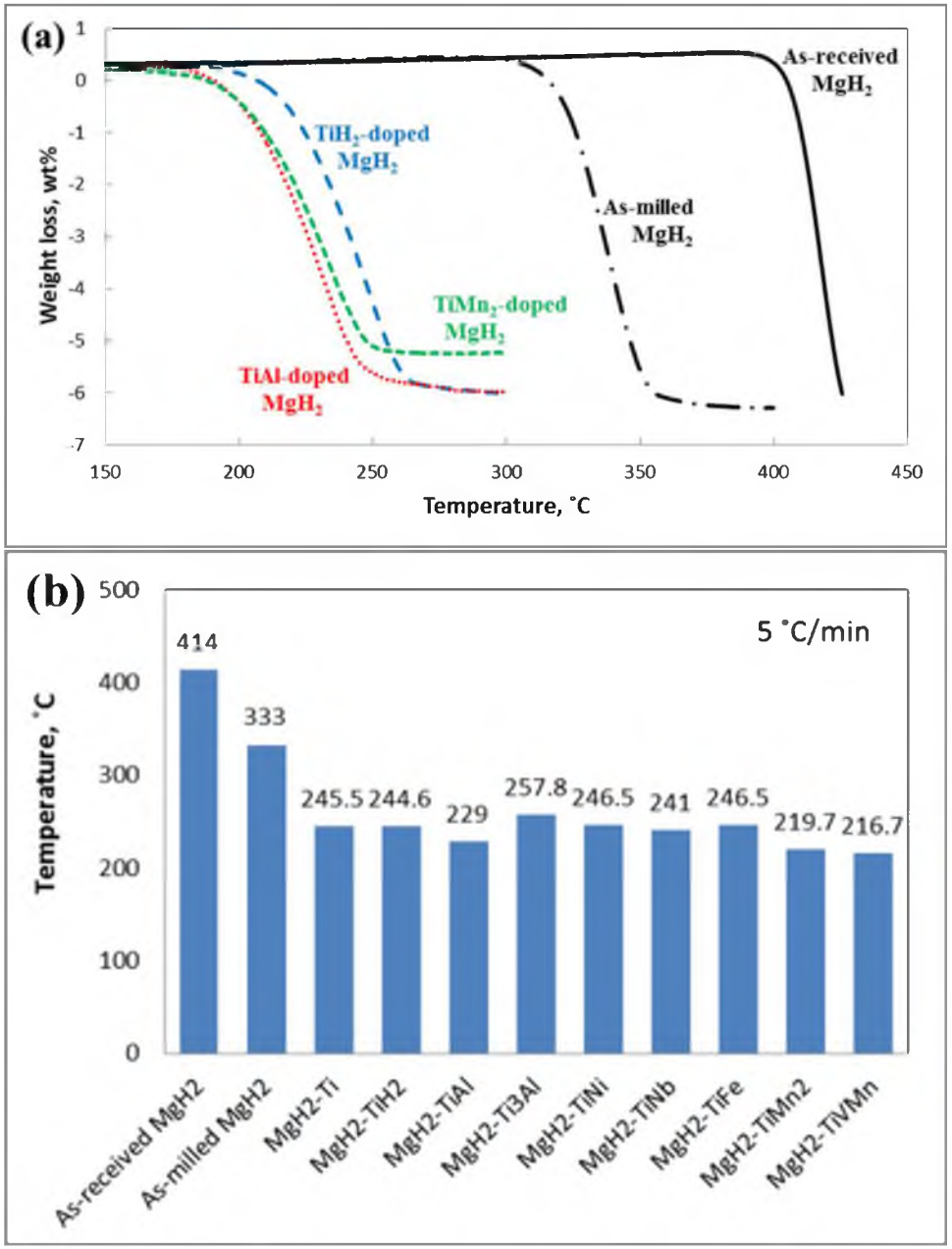

Figure 4-4. TGA results for catalyzed MgH_2 systems. (a) TGA curves of as-received, as-milled, TiH_2-doped, $TiMn_2$-doped, and TiAl-doped MgH_2 systems. (b) Dehydrogenation temperature of different Ti-based catalysts doped systems, determined by TGA profiles at fractional conversion $\alpha = 0.4$. TGA experiments were performed using a heating rate of 5 °C/min.

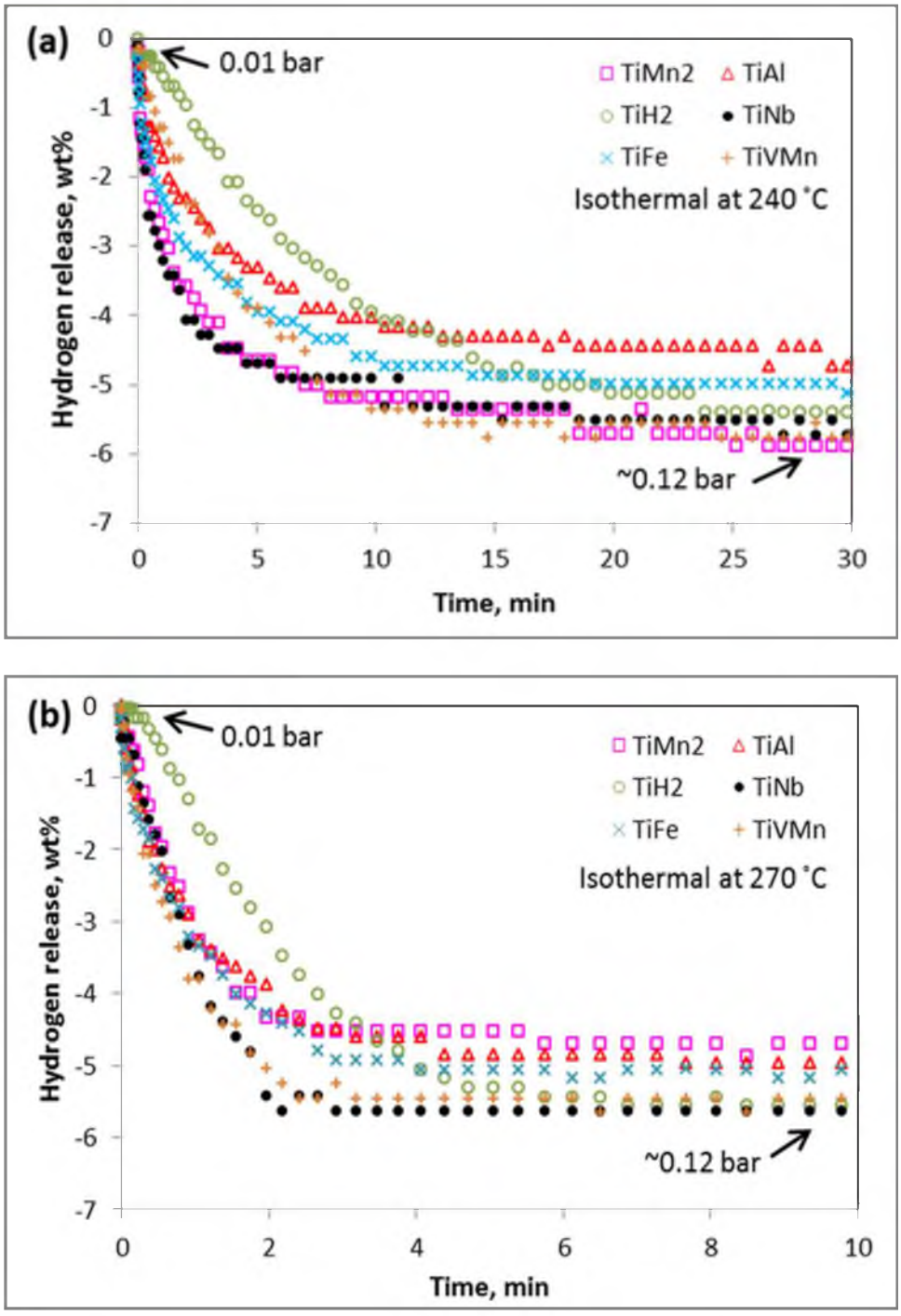

Figure 4-5. PCT dehydrogenation kinetics for different Ti-based alloys catalyzed magnesium hydrides. (a) Tests performed at 240 °C; (b) Tests performed at 270 °C.

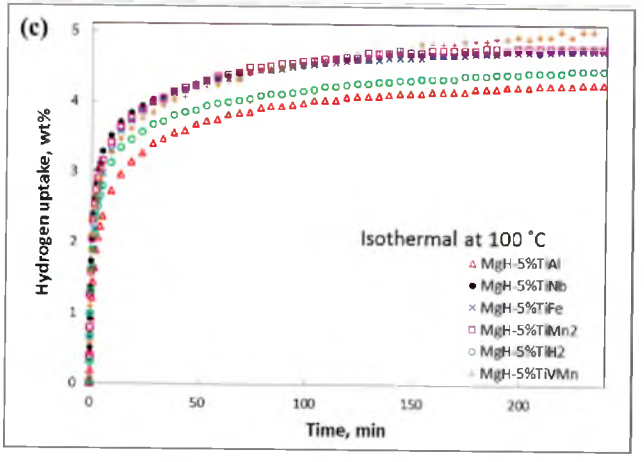

Figure 4-6. Effect of Ti-based catalysts on hydrogenation kinetics under hydrogen pressure of 1 bar. (a) Tests performed at 25 °C; (b) Tests performed at 60 °C; (c) Tests performed at 100 °C.

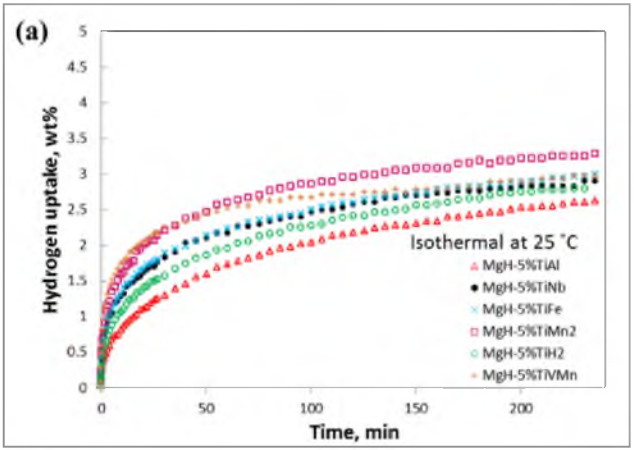
(a)
Hydrogen uptake, wt%
Time, min
Isothermal at 25 °C
MgH-5%TiAl
MgH-5%TiNb
MgH-5%TiFe
MgH-5%TiMn2
MgH-5%TiH2
MgH-5%TiVMn
(b)
Hydrogen uptake, wt%
Time, min
Isothermal at 60 °C
MgH-5%TiAl
MgH-5%TiNb
MgH-5%TiFe
MgH-5%TiMn2
MgH-5%TiH2
MgH-5%TiVMn

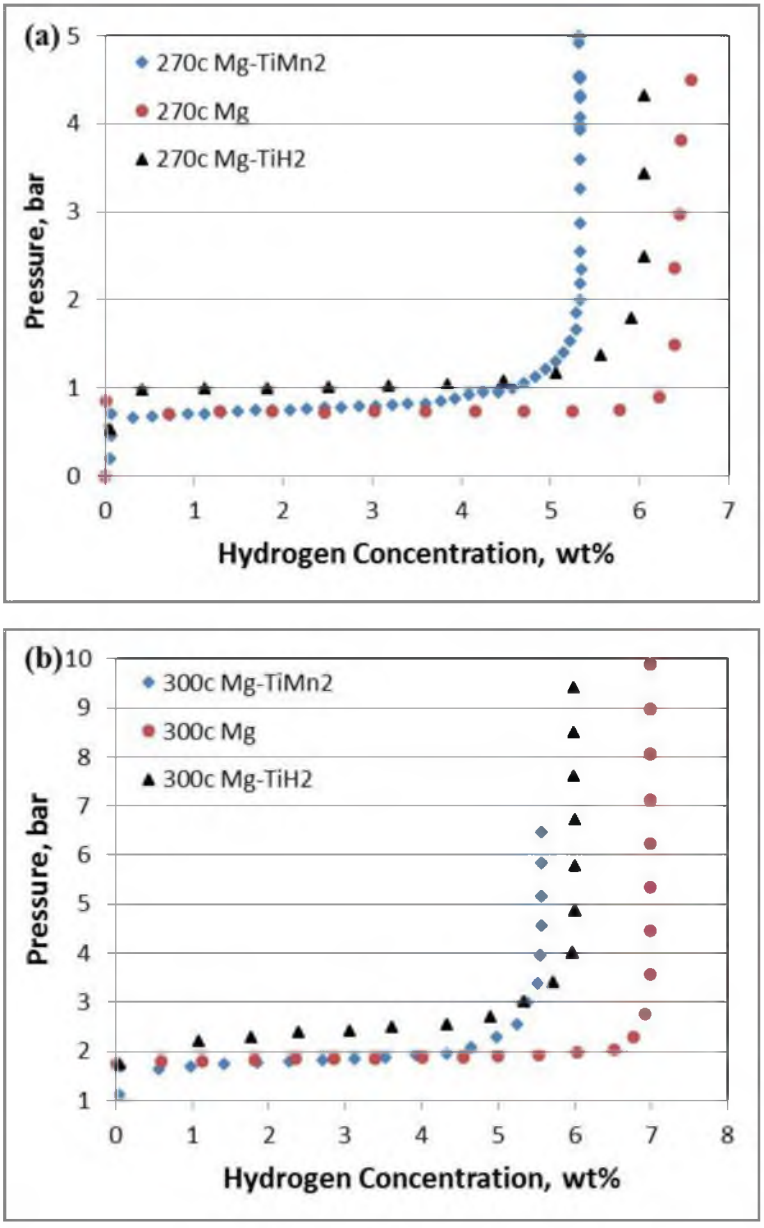

Figure 4-7. Pressure-Composition-Isothermal hydrogenating measurements for the as-milled Mg, TiH_2 and $TiMn_2$ catalyzed Mg systems. (a) Tests performed at 270 ˚C; (b) Tests performed at 300 ˚C.

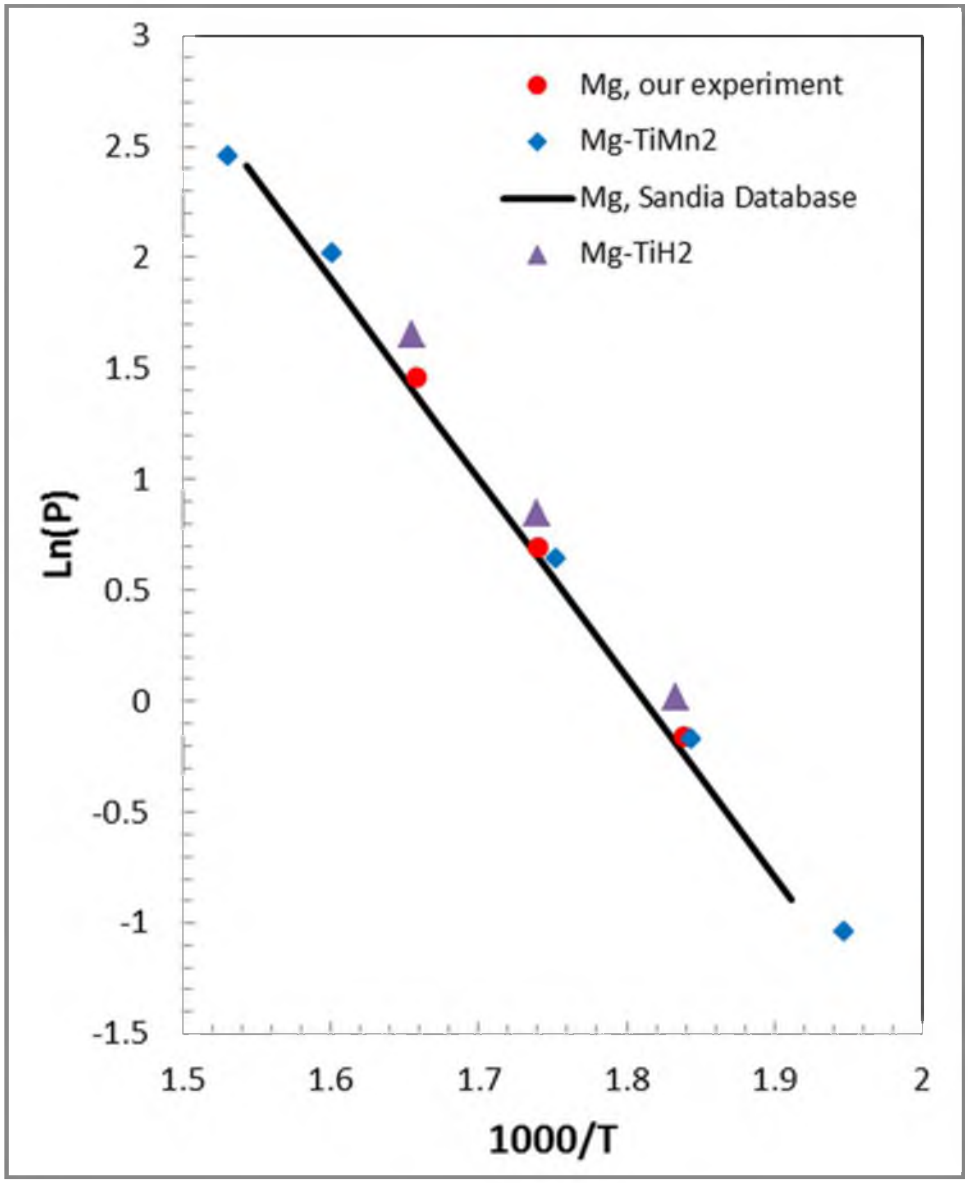

Figure 4-8. Van't Hoff plot corresponding to the PCI data shown in Figure 4-7.

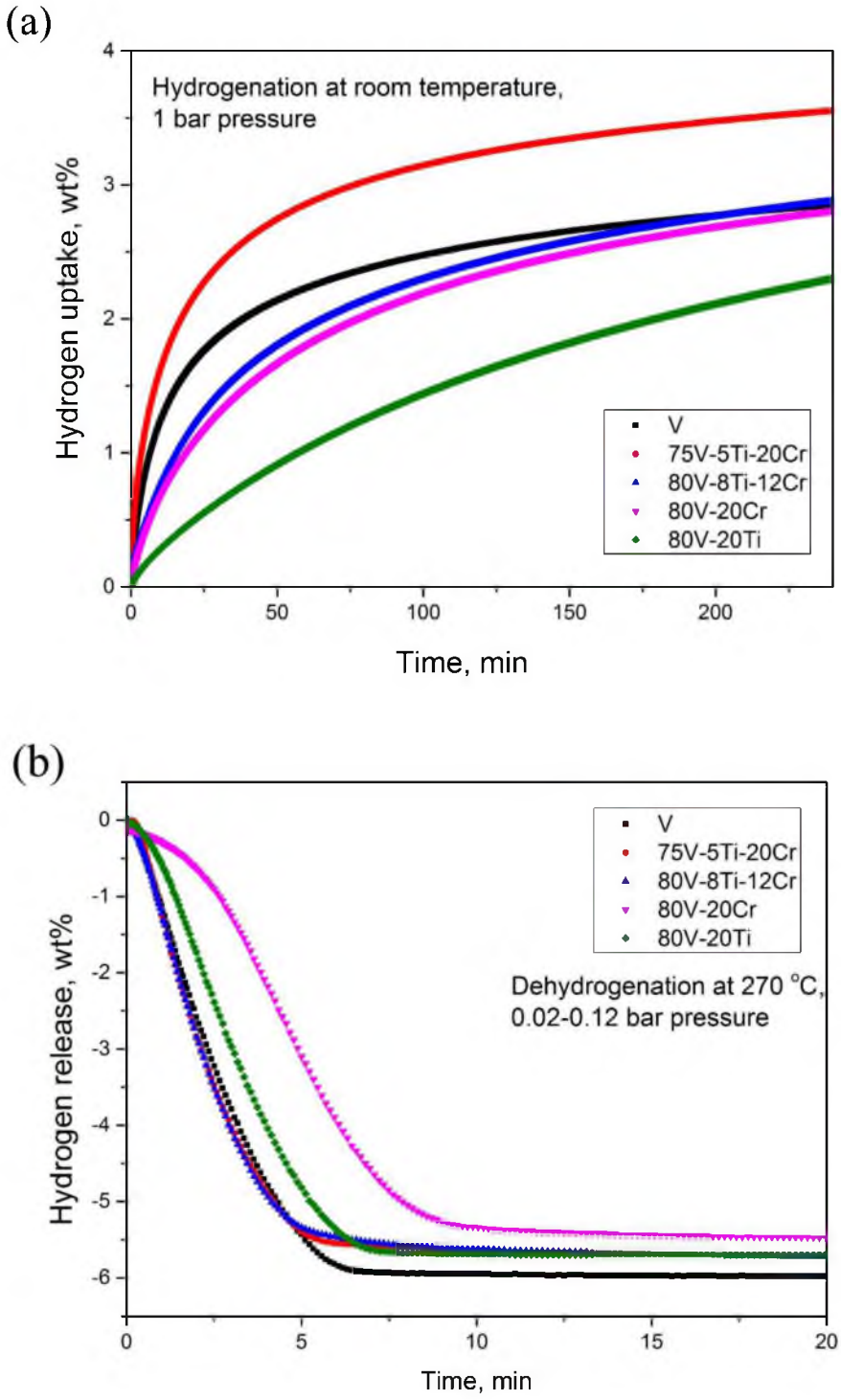

Figure 4-9. Effect of V-based catalysts on kinetics. (a) Hydrogenation kinetics; (b) Dehydrogenation kinetics.

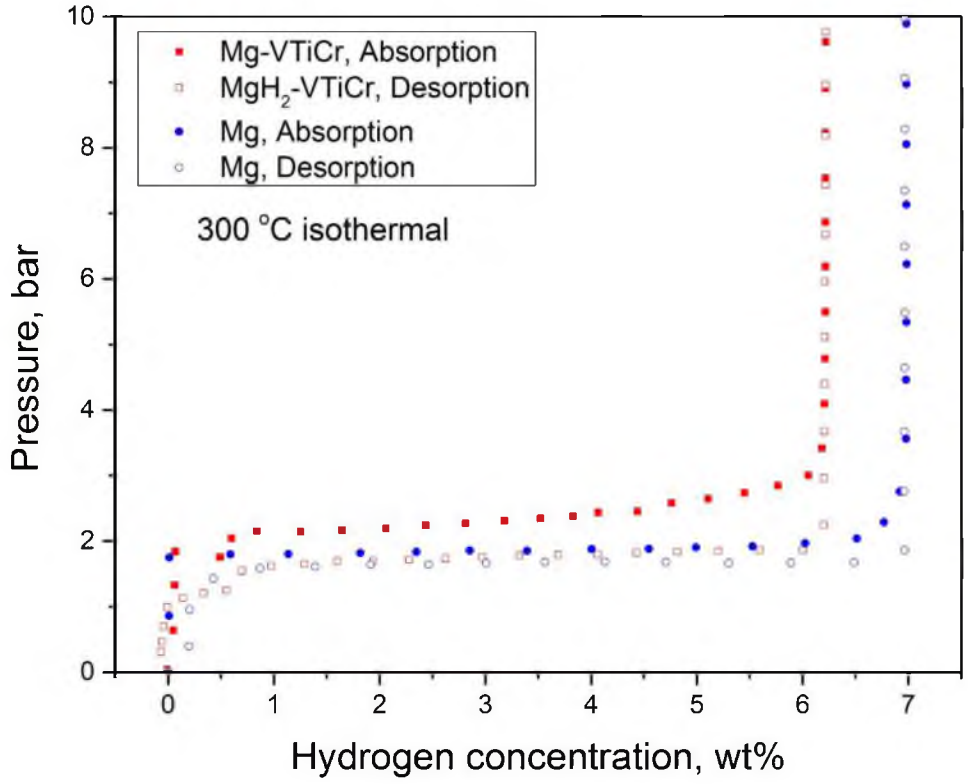

Figure 4-10. Pressure-Composition-Isothermal hydrogenating measurements at 300 ˚C of the as-milled VTiCr catalyzed Mg systems.

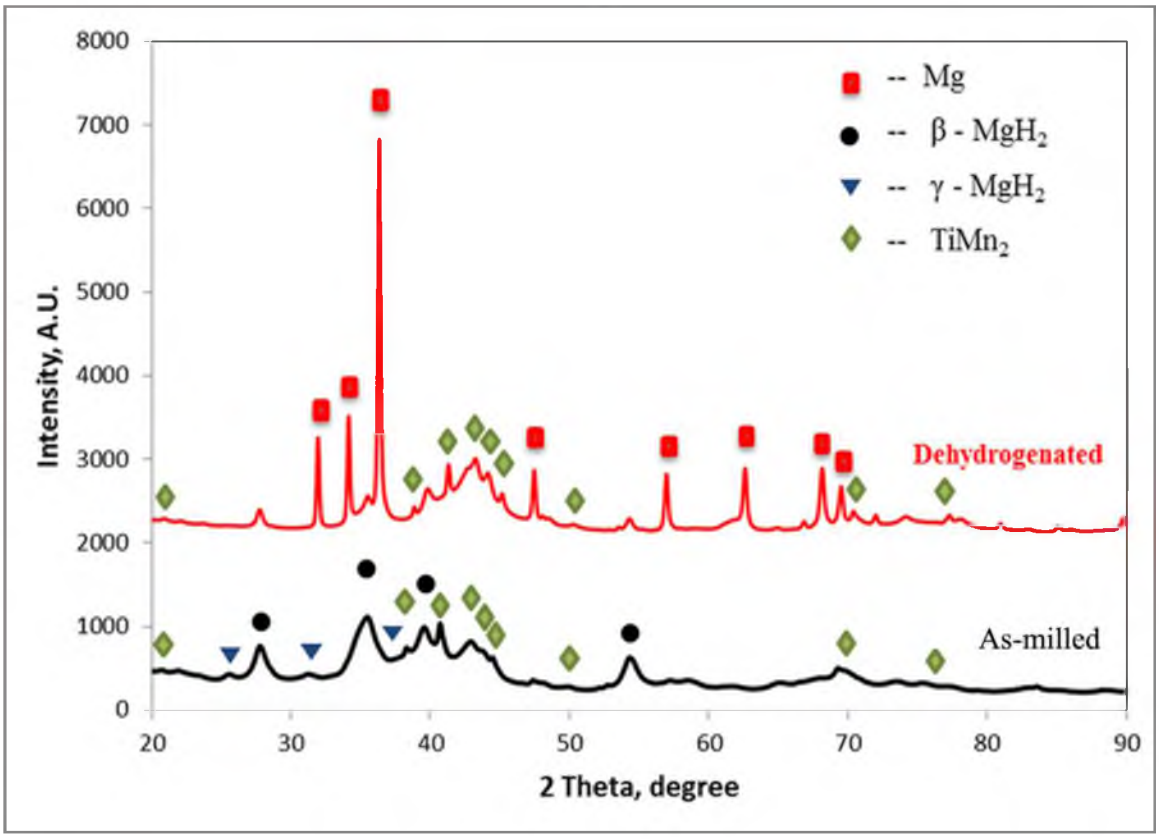

Figure 4-11. X-ray diffraction patterns of hydrogenated and dehydrogenated Mg-$TiMn_2$ system.

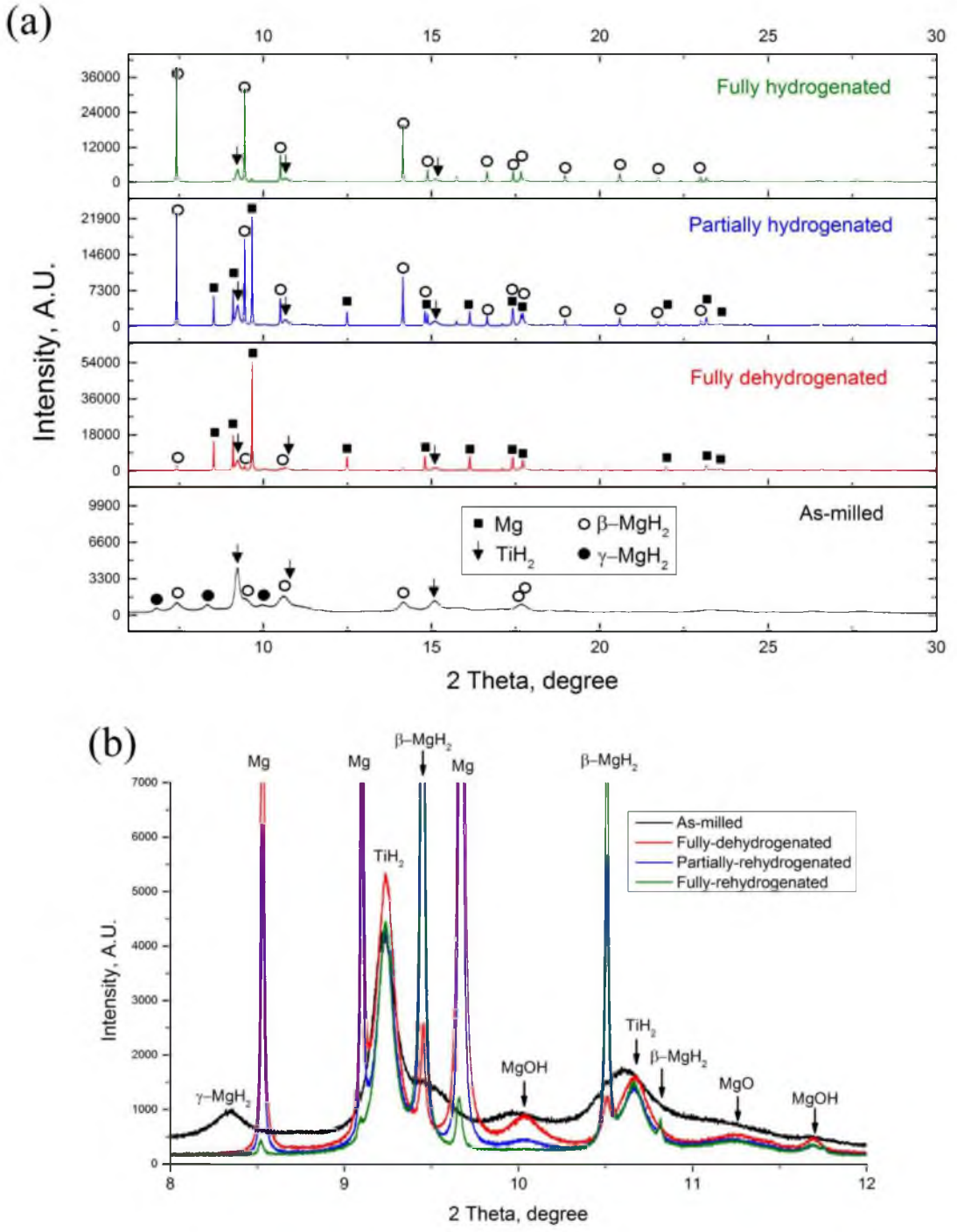

Figure 4-12. X-ray diffraction patterns of the as-milled, partially hydrogenated, fully hydrogenated, and dehydrogenated Mg-TiH_2 systems. (a) Separated spectra with identified peaks; (b) Spectra in 2θ range of 8° to 12°.

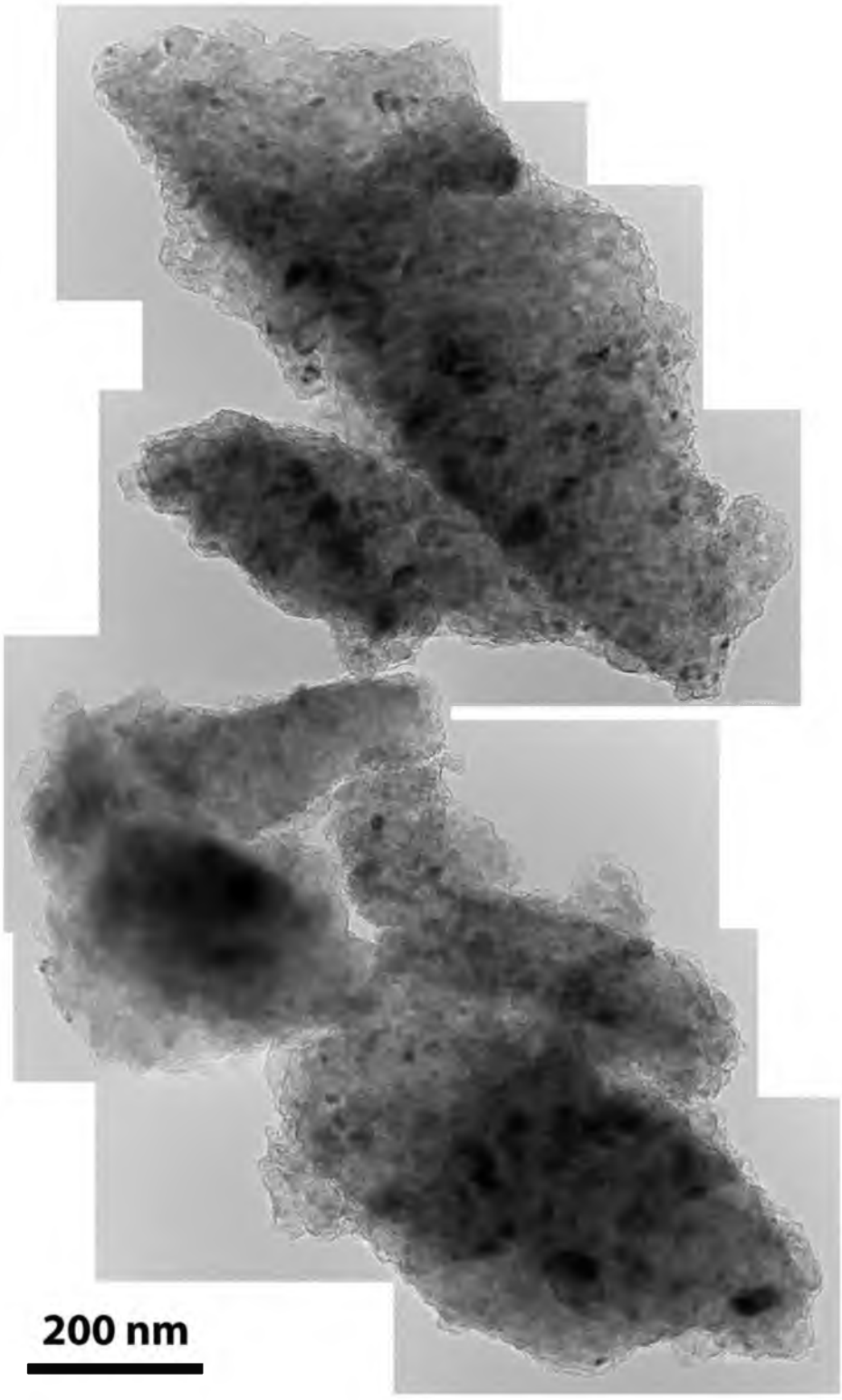

Figure 4-13. TEM micrograph of as-milled Mg-TiH_2 system.

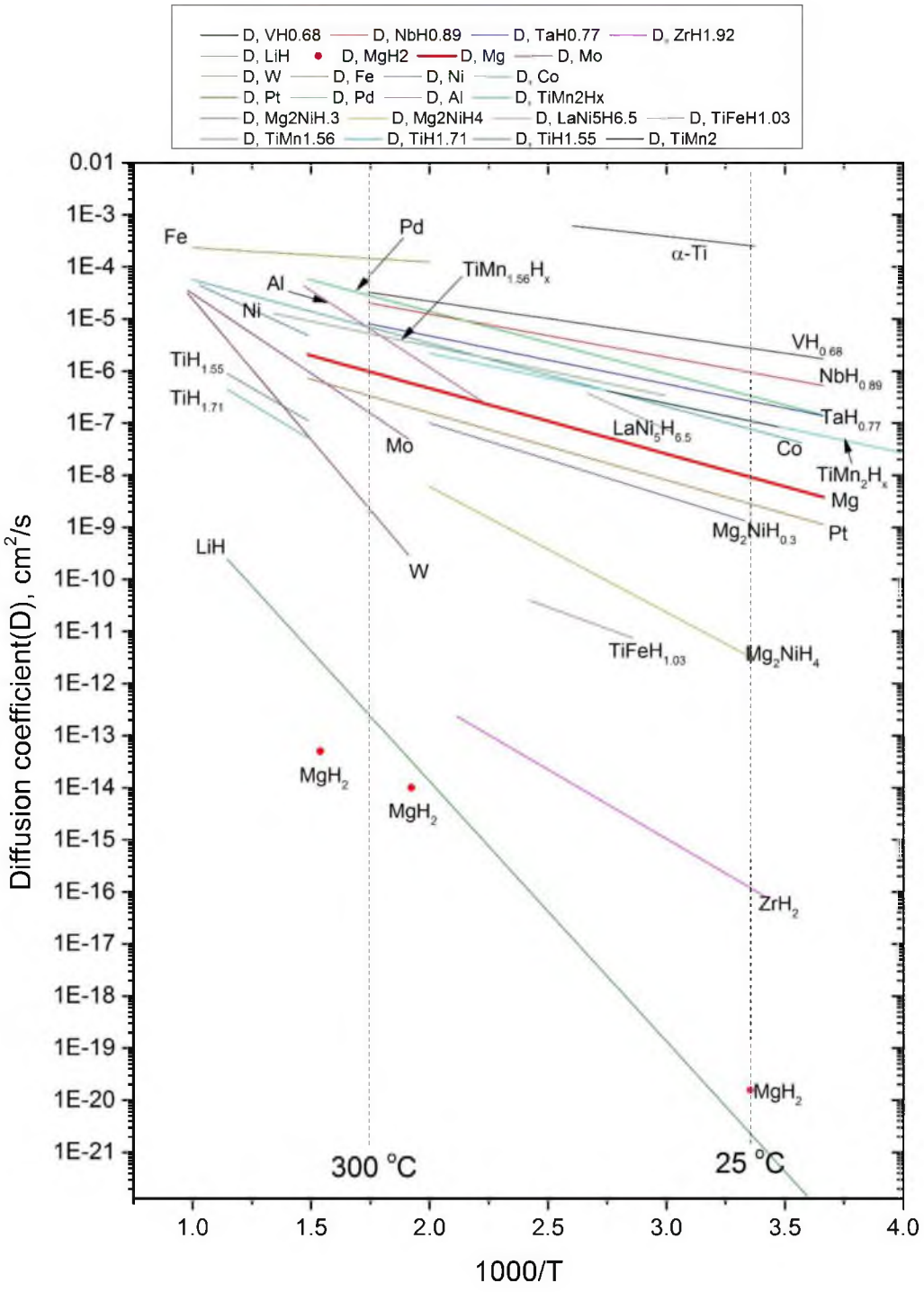

Figure 4-14. Intrinsic diffusion coefficients (D) for selected metals, intermetallics, and hydrides.

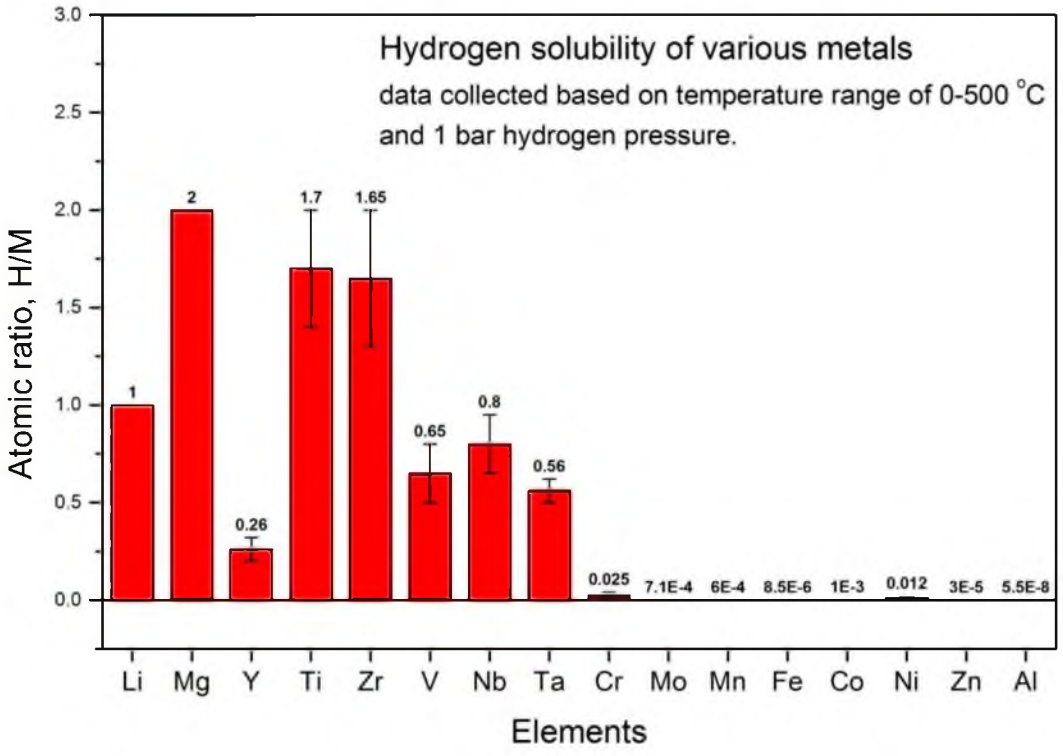

Figure 4-15. Hydrogen solubility for representative metals.

CHAPTER 5

THERMODYNAMIC DESTABILIZATION OF MAGNESIUM HYDRIDE BY FORMATION OF MAGNESIUM SOLID SOLUTION

In this chapter, the research work aims on a wide range of magnesium-based solid solution alloys and the potential of reducing the decomposition enthalpy using the solid solutions. Several alloy systems were synthesized and their thermodynamic properties were characterized using the Pressure-Composition-Isothermal (PCI) method. Further, the reaction pathways of various Mg-In alloys with hydrogen were examined by using *in situ* X-ray diffraction (XRD) technique.

5.1 PCI Measurements

The PCI measurements for all the hydride systems were shown in Figure 5-1. The hydrogenation and dehydrogenation equilibrium pressure measurements were performed using the Sieverts type apparatus (Hy-Energy LLC., PCT Pro-2000) mentioned in the chapter of experimental methods. Approximately 0.3 grams of each milled powder sample were sealed in a sample holder and loaded into a stainless steel vessel. Before Pressure-Composition-Isothermal (PCI) measurements were made, the MgH_2-additive(s) mixtures were dehydrogenated and heat treated at 400 °C for 1000 min to homogenize the

compositions.

5.2 Determination of Equilibrium Pressures (Peq) and van't Hoff Analysis

A set of formation plateau pressure (P_f) and decomposition plateau pressure (P_d) measurements is obtained under isothermal condition with temperature differences less than ± 0.2 °C. The hydrogen P_{eq} measurements can be used to determine the thermodynamic quantities using the van't Hoff relationship:

$$\ln\left(\frac{P_{eq}}{P_0}\right) = -\frac{\Delta H}{RT} + \frac{\Delta S}{R} \quad (5\text{-}1)$$

Where P_o is reference pressure of 1 bar, and R represents as gas constant of 8.3145 J/K mol H_2. Therefore, the enthalpy (ΔH) and entropy (ΔS) are calculated from a straight line on the basis of $\ln(P_{eq})$ against 1/T. In the present study, three or four measurements of different temperatures were used to accomplish the van't Hoff plots.

5.3 Effect of Alloying Elements on Equilibrium Pressure

5.3.1 Effect of Indium Content

Figure 5-2 compares Mg-In alloys from the present study with indium contents of 5, 10, 15, and 20 at.%. It can be seen that the plateau pressures of both hydrogenation and dehydrogenation increased from ~1.7 to ~ 3 bar with an increasing indium concentration from 0 to 20 at.%. The corresponding van't Hoff relationships are plotted in Figure 5-3. The measured data of pure MgH_2 in this study overlapped with previously reported values,[1] which is a good indication of the validity of the measurements of this study. Additionally, it was found that Mg-15In and Mg-20In had the same levels for plateau pressures as that

of Mg_2Ni hydride at temperatures around 350℃ and would exceed that of Mg_2Ni at higher temperatures (> 350℃).

5.3.2 Effect of Aluminum

Although indium has a positive effect with respect to destabilizing MgH_2, it has a negative effect on the hydrogen storage capacity since indium is a rather heavy element. Therefore, other elements such as Li, Al, Zn, Ga, Ag, Cd, Sn, and Pb, etc., that also form solid solutions with Mg were considered. Among them, aluminum is regarded as a suitable element because it is light and has a significant solubility in Mg at elevated temperatures (up to 10 at.% at 400℃). Therefore, the effect of Al on binary Mg-10Al and ternary Mg-5Al-5In and Mg-5Al-10In systems were studied. Figure 5-4 shows van't Hoff plots of these systems. It can be seen that Al has a moderate effect on the plateau pressure of MgH_2 compared to In. The hydrogen content of Mg-10Al in the plateau range is, however, 5−6 wt.% H_2, (see Figure 5-1(f)), significantly higher than that of Mg-10In (~3 wt.% H_2).

5.3.3 Effect of Multicomponent Alloys

The ternary systems of Mg-5Al-5In and Mg-5Al-10In showed positive characteristics. The van't Hoff plot of Mg-5Al-5In is very similar to that of Mg-10In, but with a wide plateau range of H_2 content, 4.2 wt.% H_2, compared to a 2.8 wt.% H_2 range for Mg-10In (see Figure 5-1). Compared to Mg-15In, Mg-5Al-10In also had a higher P_{eq}. Furthermore, two additional multicomponent alloys were synthesized with compositions of Mg-5Al-5In-2Zn-1Si and Mg-10Al-6In-2Ga-2Zn. The van't Hoff plots of these alloys are given in Figure 5-5, showing higher plateau pressures compared to that of Mg. These results

indicate that alloying Mg with In, as well as other elements such as Al, Ga, Zn, and so forth, provides a promising strategy to destabilize magnesium hydride.

5.3.4 Stability

Stability of the solid solution alloys and their reversible reactions with hydrogen were investigated by subjecting these materials to a small number of cycles. Cyclic PCI experiments were conducted to compare the results of the same sample (Mg-10In) after the 3rd and the 8th cycles, as shown in Figure 5-6. The results demonstrated that these materials have good thermodynamic stability and reversibility, at least within the number of short cycles studied. However, it should be pointed out that the short cycle stability is only an indication, not a certainty for long term cycle stability.

5.4 Phase Transitions of Magnesium Solid Solution Alloys during Dehydrogenation and Hydrogenation

In order to study the underlying phase transitions during hydrogen cycling, an *in situ* synchrotron X-ray diffraction (XRD) technique was used to determine the phase transformations.

5.4.1 Phase Transitions in Mg-In Systems

Figure 5-7 shows the *in situ* XRD patterns during dehydrogenation of MgH_2-10In. Three reactants were present before the reaction: β-MgH_2, γ-MgH_2, and indium. It is noted that during the high energy milling process, the peaks of MgH_2 phases were drastically broadened, indicating near amorphous nanoscale particles in contrast to the relatively sharp

peaks of indium. The fact that indium does not show broadened peaks is likely because indium metal has a very low melting point and is rather ductile and thus tends to retain its crystalline structure during milling. Further, XRD peaks of iron can be seen in the patterns, which is attributed to contamination from the sample holder used for the *in situ* measurements, or from the stainless steel balls and the milling canister during the high energy milling.

Several phase transformations can be observed in Figure 5-7. First, the peaks of indium faded gradually as the temperature increased, which is attributed to the low melting point of indium metal (157℃). Second, a Mg-In intermediate phase (In_7Mg_3) appeared at approximately 300℃, lasted for a very short period, and then disappeared. Third, only Mg peaks were present at the end of dehydrogenation, indicating other elements and compounds were dissolved in Mg and formed a solid solution of Mg-In. These observations suggest that a small fraction of MgH_2 will dehydrogenate first and react with In to form In_7Mg_3. As the temperature continues to increase, In_7Mg_3 would react with the remaining MgH_2, releasing the bound hydrogen. Thus, the reactions of dehydrogenate can be described as

$$MgH_2 + In \rightarrow In_7Mg_3 + H_2 \quad (5\text{-}2)$$

$$MgH_2 + In_7Mg_3 \rightarrow Mg(In)_{solid\ solution} + H_2 \quad (5\text{-}3)$$

For the Mg-20In solid solution system (Figure 5-8), the phase transformations are generally similar to the reactions of Mg-10In. However, one significant difference is that in the dehydrogenated state (>300℃), a fraction of Mg_3In intermediate phase was found in addition to the Mg solid solution phase at the culmination of dehydrogenation. This is because the indium content in the Mg-20In sample exceeded the solubility of indium in

Mg. Thus, there is a possibility of forming the intermetallic phase based on the Mg-In binary phase diagram. The solubility is, of course, a function of the temperature[2], the effect of which will be further discussed in the following section.

After dehydrogenation, two Mg-10In samples were rehydrogenated under different pressures (as illustrated in Figure 5-9 (b)), in order to produce two samples at different hydrogen concentrations, so that their phase compositions could be distinguished by *ex situ* XRD analysis. These XRD patterns are shown in Figure 5-9 (a). The MgH_2 phase, along with several Mg-In intermediate phases including Mg_3In, Mg_2In, and MgIn, are identified in the X-ray patterns. The absence of pure indium peaks indicates that a portion of Mg species did not reverse back to MgH_2 and instead remained in the Mg-In intermetallic compounds, resulting in a loss of hydrogen capacity after the first cycle of dehydrogenation (equation 5-3). However, a detailed comparison between two rehydrogenated samples showed increased intensities of Mg_2In peaks from the sample with higher hydrogen content, sample B, compared to sample A. This implies that the intermediate phases, including both Mg_3In (equation 5-5) and Mg_2In (equation 5-6), can react with hydrogen to form MgH_2 when they are subjected to higher H_2 pressure. The slope of the PCI curves (the range between points A and B in Figure 5-9) are characteristic of Mg-In alloys and can be explained by the reactions in equations 5-6 and 5-7.

$$Mg_{0.9}(In)_{0.1} + 0.6H_2 \leftrightarrow 0.6MgH_2 + 0.1Mg_3In \quad (5\text{-}4)$$

$$Mg_3In + H_2 \leftrightarrow MgH_2 + Mg_2In \quad (5\text{-}5)$$

$$Mg_2In + H_2 \leftrightarrow MgH_2 + MgIn \quad (5\text{-}6)$$

The result of SEM observations (Figure 5-10) shows that at first the indium phase (bright spot) was uniformly distributed in the as-milled mixture. After dehydrogenation,

no dispersed indium species instead of a relatively uniform Mg-In matrix was observed. Further, the backscattered SEM shows that a significant amount of Mg-In intermetallic particles of a few hundred nanometers appeared in the rehydrogenated Mg-10In sample, indicating these intermediate phases were precipitated out from the MgH_2 matrix during the rehydrogenation.

5.4.2 Phase Transitions in the Mg-Al System

An *in situ* XRD examination of Mg-10Al during dehydrogenation was conducted, and the results are shown in Figure 5-11. In contrast to those of the Mg-In samples, there was no intermediate phase observed in Mg-Al during dehydrogenation. However, similar to Mg-In systems, when the sample was heated to 400℃, a Mg phase was identified without concurrent Al or Mg-Al intermetallic phases, which suggests that Al was dissolved in the Mg solid solution.

5.4.3 Phase Transitions in Multicomponent Systems

For related multicomponent systems, Mg-Al-In-Zn-Si and Mg-Al-In-Zn-Ga were examined to understand the phase transformations during heating. The results are shown in Figure 5-12 and Figure 5-13. As it might be expected, it is difficult to recognize all the phases from the reactants. Thus, it is also difficult to determine the phase transformations during dehydrogenation, which generally occurred around 300℃. However, the products of dehydrogenation at 400℃ for both Mg-Al-In-Zn-Si and Mg-Al-In-Ga-Zn showed a single Mg phase, without any detectable intermediate phases. This again is an indication that all the alloying elements were able to dissolve into Mg at the relatively high

temperatures. It also demonstrates that there was no obvious formation of an intermediate phase(s) between the added elements.

5.5 Thermodynamic Properties - Enthalpy and Entropy

Using the van't Hoff relationship, the thermodynamic properties, specifically enthalpies and entropies of the hydrogenation and dehydrogenation reactions of all the alloys, were derived and listed in Table 5-1. The method used to calculate the reaction enthalpy (ΔH) and entropy (ΔS) is well established in the literature and incorporated herein within the supporting information. Considering both the calculated ΔH and ΔS from both hydrogen absorption and desorption, it can be seen that the ΔH of Mg-H reactions are significantly reduced, by as much as 9 kJ/mol H_2, when the indium content increased to 15 at%, while ΔS also decreased by about 10 J/mol H_2. Further, these enthalpy and entropy data were used to extrapolate the temperatures corresponding to equilibrium pressure at 1 bar ($T_{@Peq=1bar}$) and the equilibrium pressures at temperature of 300℃ ($P_{eq@T=300℃}$). These values are also given in Table 5-1. The data show substantial changes of $T_{@Peq=1bar}$, which decreased by 20℃, and $P_{eq@T=300℃}$, which increased by 1.0 bar. These results clearly show that the formation of Mg-In solid solutions is effective for destabilizing MgH_2 and for improving its thermodynamic properties.

However, an exception to the trend is the Mg-20In system, of which the calculated enthalpy is higher than those of other Mg-In systems. This is attributed to the inconsistent complexities of the phase compositions involved in the measurements of van't Hoff plots at different temperatures. As mentioned earlier, because 20 at.% of indium exceeded the solubility limit of In in Mg,[3] which was confirmed by the *in situ* XRD results (Figure 5-8),

a mixture of Mg-In solid solution and Mg-In intermetallic phases would be expected after dehydrogenation. As a result, the derived enthalpy and entropy of Mg-20In (Table 5-1) were not further reduced compared to Mg-10In and Mg-15In. The same situation occurred to samples in the Mg-10Al system. It can be seen that the van't Hoff plot of the Mg-10Al sample (see Figure 5-4) has a higher slope than those of Mg and Mg-In systems, which makes the Mg-10Al closer to the Mg-10In alloy at high temperatures and closer to pure Mg at low temperature. Similar to Mg-20In, this phenomenon can be explained by the increase of solubility of Al in Mg with increasing temperature. For instance, at 300℃ only 5 at.% Al can be dissolved in Mg, while at 400℃, this value increases to 10 at.% Al. The higher the solute content in Mg, the more significant the destabilization effect is.

The thermodynamic properties of the multicomponent systems, including Mg-5Al-5In, Mg-5Al-10In, Mg-5Al-5In-2Zn-1Si, and Mg-10Al-6In-2Ga-2Zn, are also provided in Table 5-1. On the basis of the *in situ* XRD analysis, both the Mg-5Al-5In-2Zn-1Si and the Mg-10Al-6In-2Ga-2Zn have a single phase of Mg solid solution at 400℃. This result does not exclude the possibility that there may still be a very small amount of alloying additives that are not fully dissolved, which may affect the accuracy of the values of ΔH and ΔS derived from the van't Hoff plots. The results do suggest, however, that multicomponent alloys could result in further enhancement of the thermodynamic destabilization of MgH_2.

5.6 Factors Affecting the Thermodynamic Stability of Magnesium Hydride

The above results clearly demonstrate that using solid solution alloys is an effective approach for destabilizing magnesium hydride. The fundamental reasons that result in the

destabilization, however, are yet to be fully understood. Several factors that may have played a role in the destabilization include crystal lattice unit cell volume, heat of mixing of the alloys, and the changes in entropy are discussed as follows.

5.6.1 Effect of Crystal Lattice Parameters and Unit Cell Volume

In general, forming solid solution alloys would result in changes to the lattice parameters and unit cell volume of the parent metal, i.e., the solvent. Several authors[4–6] have reported a linear correlation between the stability of metal/alloy-hydrogen systems and the unit cell volume. It was suggested that the smaller the unit cell volume of the alloy, the less stable the hydride is. From this point of view, the lattice parameters were calculated in this study from the XRD patterns of solid solution alloys of Mg, Mg-5In, and Mg-10In, which were collected at room temperature. The correlation between the lattice parameter and the alloy content is shown in Figure 5-14 (a). Note the lattice parameters of dehydrogenated Mg powder (a = 3.22 Å, c = 5.24 Å) are slightly higher than the reference data of Mg crystalline (a = 3.21 Å, c = 5.21 Å), which is likely due to the high energy ball milling and the nanoscale of the particles. Figure 5-14 shows that the lattice parameters including a, c, and unit cell volume, V, decreased with increasing indium content. The correlation between the volumes of unit cells and ΔH is plotted in Figure 5-14 (b). It appears that the Mg-In solid solution alloys follow the empirical rule as described above. For example, MgH_2 becomes less stable as the content of indium increased.

However, the above trend does not always hold when we compare the destabilization effects of different solute elements. According to the published data, several elements can reduce the cell volume of Mg by substituting and dissolving into the Mg lattice (see Figure

5-15)[2]. For example, Ag, Zn, Al, and Ga have stronger effects on reducing Mg lattice parameters than In. However, compared to the thermodynamic properties of Mg-10Al to those of Mg-10In, Mg-5Al-5In to those of Mg-10In, and Mg-5Al-10In to those of Mg-15In in this work, indium seems to be more effective than Al in destabilizing MgH_2. This is also consistent with Liang's observations[7] on Ag, Zn, Al, In, and Cd additions.

5.6.2 Effect of the Heat of Mixing of the Solid Solution Alloy

It is well known that one way to reduce the reaction enthalpy of a metal hydride MH_x is to react the hydride with a suitable reactant A, which can form a compound MA_y exothermically with the metal M.[8] This reaction can be expressed as

$$MH_x + y\,A \leftrightarrow MA_y + \frac{x}{2}H_2 \tag{5-7}$$

If the enthalpy and entropy changes of the reactions in equations 5-8 and 5-9 are available,

$$MH_x \leftrightarrow M + \frac{x}{2}H_2 \tag{5-8}$$

$$M + y\,A \leftrightarrow MA_y \tag{5-9}$$

then the reaction enthalpy and entropy of the reaction in equation 5-7 can be shown as

$$\Delta H_{eq(8)} = \Delta H_{eq(9)} + \Delta H_{eq(10)} \tag{5-10}$$

$$\Delta S_{eq(8)} = \Delta S_{eq(9)} + \Delta S_{eq(10)} \tag{5-11}$$

Applying this to the Mg-In binary system, we would have the following reaction

$$MgH_2 + Mg_xIn_{y\ (intermediate\ phase)} \rightarrow (MgIn)_{solid\ solution} + H_2 \tag{5-12}$$

of which reaction enthalpy and entropy can be calculated from the reactions

$$MgH_2 \rightarrow Mg + H_2 \tag{5-13}$$

$$Mg + Mg_xIn_{y\ (intermediate\ phase)} \rightarrow (MgIn)_{solid\ solution} \tag{5-14}$$

Here, in order to destabilize the solid solution alloy to hydrogen reactions, the most crucial criterion that must be met is that the solid solution formation reaction (equation 5-14) must be exothermic. Some available heat of mixing values of the Mg-based liquid alloys are listed in Table 5-2, showing that the heat of mixing of Mg-Ag, Mg-Al, Mg-Cd, Mg-Ga, and Mg-In are all negative, or exothermic. Unfortunately, since there is generally a lack of thermodynamic data of the intermetallic phases, such as Mg_3In, we were unable to estimate the heat of formation of the reaction (equation 5-12).

5.6.3 Effect of Entropy

Another important factor that affects the equilibrium pressure of metal hydrides is the entropy of the reaction, ΔS. It is often assumed as constant during hydrogenation and dehydrogenation reactions. However, several recently published reports have shown that the reduction of ΔH is often accompanied by a reduction of ΔS, which counteracts the effect of decreasing ΔH. For instance, Zhao-Karger et al.[9] reported that the ΔH of dehydrogenation was reduced to 63.8 kJ/mol H_2 with a ΔS of 117.2 J/mol H_2, resulting in a lower than expected decrease of $T_{@Peq=1bar}$ (only 11℃). Similar trends were reported by Paskevicius et al.[10] and Anastasopol et al.[11]. Regarding MgH_2 with a TiH_2 additive, Lu et al.[12] also reported that although ΔH was reduced, the equilibrium pressure was not changed due to the concurrent changes in ΔS. In this work, ΔS was also reduced with ΔH decreasing. For example, for Mg-15In, ΔS decreased by 11.45 J/mol H_2, corresponding to a decrease in ΔH by 9.56 kJ/mol H_2. Therefore, a simple explanation for the decrease of ΔS of the overall reaction in equation 5-8 can be attributed to the entropy change seen in the reaction in equation 5-9.

5.7 Summary

In conclusion, formation of magnesium solid solution with elements such as In, Al, Ga, and Zn has been proved to be an effective route to destabilize MgH_2. PCT characterizations showed that all magnesium solid solutions had higher equilibrium hydrogen pressure than that of magnesium. In particular, the calculated reaction enthalpy (ΔH) of magnesium solid solution alloy can be reduced 69.18 kJ/mol H_2, compared to 77.20 kJ/mol H_2 of pure magnesium hydride, and the $T_{1\ bar}$ can be reduced to 259.59℃, compared to 280.68℃ of pure magnesium hydride. *In situ* XRD analysis indicated that the solute element(s) and MgH_2 will form solid solution after dehydrogenation. Further, *ex situ* XRD results revealed that magnesium intermediate phases with MgH_2 appeared in the rehydrogenated-state solid solution. This results in a reversible hydrogen absorption/desorption reaction but a lower hydrogen capacity.

5.8 References

1. Sandrock, G.; Thomas, G., The Iea/Doe/Snl on-Line Hydride Databases. *Appl. Phys. A* **2001**, *72*, 153−155.

2. Nayeb-Hashemi, A. A.; Clark, J. B., *Phase Diagrams of Binary Magnesium Alloys*; ASM International Metals Park, OH, 1988.

3. Baker, H.; Okamoto, H., *ASM Handbook, Volume 03 - Alloy Phase Diagrams*. ASM International.

4. Bechman, C. A.; Goudy, A.; Takeshita, T.; Wallace, W. E.; Craig, R. S., Solubility of Hydrogen in Intermetallics Containing Rare Earth and 3d Transition Metals. *Inorg. Chem.* **1976**, *15*, 2184−2187.

5. Mendelsohn, M. H.; Gruen, D. M.; Dwight, A. E., Lani5-Xalx Is a Versatile Alloy System for Metal Hydride Applications. *Nature* **1977**, *269*, 45−47.

6. Hirscher, M.; Züttel, A.; Borgschulte, A.; Schlapbach, L., *Handbook of Hydrogen Storage*, Wiley-VCH Verlag GmbH & Co. KGaA, Weinheim, Germany, 2009.

7. Liang, G., Synthesis and Hydrogen Storage Properties of Mg-Based Alloys. *J. Alloys Compd.* **2004**, *370*, 123−128.

8. Vajo, J. J.; Mertens, F.; Ahn, C. C.; Bowman, R. C.; Fultz, B., Altering Hydrogen Storage Properties by Hydride Destabilization through Alloy Formation: LiH and Mgh2 Destabilized with Si. *J. Phys. Chem. B* **2004**, *108*, 13977−13983.

9. Zhao-Karger, Z.; Hu, J.; Roth, A.; Wang, D.; Kubel, C.; Lohstroh, W.; Fichtner, M., Altered Thermodynamic and Kinetic Properties of MgH_2 Infiltrated in Microporous Scaffold. *Chem. Commun.* **2010**, *46*, 8353−8355.

10. Paskevicius, M.; Sheppard, D. A.; Buckley, C. E., Thermodynamic Changes in Mechanochemically Synthesized Magnesium Hydride Nanoparticles. *J. Am. Chem. Soc.* **2010**, *132*, 5077−5083.

11. Anastasopol, A.; Pfeiffer, T. V.; Middelkoop, J.; Lafont, U.; Canales-Perez, R. J.; Schmidt-Ott, A.; Mulder, F. M.; Eijt, S. W., Reduced Enthalpy of Metal Hydride Formation for Mg-Ti Nanocomposites Produced by Spark Discharge Generation. *J. Am. Chem. Soc.* **2013**, *135*, 7891−7900.

12. Lu, J.; Choi, Y. J.; Fang, Z. Z.; Sohn, H. Y.; Rönnebro, E., Hydrogen Storage Properties of Nanosized Mgh_2−$0.1TiH_2$ Prepared by Ultrahigh-Energy−High-Pressure Milling. *J. Am. Chem. Soc.* **2009**, *131*, 15843−15852.

13. Hultgren, R.; Desai, P. D.; Hawkins, D. T.; Gleiser, M.; Kelley, K. K. *Selected Values of the Thermodynamic Properties of Binary Alloys*; DTIC Document: 1973.

Table 5-1. Thermodynamic properties of Mg-based solid solution alloys systems.

Systems		Enthalpy ΔH, kJ/mol H_2	Entropy ΔS, J/mol H_2	$T_{@Peq=1bar}$, °C	$P_{eq@T=300℃}$, bar
Mg	Absorption	-76.07±1.21	-137.89±1.97	278.50	1.86
	Desorption	78.60±0.43	141.39±0.70	282.78	1.67
Mg-5In *	Absorption	-74.21±1.09	-136.93±1.78	268.82	2.45
	Desorption	74.99±1.20	137.82±1.96	270.98	2.31
Mg-10In *	Absorption	-68.88±0.52	-129.15±0.85	260.21	2.94
	Desorption	75.33±1.60	138.59±2.61	270.41	2.36
Mg-15In *	Absorption	-72.46±1.85	-135.16±2.93	263.02	2.85
	Desorption	69.04±1.85	129.94±3.08	262.33	2.77
Mg-20In ×	Absorption	-74.38±0.55	-138.56±0.89	263.61	2.88
	Desorption	76.83±1.27	141.68±2.07	269.12	2.50
Mg-10Al ×	Absorption	-78.32±0.52	-142.67±0.85	275.81	2.06
	Desorption	80.37±0.46	144.51±0.74	283.02	1.67
Mg-5Al-5In ?	Absorption	-70.89±2.54	-131.77±4.10	264.88	2.64
	Desorption	73.22±1.08	135.15±1.74	268.65	2.43
Mg-5Al-10In ?	Absorption	-71.45±0.86	-133.82±1.37	260.82	3.01
	Desorption	73.98±1.94	137.28±3.10	265.76	2.68
Mg-5Al-5In-2Zn-Si ?	Absorption	-72.01±0.12	-133.74±0.21	265.32	2.65
	Desorption	74.53±1.59	138.00±2.58	266.94	2.61
Mg-10Al-6In-2Zn-2Ga ?	Absorption	-69.18±0.01	-129.85±0.02	259.60	3.01
	Desorption	73.45±1.12	135.99±1.74	266.97	2.57

Remarks: * Additive does not exceed solubility limit; × Additive(s) exceeds solubility limit; ? Uncertainty exists concerning precise solubility limit.

Table 5-2. Selected data for heat of mixing of Mg liquid alloys.

Systems	Heat of mixing, ΔH_m, kJ/mol	Entropy changes, ΔS_m, J/mol	Temperature, ^oC	References
Mg-10Ag	-4.354	--	1050	2
Mg-10Al	-0.962	2.343	800	13
Mg-10Cd	-2.025	2.130	650	13
Mg-10Ga	-3.820	2.368	650	13
Mg-10In	-2.807	2.925	650	13

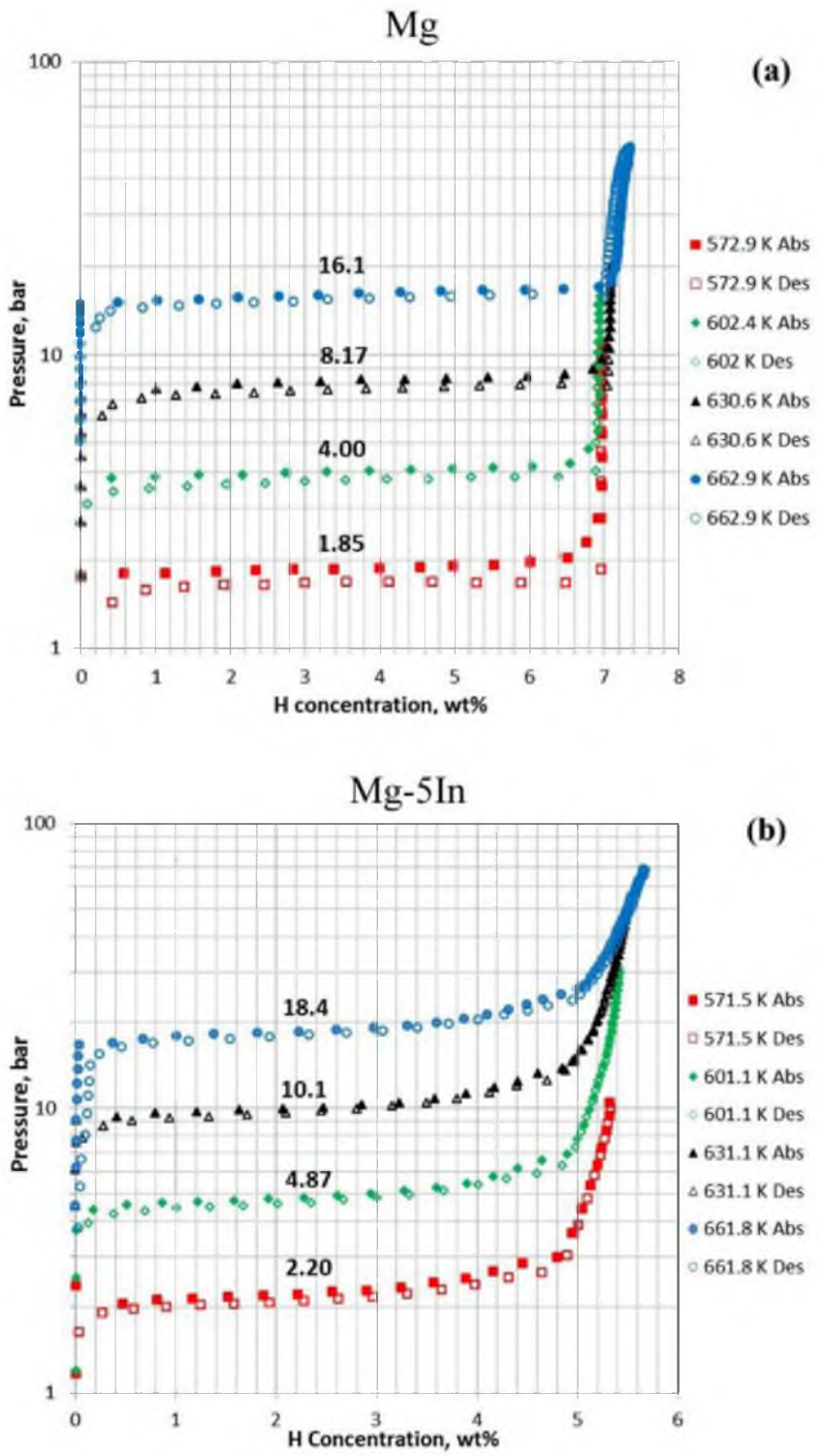

Figure 5-1. Hydrogen absorption and desorption PCI curves of different Mg-based solid solution systems. (a) Mg; (b) Mg-5In; (c) Mg-10In; (d) Mg-15In; (e) Mg-20In; (f) Mg-10Al; (g) Mg-5Al-5In; (h) Mg-5Al-10In; (i) Mg-5Al-5In-2Zn-1Si; (j) Mg-10Al-6In-2Ga-2Zn.

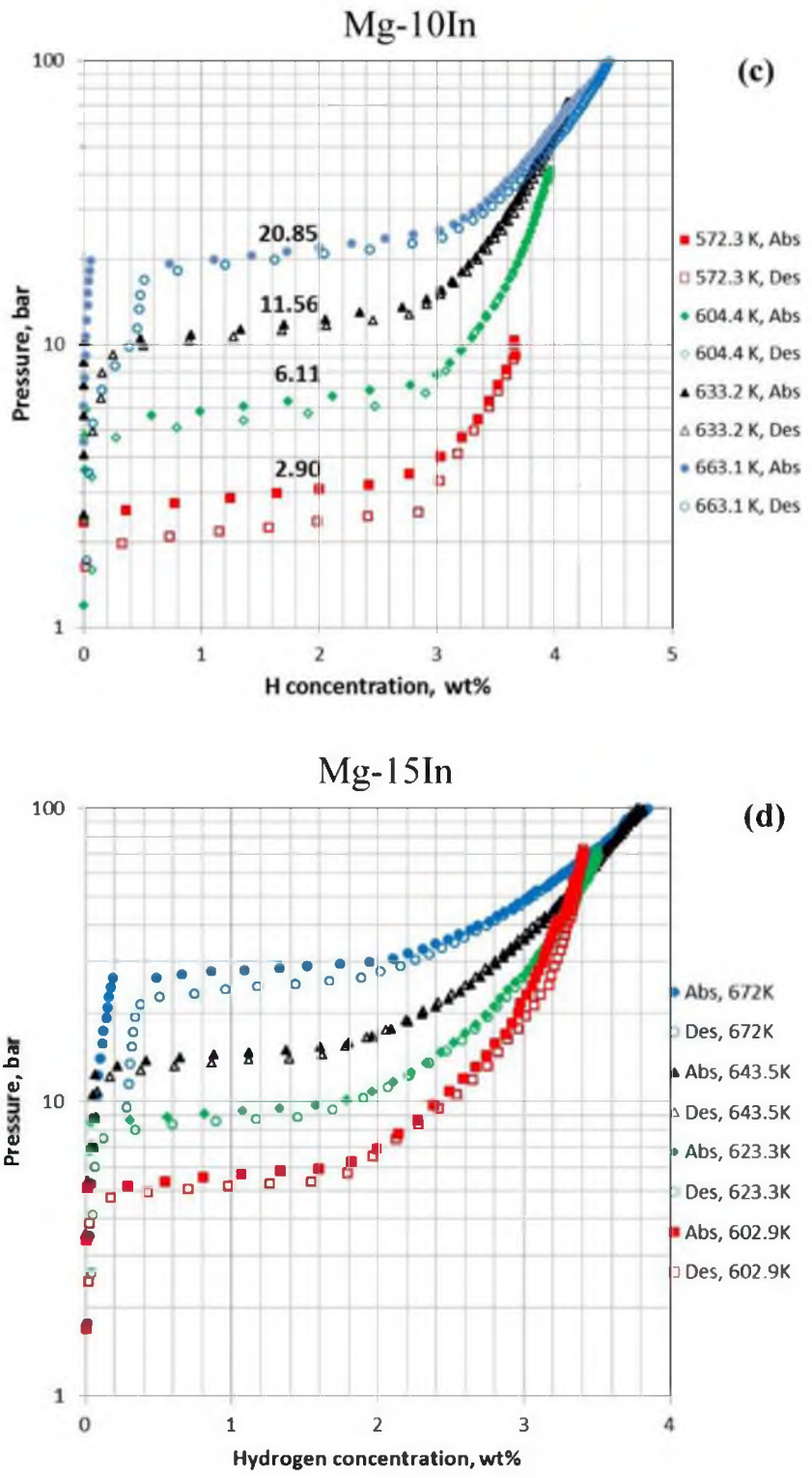

Figure 5-1. Continued.

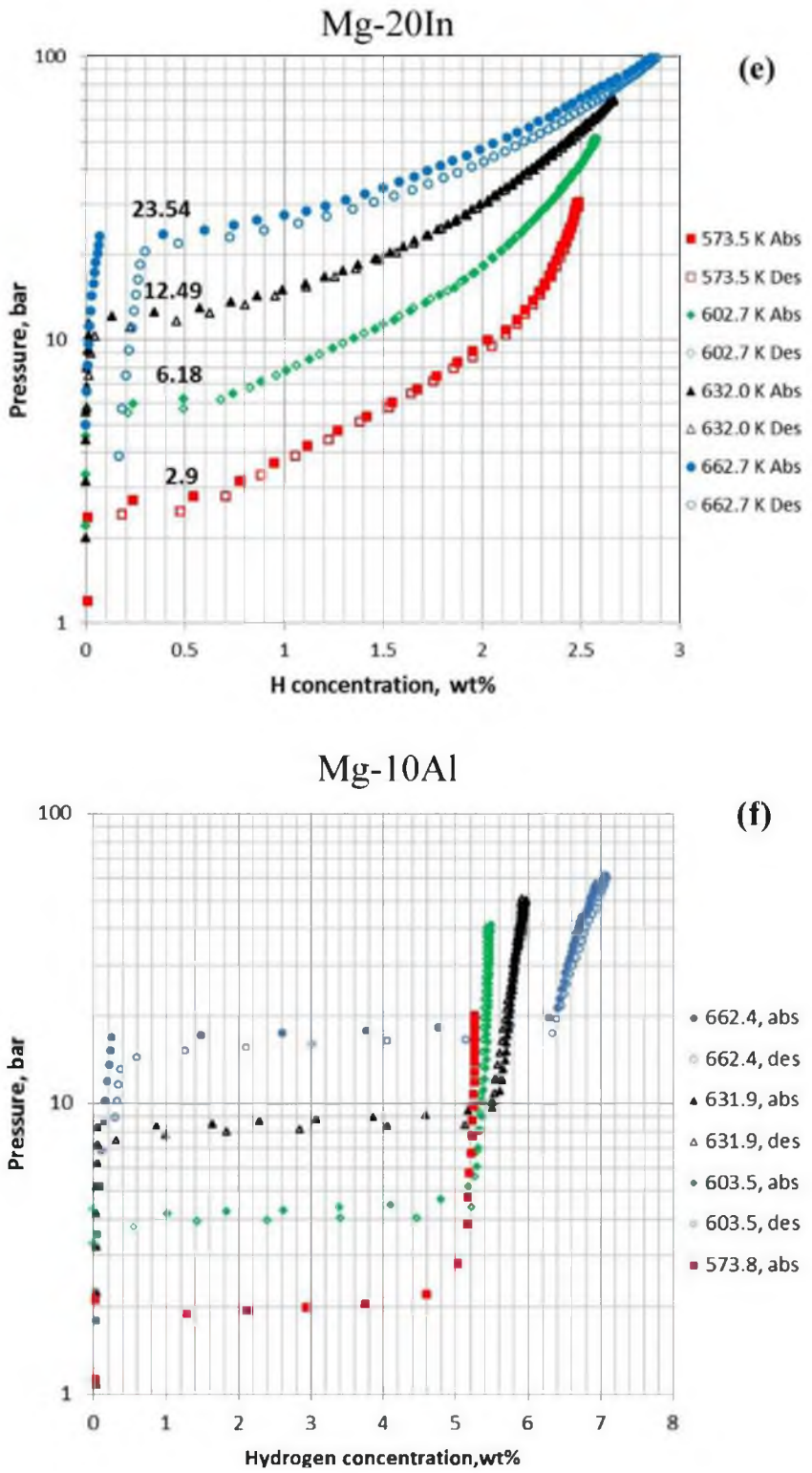

Figure 5-1. Continued.

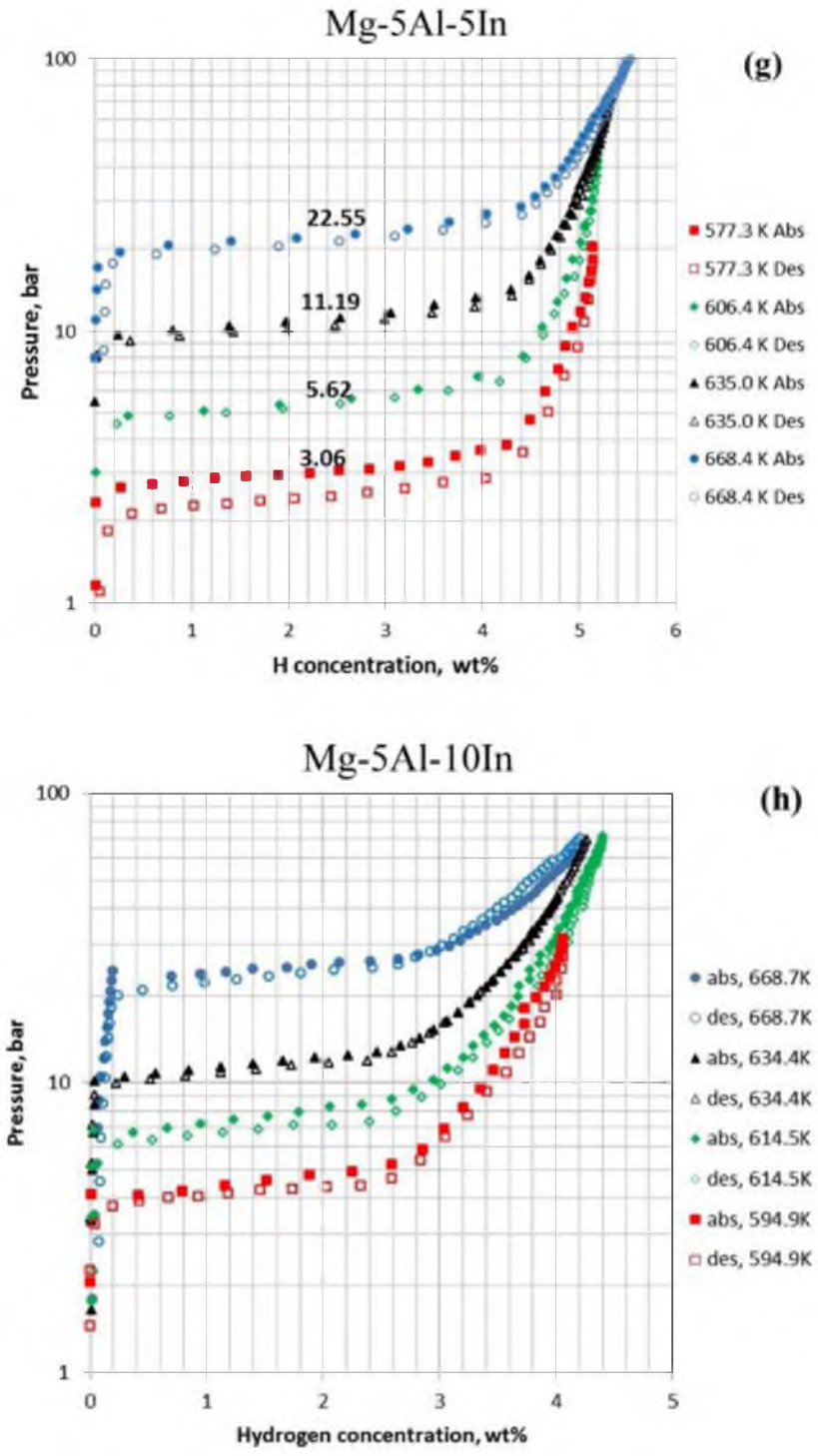

Figure 5-1. Continued.

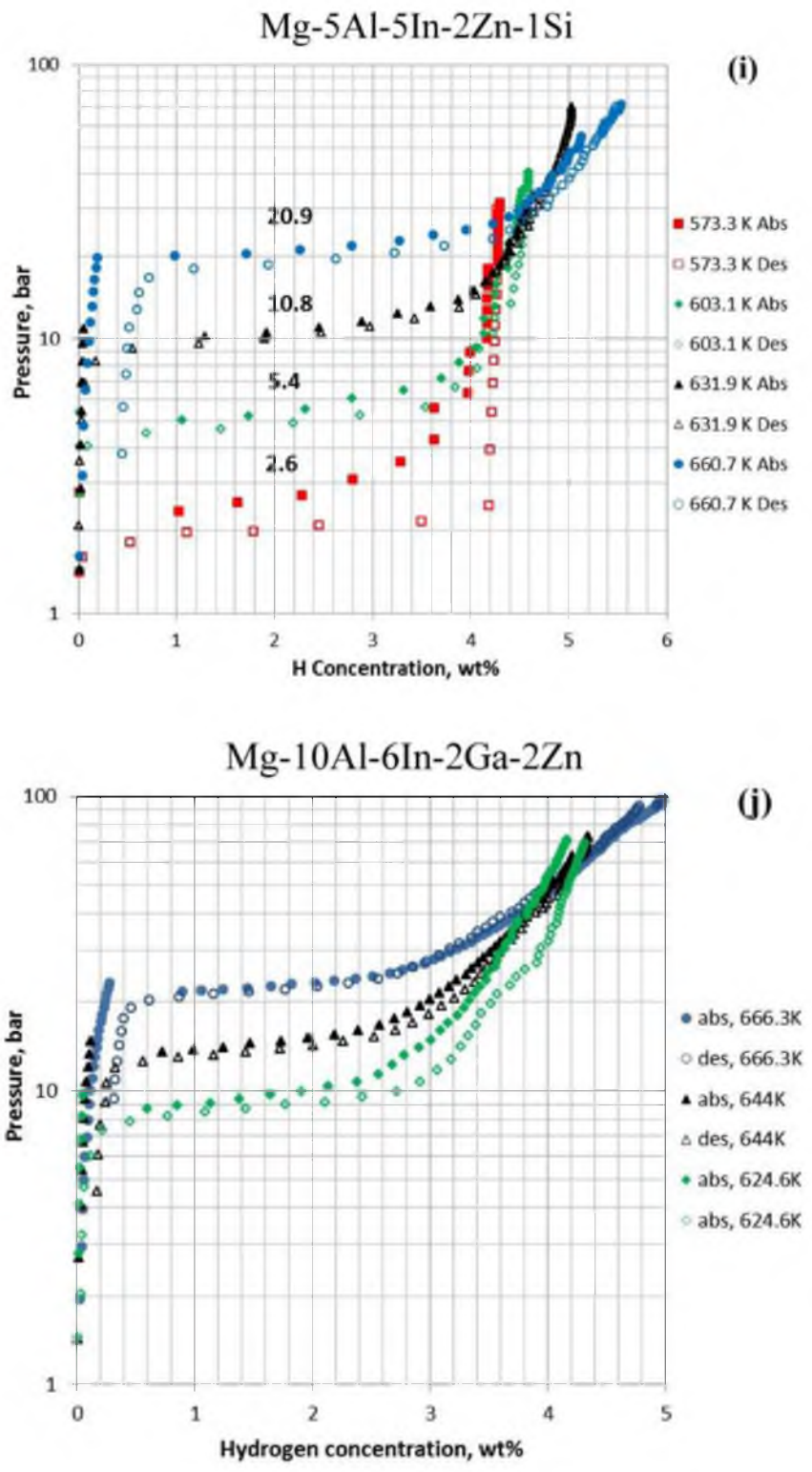

Figure 5-1. Continued.

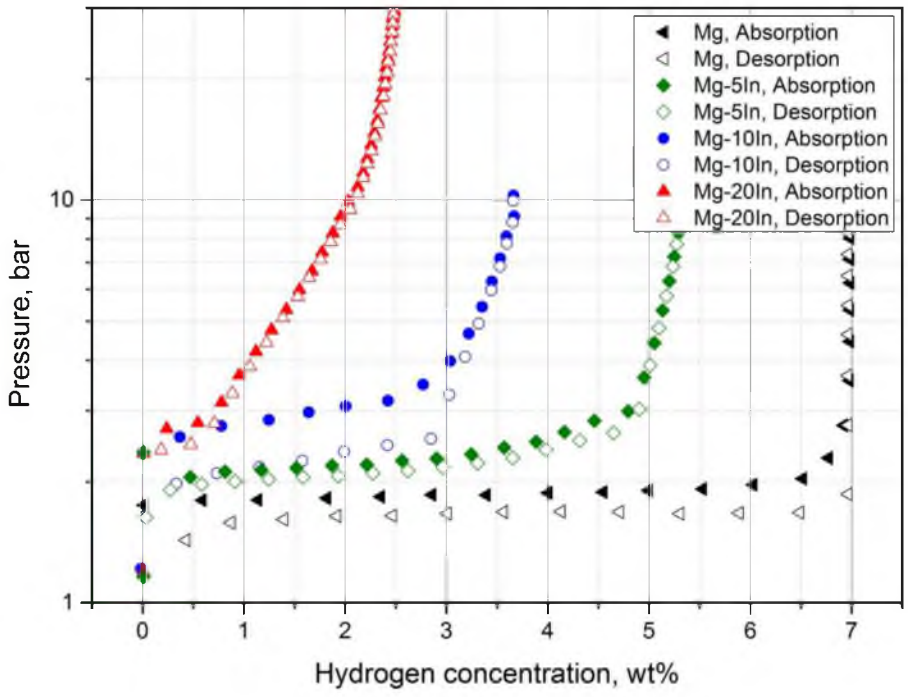

Figure 5-2. PCI curves of various Mg-In solid solution systems performed at 300 °C.

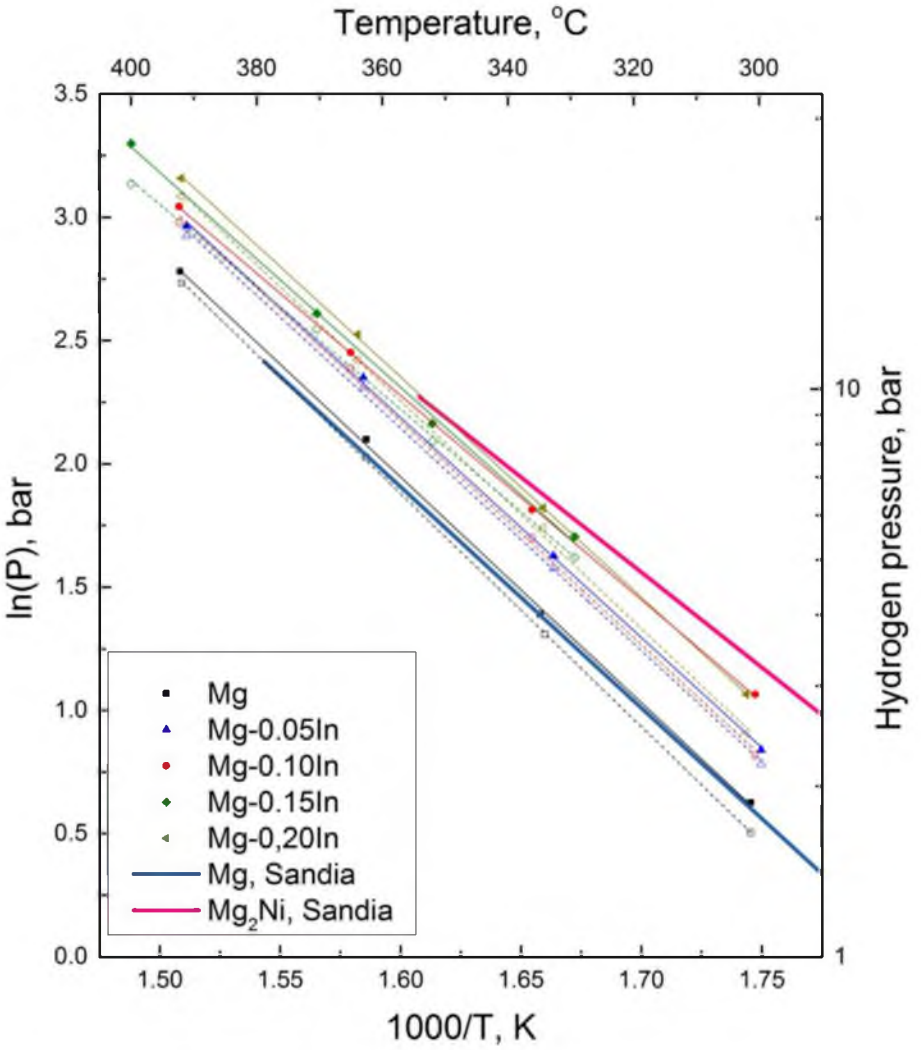

Figure 5-3. A van't Hoff plot of Mg-In solid solution alloys systems with different indium contents. The solid markers indicate the hydride formation (H_2 absorption) plateau pressures; and the open markers indicate the hydride decomposition (H_2 desorption) plateau pressures. The blue lines and purple lines represent the van't Hoff lines of Mg and Mg_2Ni, respectively. (Data were obtained from Sandia metal hydride database[1].)

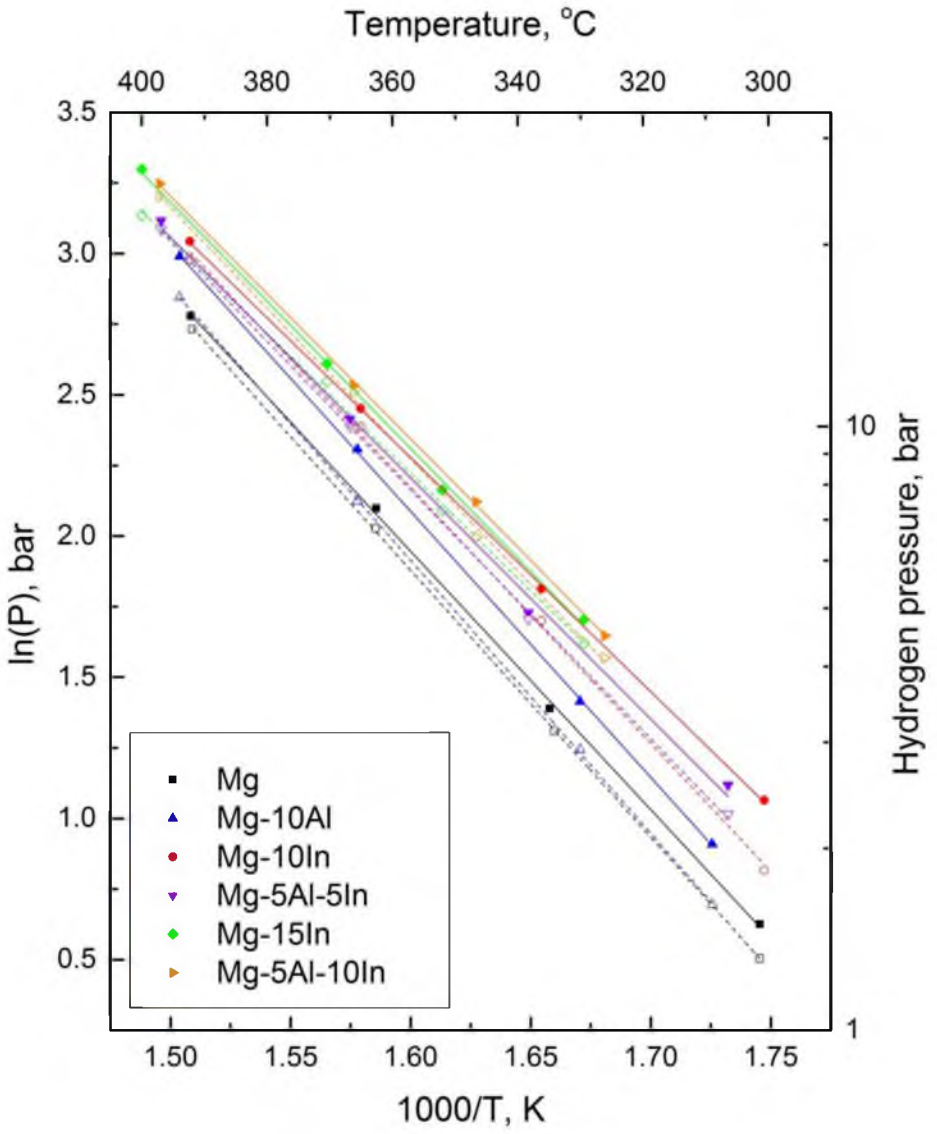

Figure 5-4. A van't Hoff plot of binary Mg-Al and ternary Mg-Al-In solid solution systems. The solid markers indicate the hydride formation (H_2 absorption) plateau pressures, and the open markers indicate the hydride decomposition (H_2 desorption) plateau pressures.

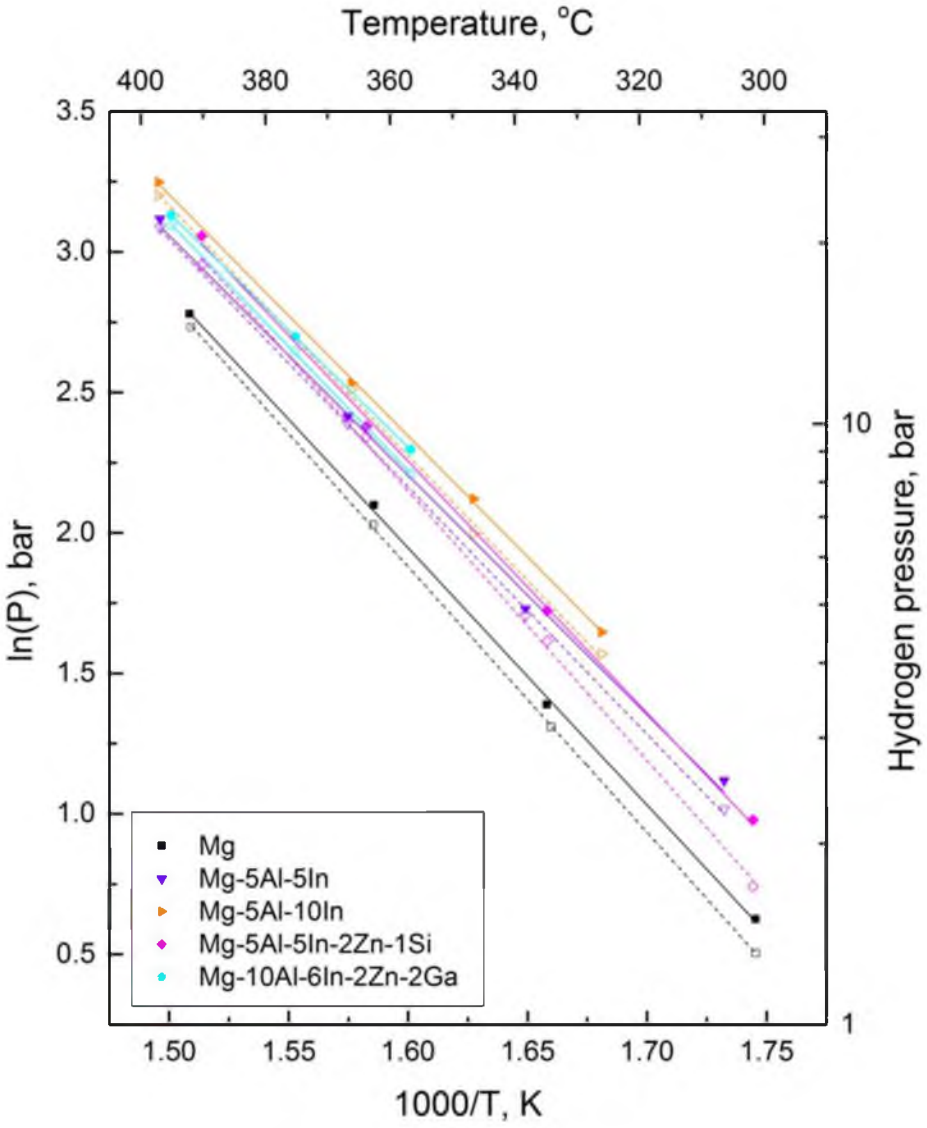

Figure 5-5. A van't Hoff plot of Mg-Al-In-Zn-Si and Mg-Al-In-Zn-Ga solid solution systems. The solid markers indicate the hydride formation (H_2 absorption) plateau pressures, and the open markers indicate the hydride decomposition (H_2 desorption) plateau pressures.

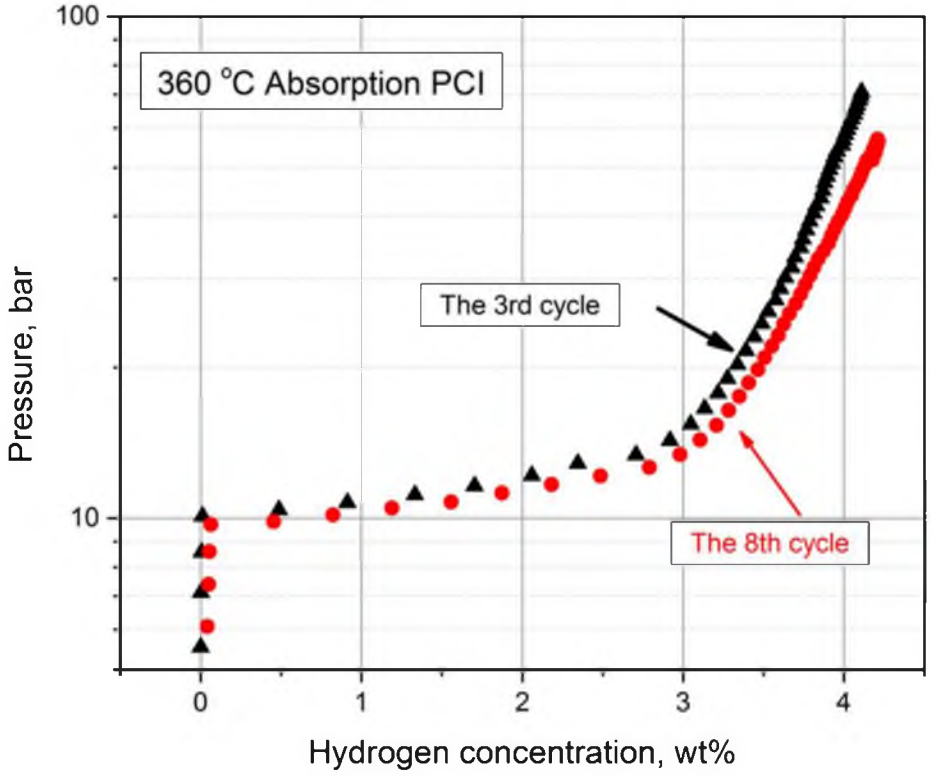

Figure 5-6. A comparison of PCI curves for a Mg-10In sample after the 3rd and 8th cycles. Tests were carried out at 360 °C.

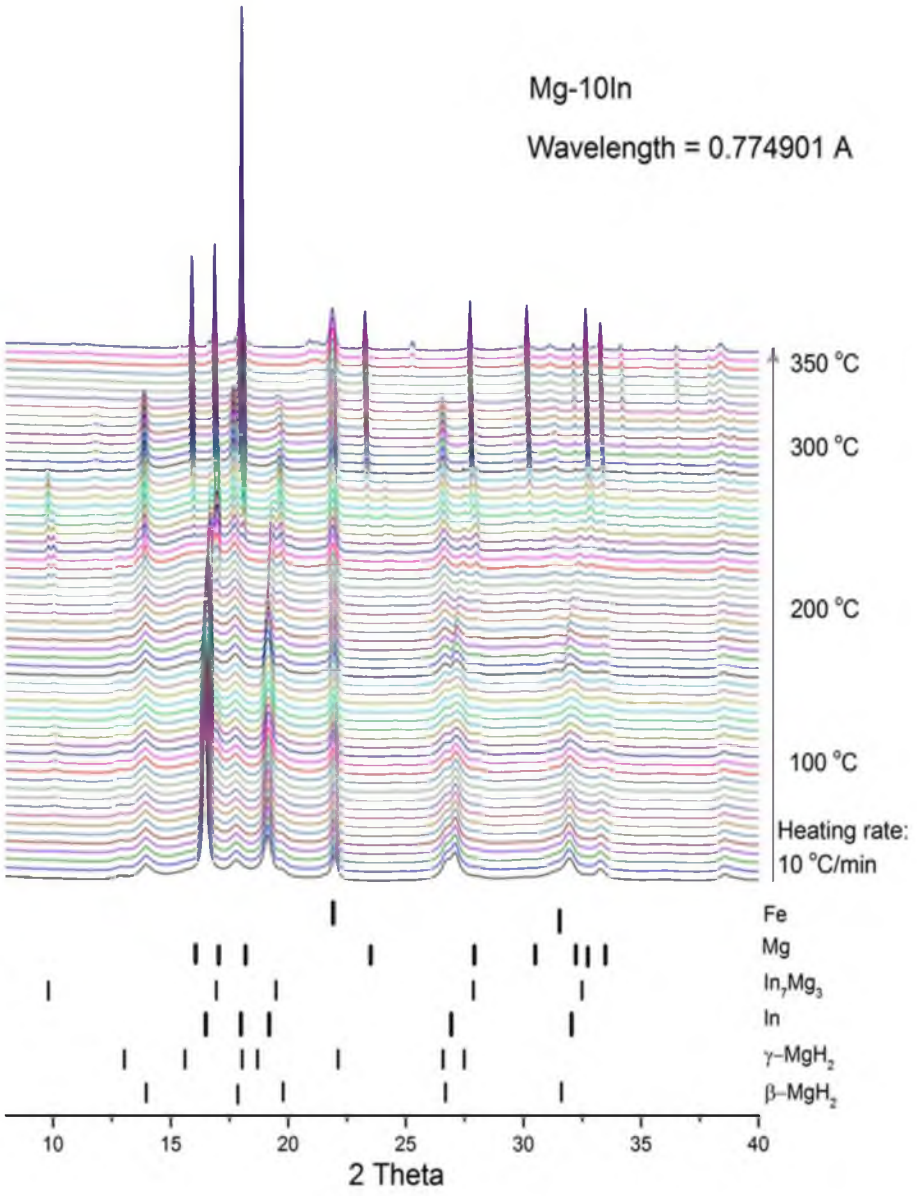

Figure 5-7. Plots of data from *in situ* XRD experiments for the dehydrogenation of MgH_2-10In. The wavelength of the X-ray source was 0.774901 Å.

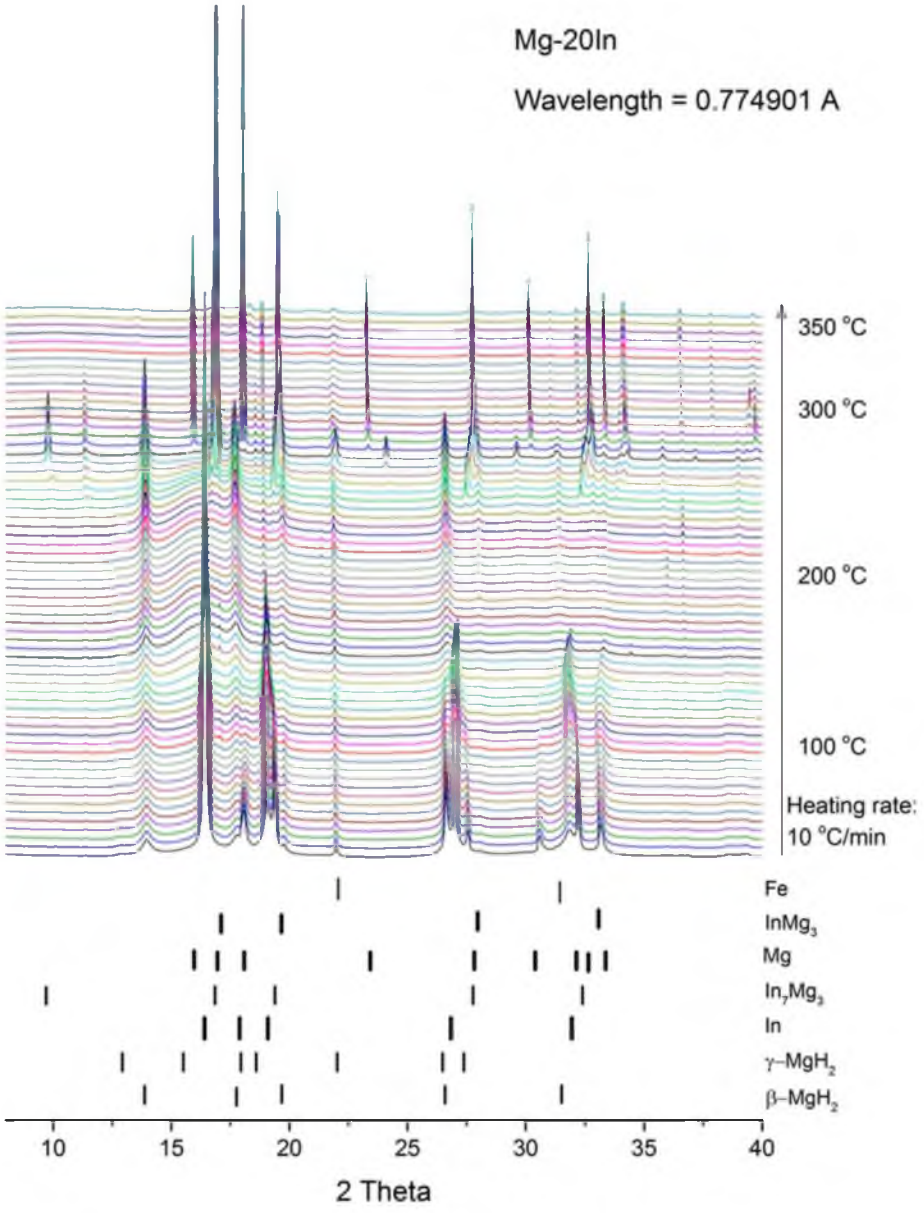

Figure 5-8. Plots of data from *in situ* XRD experiments for the dehydrogenation of MgH_2-20In. The wavelength of the X-ray source was 0.774901 Å.

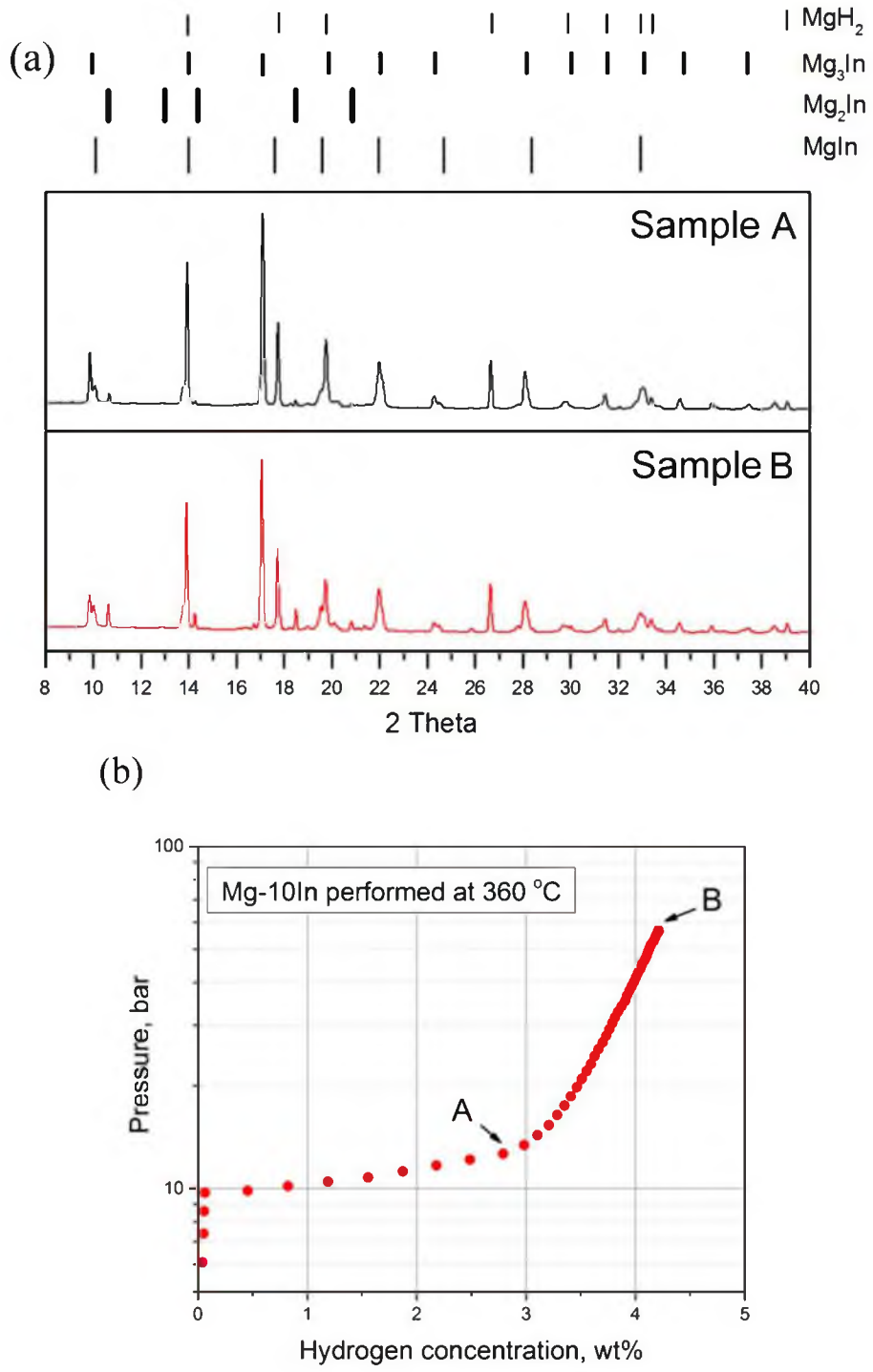

Figure 5-9. X-ray diffraction patterns of rehydrogenated Mg-In samples. The X-ray wavelength was 0.774901 Å, as illustrated in the right PCI curve, sample A contained 2.8 wt% hydrogen, and sample B contained ~4.2 wt% hydrogen.

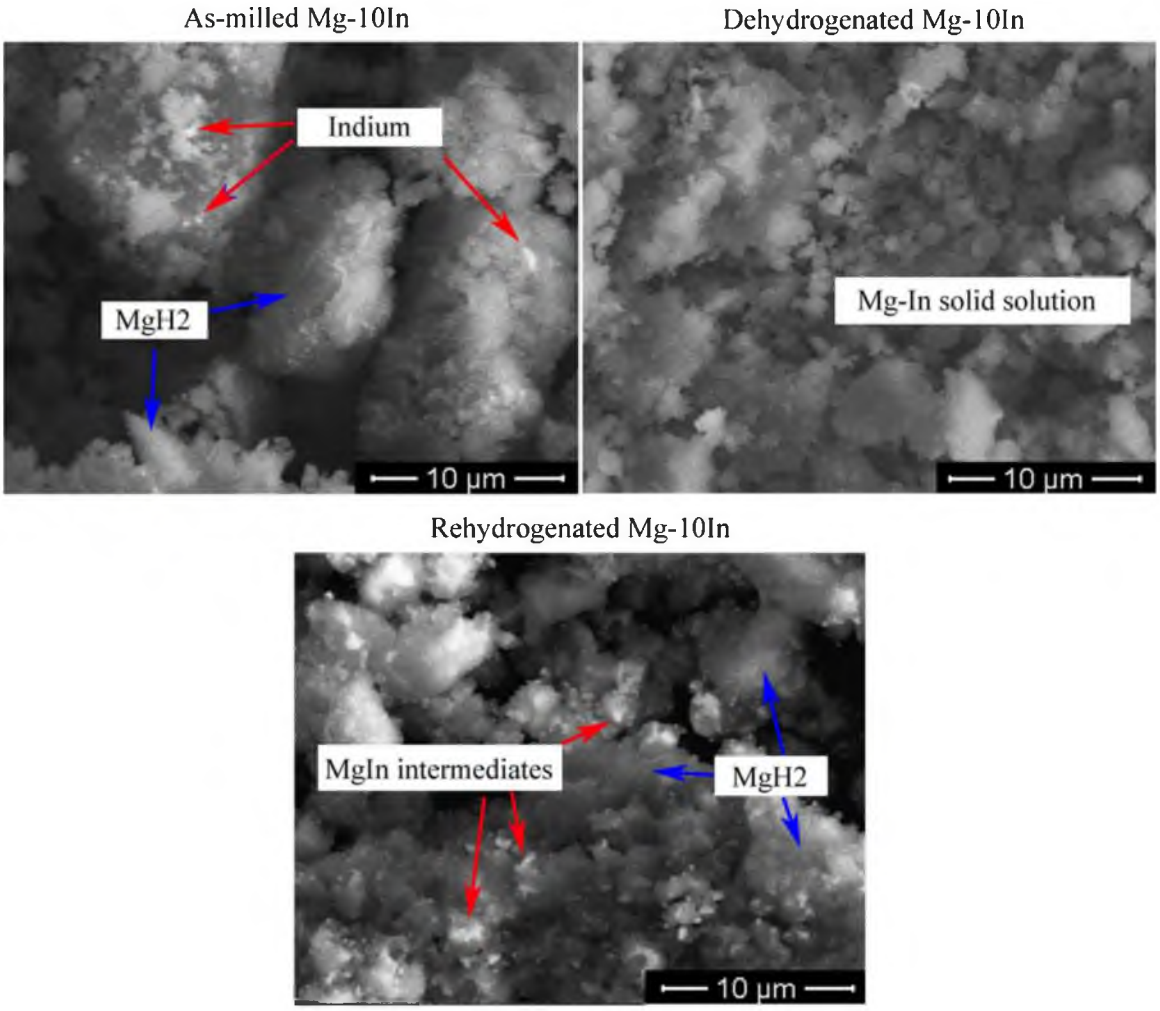

Figure 5-10. Backscattered electrons (BSE) SEM images of as-milled, dehydrogenated, and rehydrogenated Mg-10In samples.

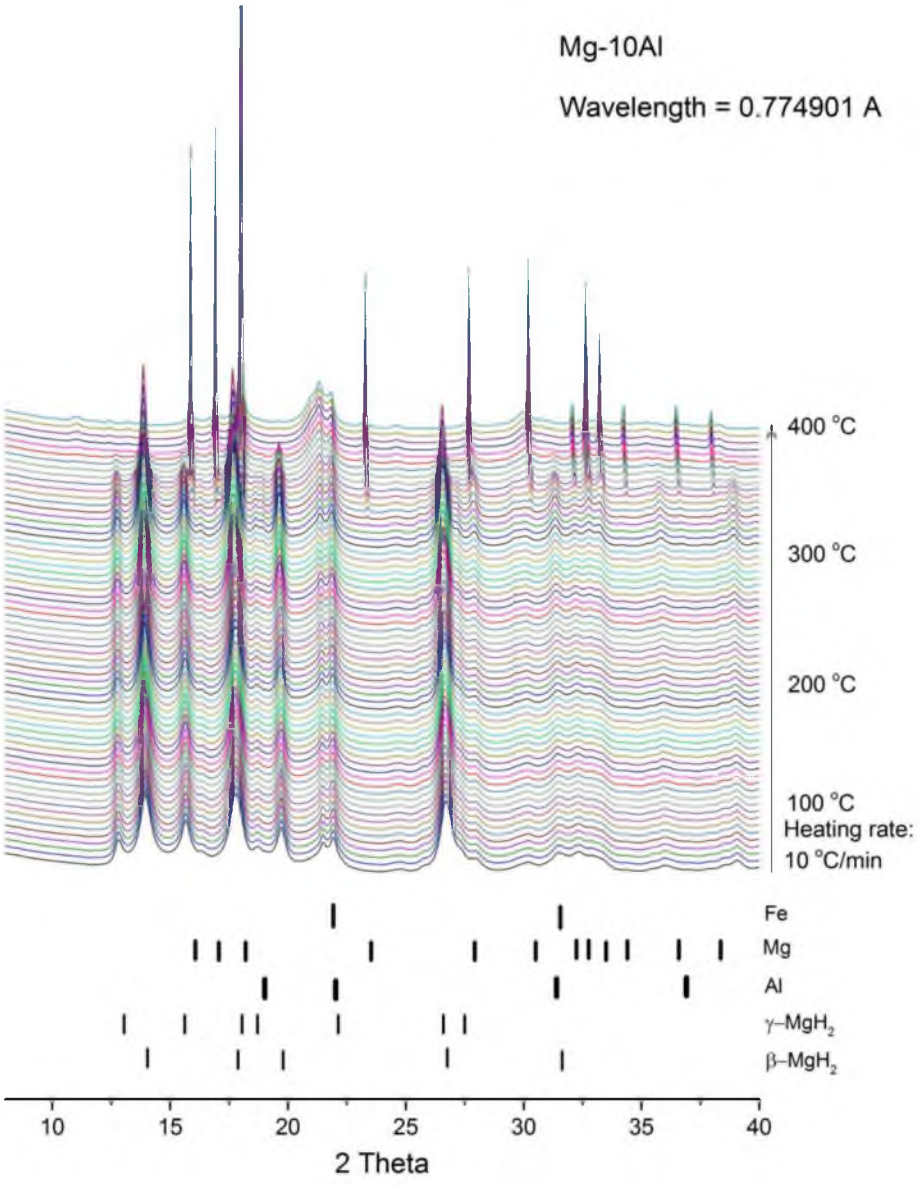

Figure 5-11. Patterns for *in situ* XRD during dehydrogenation of MgH_2-10Al. The wavelength of the X-ray source was 0.774901 Å.

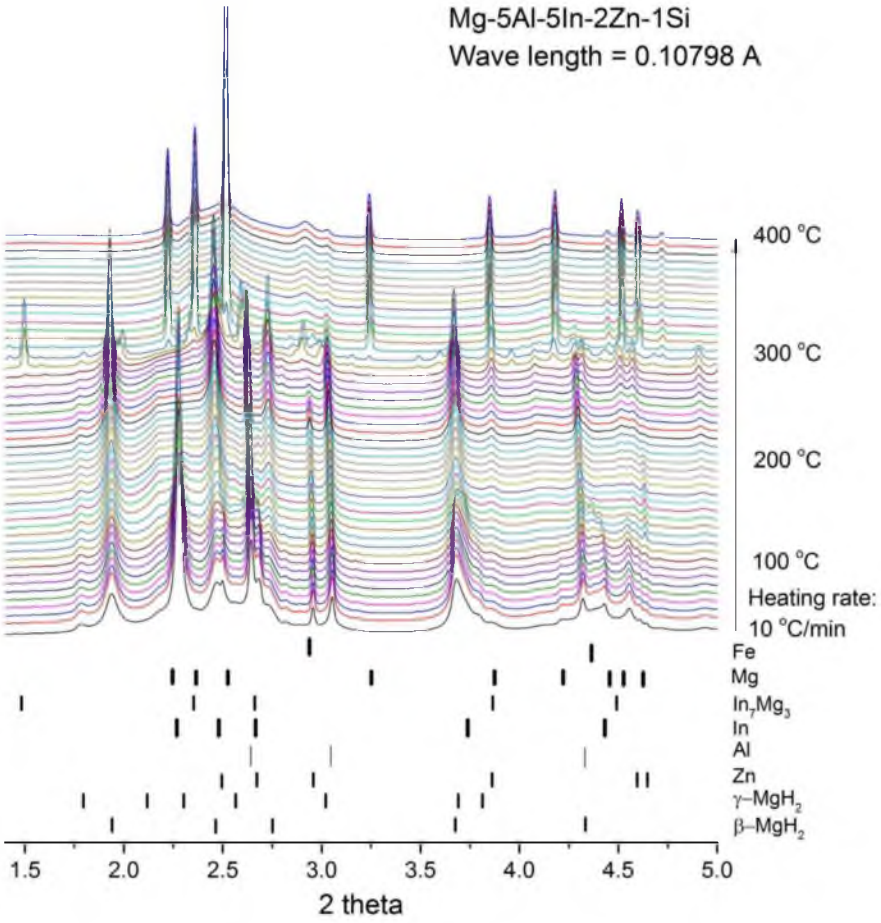

Figure 5-12. Patterns for *in situ* XRD during dehydrogenation in the Mg-Al-In-Zn-Si system. The wavelength of the X-ray source was 0.10798 Å.

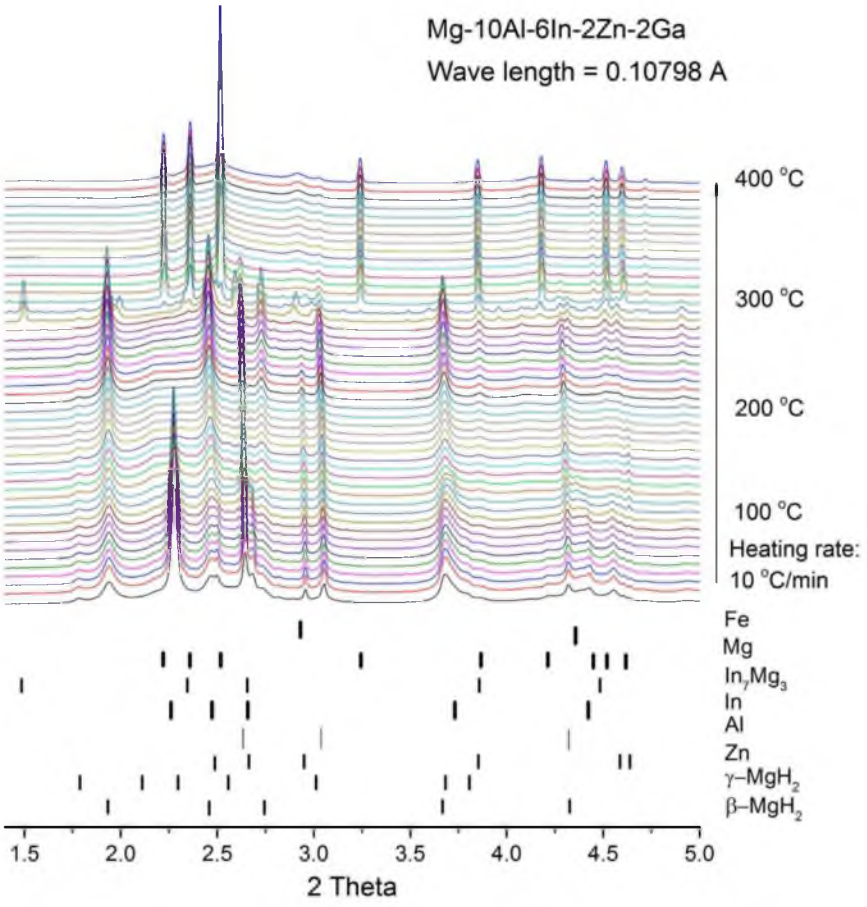

Figure 5-13. Patterns for *in situ* XRD during dehydrogenation in the Mg-Al-In-Zn-Ga system. The wavelength of the X-ray source was 0.10798 Å.

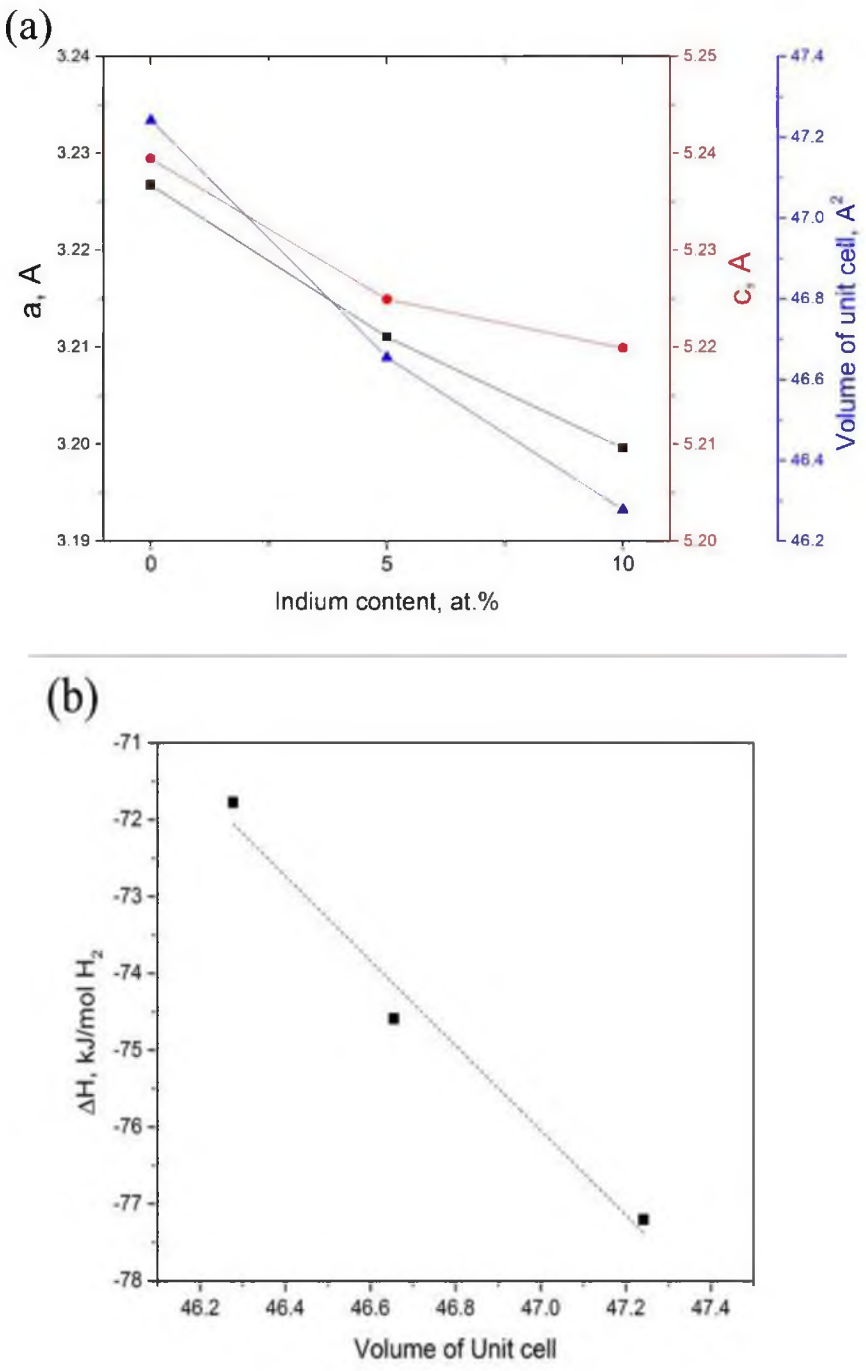

Figure 5-14. Effect of indium content on lattice parameters of Mg solid solution. (a) Lattice parameters, including a, c, and volume of unit cell, V of Mg, Mg-5In, and Mg-10 samples; (b) the volume of the unit cell, V, against the enthalpy of Mg-In solid solutions, ΔH.

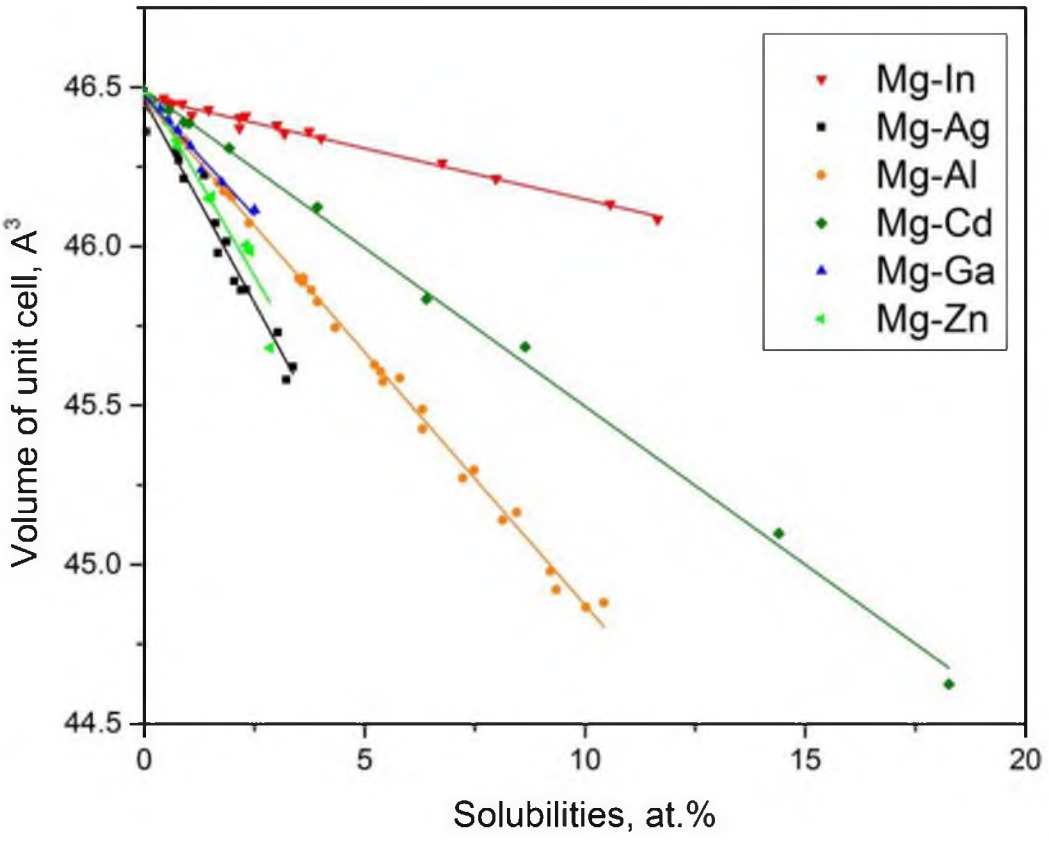

Figure 5-15. The correlations between volume of unit cell and different solute elements. Data are adapted from Nayeb-Hashemi and Clark.[2]

CHAPTER 6

CYCLIC STABILITY OF CATALYZED MAGNESIUM HYDRIDE

In this chapter, a comprehensive investigation is designed to study kinetic stability of nanocrystalline MgH_2 doped with transition metal based catalysts. The first object is to test the stability of the dehydrogenating/hydrogenating properties at high temperature during cycling. The second purpose is to evaluate the degradation of room temperature hydrogenation behaviors along with extended cycling under different conditions. The third aim is to characterize the evolution of the microstructure of the doped Mg/MgH_2 systems.

6.1 Isothermal Hydrogen Cycling

Volumetric cycling measurements were performed using PCI method on an automated Sieverts type apparatus (Hy-Energy LLC., PCTPro-2000). About 0.1 g of each milled powder was loaded into a stainless steel vessel and sealed in a PCT sample holder. During the experiment, the temperature of the sample was held constant (± 0.5 °C) by a PID controller (Watlow, PID Controller SD).

It has been reported by some researchers[1, 2] that a catalyzed MgH_2 system showed very good stability when cycling at a temperature of 300 °C. As mentioned in section 1.3, for the application of a thermal battery, the kinetics of MgH_2 (hot hydride) is required to be

fast and stable for not only high temperature dehydrogenation (taking recharge into account) but also for hydrogenation at low temperatures (taking discharge into account). However, reported research on such a cyclic assessment is very limited.

Therefore, isothermal cycling experiments were designed for evaluating dehydrogenation kinetics under relatively low-temperature and low-hydrogen-pressure-differentiation, and the MgH_2-VTiCr system was used in the experiments.

Figure 6-1 (a) and (b) show the comparisons of dehydrogenation kinetics at the 1st, 10th, 50th, and 100th cycles performed at temperatures of 250 °C and 270 °C. In order to keep the reaction driving forces low, the dehydrogenation was carried out in a pressure range of 0.2 to 0.3 bar at 250 °C (P/P_{eq} = 0.54 ~ 0.79) and in a pressure range of 0.5 to 0.6 bar at 270 °C (P/P_{eq} = 0.68 ~ 0.82). Besides the different pressures during the dehydrogenation of the two tests, their hydrogenation reactions were used at the same hydrogen pressure (10 bar).

As shown in Figure 6-1 (a), after 10 cycles at 250 °C, the dehydrogenation kinetics degraded. The desorption rate of the 50th cycle is slightly slower than those of the 1st and 10th cycles. And at the 100th cycle, the rate is significantly slower and only released 3.5 wt% of hydrogen after 120 minutes. However, when the temperature increased to 270 °C, no obvious degradation was observed. Moreover, it is interesting to see that with a temperature increase of only 20 °C, much faster kinetics can be achieved. For the dehydrogenation performed at 270 °C, approximately 5 wt% hydrogen was desorbed in less than 15 minutes, compared to the release of 3.5−4.5 wt% hydrogen in 120 minutes at 250 °C.

6.2 Nonisothermal Hydrogen Cycling

6.2.1 Experimental Methods

The cycling tests were performed to evaluate the stability of low temperature hydrogenation during thermal cycling. Samples were cycled under isothermal temperature. Each step (repeating dehydrogenation-hydrogenation reactions) of cycling was controlled by a programmable PCT-Pro 2000 machine. During the cycling, hydrogenation was performed when introducing 4 bar hydrogen pressure to the sample chamber, and the dehydrogenation was performed when the hydrogen pressure was adjusted to 0.01 bar. To conduct the hydrogenation tests, the cycling program was manually stopped after certain numbers of cycles, namely the 1^{st}, 5^{th}, 20^{th}, 50^{th}, and 100^{th} cycle. After the program was stopped, the sample (dehydrogenated-status) was cooled to room temperature or a lower temperature, and then a hydrogenation test was performed. After that, the sample was heated again to high temperature, and the programmed isothermal cycling was continued.

6.2.2 Effect of Different Catalysts

Three samples, namely 5 mol% TiH_2-catalyzed, 5 mol% $TiMn_2$-catalyzed, and 5 mol% VTiCr-catalyzed MgH_2, were prepared using UHEHP planetary milling for 4 hours. Cyclic experiments were conducted at 300 °C. The hydrogenation and dehydrogenation kinetics during the thermal cycling were compared in Figure 6-2, showing the kinetics at different cycles (the 2^{nd}, 10^{th}, 51^{st}, and 99^{th}) for both hydrogenation kinetics and dehydrogenation kinetics of the three systems. It can be seen that the three materials present sluggish kinetics in the initial stage of cycling (the 2^{nd} cycle) compared to the kinetics of later cycles (the 10^{th}, 51^{st}, and 99^{th} cycles). For the hydrogenation rate, it slightly improved and became

stable with cycling extending. There are losses of hydrogen capacity during the cycling for all the systems. The hydrogen capacities of different samples are reduced by 0.4 wt% for TiH_2-catalyzed MgH_2, 0.2 wt% for $TiMn_2$-catalyzed MgH_2, and 1.0 wt% for VTiCr-catalyzed MgH_2. Similar to the evolution of kinetics, the reduction of the capacities generally occurred at the first 10 cycles. However, the dehydrogenation kinetic rates at different cycles were essentially unchanged compared to those of hydrogenation.

Further analysis was conducted to compare the three systems in detail through plotting values of time-to-3wt% hydrogen uptake/releasing against cycle number, as shown in Figure 6-3, which provides a panoramic evolution of the kinetics during the 100 cycles. First, it can be seen that there is no obvious kinetic degradation for both desorption and absorption of all the systems. Second, comparing the kinetic variances of the three hydride systems, the dehydrogenation is generally more stable than those of hydrogenation kinetics, or, in other word, the hydrogenation rates are more scattered through the cycling compared to dehydrogenation. The variances of kinetics at different cycles are probably due to the deviation of hydrogen pressure provided by the PCT machine when the cycling was performed. Third, according to the average of the kinetics of 100 cycles, the MgH_2-TiH_2 and MgH_2-VTiCr had better desorption kinetics, and the MgH_2-VTiCr had the best absorption kinetics. Among the three different systems, the MgH_2-VTiCr material seems to be more robust against the thermal cycling and also possesses better kinetics combining with both hydrogenation and dehydrogenation.

Previous studies[3-5] have demonstrated that catalyzed nanoscale Mg particles were capable of absorbing a significant amount of hydrogen at room temperature. However, reported research on cyclic stability of room temperature hydrogenation kinetics is very

limited. To explore it, the thermal cycling of MgH_2-TiH_2, MgH_2-$TiMn_2$, and MgH_2-VTiCr samples were intermitted at the 1^{st}, 5^{th}, 20^{th}, 50^{th}, and 100^{th} cycles. During each intermission, the samples were cooled down to room temperature, and a hydrogenation test was performed under 1-bar hydrogen pressure. The results of hydrogenation kinetic curves were shown in Figure 6-4, showing an obvious degradation of all the catalyzed materials. Hydrogen uptake of 2.5 to 3.0 wt% in 120 minutes was observed after 1 cycle; however, after 100 cycles, only 0.5 to 1.0 wt% of hydrogen were able to be absorbed in the same period of time. In comparison to other systems, MgH_2-VTiCr presents relatively better hydrogenation properties against the thermal degradation.

6.2.3 Hydrogenation Kinetics at Different Temperature

The above results clearly demonstrated severe degradations of the room temperature hydrogenation kinetics of the catalyzed MgH_2 samples after extended hydrogen cycling. However, it also showed that no degradation of the kinetics occurred when hydrogenation performed at 300 °C. To find out the degradation behaviors of hydrogenation kinetics at different temperatures, three experiments were conducted. The cycling experiments were followed the same procedure described in section 6.2.2, and the hydrogenation tests were performed at 60 °C, 100 °C, and 150 °C.

Figure 6-5 shows a comparison of the degradation behavior of the hydrogenation kinetics at 25 °C, 60 °C, 100 °C, and 150 °C. It can be seen that the degradations were still observed in the course of 1−50 cycles for 60 °C hydrogenation tests and in the course of 1−20 cycles for 100 °C hydrogenation tests. Results also showed that when the cycling was further extended, the degradation tended to diminish. For example, the 60 °C kinetics after

50 cycles did not degrade; the 100 °C hydrogenation after 20 cycles showed no obvious decrease as well.

When the hydrogenation temperature was further increased to 150 °C, the degradation of the kinetics was still observed in the first 20 cycles, which is similar to the tests examined at 100 °C. The 150 °C kinetics curves present no big change after 20 cycles. Moreover, the kinetic after 100^{th} cycles shows that 3.3 wt% hydrogen can be absorbed in 250 min, which is higher than the room temperature hydrogen absorption in the 1^{st} cycle.

6.2.4 Effect of Cycling Temperature on Room Temperature Hydrogenation Kinetics

The MgH_2-VTiCr system was used for the cycling experiments in this section. The effect of cycling temperature (250 °C, 300 °C, and 350 °C) on room temperature hydrogenation kinetics was studied, and the kinetics (after 1, 5, 20, 50, and 100 cycles) were shown in Figure 6-6. The temperature dependence of degradation of hydrogenation kinetics (after 1, 20, and 100 cycles) was given in Figure 6-7, showing that the cycling temperature has a significant impact on the properties of room temperature hydrogenation – higher cycling temperature results in faster degradation rate. The thermal-induced impact on degradation of the kinetics is significant so that the kinetic differences appeared even after one cycle that performed at the different temperatures of 250 °C, 300 °C, and 350 °C.

6.2.5 Effect of Packing Status of the Material on Room Temperature Hydrogenation

Two MgH_2-VTiCr samples with different packing densities were prepared and tested. The cycling experiments were followed by the same procedure described in section 6.2.2, and the hydrogenation tests were performed at 25 °C. One sample was loose powder with density in a range of 0.45 g/cm^3 and estimated porosity of 71 vol%. Another sample used the same batch of material but was pressed into a pellet with a density of 1.06 g/cm^3 and estimated porosity of 31.6 vol%, as listed in Table 6-1. The two samples were then loaded for comparative tests. As shown in Figure 6-8, the two samples exhibited the similar kinetics and degradation rate, indicating that the packing status of catalyzed MgH_2 in terms of the density and porosity of the material did not affect the hydrogenation kinetics.

6.3 Thermodynamics Properties Before and After Cycling

Thermodynamic properties of MgH_2-VTiCr were characterized by using pressure-composition-isothermal (PCI) measurement, and their PCI equilibrium curves at 300 °C were compared in Figure 6-9 (a). First of all, the range of the plateau of the sample after 500 cycles indicates an available hydrogen capacity of 6.2 wt%, which is the same as that of the as-milled sample, demonstrating no loss of the hydrogen capacity after the 500 cycles. The results also show that the equilibrium pressure of the cycled material remains essentially unchanged compared to the one of the as-milled sample. Moreover, the van't Hoff plot of as-milled and as-cycled samples is provided in Figure 6-9 (b). It was found that the cycled material had less hysteresis compared to the as-milled one, especially at higher temperatures (>300 °C).

6.4 Discussion

From the results that have been shown in sections 6.1 and 6.2, it has been demonstrated that the catalyzed MgH_2 systems have good stability at high temperatures (refers to the temperature range 300−400 °C). However, it has been realized that the hydrogenation kinetics of catalyzed MgH_2 at low temperature (refers to room temperature to 150 °C) suffer severe deterioration after cycling. Also, isothermal cycling results showed that moderate degradation of dehydrogenation occurred when the system was cycled at temperatures lower than 270 °C with a low pressure driving force.

It has to be pointed out that for different catalyst-doped systems (TiH_2-catalyzed, $TiMn_2$-catalyzed, and VTiCr-catalyzed MgH_2), their behaviors of degradation in terms of room temperature hydrogenation kinetics are similar, although the MgH_2-VTiCr system presents slightly better cyclic properties. Overall the degradation seems to be a common behavior for this kind of materials.

Generally, it is considered that the degradation is due to following potential reasons:

(1) Reduction of effective surface area due to the sintering effect;

(2) Grain growth of Mg/MgH_2;

(3) Oxidation and/or contamination of material;

(4) Grain growth of catalyst particle;

(5) Agglomeration of catalyst particles.

The underlying mechanism of the kinetic degradation will be discussed in this section.

6.4.1 Thermal Holding under Different Conditions

Based on the previous assessment on room temperature hydrogenation kinetics during thermal cycling, the deterioration of the material gradually occurred during cycling. Each cycle comprises two reactions: the hydrogenation and the dehydrogenation. The circumstance of hydrogen pressure during cycling varied, and therefore phase compositions were changing (Mg or MgH_2 or mixture of Mg and MgH_2). To simplify the problem, it will be useful to understand at which circumstance(s) the degradation will occur.

The experiments in this section are designed to test the changes of kinetics of the VTiCr catalyzed MgH_2 sample after holding at different pressure and temperature conditions. A series of tests was performed before and after holding the catalyzed MgH_2 sample under different temperature conditions and hydrogen pressure. Room temperature hydrogenation tests and 300 °C dehydrogenation test were performed to compare the properties before and after holding. The experimental procedure is described as follows:

(1) As-milled MgH_2-VTiCr was prepared for PCT test;

(2) 300 °C dehydrogenation test;

(3) Room temperature hydrogenation test under 1 bar pressure;

(4) Isothermal holding under specified pressure and temperature condition;

(5) Recharge the sample at 300 °C with 10 bar H_2. Then a 300 °C dehydrogenation test was performed;

(6) Room temperature hydrogenation test under 1 bar pressure.

The temperature and pressure conditions were described in Table 6-2. The holding time was 40 hours. The comparison of the kinetics curves is plotted in Figure 6-10.

From Figure 6-10 (a) and (b), it can be seen that there is essentially no degradation after the sample was held at pressurized hydrogen (10 bar) and 300 °C (test No. 1). Both the hydrogenation and dehydrogenation kinetics even slightly improved after the holding. The improvement of kinetics is probably attributed to removal of contaminant(s) on the surface of material or activation of the catalyst.

In the No. 2 and No. 3 tests, the samples were annealed at the same temperature (300 °C), but the pressures were reduced to 1 bar and 0 bar. Consequently, the primary phase of the material during the annealing will be Mg metal under those pressures. As shown in Figure 6-10 (c) and (e), moderate degradation was shown on both room temperature hydrogenation and 300 °C dehydrogenation kinetics after the holding. The curves of dehydrogenation after the holding also showed incubation phenomena, which means the materials did not start to desorb hydrogen in the beginning but incubated for a period of time (~ 10 min in these cases). Although no measurements were conducted to quantitatively compare the grain sizes of Mg and MgH_2 before and after holding, it still can be expected that there should be grain growth for soaking nanosized Mg and MgH_2 at such a high temperature (300 °C) for a long time (40 hrs). Consequently, a key lesson from test No. 2 and No. 3 is that grain sizes of Mg and MgH_2 have limited impact on the degradation.

The sample in test No. 4 was continuously evacuated by a vacuum pump (ultimate pressure 1.6×10^{-2} mbar) while being heated to 300 °C for 40 hours. Afterward, the hydrogenation and dehydrogenation kinetics became significantly sluggish, as shown in Figure 6-10 (g) and (h). This should be due to contamination and/or oxidization (O_2 and H_2O) to the sample due to the long-term vacuum pumping. Moreover, the contamination occurred even at room temperature, as shown in test No. 5 and Figure 6-10 (i) and (j). From

tests No. 4 and 5, a key lesson is that the nanocatalyzed MgH_2 system is very sensitive to contaminant(s) and therefore must be well sealed in an impurity-free environment and protected during operation.

A further investigation was performed by applying an oscillating temperature at the range of 290 °C to 330 °C. In the experiment, the sample (0.08 g) was sealed in a vessel with a volume of 18 mL. As shown in Figure 6-11, the cycling was carried out as followed steps: (1) A high temperature period (310−330 °C) − when the sample was heated, increasing the equilibrium pressure of MgH_2 led to dehydrogenation of the sample; (2) A low temperature period (290−310 °C) − when the sample was then cooled to low temperature, decreasing the equilibrium pressure of MgH_2 resulted in hydrogen absorption of the sample. The evolution of room temperature hydrogenation with cycling is plotted in Figure 6-12. The results show that a serious deterioration happened during the cycling. Because the cycling was achieved by changing temperatures of the sample and the material was isolated without feeding hydrogen gas and evacuation, it should have significantly reduced the possibility of introducing contaminants into the sample chamber. Therefore, the degradation that happened here cannot be attributed to contamination or oxidization. Moreover, the other dubious reason, the high temperature thermal effect, is considered to be less important since the previous tests demonstrated that the sample (either in Mg phase or in MgH_2 phase) showed no obvious degradation on the kinetics after heating at 300 °C for 40 hours. Consequently, it is suspected that the degradation was primarily due to the hydrogenation-dehydrogenation cycling.

6.4.2 Microstructure Evolution

Given the results and the discussion above, electron microscopy techniques including HR-SEM and TEM were employed to characterize the microstructure of the samples. Figure 6-13 shows the high-resolution SEM images about the evolution of the microstructure of VTiCr catalyzed sample during cycling. It can be found that the morphology of the material significantly changed after cycling 100 times. First, the as-milled sample and the 1st cycled sample have particles well dispersed in the field of view, and the particles have a size less than 10 μm. After 100 cycles, the particles tended to agglomerate together, and the size of particle grew to 30 to 60 μm. Second, the structure of the sample after 100 cycles changed to a porous, sponge-like morphology. Third, on the surface of the material after 100 cycles, there is a large amount of nanosized particles, which is likely to be the higher atomic number catalyst phase due to its brightness contrasted to the matrix of Mg.

Figure 6-14 shows high-resolution S/TEM and EDS analysis of as-milled MgH_2-$TiMn_2$. The images clearly show that catalyst particles ($TiMn_2$) dispersed in the matrix of MgH_2. There are few large catalyst grains with a size of about 100 nm. Also there are many fine catalyst particles with a size from 10 to 20 nm, indicating they have been well milled and pulverized. Moreover, the oxygen distribution (see Figure 6-14) shows that the surface Mg/MgH_2 was oxidized, which could be due to the milling process or sample transferring for the TEM analysis.

Figure 6-15 shows the high-resolution S/TEM and EDS analysis of the 100 cycled MgH_2-$TiMn_2$. It is interesting to note that the big catalyst particle was absent in the cycled sample compared to the presence of large catalyst particle (>100 nm) in the as-milled

material. This is probably because the catalyst itself is a hydride-forming material, and it can absorb and desorb hydrogen, and a big particle of the catalyst can decrepitate into small grains during the cycling due to the intrinsic nature of metal hydrides.

More importantly, a clear segregation between Mg and the elements of the catalyst (Ti, V, Mn) is shown in Figure 6-15. This could be the main reason that leads to the kinetic degradation of catalyzed MgH_2. Moreover, another interesting observation is that those catalyst-rich zones have a high oxygen concentration, which is the opposite of the as-milled sample. Considering that the elements such as Ti, V, and Mn are generally less reactive with oxygen and moisture than Mg, the high concentration of oxygen should represent a large amount of MgO or $Mg(OH)_2$ that aggregated with catalyst particles. It can be expected that the catalyst will be deactivated due to being covered or surrounded by an inert MgO or $Mg(OH)_2$ phase.

TEM analysis on the cycled and uncycled MgH_2-VTiCr system was performed to confirm the above observation. The results of one cycled MgH_2-VTiCr are shown in Figure 6-16, showing the relatively homogenous distribution of catalytic phase.

The 100-times cycled MgH_2-VTiCr sample was further characterized, and a microstructure similar to a 100-times cycled MgH_2-$TiMn_2$ was found. In this sample, a cluster of VTiCr catalyst-rich particles was found and imaged as shown in Figure 6-17. Figure 6-17 also includes a secondary electron image of the particle, which coincides with HR-SEM photographs of cycled MgH_2-VTiCr (Figure 6-13). Moreover, a quantitative elemental analysis of this VTiCr catalyst-rich particle (Figure 6-17) was conducted, showing 72.3 at.%, 20.5 at.%, 1.3 at.%, and 5.9 at.% of Mg, V, Ti, and Cr, respectively, as shown in Table 6-3. To compare with that, quantitative elemental analysis of the sample

before cycling (Figure 6-16) shows that Mg, V, Ti, and Cr are 96.2 at.%, 0.2 at.%, 2.9 at.%, and 0.7 at.%, respectively. The analysis of element content clearly supports the observation of catalyst aggregation.

6.4.3 Mechanism of Kinetics Degradation

First of all, it is necessary to review the previous hypothesis of the catalytic effect on MgH_2. As suggested in the prior literature,[3, 6] the hydrogenation of magnesium involves several steps taking place in sequence: (1) hydrogen chemisorption on the surface, (2) hydrogen molecule dissociation to H, (3) H diffusion in metal, and (4) nucleation and growth of the hydride phase. The addition of catalysts is considered to enhance the hydrogen dissociation step (2) and hydrogen diffusion step (3). Therefore, a structure with lots of fine catalyst grains attached on the surface of magnesium can be expected to be a most effective conduit.

In the TEM observation of present study, we observed inhomogeneous distribution of catalyst particles in the cycled sample. A catalyst-dense region was also identified by EDS analysis (Figure 6-17 and Table 6-3). These observations are in accordance with results reported by Tan et al.,[7] showing similar phenomenon in the MgH_2-Nb-V system. It is realized that substrate phases (Mg/MgH_2) must undergo significant changes so that the catalyst particles were forced to migrate inside of the substrate phase during hydrogen cycling. This can be attribute to a substantial volume change between the Mg metal and MgH_2 phases. Because the theoretical density of metallic Mg is 1.74 g/cm^3 and the theoretical density of MgH_2 is 1.42 g/cm^3, there would be up to 20% volumetric expansion or shrinkage when the phase has been fully hydrogenated/dehydrogenated. As a result, the

catalytic particles will likely suffer repeating stresses from the surrounding Mg/MgH_2 substrate when the reactions take place. The stress might be strong enough so that a "migration" of catalyst particle is possible. Also the MgH_2 substrate might tend to separate from the originally close-contacted catalyst particle due to the shrinkage during dehydrogenation. Figure 6-18 schematically depicts this hypothetical evolution of one catalyst particle that was attached on the surface of the Mg/MgH_2 substrate. After a number of cycles, the nearly embedded catalyst eventually protruded from the substrate, which can lead to a decrease of catalytic efficiency. Overall, a schematic pictured a cycling-induced morphology evolution is shown in Figure 6-19. It depicts the course of decrepitation, migration, and surface contamination of the catalysts.

It has to be pointed out that we cannot rule out other factors such as grain growth, including the Mg/MgH_2 and catalyst phase, reduction of surface area of the material, etc, that might also contribute to the degradation. In the cycling research reported by Tan et al.,[7] grain growths from an average 25 nm to 55 nm, 25 nm to 50 nm, and 3 nm to 4 nm, for Mg, MgH_2, and catalyst (V), respectively, were observed as the cycle number increased to 200. Another system of Mg-V materials exhibited faster grain growths and also showed worse kinetics after cycling. However, it is also known that catalyst particle may act as a grain growth inhibitor that prevents the coarsening of Mg or MgH_2 particles during the course of cyclic reactions.[8] It means that a uniform distribution of the catalyst inside the Mg/MgH_2 particle can help preserving the nanosized Mg and MgH_2 phases. Instead, as catalysts became agglomerated, the Mg and MgH_2 grain inevitably grew faster, as shown in Figure 6-19.

Another important observation is the change of oxygen distribution after the course of

the cycling experiment. It is known that the oxygen contamination can result from either the cycling experiment or the sample transferring of TEM characterization, or both. However, it is rational to suspect that the catalyst particles were easy to get contaminated since the size of those particles was very fine (less than 10 nm) and have been protruded from the body of Mg/MgH_2. If the contamination occurred during the reactions, it will no doubt have a poisoning effect to the catalyst.

A question that has not been well elucidated is the stability of the high temperature kinetic behaviors versus the deterioration of low temperature kinetics during the hydrogen cycling. It can be expected to have a more robust kinetic behavior at high temperatures. However, significant morphology changes of the sample were indeed observed after hydrogen cycling, and it seems that high temperature kinetics were not affected. It implies that the mechanism of the hydrogenation and dehydrogenation at high temperatures are different from what happens at low temperatures. One possibility is that the rate-limiting step in high temperature reactions is heat transferring.

6.5 Summary

In conclusion, a comprehensive study of cyclic stability of catalyzed MgH_2 was conducted in this chapter. Results show that both the hydrogenating and dehydrogenating kinetics at high temperatures were generally stable during 100 cycles. However, the low temperature (25 °C to 150 °C) hydrogenation kinetics suffered a severe degradation during cycling. Further experiments confirmed that the low temperature kinetic degradation can be mainly attributed to the extended hydrogenation-dehydrogenation reactions. TEM with high-resolution EDS technique was utilized to characterize the evolution of the

microstructure of cycled materials, showing an agglomeration of the catalyst occurred during cycling. The catalyst agglomeration is considered to be the main reason that causes the degradation of the kinetics.

6.6 References

1. Dehouche, Z.; Djaozandry, R.; Huot, J.; Boily, S.; Goyette, J.; Bose, T. K.; Schulz, R., Influence of Cycling on the Thermodynamic and Structure Properties of Nanocrystalline Magnesium Based Hydride. *J. Alloys Compd.* **2000**, *305*, 264−271.

2. Dehouche, Z.; Goyette, J.; Bose, T. K.; Schulz, R., Moisture Effect on Hydrogen Storage Properties of Nanostructured MgH_2–V–Ti Composite. *Int. J. Hydrogen Energy* **2003**, *28*, 983−988.

3. Lu, J.; Choi, Y. J.; Fang, Z. Z.; Sohn, H. Y.; Rönnebro, E., Hydrogenation of Nanocrystalline Mg at Room Temperature in the Presence of TiH_2. *J. Am. Chem. Soc.* **2010**, *132*, 6616−6617.

4. Hanada, N.; Ichikawa, T.; Fujii, H., Hydrogen Absorption Kinetics of the Catalyzed MgH_2 by Niobium Oxide. *J. Alloys Compd.* **2007**, *446-447*, 67−71.

5. Kalisvaart, W. P.; Luber, E. J.; Poirier, E.; Harrower, C. T.; Teichert, A.; Wallacher, D.; Grimm, N.; Steitz, R.; Fritzsche, H.; Mitlin, D., Probing the Room Temperature Deuterium Absorption Kinetics in Nanoscale Magnesium Based Hydrogen Storage Multilayers Using Neutron Reflectometry, X-Ray Diffraction, and Atomic Force Microscopy. *J. Phys. Chem. C* **2012**, *116*, 5868−5880.

6. Schimmel, H. G.; Huot, J.; Chapon, L. C.; Tichelaar, F. D.; Mulder, F. M., Hydrogen Cycling of Niobium and Vanadium Catalyzed Nanostructured Magnesium. *J. Am. Chem. Soc.* **2005**, *127*, 14348−14354.

7. Tan, X.; Zahiri, B.; Holt, C. M. B.; Kubis, A.; Mitlin, D., A TEM Based Study of the Microstructure During Room Temperature and Low Temperature Hydrogen Storage Cycling in MgH_2 Promoted by Nb–V. *Acta Mater.* **2012**, *60*, 5646−5661.

8. Lu, J.; Choi, Y. J.; Fang, Z. Z.; Sohn, H. Y.; Rönnebro, E., Hydrogen Storage Properties of Nanosized MgH_2−$0.1TiH_2$ Prepared by Ultrahigh-Energy−High-Pressure Milling. *J. Am. Chem. Soc.* **2009**, *131*, 15843−15852.

Table 6-1. Sample density and porosity of the loose powder and compact pellet.

Samples	Density, g/cm^3	Porosity, %	Mass of dose, gram
Loose MgH_2-VTiCr powder	0.45	71	0.1861
Compact MgH_2-VTiCr pellet	1.06	31.6	0.1712

Table 6-2. Isothermal temperature and hydrogen pressure conditions.

Test Number	Temperature, °C	Pressure, bar	Phase (Mg or MgH_2)
1	300	10	MgH_2
2	300	1	Mg
3	300	0, (sample sealed in closed vessel)	Mg
4	300	0, (sample was actively vacuum pumped)	Mg
5	25	0, (sample was actively vacuum pumped)	Mg

Table 6-3. Comparison of quantitative elemental analysis of 1 cycle sample and catalyst-rich aggregates from 100 cycled sample.

Elements	Quantitative analysis of sample before cycling, according to Figure 6-16. at. %	Quantitative analysis of a catalyst-rich aggregates from cycled sample, according to Figure 6-17. at. %
Mg	96.2±0.4	72.3±0.3
V	2.9±0.01	20.5±0.1
Ti	0.2±0.01	1.3±0.02
Cr	0.7±0.01	5.9±0.03

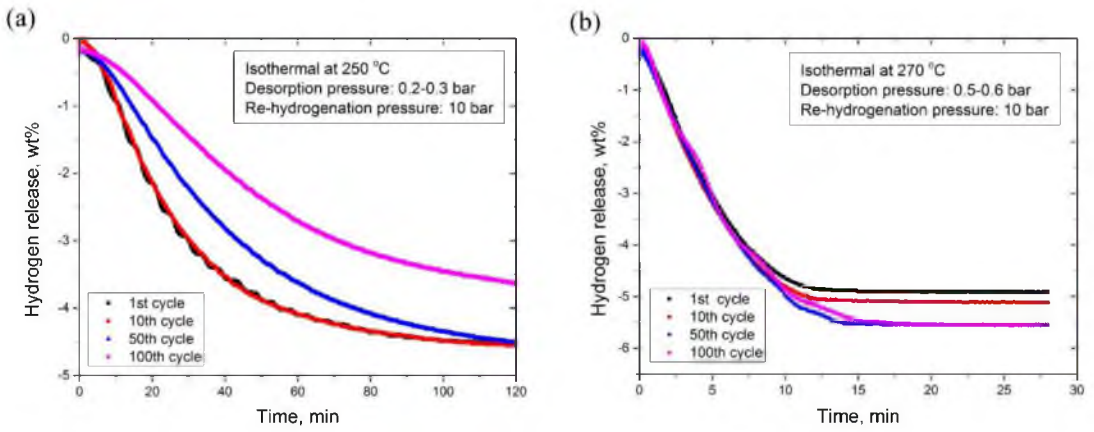

Figure 6-1. Dehydrogenation kinetics at different cycles. (a) Tests performed at 250 °C; (b) Tests performed at 270 °C.

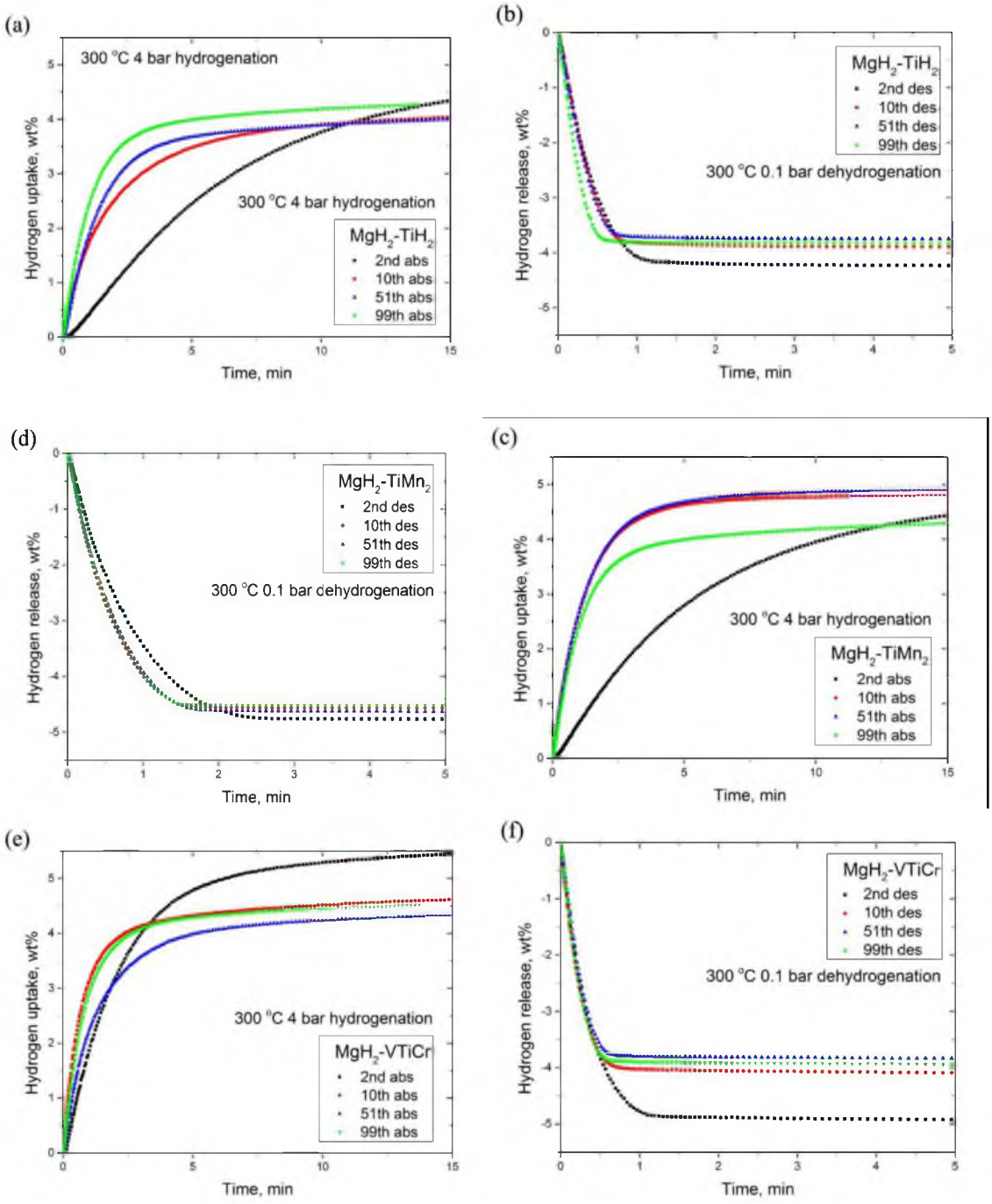

Figure 6-2. 300 °C hydrogenation and dehydrogenation kinetics at different cycles. (a) Hydrogenation of MgH_2-TiH_2 system; (b) Dehydrogenation of MgH_2-TiH_2 system; (c) Hydrogenation of MgH_2-$TiMn_2$ system; (d) Dehydrogenation of MgH_2-$TiMn_2$ system; (e) Hydrogenation of MgH_2-VTiCr system; (f) Dehydrogenation of MgH_2-VTiCr system.

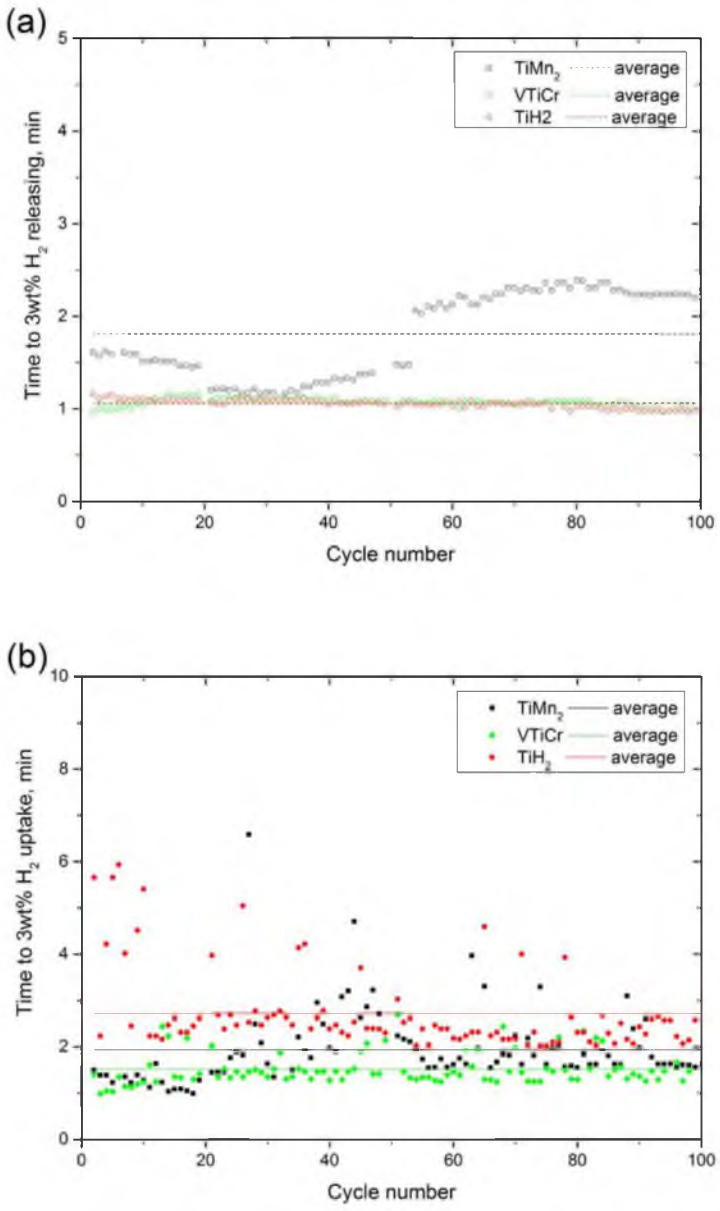

Figure 6-3. Plot of time-to-3wt% hydrogen release and uptake as a function of cycle number. The samples were cycled at 300 °C. (a) Hydrogen release; (b) Hydrogen uptake.

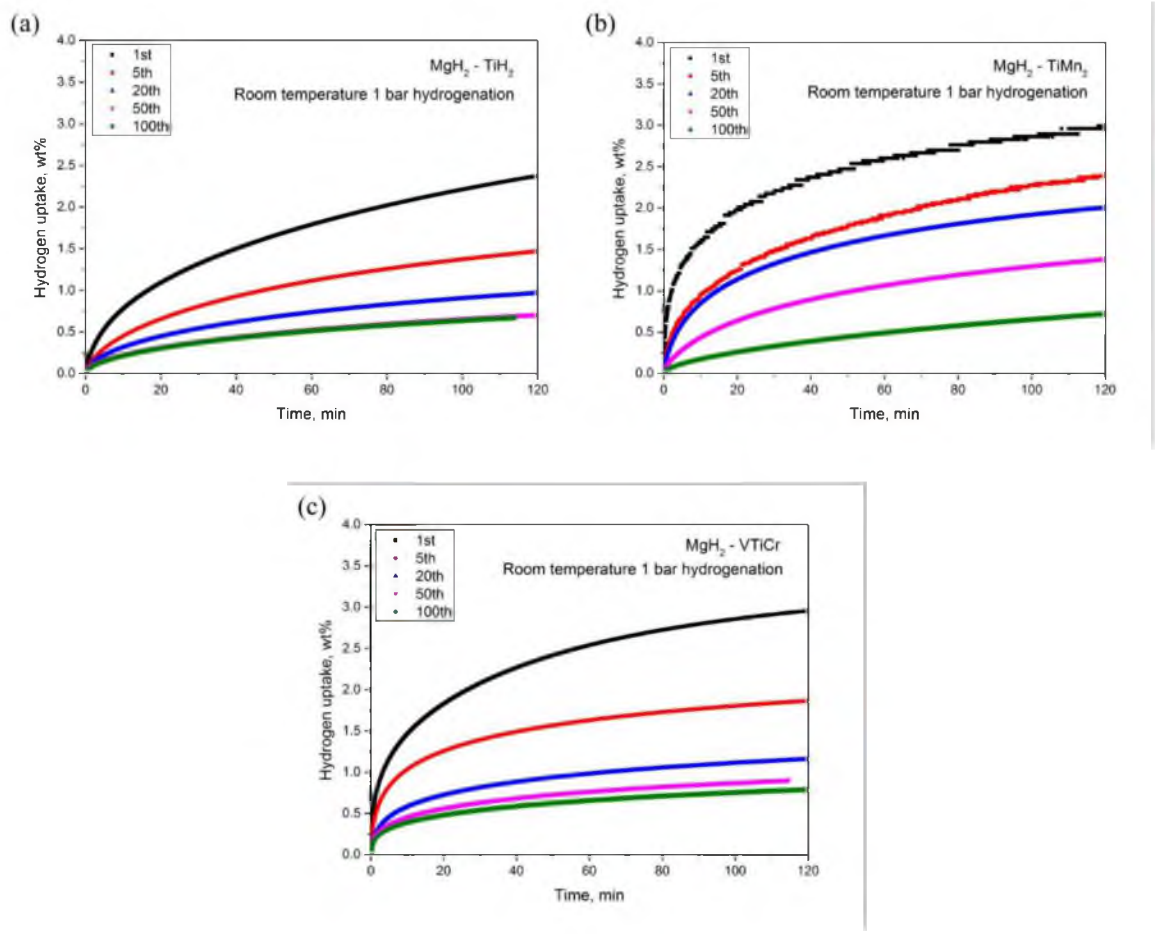

Figure 6-4. Room temperature hydrogenation kinetics after different cycles of MgH_2-TiH_2, MgH_2-$TiMn_2$, and MgH_2-VTiCr. The isothermal cycling tests were performed at 300 °C. (a) MgH_2-TiH_2; (b) MgH_2-$TiMn_2$; (c) MgH_2-VTiCr.

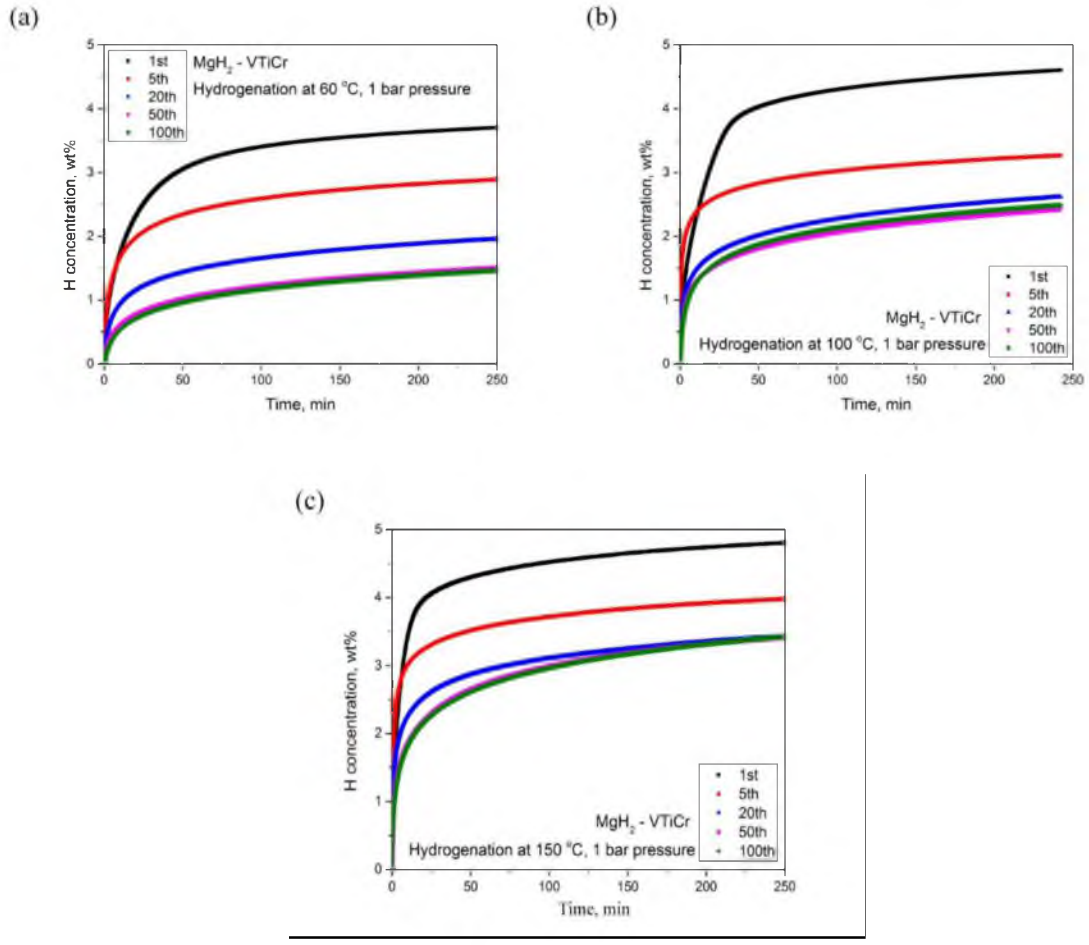

Figure 6-5. Hydrogenation kinetics at different temperature after different cycles of MgH_2-VTiCr. The isothermal cycling tests performed at 300 °C. (a) Tests performed at 60 °C; (b) Tests performed at 100 °C; (c) Tests performed at 150 °C.

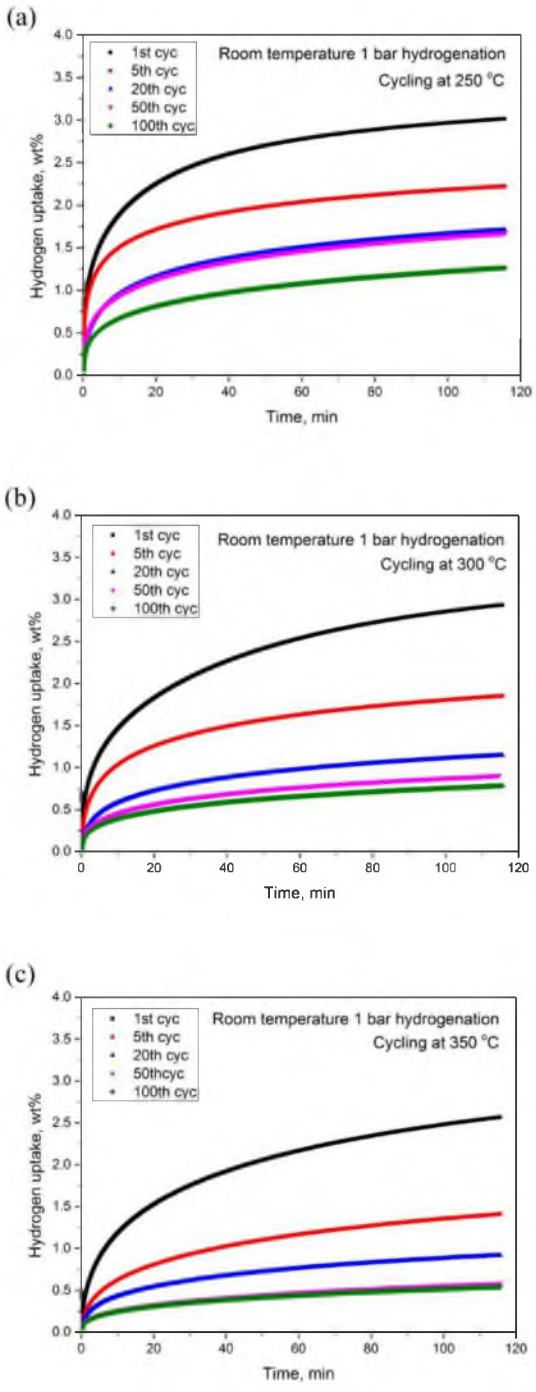

Figure 6-6. Effect of cycling temperature on hydrogenation of MgH_2-VTiCr. (a) The isothermal cycling tests were performed at 250 °C; (b) Tests performed at 300 °C; (c) Tests performed at 350 °C.

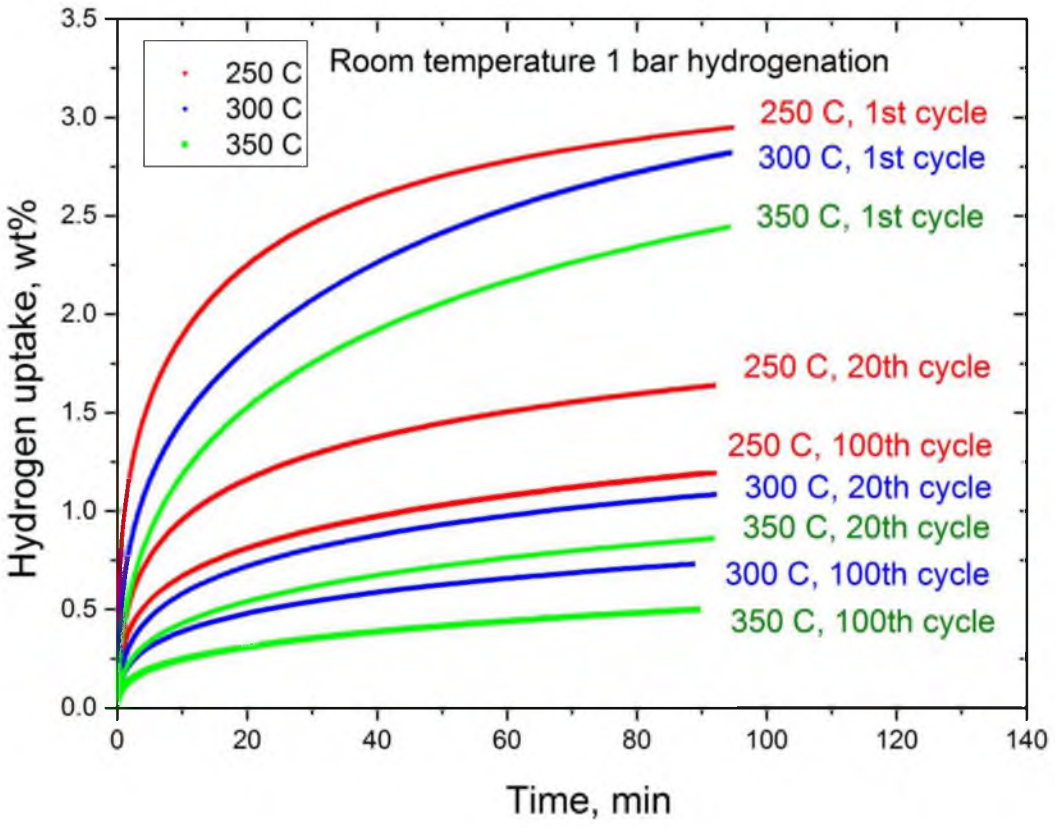

Figure 6-7. A comparison of room temperature hydrogenation kinetics after different cycles, the isothermal cycling tests performed at 250 °C, 300 °C and 350 °C, respectively.

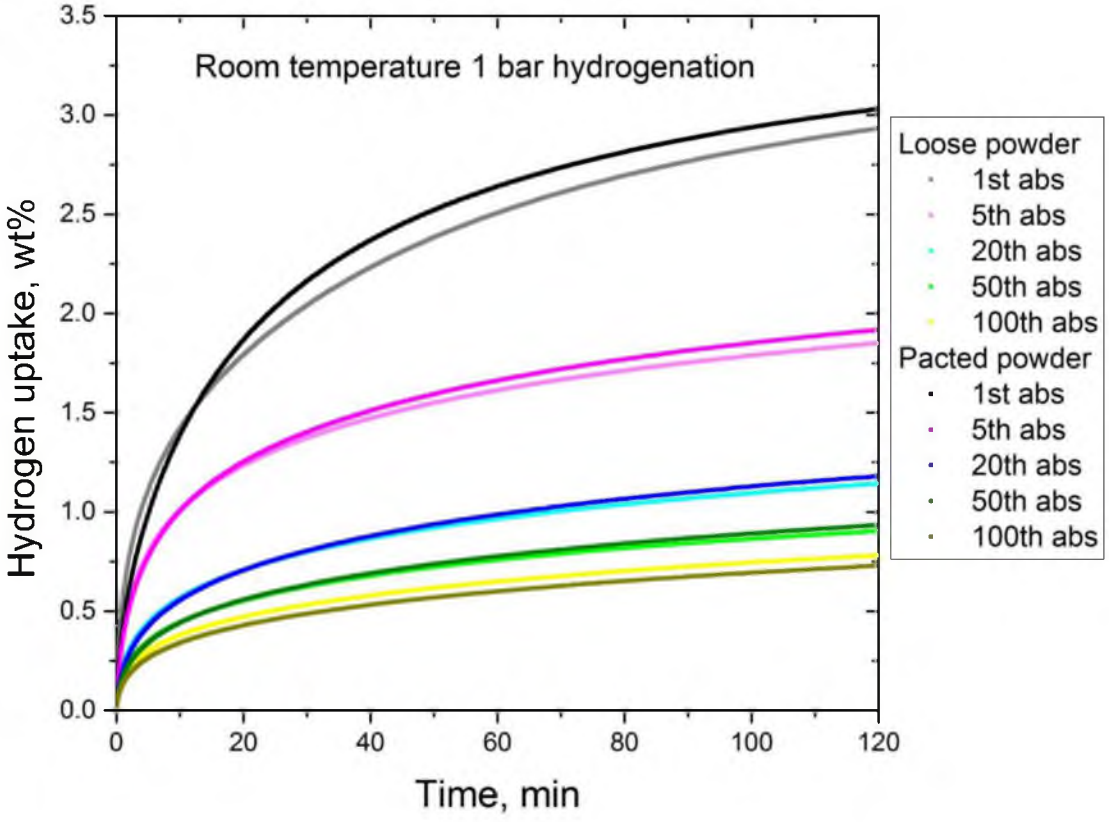

Figure 6-8. Room temperature hydrogenation kinetics of packed and unpacked powder samples after different cycles.

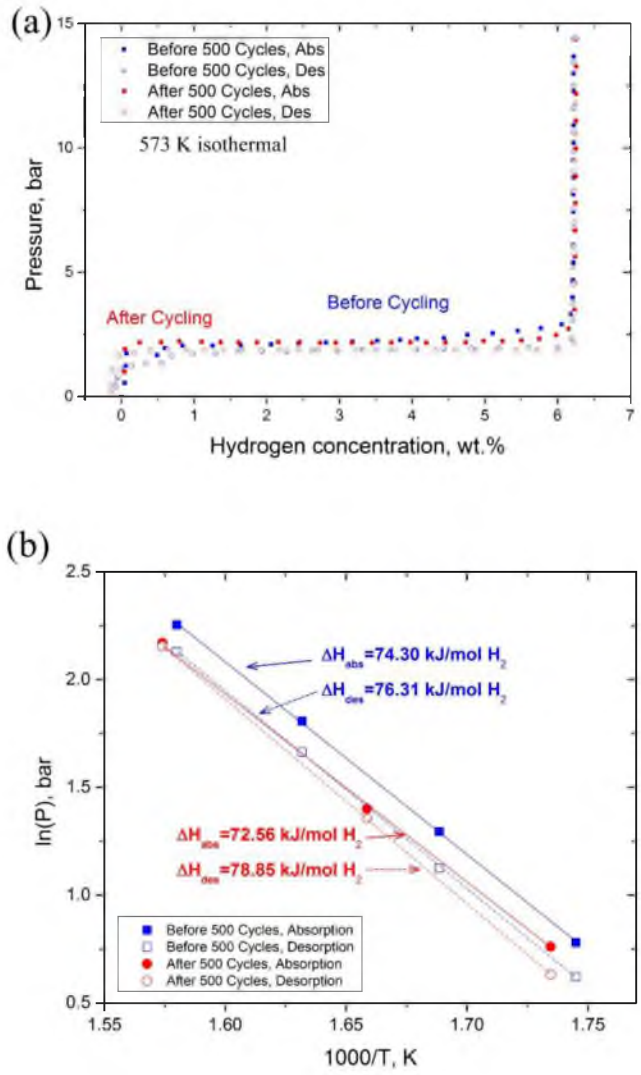

Figure 6-9. Thermodynamic properties of the MgH_2-VTiCr system before and after 500 cycles. (a) Equilibrium pressure measurements performed at 300 °C; (b) Relative van't Hoff plot of the MgH_2-VTiCr system before and after 500 cycles.

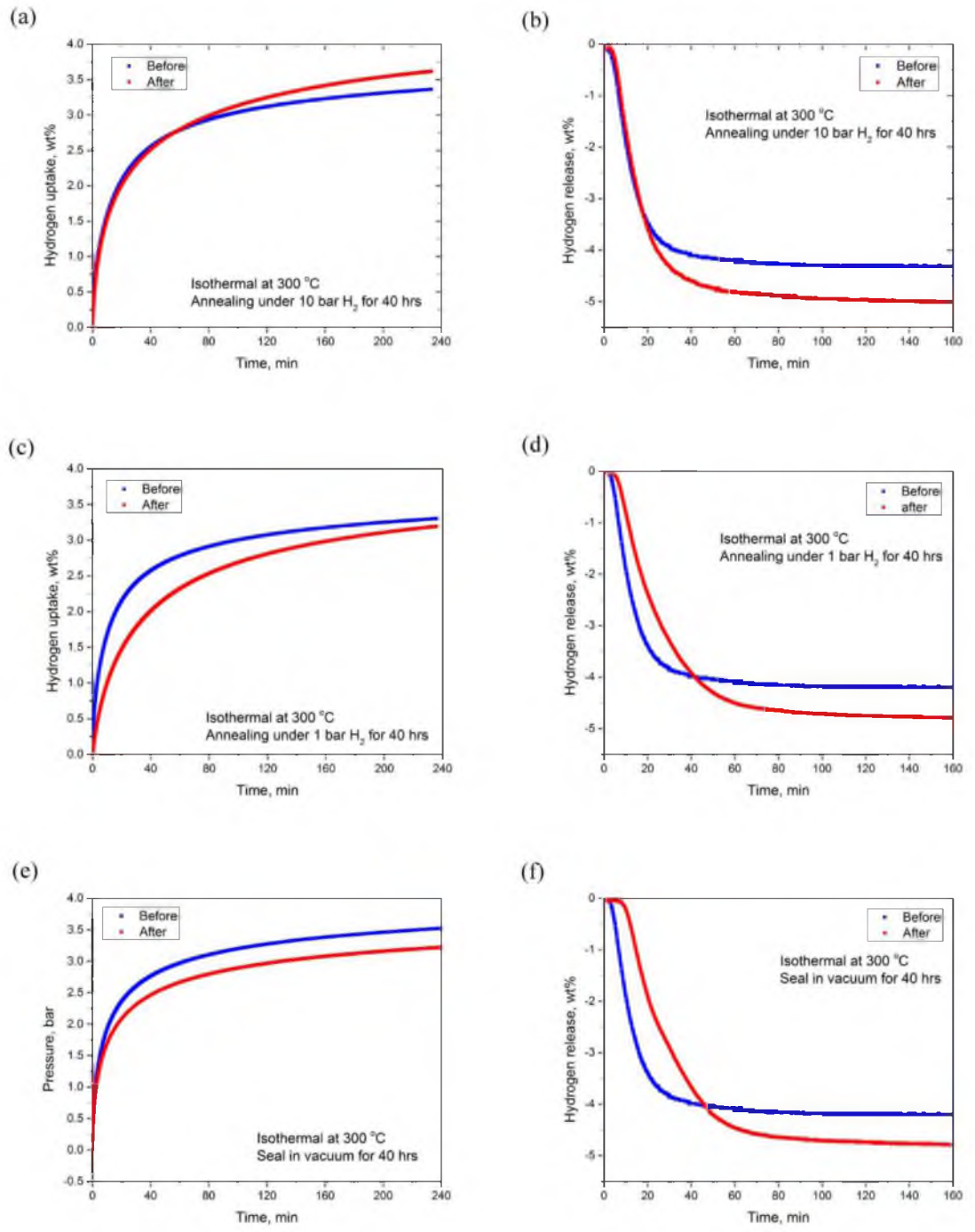

Figure 6-10. Comparisons of hydrogenation kinetics and dehydrogenation kinetics of MgH_2-VTiCr before and after different holding conditions: (a) and (b):300 °C and 10 bar hydrogen pressure; (c) and (d), 300 °C and 1 bar hydrogen pressure; (e) and (f), 300 °C and 0 bar hydrogen pressure; (g) and (h), 300 °C and vacuuming; (i) and (j), 25 °C and vacuuming. All the holding times were 40 hours.

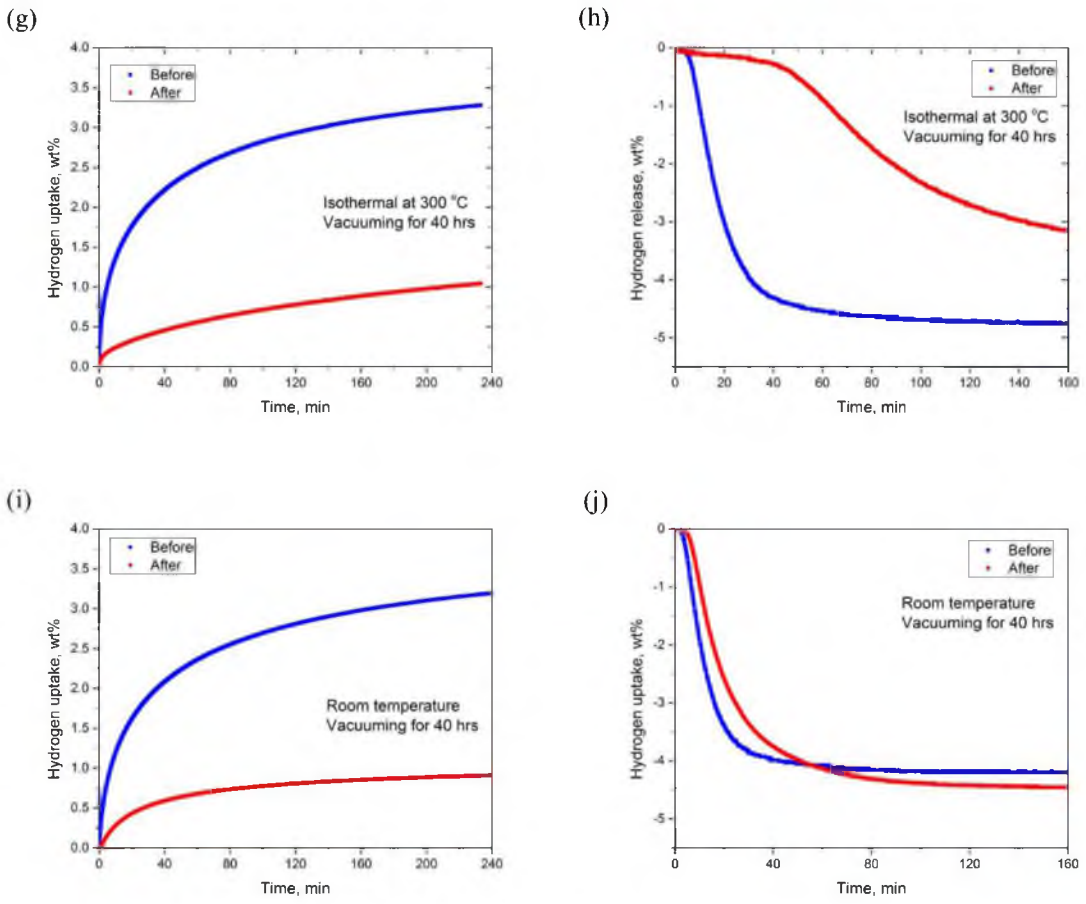

Figure 6-10. Continued.

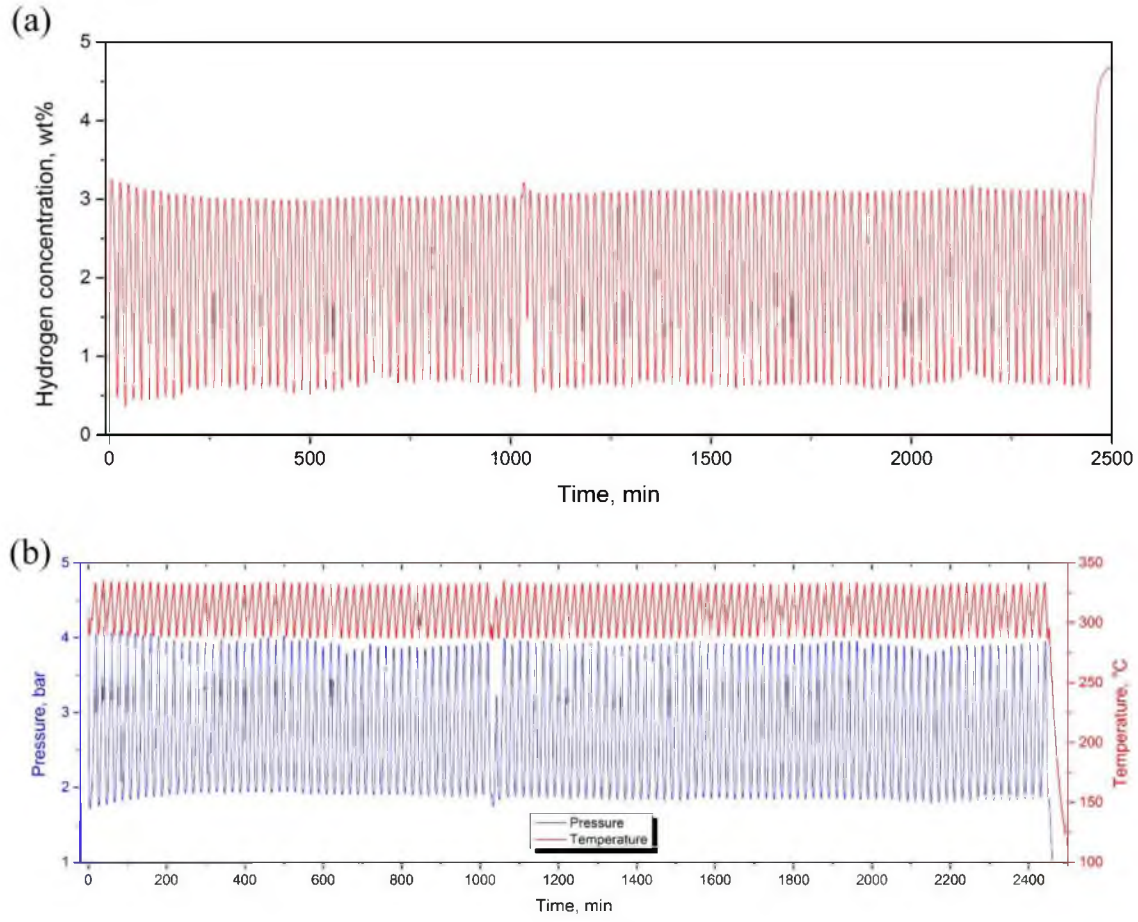

Figure 6-11. Cycling experiment performed though temperature oscillation at the range of 290 °C to 330 °C. (a) Cycling test; (b) Temperature and pressure profile of the experiment.

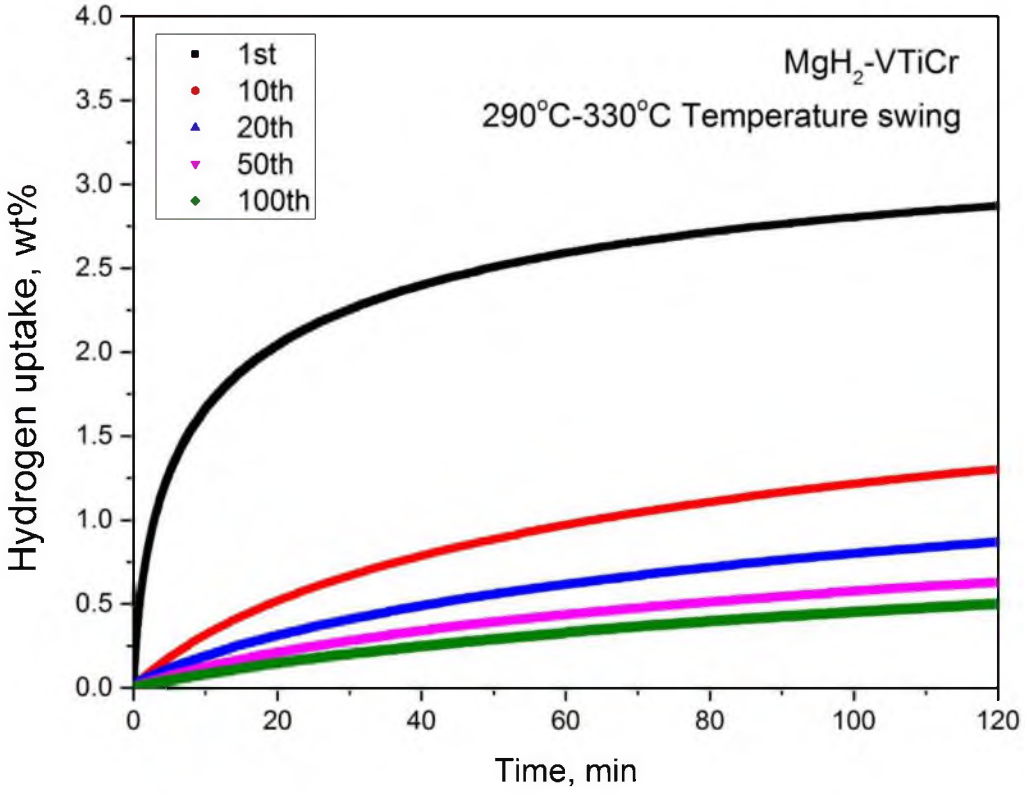

Figure 6-12. Hydrogenation kinetics after temperature-swing cycling of different cycles.

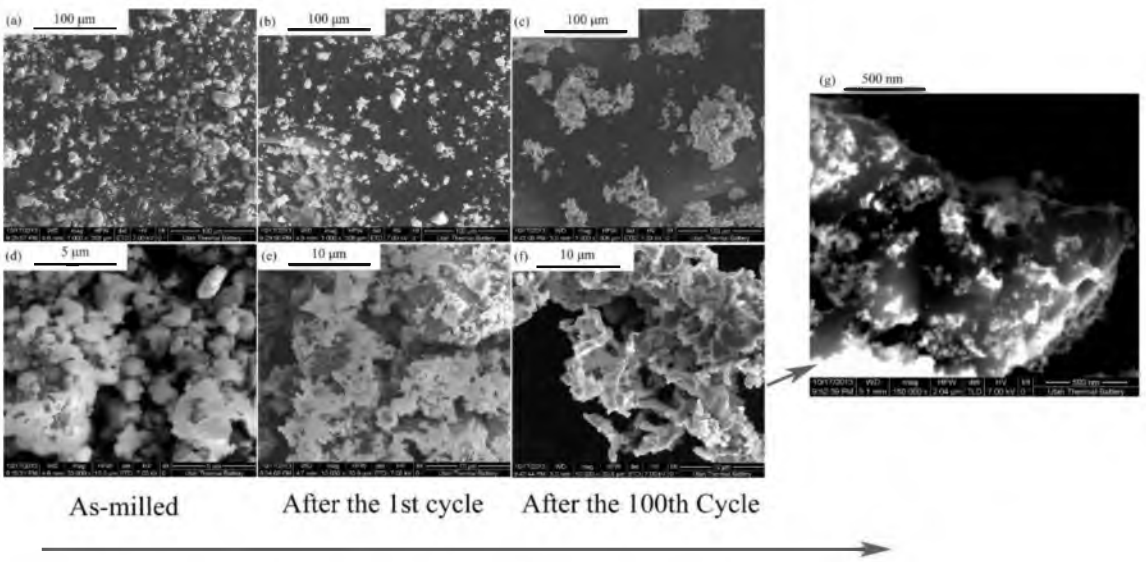

Figure 6-13. SEM images of as-milled MgH_2-VTiCr and the sample after 1 cycle and 100 cycles.

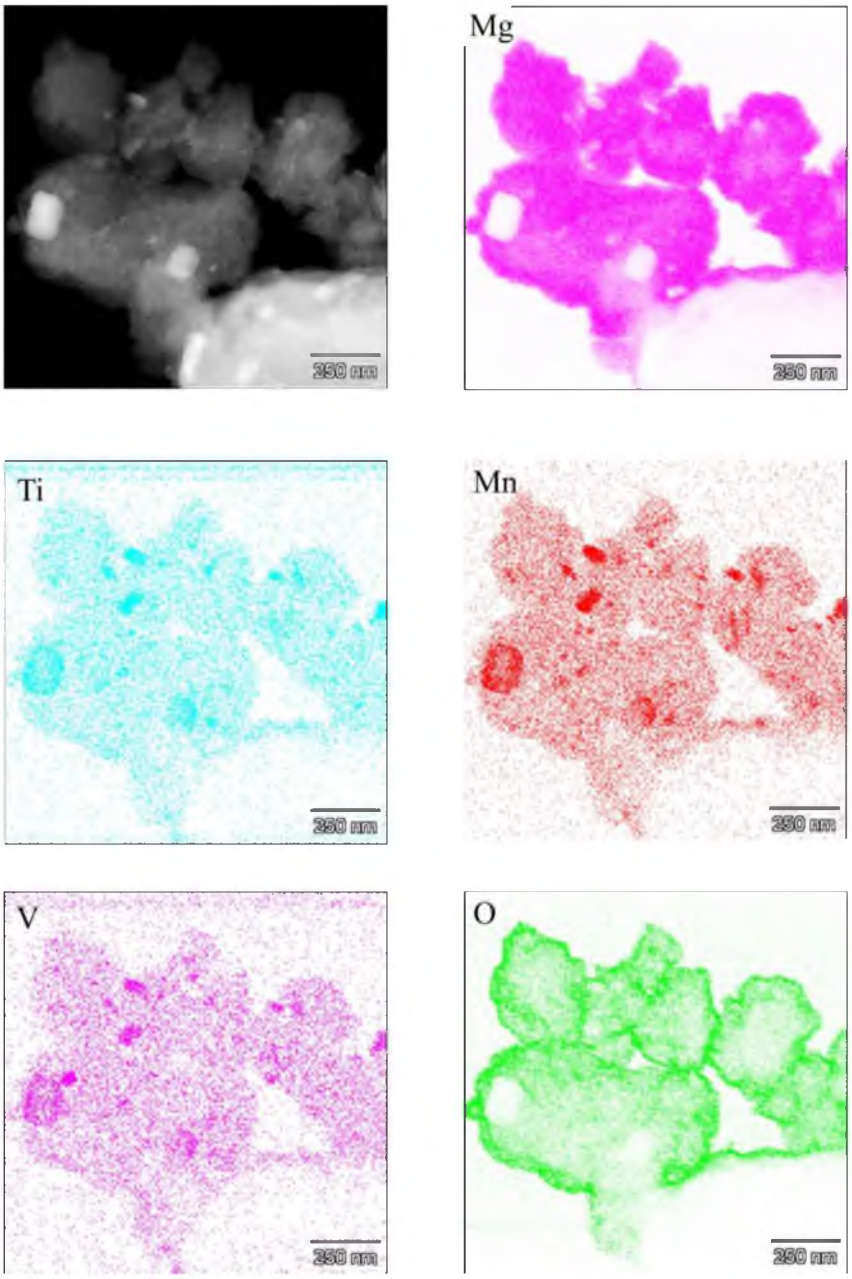

Figure 6-14. TEM images and EDS mapping of as-milled MgH_2-$TiMn_2$.

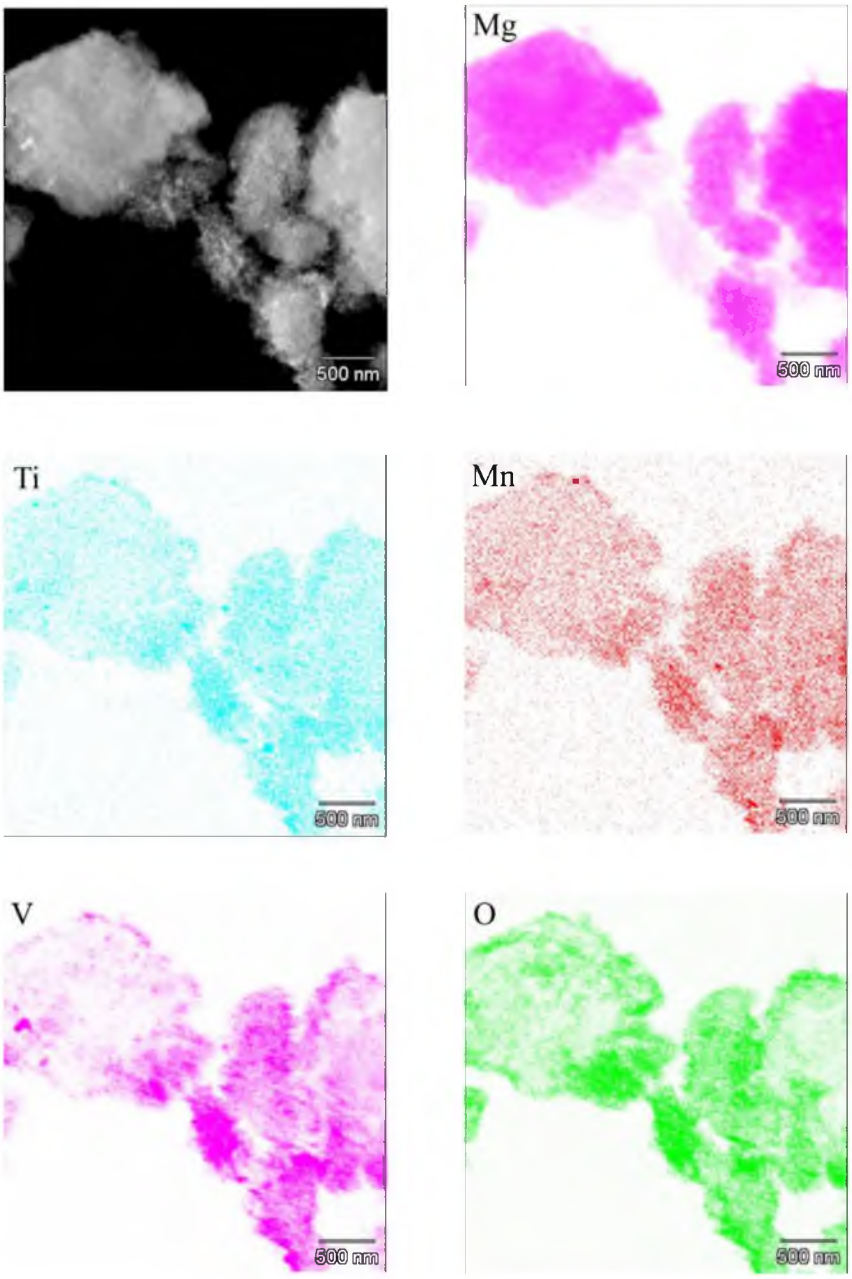

Figure 6-15. TEM images and EDS mapping of MgH_2-$TiMn_2$ after 100 cycles.

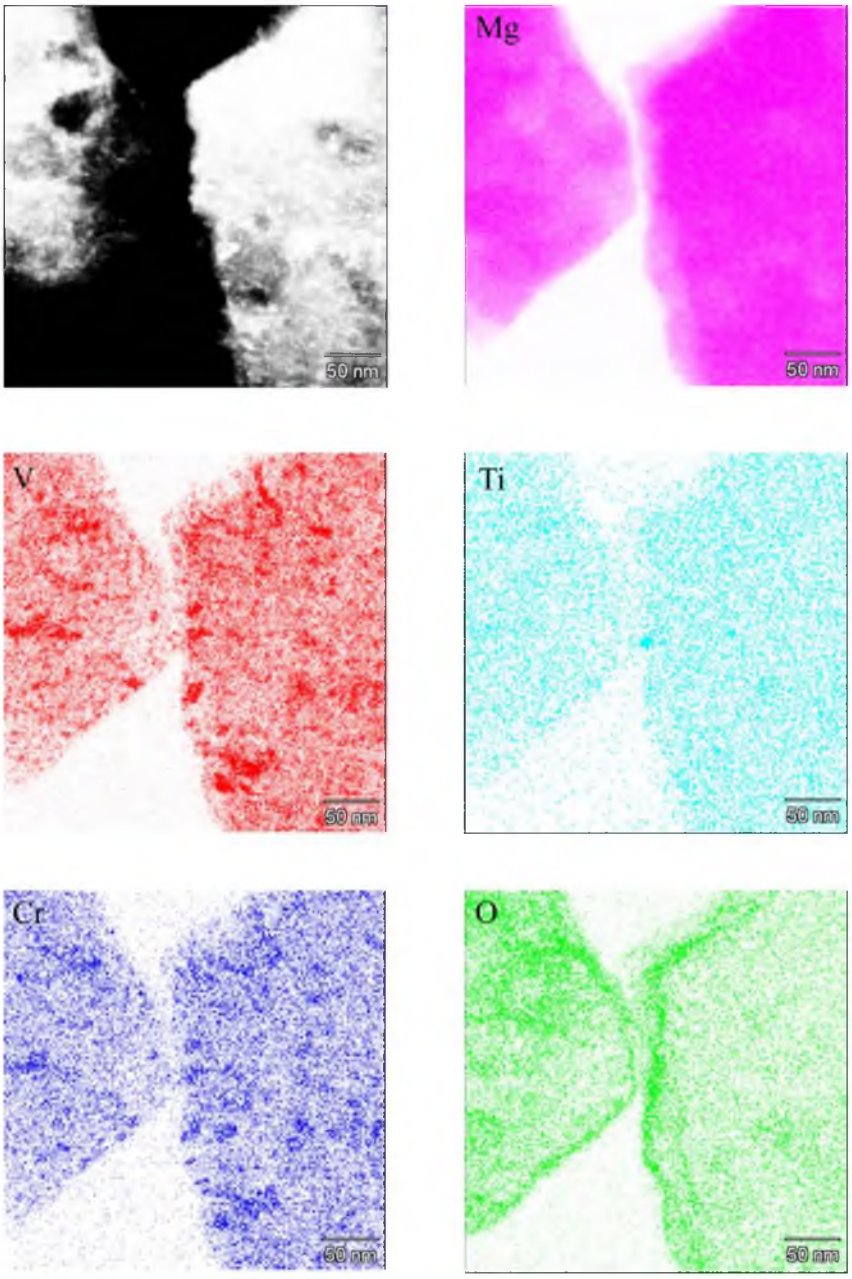

Figure 6-16. TEM images and EDS mapping of MgH_2-VTiCr after 1 cycle.

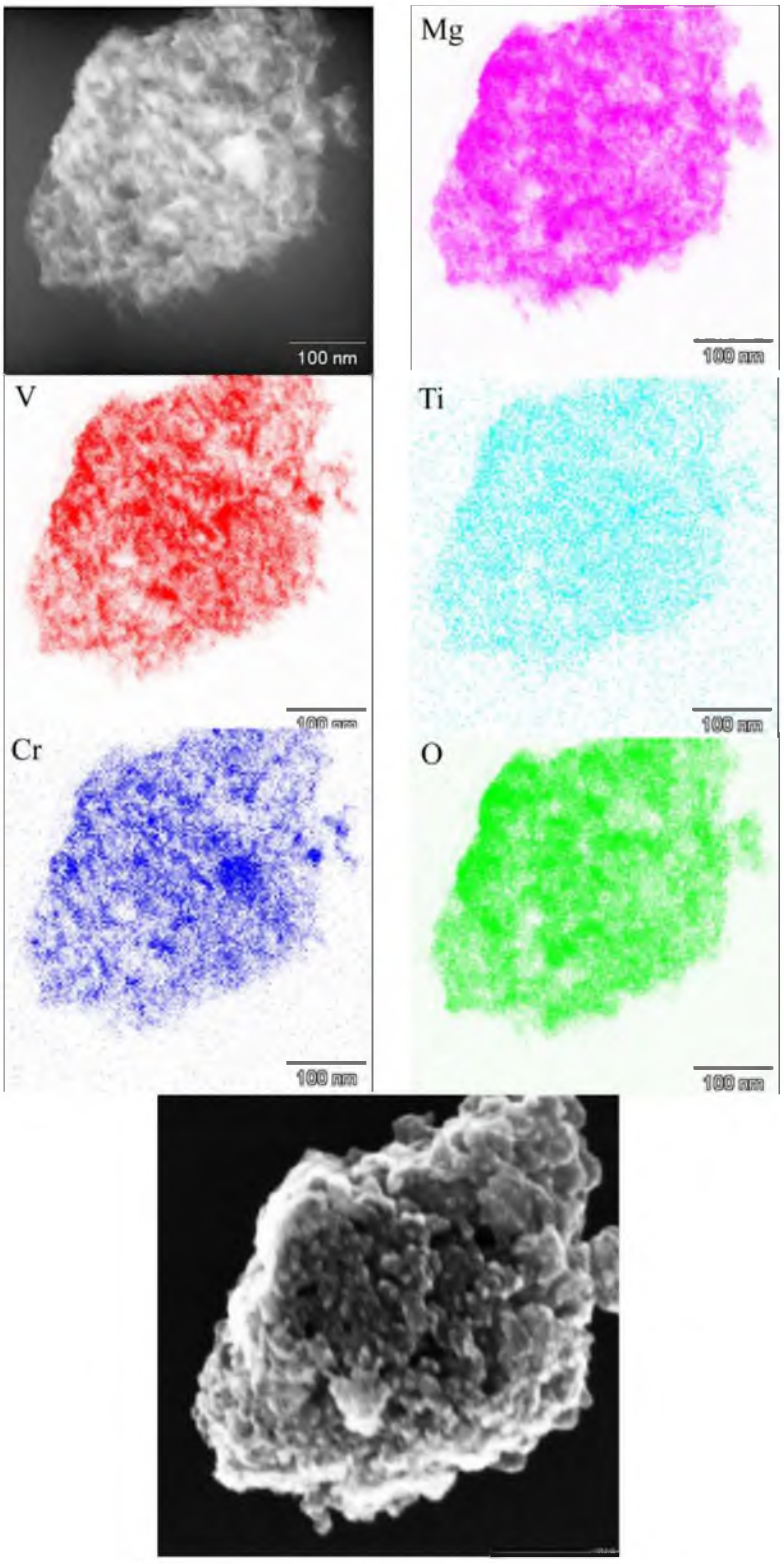

Figure 6-17. TEM images and EDS mapping of an agglomerate of catalyst-rich particle from the MgH_2-VTiCr cycled for 100 cycles.

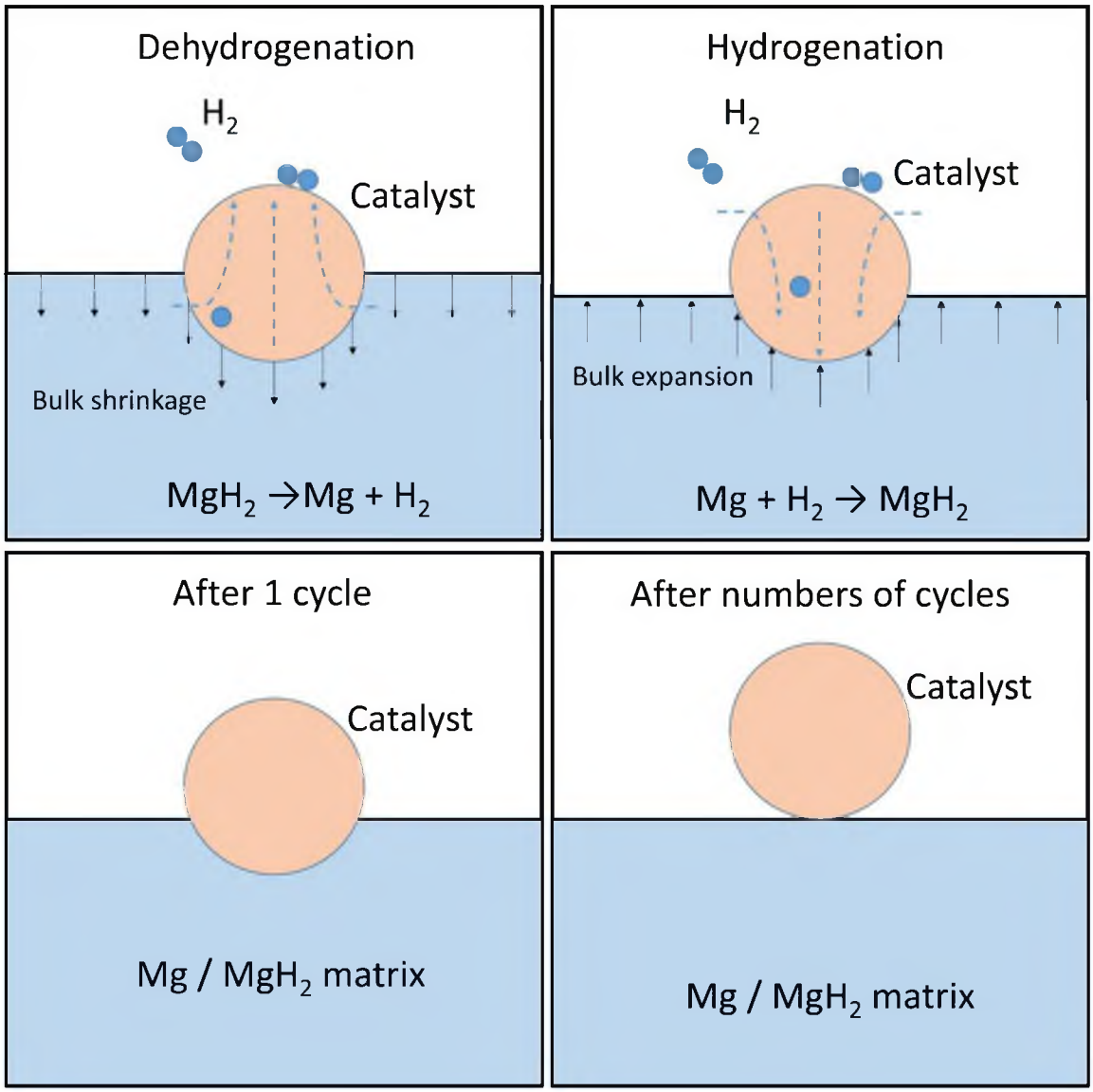

Figure 6-18. Schematics show the evolution of the morphology of a catalyst particle in relation to the hydrogen-induced volume changes during cycling.

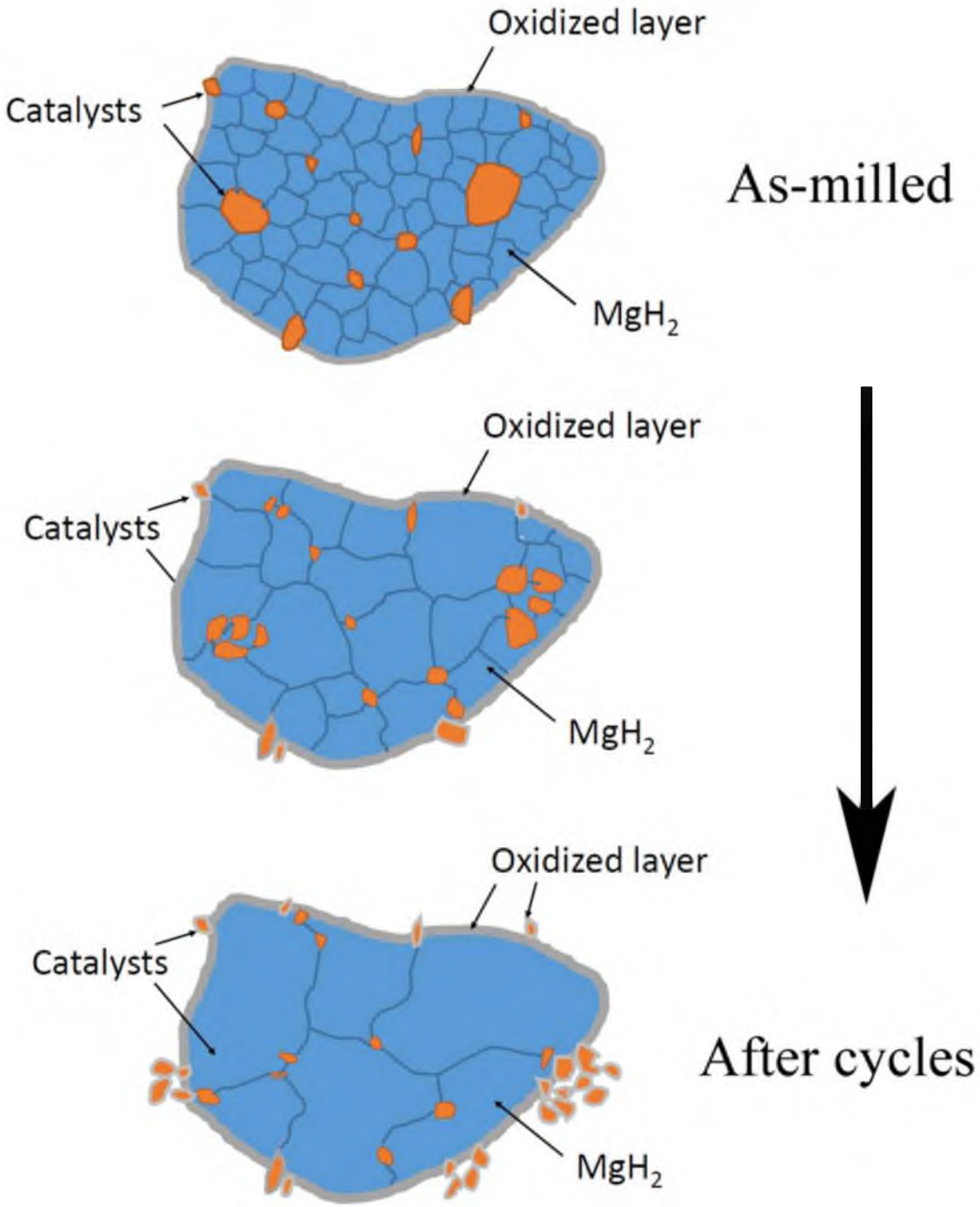

Figure 6-19. A schematic depicts the evolution of the microstructure of the catalyzed MgH_2 particle during cycling.

CHAPTER 7

DEVELOPMENT AND LABORATORY TESTING OF THERMAL BATTERY PROTOTYPE

In Chapter 1, the concept of thermal battery based on advanced metal hydrides for heating and cooling of cabins of electric vehicles was introduced. The described system utilized a pair of thermodynamically matched metal hydrides as energy storage media. Catalyzed MgH_2 has been selected as hot hydride material due to its high thermal energy density. Cold hydride for the system has been restricted in the group of intermetallic compound hydrides. This chapter will focus on developing and testing systems of the thermal battery prototype. The effect of the properties of hydride and system design factors on the performance of the thermal battery will be discussed in this chapter.

7.1 Materials Preparation and Handling

$TiMn_2$ catalyzed MgH_2 and VTiCr catalyzed MgH_2, as suitable hot hydrides that were developed and tested in previous chapters, were used as hot hydrides of prototypes of the thermal battery. Some properties of these materials are listed in Table 7-1. It can be seen that both systems have similar kinetic and thermodynamic properties, and the VTiCr catalyzed system has slightly better kinetic properties against the degradation after long-term cycling.

100 grams of $TiMn_2$ catalyzed MgH_2 were produced, and half (50 g) was mixed with 5 wt.% expanded graphite. Then, the hot hydride materials with and without graphite were loaded into two hot hydride beds, respectively.

As-received $TiMn_{1.5}V_{0.62}$ alloy (GfE, Hydralloy C) and $LaNi_5$ alloy (Sigma-Aldrich, 685933) were activated in an autoclave. The activation process was followed by the procedure: (1) hydrogenation under 100 bar H_2 at room temperature pressure for 30 min, (2) dehydrogenation under vacuum at room temperature for 15 min, and (3) repeat the hydrogenation-dehydrogenation cycle 3 times. After activation, 190 grams of the $TiMn_{1.5}V_{0.62}$ alloy powder was loaded into a low temperature hydride bed denoted as LT-HB. All the material handling was carried out in a glove-box filled with circulating purified argon (99.999%), which contains less than 1 ppm water vapor and 1 ppm oxygen, respectively.

7.2 Thermodynamic Characterization of Selected Hydrides

It should be noted that the thermodynamic properties (Table 7-1) calculated on the basis of the van't Hoff equation (5-1) are only rough estimations that may significantly deviate from the real characteristics of metal hydride materials. There are two major factors affecting the real properties of metal hydride: the plateau slope and hysteresis. Figure 7-1 shows the PCI measurements of the TiMnV alloy that were measured at room temperature. Both absorption and desorption curves show sloping plateaus, one from 10 bar to 20 bar, and desorption from 6 bar to 10 bar. Moreover, a hysteresis between the hydrogen absorption curve and the desorption curve is about 5 bar. Figure 7-1 indicates that 20 bar is needed to fully hydrogenate TiMnV alloy, and when it is fully dehydrogenated, only 6

bar hydrogen will be provided. Further, the usable hydrogen capacity (1.2~1.3 wt%) will be lower than its theoretical value (2.15 wt%).

The plateau slopes and hysteresis of various metal hydrides are different. Figure 7-2 shows the PCI measurements of different metal hydride including, $LaNi_5$, 80V-8Ti-12Cr, and 75V-5Ti-20Cr. The results indicate that $LaNi_5$ as an AB_5-type alloy and has a rather flat plateau for both hydrogen absorption and desorption reaction. The hysteresis of $LaNi_5$ was also less. 80V-8Ti-12Cr and 75V-5Ti-20Cr alloys, known as BCC solid solution alloys, present large plateau slopes (the Y-axis is log-scale) and significant hysteresis.

It has to be noted that MgH_2 usually presents nearly flat plateau and very small hysteresis,[1] and the relevant data measured have been shown in Chapter 5.

7.3 Analysis of System Performance

The theoretical COP (Coefficient of Performance) can be calculated as follows:

$$COP_{cooling} = \frac{\Delta H_l}{\Delta H_h} \tag{7-1}$$

$$COP_{heating} = \frac{\Delta H_h}{\Delta H_h} = 1 \tag{7-2}$$

where ΔH_l and ΔH_h are the reaction enthalpies of LT hydride and HT hydride, respectively. It can be seen that the theoretical COP of heating will be 1. The theoretical COP of cooling is determined by the selection of hydride pair. Taking the pair of $TiV_{0.62}Mn_{1.5}$ and MgH_2, for example, the theoretical COP of cooling is 0.384. The values of $COP_{cooling}$ for possible hydride pairs are summarized in Table 7-2.

7.4 Prototype Design and Fabrication

Two metal hydride thermal battery prototypes were designed and fabricated, denoted Prototype-I and Prototype-II. Prototype-I was developed for the purpose of demonstrating the functionality of the heating and cooling operation (discharging). Prototype-II was further developed for the purpose of testing the performance along with cyclic operation (including discharging and recharging).

7.4.1 Prototype-I

A laboratory demonstration prototype-I was designed and fabricated, as shown in Figure 7-3 (a). Due to the differences in density and stoichiometry with hydrogen between the hot hydride and cold hydride, the prototype used 190 g of cold hydride (TiMnV) and 100 g of hot hydride ($TiMn_2$ catalyzed MgH_2). Two hot hydride beds were coupled with one cold hydride bed because the density of the cold hydride is about four times that of the hot hydride. A mass flow meter (Model: GFM 37 AALBORG Inc., Accuracy: ±1.5% of full scale, Range: 0-20 L/min) and pressure gauges (PGI series, Swagelok) were mounted on the system to monitor the hydrogen flow rate and hydrogen pressure during operation. Temperatures of the hydride beds were recorded by K-type thermocouples. Detailed information of the components is given in Table 7-3. Figure 7-3 (b) illustrates the design details of the three hydride beds.

7.4.2 Prototype-II

The design and photographs of assembled prototype-II hardware are shown in Figure 7-4. One hot hydride bed was coupled with one cold hydride bed. These prototype beds

contained 50 g of cold hydride ($LaNi_5$) and 10 g of hot hydride ($TiMn_2$ catalyzed MgH_2), respectively. Two pneumatic valves were used to control the hydrogen flow between the hot bed and the cold bed. A mass flow meter (AALBORG) and pressure transducers (AST) were mounted on the system to monitor the hydrogen flow rate and hydrogen pressure of the system during operation. Based on the design of hydride bed of prototype-I, temperature measurement of the hydride bed (Figure 7-3 (b)) was modified. Instead of measuring the temperature on the outside surface of beds, a stainless steel protection tube was placed in the center of bed to get a more accurate reading of temperature of hydride. Temperatures of the hydride beds were recorded by K-type thermocouples. The data acquisition device (LabJack, U6-Pro) was applied to control the heater for the hot hydride bed and valve status and also record pressure, temperature, and hydrogen flow.

7.5 Experimental Testing of Prototype-I

7.5.1 Discharge

In order to understand the effect of thermal conductivity of hydride material, one hot hydride bed (HHB-1) was loaded with catalyzed MgH_2, and the other (HHB-2) was loaded with a mixture of catalyzed MgH_2 with 5 wt% graphite. The graphite served as a heat transfer enhancer.[2-4] Before discharging, the hot hydride beds were heated to and held at 270 °C for 3 hrs to fully dehydrogenate the hot hydride, and the cold hydride was hydrogenated using 20 bar pressure. After the dehydrogenation of the hot hydride beds and the hydrogenation of the cold hydride bed, all the hydride beds were cooled to room temperature. Then the valve between the hot hydride beds and the cold hydride bed was opened to discharge the thermal battery. The temperature profiles of the hydride beds

during discharging are shown in Figure 7-5 (a), and the flow rate of hydrogen and the pressure of the system are plotted in Figure 7-5 (b). First, it can be seen that the HHB-1 (without addition of graphite) heated up to 228 °C within 5 minutes. In contrast, the HHB-2 (with addition of graphite) heated up at a much slower rate; it took 40 minutes to reach the maximal temperature of 96 °C. Second, the cold hydride bed cooled down to -12 °C within the same time period. Third, once the valve was opened, the pressure of the system quickly decreased from 12.5 bar to below 1 bar. Corresponding to the pressure drop, a spike of hydrogen flow was observed within 3 minutes, indicating very fast kinetic rates for reactions in both HHB-1 and the cold hydride bed.

An interesting observation during the discharging is the quick thermal response of HHB-1 (hot hydride without graphite) in contrast to a slow heating rate of HHB-2. Considering all the data including the temperature profiles, the pressure, and the flow rate, it is believed that the reaction rate of the material in HHB-1 was much higher than that of the material in HHB-2. It should be pointed out that kinetics studies of the two hot hydride materials (catalyzed MgH_2 with and without addition of graphite) did not show an obvious kinetic difference[5]. Therefore, the critical difference in temperature responses between the two hot beds is attributed to the differences in the thermal conductivity within the two beds. Therefore, the quick thermal response of the HHB-1 is likely due to a "self-heating" effect. The hydrogenation of Mg is a highly exothermic reaction, thus usually causing a temperature rise of the material itself. For the materials without heat transfer enhancement (MgH_2 without graphite), the rise of temperature was faster. The increase of the temperature would in turn boost the rate of hydrogenation, which is demonstrated in a separate measurement of the hydrogenation of catalyzed nano MgH_2 at different

temperatures (see Figure 4-6). Therefore, the thermal conductivity of the hot bed plays an important role on its heating behavior.

Note that there was a pressure rise after the initial absorption (after discharge for 10 min). This is directly correlated to the increase of temperature of the LT bed, which provides high hydrogen pressure. However, the pressure and temperature changes of the LT bed depends also on the rate of absorption of the HT beds. Therefore, the pressure rise is likely due to the kinetic limitation of HT-HB#2 and the quicker completion of the reaction in HT-HB#1. When the kinetic rate of absorption of HT-HB#2 improved gradually (after 30 min in Figure 7-5 (b)), the hydrogen pressure of the system started to decrease again.

Further, cooling and heating performance of the system can be determined by the measurement of hydrogen flow between LT bed and HT bed. The wattages of heating and cooling power of the thermal battery system can be obtained by the following equations:

$$W_c = \frac{v_{H_2}}{V_m} \times \Delta H_l \tag{7-3}$$

$$W_h = \frac{v_{H_2}}{V_m} \times \Delta H_h \tag{7-4}$$

where v_{H2} is the flow rate of hydrogen and V_m is molar volume of hydrogen. Figure 7-5 (c) plots the wattage of heating and cooling during the discharge. By integrating the wattage-time profile, the total cooling and heating energy are therefore estimated as 13.6 Whr and 35.4 Whr, respectively.

7.6 Experimental Testing of Prototype-II

7.6.1 Cyclic Performance

Because Prototype-II was developed for the purpose of testing the cyclic performance of the thermal battery, modifications based on the design of Prototype-I were made to allow the prototype to be recharged and automatically cycled. One change made was that $LaNi_5$ was used as the cold hydride. This is because $LaNi_5$ has a lower equilibrium pressure (1.7 bar at room temperature) than that of TiMnV alloy. According to the thermodynamic estimation in section 4.2, using a TiMnV alloy as a cold hydride would require the hot bed (hot hydride, MgH_2) to be heated over 400 °C to provide sufficiently high H_2 pressure (>20 bar) to hydrogenate TiMnV. Applying higher temperature and high hydrogen pressure to the system would lead to a series of problems in terms of system design. First, significant degradation of kinetics of MgH_2 may occur at temperatures above 400 °C due to powder sintering and grain growth[6]. Second, safety concerns due to higher temperatures and pressures mandate a more robust and thus costly system.

Before the discharge, the system was prepared by the following procedure: (1) the hot hydride bed was dehydrogenated at 270 °C for 3 hrs and (2) the cold hydride bed was hydrogenated under 5 bar pressure. Figure 7-6 (a) shows the temperature profiles during the discharging. And Figure 7-6 (b) shows the pressure and the hydrogen flow rate against time. It can be seen that the "heating effect" and the cooling effect are not as significant as those of the discharging test of Prototype-I. The highest temperature the hot hydride bed reached was 161 °C, lower than the 228 °C of Prototype-I. For the lowest temperature of the cold hydride bed, it was the -4 °C as compared to the -12 °C of Prototype-I. These differences may be attributed to two reasons. First, the amount of hydride material that was

used in Prototype-II was reduced, which certainly caused less thermal effect than that of the prior one. Second, the usage of $LaNi_5$ leads to lower hydrogen pressure in the system during the discharge (Figure 7-6 (b)), which affects the kinetic rate on both hydrides and reduces the thermal effect.

The recharge process was carried out by heating the hot hydride bed to 320−330 °C for 2 hrs, as shown in Figure 7-7. After recharging, the valve between the two beds was closed, and the hot hydride bed was cooled to room temperature, then the next discharging was performed. Figure 7-8 (a) shows the temperature and pressure profile of the next discharge (i.e., the 2-4 cycles). The results show that the thermal performance deteriorated significantly after the first recharge. The temperature of the hot bed only increased by 15 °C, and the temperature of the cold bed only decreased to 20 °C.

Additional cyclic tests (5−100 cycles) were performed under the same recharging condition (hot hydride bed heated to 330 °C for 2 hrs). But in order to minimize the internal time between the end of recharging and the start of discharging, the discharge process was started as soon as the temperature of the hot hydride bed was cooled to 90 °C. Figure 7-8 (b) compares the temperature profiles of hot and cold beds as well as the pressure changes of the system. It can be found that degradation of the thermal effect occurred gradually with prolonging the cycle test, especially after 20 cycles.

7.6.2 Pressurizing Testing of Hot Hydride Bed

Prototype tests have shown that both the prototypes present very good performances in the first cycle, presenting a quick "self-heating" effect in the very beginning of the discharging. However, results also showed that a significant degradation appeared during

the test of the Prototype-II system. To further understand the "self-heating," a series of hydrogen pressurizing experiments for the hot hydride bed were conducted.

In these experiments, two cycles were performed on the Prototype-II system. The hot hydride bed in Prototype-II was directly connected to a hydrogen gas cylinder for hydrogenation and a vacuum system for dehydrogenation. The temperature profiles and pressure conditions are provided in Figure 7-9. As shown in Figure 7-9 (a), by supplying 17 bar hydrogen into the hot hydride bed, the temperature increased from room temperature to 375 °C in 100 seconds. However, introducing 5 bar or 7 bar pressure to the hot bed led to slow temperature increases, and a further increase of pressure to 10 bar did not lead to "self-heating." The maximal temperature did not even reach 75 °C (see Figure 7-9 (b) and (c)). Figure 7-9 (d) and (e) show that pressurizing the hot bed with 9 bar or 10.5 bar hydrogen causes a temperature spike over 350 °C. Moreover, when the hot hydride bed was pressurized with a very short period of time (~10 seconds) and 10 bar hydrogen, around 10 °C temperature increase was observed, as shown in Figure 7-9 (f). Then the same pressure of hydrogen was subsequently introduced, which led to a much slower temperature climbing and eventually reached 300 °C. The results mentioned above were summarized in Table 7-4.

7.7 Discussion

7.7.1 Preconditioning for Improving Performance

From a practical point of view, the room temperature "self-heating" effect is a very attractive property because it can offer a cold-start and fast heating/cooling rate for an on-board air conditioning system. According to the prototype cyclic test, however, the "self-

heating" phenomenon diminished after one recharge process, which should be attributed to degradation of the kinetic of the catalyzed MgH_2 at room temperature and low pressure.

A key lesson from section 7.6 is that the initial pressure that fed into the bed is a crucial factor to the subsequent kinetic rate of the system. It has been found that if the initial feeding pressure is above 9 bar, the temperature of the hot hydride bed of Prototype-I is likely raised to over 300 °C. When the pressure is lower than 7 bar, the temperature will not exceed 100 °C. To ensure a good discharge performance of the thermal battery system, a cold hydride with equilibrium pressure higher than 9 bar is preferred. However, such a high-pressure hydride faces several disadvantages – difficulty in system design, an increase of cost, and materials degradation, as mentioned before.

It has to be pointed out that the heating behavior of the hydride bed is also related to many other factors such as amount of loaded hydride material. The more hydride loaded into bed, more heat is likely accumulated inside bed during the process. This means less pressure may be required to result a fast heating when a large hydride bed with more hydride loaded is applied. The heating behavior can be also impacted by the heat transfer rate of the system including both hydride material and hydride bed. An overall analysis to the energy balance of the system allows to predict the temperatures of hydride beds and the system energy output. However, modelling the thermal battery system is beyond the research scope of this dissertation. Detailed modelling and energy analysis of metal hydride thermal battery system has been provided by Gareth.[7]

From the material analysis in Chapter 6, we have known that the catalyzed MgH_2 material presents no kinetic degradation at a higher temperature under sufficient hydrogen pressure. Therefore, it is safe to presume that if the hot hydride bed is preheated to an

elevated temperature and fed with sufficient hydrogen pressure, no degradation of the thermal effect should be observed. This assumption leads to an idea of "preconditioning" of the thermal battery system. As shown in Figure 7-10, a thermal battery system can use a cold hydride bed array and a hot hydride bed array, consisting of multiple cold hydride beds and hot hydride beds, respectively. The operating strategy is described below and illustrated in Figure 7-10.

(1) Heat one of the cold hydride beds to an elevated temperature. The cold hydride with higher temperature can generate higher hydrogen pressure;

(2) Heat one of the hot hydride beds to an elevated temperature (100−200 °C);

(3) Connect the heated cold bed and hot bed. This will cause a quick "self-heating" effect, and the temperature of the hot bed should quickly increase to over 300 °C;

(4) The excessive heat generated from the hydrogenation of the hot bed can heat other hot beds;

(5) Connect all cold beds and hot beds together.

Although the preconditioning process will consume excessive energy from the electric battery of EV, preheating for cold and hot beds before the discharge could be a simple method to prevent the degradation of performance. Fortunately, by using the strategy described above, only a small fraction of hydride material needs to be preheated, so the energy consumption should be limited. Further research and engineering development are required to assess and address this method.

7.7.2 Aspects of Scale-up System

The two prototypes that were built and tested in the current research were laboratory-scale thermal battery systems dealing with the limited amount of hydride material (at most a few hundreds grams). It can be expected that many scientific and engineering problems will emerge when the system is scaled up.

7.7.2.1 Materials

It is known that both the cold and hot hydride used in this research is powdered material. To achieve the high volumetric energy density of the system, a dense packed hydride material inside the hydride bed is preferred. For example, a compact pellet of the catalyzed MgH_2 can easily achieve twice the density of the loose powder bed (1.06 g/cm^3 for packed MgH_2 vs. 0.45 g/cm^3 for loose MgH_2 powder bed). The result from section 6.2.5 shows no significant difference in terms of kinetics and degradation behavior, comparing the densely packed and loose MgH_2 material. On the other hand, packing the powder too densely may reduce permeability of hydrogen though the hydride bed. Therefore, hydrogen gas conduits inside the hydride bed may be a necessary design element.

Cold hydride candidates such as TiMnV, $LaNi_5$, etc., undergo severe lattice (volume) expansion (typically $\Delta V/V_o$ = 15 to >30 vol%) during hydrogenation.[8] This feature may cause problems such as hydride migration, deforming of the reactor vessel, and even damaging the vessel. Nasako et al.[9] suggested that the filling density of the $LaNi_5$-type alloy should not exceed 61% to avoid safety problems as the expansion during hydrogenation.

7.7.2.2 Thermal Transfer

Thermal conduction is expected to become a much more important factor as the system is scaled up. The faster heat transfer rate is certainly beneficial to the rate of heating/cooling that the system can deliver, especially for the side of cold bed since the ΔT (cold hydride to cooled air) might be merely a few degrees. A simple and efficient method is compacting the hydride powder with a heat-conductive material, including porous metals and expanded natural graphite (ENG). More solutions include heat conductive fins, a coiled tube heat exchanger, metal foams, or a honeycomb metallic structure.[8]

It has to be noted that the enhancement of thermal conductivity of the hot hydride will reduce the rate of the "self-heated" reaction, as mentioned in section 7.5.1. This conflicting trend should be taken into account for the scaled-up design.

7.7.2.3 Systematic Control

In reality, the thermal battery as an air-conditioning system must be tunable for its heating/cooling rate. To accomplish that, there are two basic ways to adjust the energy output of the thermal battery system:

(1) Adjust the hydrogen flow rate between cold beds and hot beds.

(2) Adjust the thermal energy flux.

The first option is a straightforward approach and can be easily achieved by opening/closing the valve between them or by installing a mass flow controller. Once the hydrogen flow was shut off, the reactions on both sides can be immediately stopped.

The second option is complex but may be useful in some particular cases. For example, heat production from the hot bed can be boosted by enhancing the heat transfer

of the cold bed. In other words, forcing a fast heat transfer rate of the cold bed causes a temperature rise and therefore leads to an increase of pressure in the system. The higher pressure results in a higher driving force for the reaction of hot hydride and therefore leads to an increase of heat production and the temperature of hot hydride. Similarly, the same approach can be applied when the system was operating at cooling mode.

7.8 Summary

Two laboratory prototypes were designed, fabricated, and tested. The results successfully demonstrate the principles of the thermal battery using metal hydrides. Cyclic test show a significant degradation of the heating/cooling performance. Further, hot hydride bed hydrogen pressurizing tests showed that a hydrogen pressure above 9 bar is needed to achieve fast kinetics for the present hot hydride design. Moreover, some type of precondition process may be in order to improve the system performance, and several aspects for a scaled-up thermal battery were discussed.

7.9 References

1. Stampfer, J. F.; Holley, C. E.; Suttle, J. F., The Magnesium-Hydrogen System. *J. Am. Chem. Soc.* **1960**, *82*, 3504−3508.

2. Kim, K. J.; Montoya, B.; Razani, A.; Lee, K. H., Metal Hydride Compacts of Improved Thermal Conductivity. *Int. J. Hydrogen Energy* **2001**, *26*, 609−613.

3. Chaise, A.; de Rango, P.; Marty, P.; Fruchart, D.; Miraglia, S.; Olivès, R.; Garrier, S., Enhancement of Hydrogen Sorption in Magnesium Hydride Using Expanded Natural Graphite. *Int. J. Hydrogen Energy* **2009**, *34*, 8589−8596.

4. Pohlmann, C.; Röntzsch, L.; Weißgärber, T.; Kieback, B., Heat and Gas Transport Properties in Pelletized Hydride–Graphite-Composites for Hydrogen Storage Applications. *Int. J. Hydrogen Energy* **2012**, 38, 1685−1691.

5. Li, J.; Fan, P.; Fang, Z. Z.; Zhou, C., Kinetics of Isothermal Hydrogenation of

Magnesium with Tih2 Additive. *Int. J. Hydrogen Energy* **2014**, *39*, 7373−7381.

6. Bogdanovic, B., et al., Ni-doped versus undoped Mg-MgH_2 materials for high temperature heat or hydrogen storage. *J. Alloys Compd*, **1999**, 292: p.57−71.

7. Gareth D.W. Metal hydride thermal battery design, lumped capacitance modeling and validity criteria. Master Thesis, The University of Utah, Salt Lake City, Utah, 2013.

8. Lototskyy, M. V.; Yartys, V. A.; Pollet, B. G.; Bowman, R. C., Metal Hydride Hydrogen Compressors: A Review. *Int. J. Hydrogen Energy* **2014**, *39*, 5818−5851.

9. Nasako, K.; Ito, Y.; Hiro, N.; Osumi, M., Stress on a Reaction Vessel by the Swelling of a Hydrogen Absorbing Alloy. *J. Alloys Compd.* **1998**, *264*, 271−276.

Table 7-1 Properties of selected hot hydride materials. Data obtained in the present study.

	$TiMn_2$ catalyzed MgH_2	VTiCr catalyzed MgH_2
Hydrogen capacity, wt%	6	6
ΔH, kJ/mol H_2	74.5	74.5
P_{eq} @ 300 °C, bar	1.8	2
H_2 uptake in 30 min at 25 °C, wt%		
1st cycle	2.3	2.5
100th cycle	0.3	0.5
H_2 uptake in 10 min at 300 °C, wt%		
1st cycle	3.8	5.2
100th cycle	4.1	4.4
Time to fully dehydrogenated at 300 °C, min		
1st cycle	2.5	1.1
100th cycle	1.6	0.7

Table 7-2. Theoretical COP of cooling of different hydride pairs.

Hot hydride	Cold hydride	$COP_{cooling}$
Mg	$TiV_{0.62}Mn_{1.5}$	0.384
Mg	$LaNi_5$	0.413
Mg	75V-5Ti-20Cr	0.443
Mg	$TiMn_2$	0.368
Mg_2Ni	$TiV_{0.62}Mn_{1.5}$	0.443
Mg_2Ni	75V-5Ti-20Cr	0.512
Mg_2Ni	$TiMn_2$	0.425
$LaNi_{4.25}Al_{0.75}$	$TiV_{0.62}Mn_{1.5}$	0.649
$LaNi_{4.25}Al_{0.75}$	$TiMn_{1.5}$	0.651
$LaNi_{4.25}Al_{0.75}$	$TiMn_2$	0.621

Table 7-3. Sensors and components used in the prototypes.

Items	Manufacturer	Model/Part Number
Mass flow meter	AALBORG instrument and controls, Inc.	GFM 37
Pressure transducer	American Sensor Technologies, Inc.	AST4300A00500P3I1000
Pneumatic valve	Swagelok	6LVV-DPHFR4-P1-C
DAQ broad	LabJack Corp.	U6-Pro

Table 7-4. Summary of hot bed hydrogen pressurizing tests.

Test No.	Cycle No.	Pressuring condition	Maximal temperature T_{max}, °C	Time to T_{max} t, sec
1	3	17 bar for 60 sec	377.5	79
2	4	6 bar for 160 sec, Then 9.5 bar to the end	72.4	870
3	5	7 bar for 70 sec, Then 10 bar to the end	67	872
4	6	9 bar for 170 sec	351.6	190
5	8	10 bar to the end	360.2	242
6	9	10 bar for 20 sec, Then 10 bar to the end	299.5	960

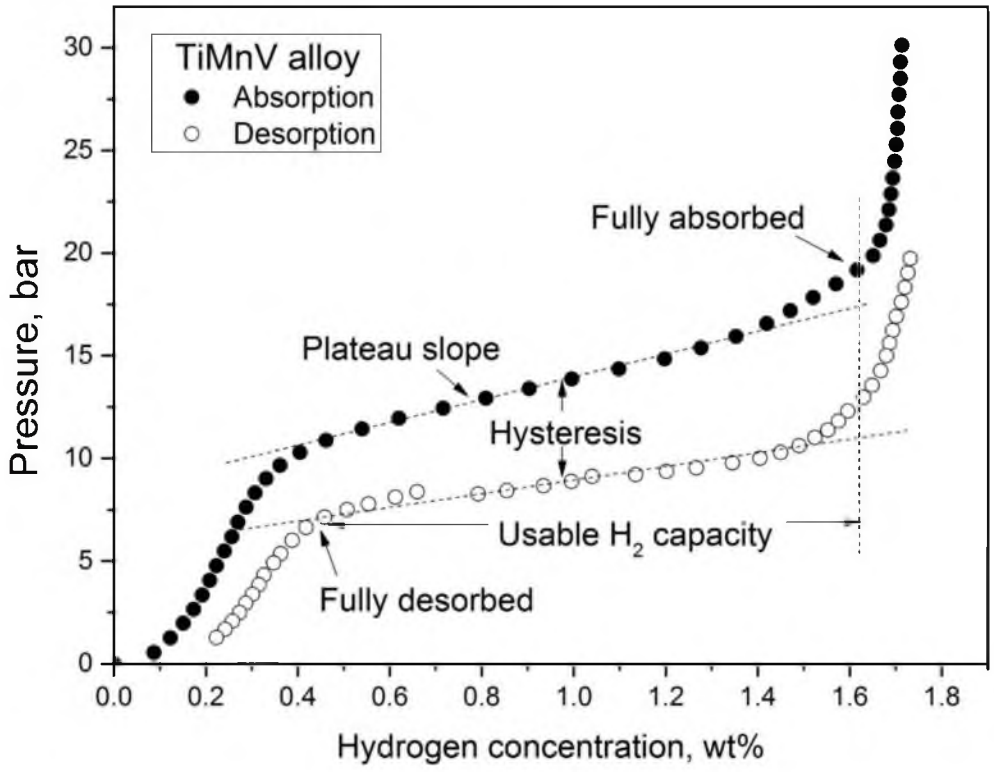

Figure 7-1. PCI curves of TiMnV alloy at room temperature (25 °C).

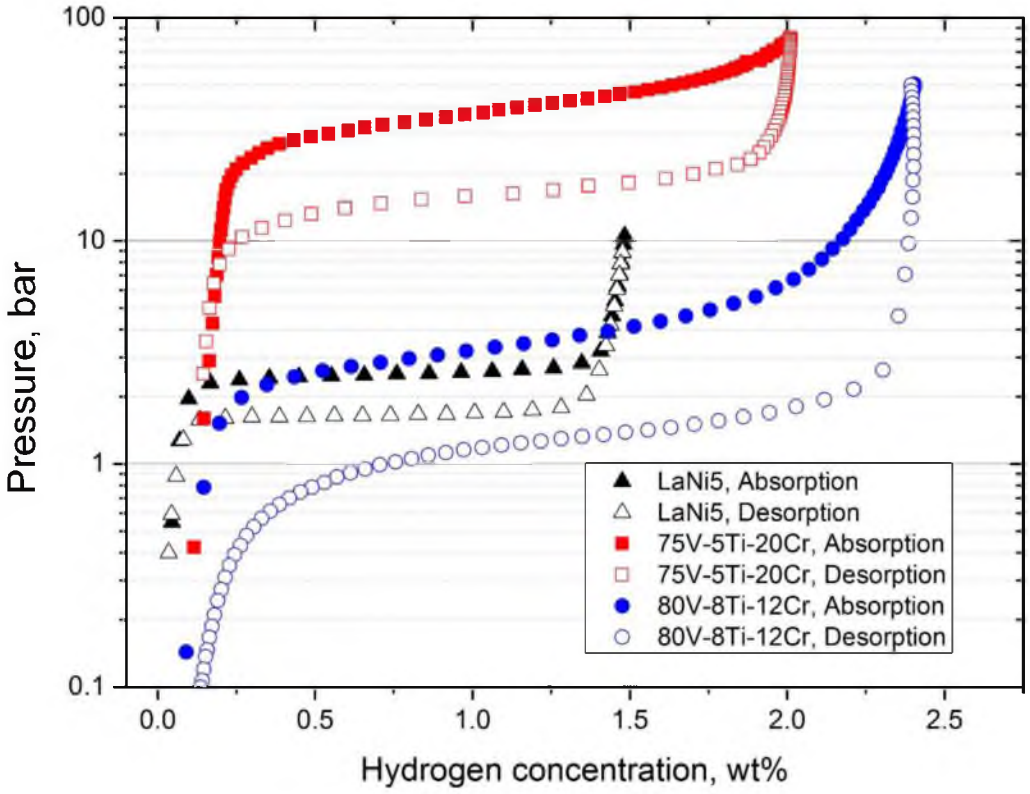

Figure 7-2. PCI curves of $LaNi_5$, 75V-5Ti-20Cr, and 80V-8Ti-12Cr alloys, measured at room temperature.

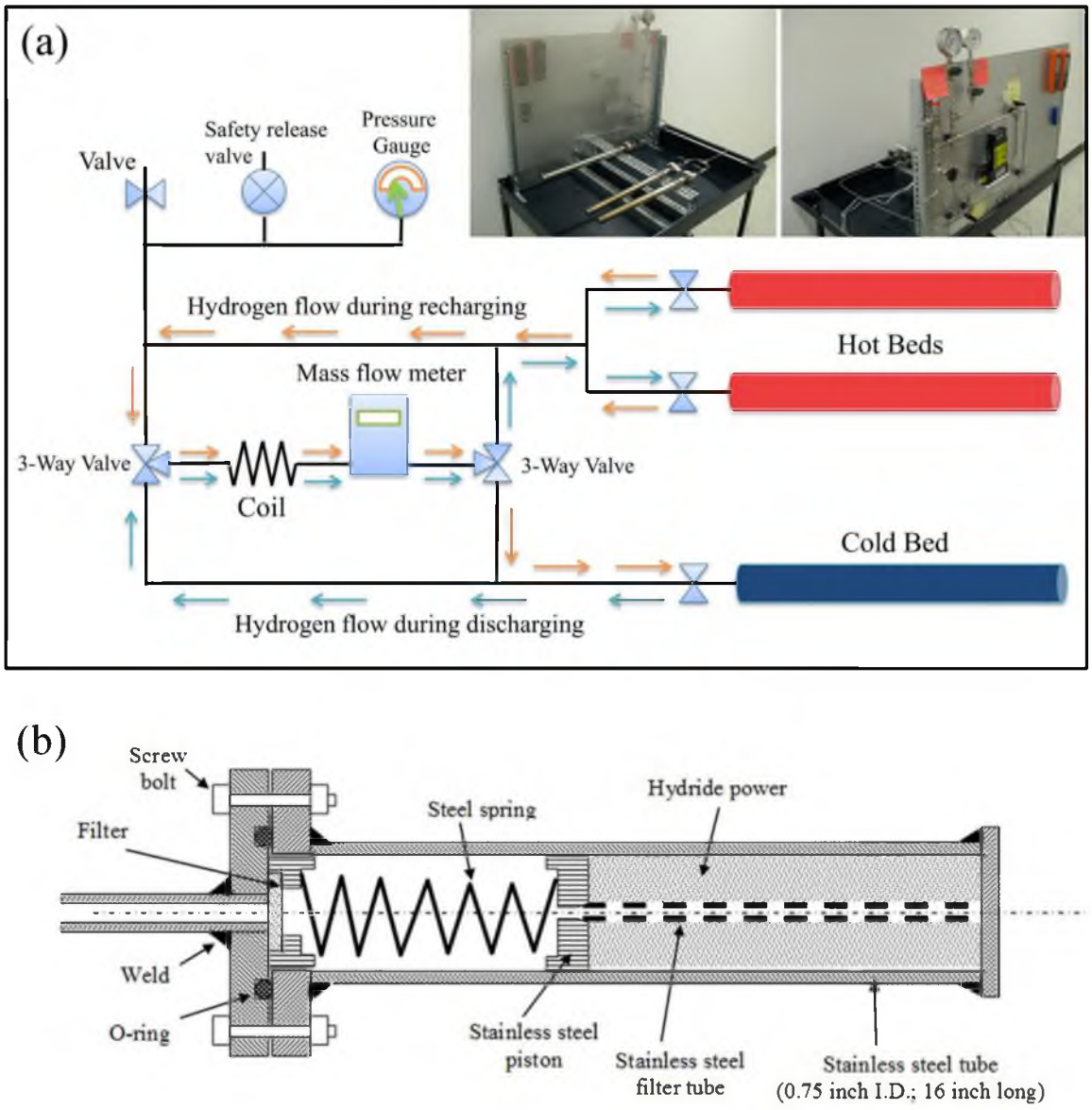

Figure 7-3. Prototype-I. (a) Schematic and photos of Prototype-I; (b) Hydride bed design of the Prototype-I.

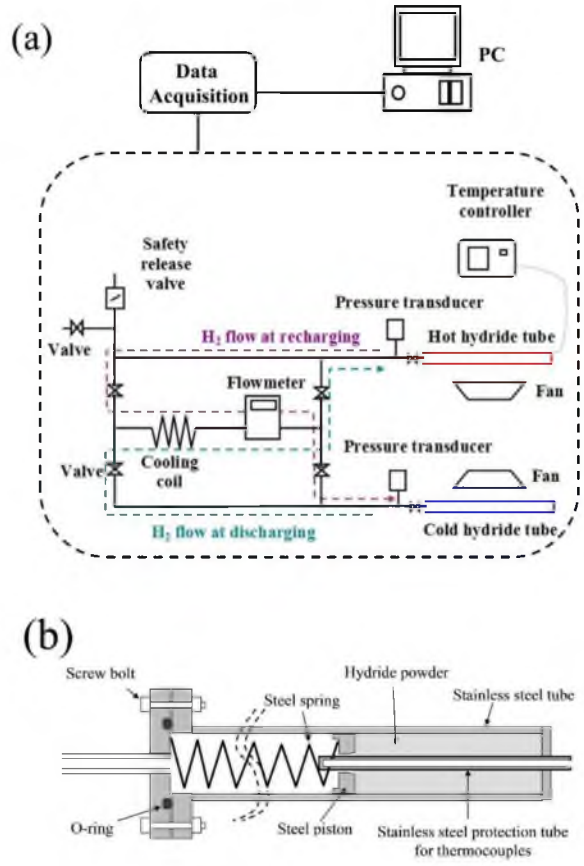

Figure 7-4. Metal hydride thermal battery Prototype-II. (a) Schematic, (b) Hydride bed design, (c) Photographs.

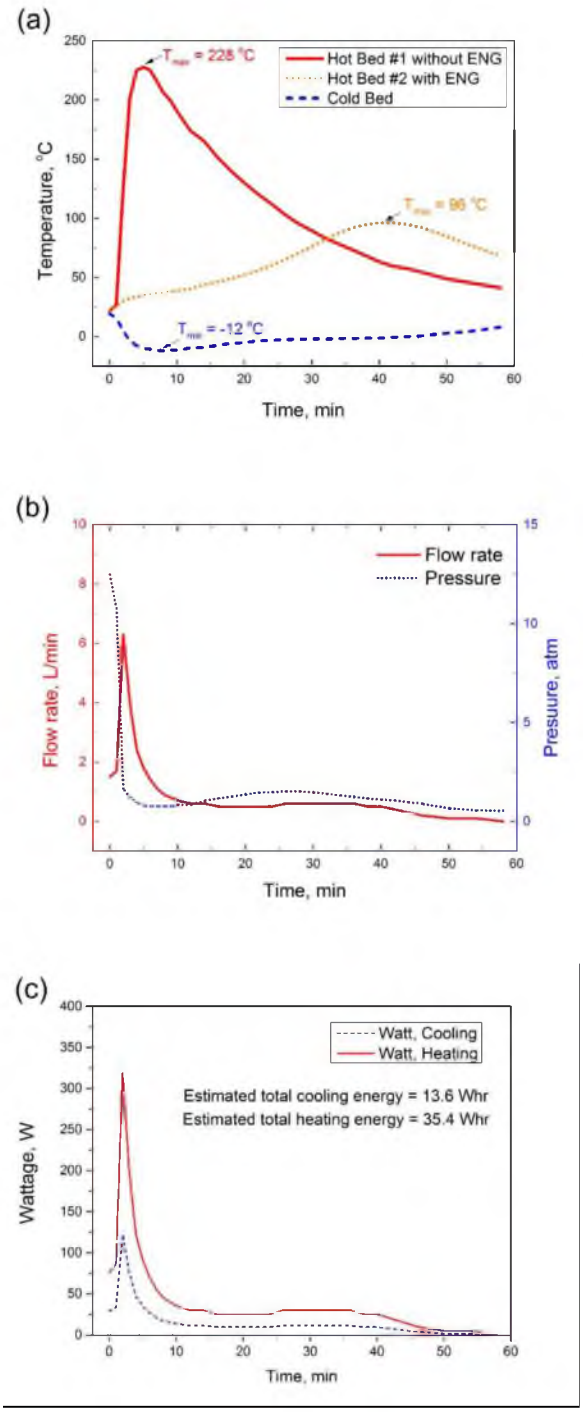

Figure 7-5. Discharge test of Prototype-I. (a) Temperature profiles of hot beds and cold bed; (b) The pressure changes and flow rate measure; (c) Wattage values derived for the heating and cooling processes.

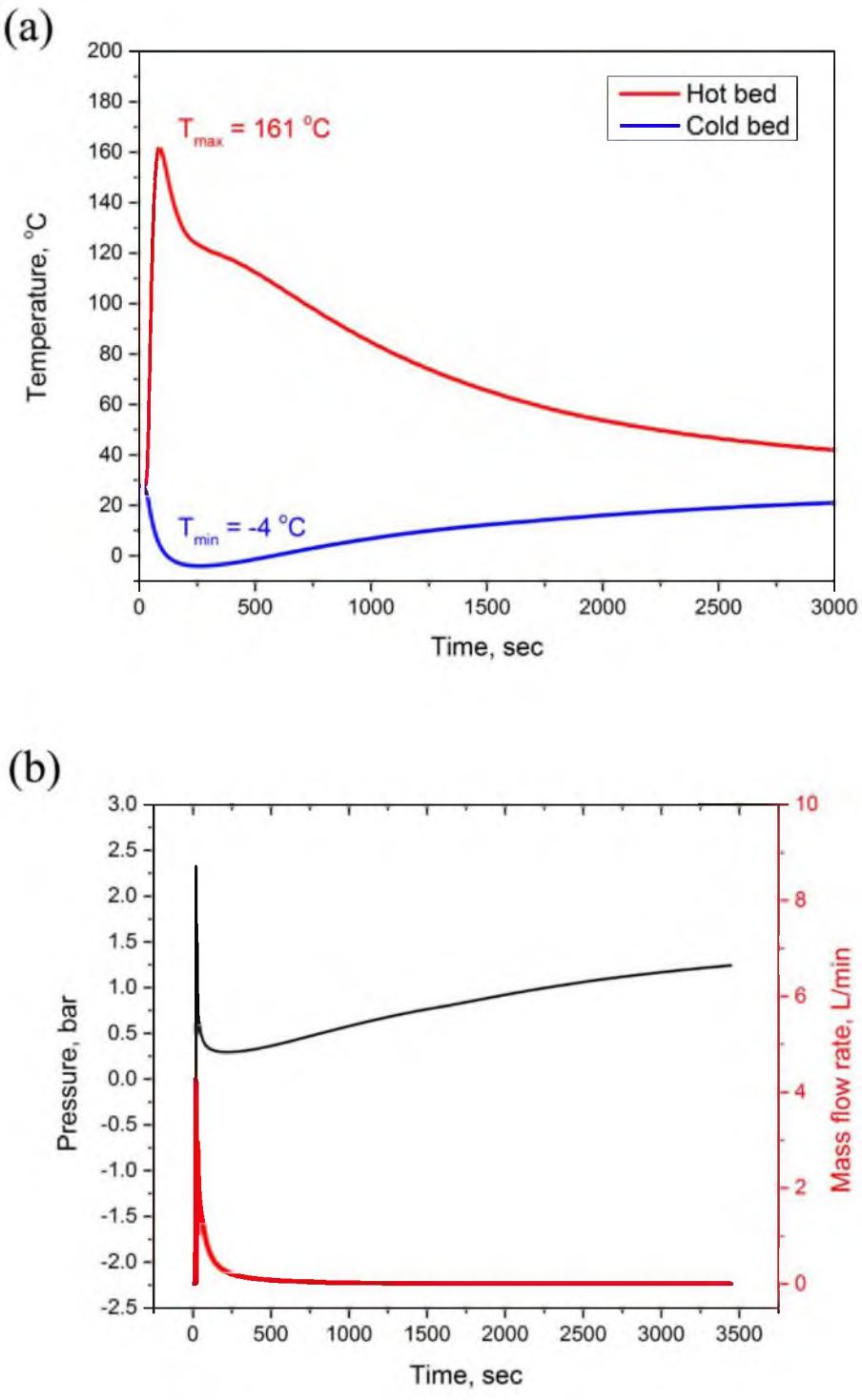

Figure 7-6. The 1st cycle discharge test of Prototype-II. (a) Temperature profiles of hot bed and cold bed of Prototype-II; (b) Flow rate and the pressure changes.

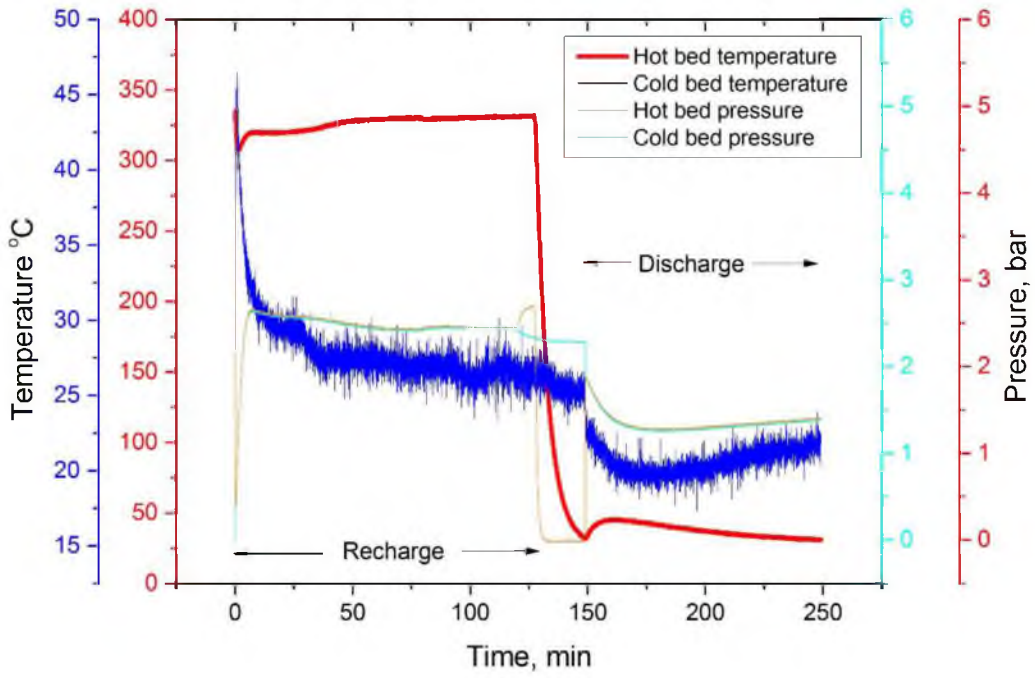

Figure 7-7. The first recharge-discharge cycle of the Prototype-II hydride beds.

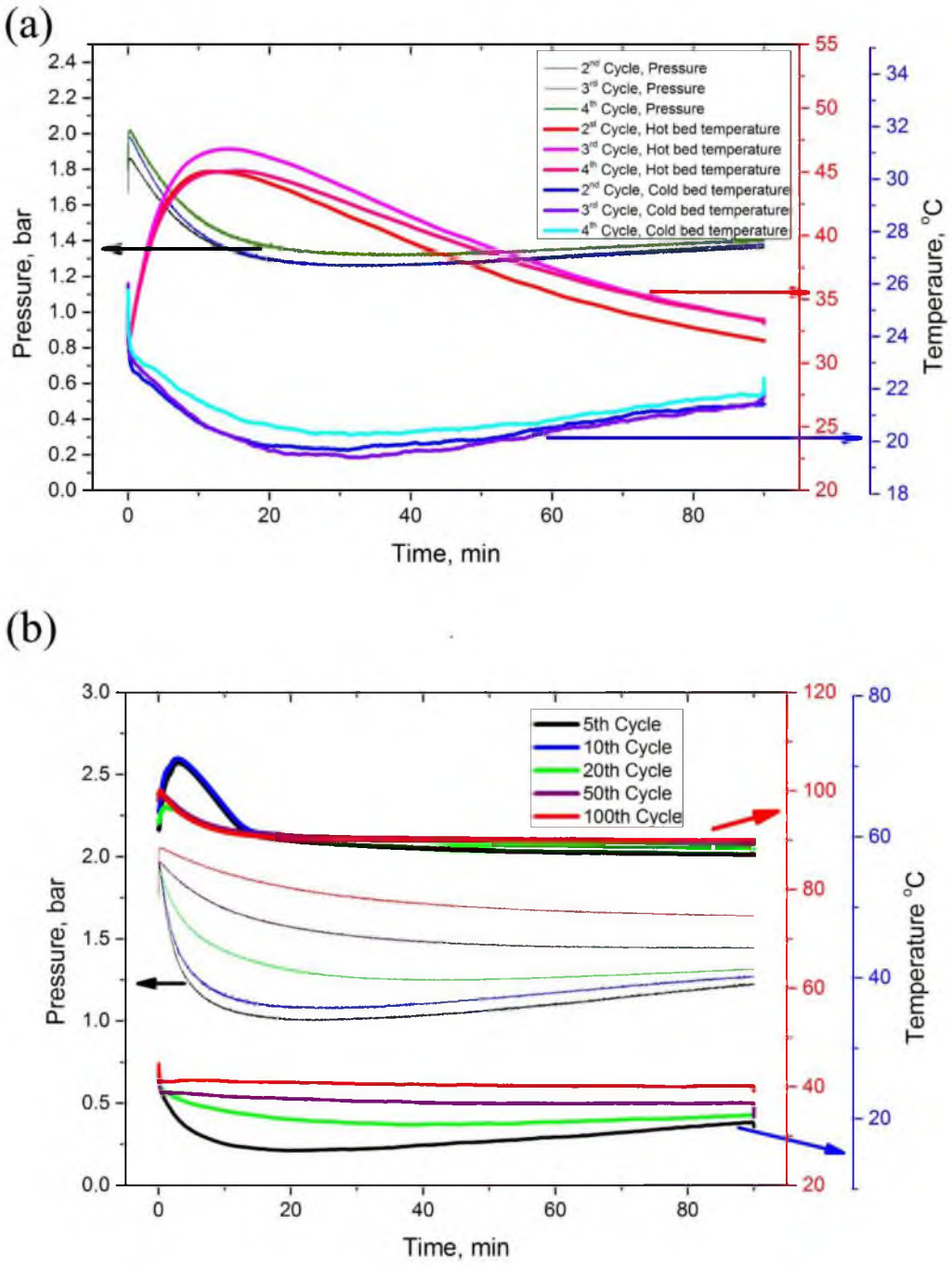

Figure 7-8. Cyclic test of Prototype-II. (a) Temperature and pressure profiles of 2nd to 4th cycles; (b) Temperature and pressure profiles at the 5th, 10th, 20th, 50th, 100th cycles.

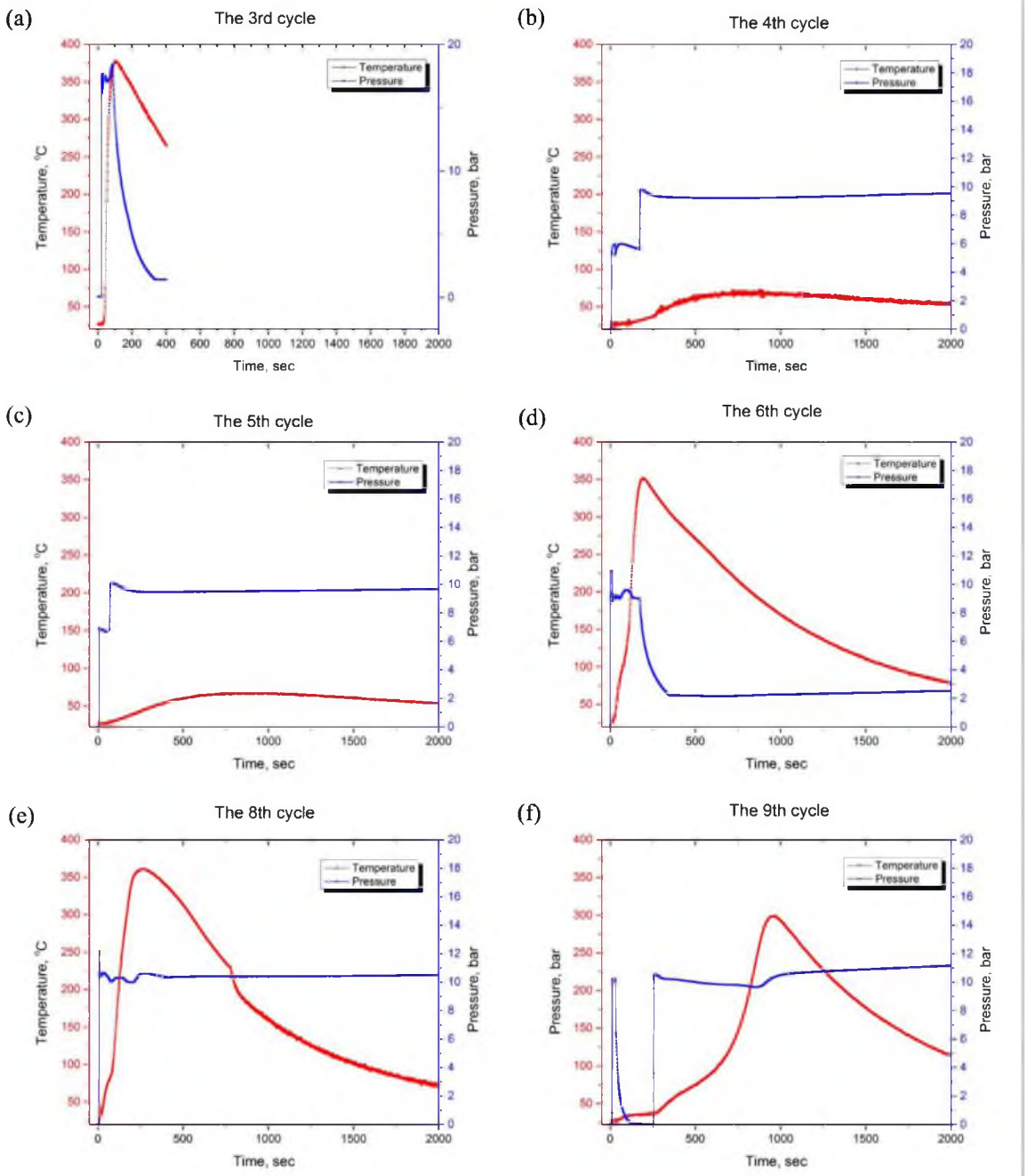

Figure 7-9. Temperature changes of hot hydride bed during hydrogen pressurizing tests. (a) The 3rd cycle; (b) The 4th cycle; (c) The 5th cycle; (d) The 6th cycle; (e) The 8th cycle; (f) The 9th cycle.

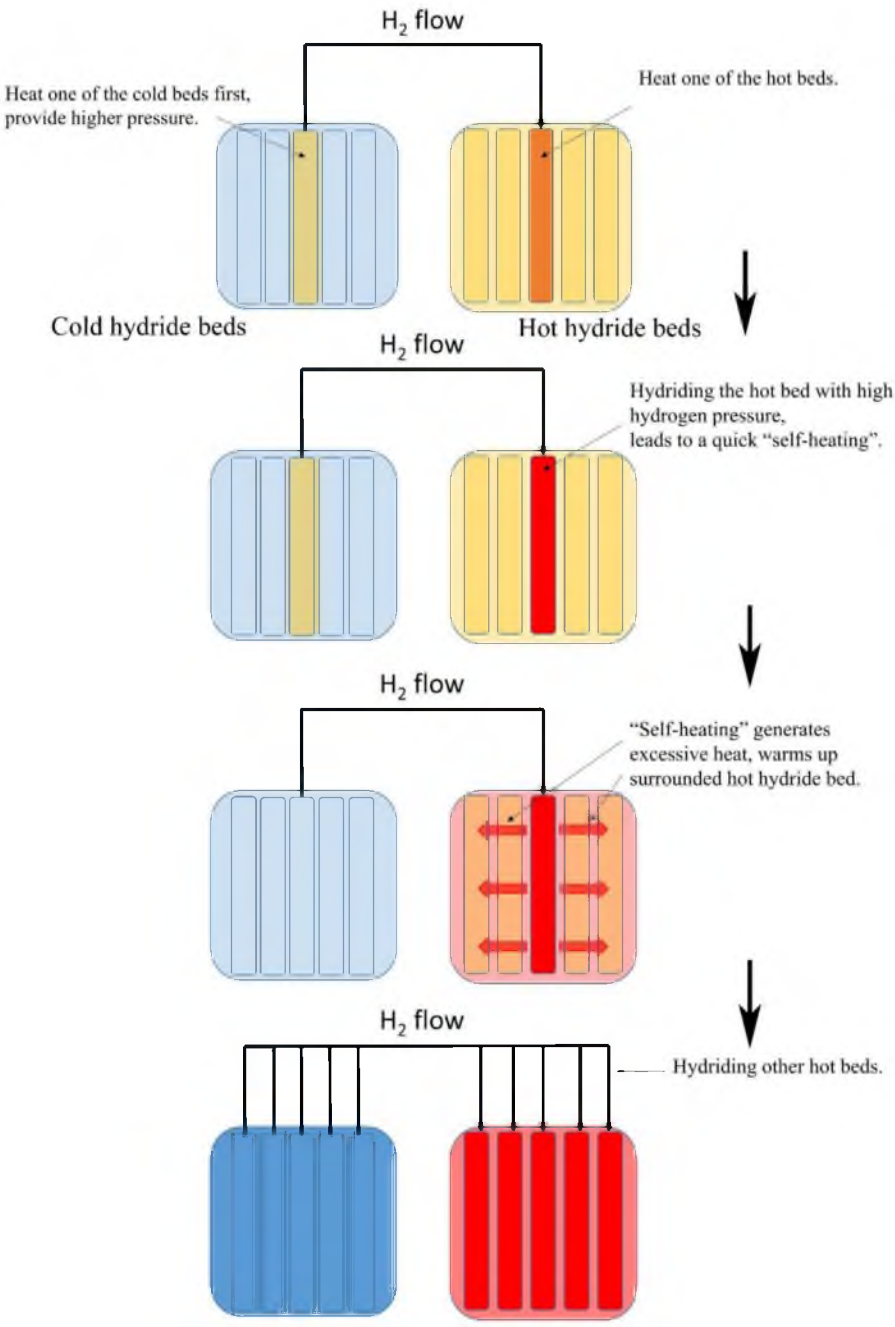

Figure 7-10. A preconditioning strategy for a thermal battery system.

CHAPTER 8

THERMAL BATTERY WITH A METAL HYDRIDE HYDROGEN COMPRESSOR

In Chapter 7, it was demonstrated that the use of low-pressure cold hydride leads to a deterioration of the performance of thermal battery. However, choosing a high-pressure cold hydride faces an equally serious problem that it is difficult to regenerate the system. The research work in this chapter was focused on a concept that combines the thermal battery system with a metal hydride based hydrogen compressor. The hydrogen compressor, driven by external thermal heat, can boost hydrogen from low-pressure (hot bed) to high-pressure for recharging the cold bed.

8.1 Concept of Metal Hydride Hydrogen Compressor

Metal hydride hydrogen compressor technology has been studied for decades. This technique allows a conversion of energy from heat into pressurized hydrogen gas. The principle of a hydrogen compressor using metal hydrides, and the relevant research efforts, were reviewed by Lototskyy et al.[1] It has been realized that compression of hydrogen gas can be fulfilled when hydrogen is absorbed at low pressure (low temperature) and then desorbed at high temperature with high pressure.

Figure 8-1 illustrates the concept of a hydrogen compressor combined with the thermal

battery system. During the recharging mode of thermal battery system, the compressor first absorbs low pressure hydrogen from the hot hydride bed. Then the compressor is heated to high temperatures and provides high pressure hydrogen to the cold hydride bed. These procedures will be an absorption-desorption round (cycle) during the operation of the compressor. Obviously, a whole recharge process of the thermal battery will require a number of absorption-desorption cycles, which depends on the capacity of the compressor. The use of a hydrogen compressor is expected to offer the following advantages:

(1) Improve the system performance (enhanced cooling/heating rate) by using high pressure cold hydride.

(2) Increase the cycle life of the hot hydride by reducing the heating temperature of hot hydride during recharging mode.

8.2 Hydride Selection for the Hydrogen Compressor

Based on the thermodynamic of the hot hydride candidate (MgH_2) and cold hydride candidate (TiMnV), the hydride that is used for the hydrogen compressor (intermediate hydride) must meet the following criteria:

(1) The equilibrium pressure of the intermediate hydride at a low temperature range (25 °C to 50 °C) must be lower than 0.5 bar (the equilibrium pressure of MgH_2 at 250 °C).

(2) The equilibrium pressure of the intermediate hydride at a high temperature range (100 °C to 200 °C) must be higher than 20 bar (the equilibrium pressure of TiMnV at 40 °C).

(3) The intermediate hydride should have fast kinetics and good capacity stability when

the absorption and desorption reactions were carried out under the temperature and pressure condition mentioned above.

According to the above criteria, a survey of hydrides shows that AB_5-type alloys such as $LaNi_{5-y}Sn_y$ and $LaNi_{5-y}Al_y$ are suitable for this intermediate hydride. Figure 8-2 shows the van't Hoff plots of MgH_2, TiMnV, and $LaNi_{4.7}Sn_{0.3}$. It can be seen that $LaNi_{4.7}Sn_{0.3}$ was able to absorb 0.4 bar hydrogen at 40 °C and provides 20 bar hydrogen at 180 °C.[2–4] Moreover, the published literature showed that $LaNi_{4.7}Sn_{0.3}$ has excellent kinetics and thermal stability up to 200 °C[5]. Therefore, $LaNi_{4.7}Sn_{0.3}$ is considered thermodynamically and kinetically feasible as an intermediate hydride.

8.3 Prototype Design and Fabrication

A small-scale hydrogen compressor was designed and fabricated, as shown in Figure 8-3. The 10 ml vessel of the intermediate hydride bed was purchased from Swagelok (double-ended miniature sample cylinder, Part No.: SS-4CD-TW-10). A heating cartridge was embedded into the vessel and controlled by a PID heating controller. The vessel was connected with two check valves (Swagelok check valve, Part No.: 6L-CW4FR4). These valves were placed in direction (Figure 8-3 (a)) to allow that low-pressure hydrogen flows in from one side and high-pressure hydrogen flows out to the other side.

Then the hydrogen compressor was connected with the cold hydride bed and the hot hydride bed. The configuration of the hydrogen gas line forms a loop as illustrated in Figure 8-1 (a). The thermal battery prototype with the hydrogen compressor was denoted as Prototype-III. Six grams of VTiCr catalyzed MgH_2, 20 grams of TiMnV alloy, and 28 grams of $LaNi_{4.7}Sn_{0.3}$ alloy were loaded into the hot bed, cold bed, and intermediate bed,

respectively.

8.4 Results

8.4.1 Recharge with the Hydrogen Compressor

As mentioned before, the operation of the compressor can be divided into two steps: (1) absorbing low-pressure hydrogen at low temperatures and (2) desorbing high-pressure hydrogen at high temperatures. Corresponding to the absorption and desorption of the compressor, the hot hydride bed (catalyzed MgH_2) was heated to 280 °C, and the cold hydride bed was at temperatures around 25 °C to 30 °C during the recharge. Figure 8-4 shows a typical recharge process in terms of the temperature and pressure profiles for the three beds. In step (1), the intermediate hydride bed was kept at room temperature and picked up hydrogen from the hot bed. Then in step (2), the intermediate hydride bed (compressor bed) was heated to 180 °C, and the hydride provided 15−20 bar hydrogen for the cold bed. Three absorption-desorption cycles were required to deplete the hydrogen from the hot bed and transfer it to the cold bed.

8.4.2 Discharge

After the recharge process, the connection of the hydrogen compressor to the hot and cold beds was shut off, and the valve between the hot bed and cold bed was opened. Hot bed and cold bed temperatures were recorded to evaluate the performance of the thermal battery. The temperature profiles from the 1^{st} to the 15^{th} discharges were plotted in Figure 8-5 (a). At the first cycle of discharge, the maximum temperature of the hot bed was 114 °C and the minimum temperature of the cold bed was -6 °C. The temperature profiles

shows that the kinetics of hot hydride underwent severe deterioration when the system cycled. Moreover, after the recharge of the 5th cycles, the system was dormant for 3 days. The next cycle of discharge (the 6th) shows a big degradation that the maximum temperature of the hot bed reached only 55 °C, and the temperature of the cold bed only decreased to less than 10 °C. This is probably due to a very small level of leakage of the system, which resulted in kinetic deterioration of hot hydride. After the 15th cycle, the discharge test was started when the hot bed was preheated to 100 °C, and results are shown in Figure 8-5 (b). Interestingly, the following cycles of discharge (16th to 22nd) present no obvious degradation of kinetics, even though the system was dormant for 4 days in between the 21st and 22nd cycles. The results indicate that the kinetic degradation can be prevented at elevated temperature and pressure, which is coincident with the material study in Chapter 6. However, the long-term performance of the system is worth further detailed study.

8.5 Discussion

Although the concept of the hydrogen compressor has been demonstrated, there are a few aspects that should be noted for future practical design. First, a hydrogen compressor will add extra weight to the thermal battery system and therefore reduce the energy density. To minimize this, a compact, high-efficiency hydrogen compressor is favorable. For an ideal hydrogen compressor, a large number of sorption-desorption cycles should be accomplished in a short time so that a limited mass of the hydride should be needed. This requires that the hydride have excellent kinetic properties. Moreover, to ensure fast absorption and desorption cycles, it is not possible to achieve fast kinetics of the intermediate hydride bed without enhanced thermal management for both the hydride

material and the vessel. Needless to say, more efforts are required to improve the compressor.

It is also realized that the hydrogen compressor will consume more energy during recharge process. External energy has to be supplied for not only decomposition of MgH_2 but also the thermal cycle of $LaNi_{4.7}Sn_{0.3}$. Based on the enthalpies of MgH_2 and $LaNi_{4.7}Sn_{0.3}$, at least 50 % more energy will be needed for the hydrogen compressor aided recharging.

8.6 Summary

A metal hydride based hydrogen compressor was developed to aid recharging the thermal battery. A thermodynamic survey shows that $LaNi_{4.7}Sn_{0.3}$ is a suitable candidate for the compressor. The hydrogen absorption-desorption cycle was performed by the temperature swing between room temperature and 180 °C, providing compression of hydrogen from 0.5 bar to 20 bar. The cyclic test of Prototype-III shows degradation of performance when the system was discharged at room temperature. However, when the hot bed was preheated to 100 °C, the discharge shows no degradation.

8.7 References

1. Lototskyy, M. V.; Yartys, V. A.; Pollet, B. G.; Bowman, R. C., Metal Hydride Hydrogen Compressors: A Review. *Int. J. Hydrogen Energy* **2014**, *39*, 5818−5851.

2. Luo, S.; Luo, W.; Clewley, J. D.; Flanagan, T. B.; Wade, L. A., Thermodynamic Studies of the $LaNi_5$−XSn_X−H System from X = 0 to 0.5. *J. Alloys Compd.* **1995**, *231*, 467−472.

3. Luo, S.; Clewley, J. D.; Flanagan, T. B.; Bowman Jr, R. C.; Cantrell, J. S., Split Plateaux in the $LaNi_5$–H System and the Effect of Sn Substitution on Splitting. *J. Alloys Compd.* **1997**, *253–254*, 226−231.

4. Luo, S.; Clewley, J. D.; Flanagan, T. B.; Bowman Jr, R. C.; Wade, L. A., Further Studies of the Isotherms of $LaNi_5$–XSn_x–H for X=0–0.5. *J. Alloys Compd.* **1998**, *267*, 171−181.

5. Bowman Jr, R. C.; Luo, C. H.; Ahn, C. C.; Witham, C. K.; Fultz, B., The Effect of Tin on the Degradation of $LaNi_5$−YSn_y Metal Hydrides During Thermal Cycling. *J. Alloys Compd.* **1995**, *217*, 185−192.

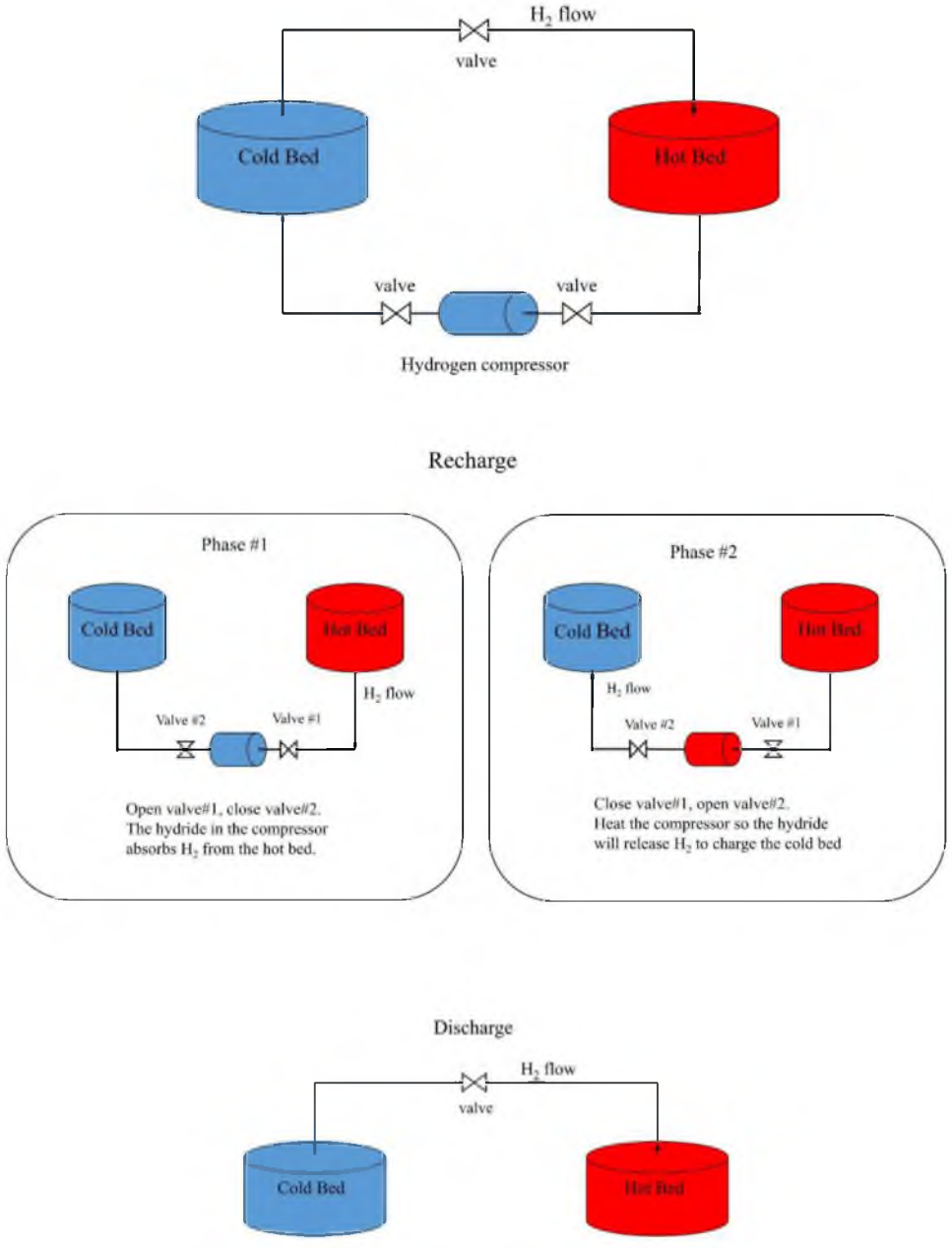

Figure 8-1. The concept of using a hydrogen compressor with a thermal battery.

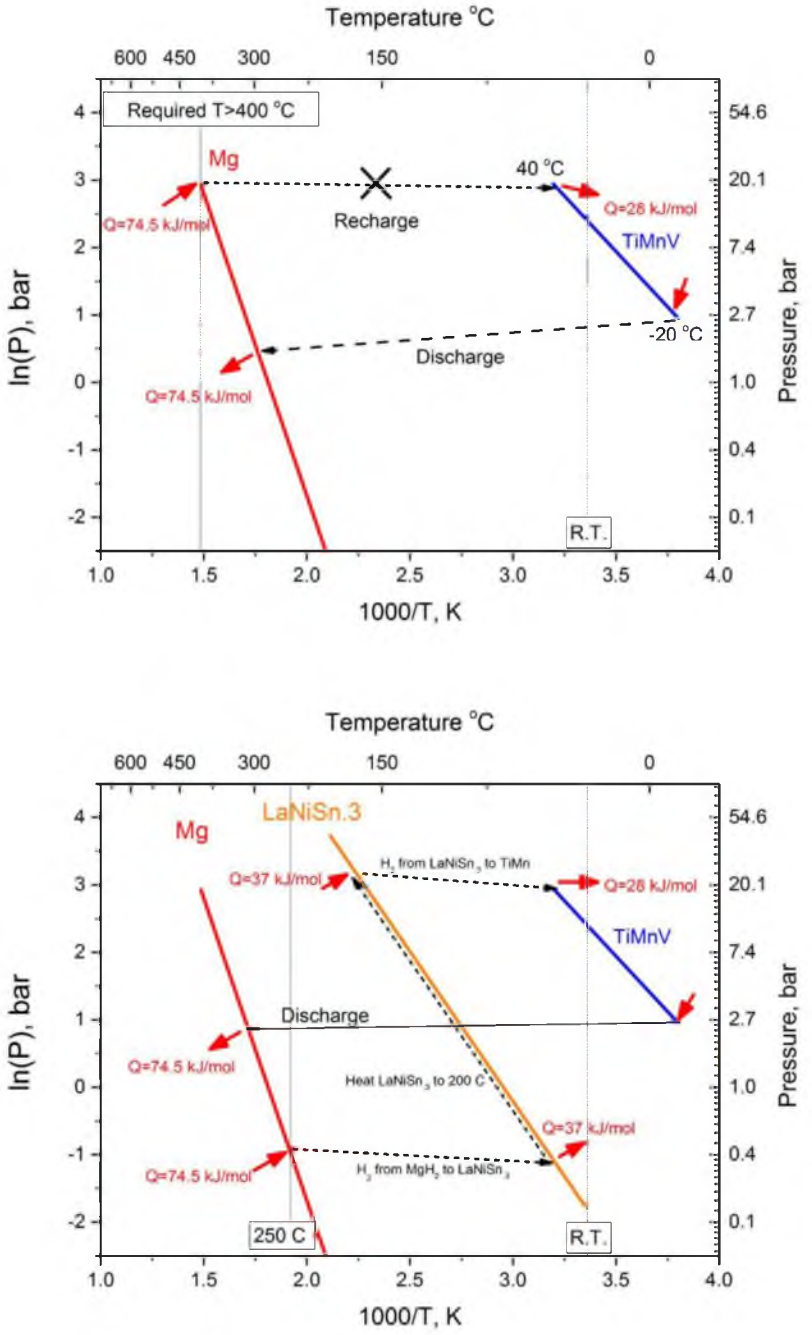

Figure 8-2. van't Hoff analysis of MgH_2, TiMnV, and $LaNi_{4.7}Sn_{0.3}$.

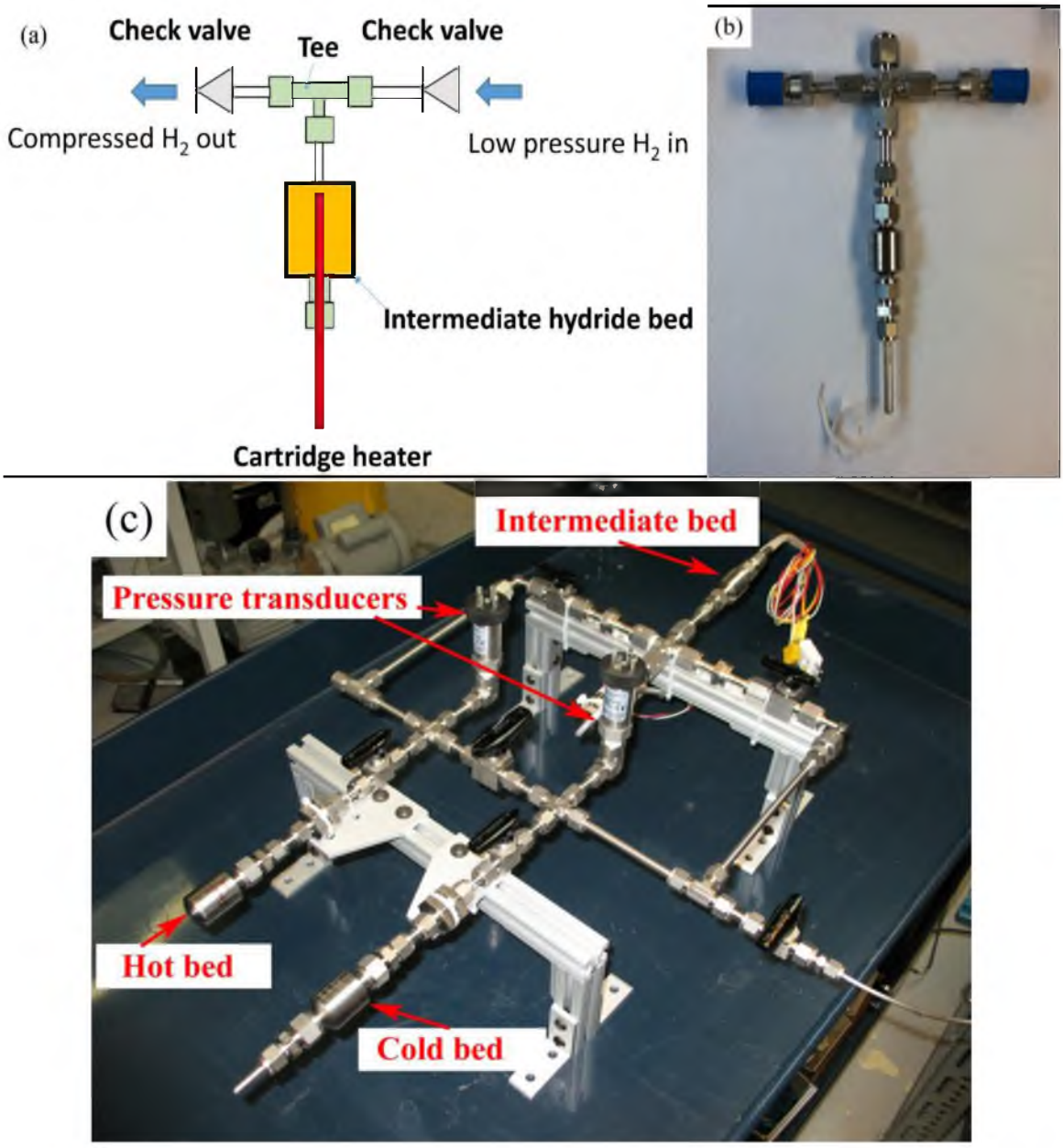

Figure 8-3. Prototype-III. (a) Schematic of a metal hydride based hydride compressor; (b) Photograph of the metal hydride hydrogen compressor; (c) Photograph.

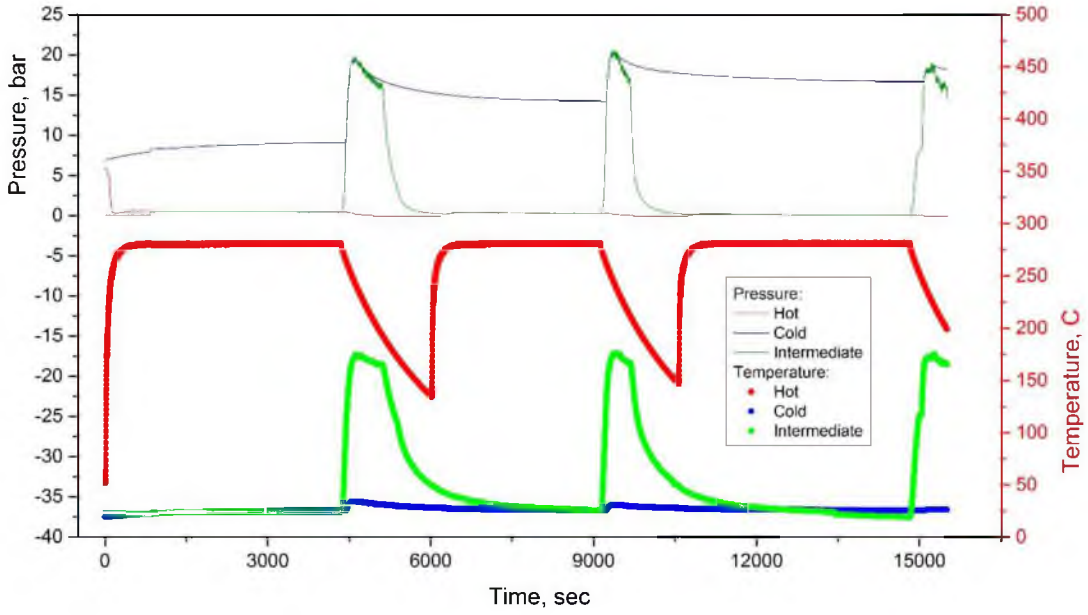

Figure 8-4. A typical recharge process with the hydrogen compressor.

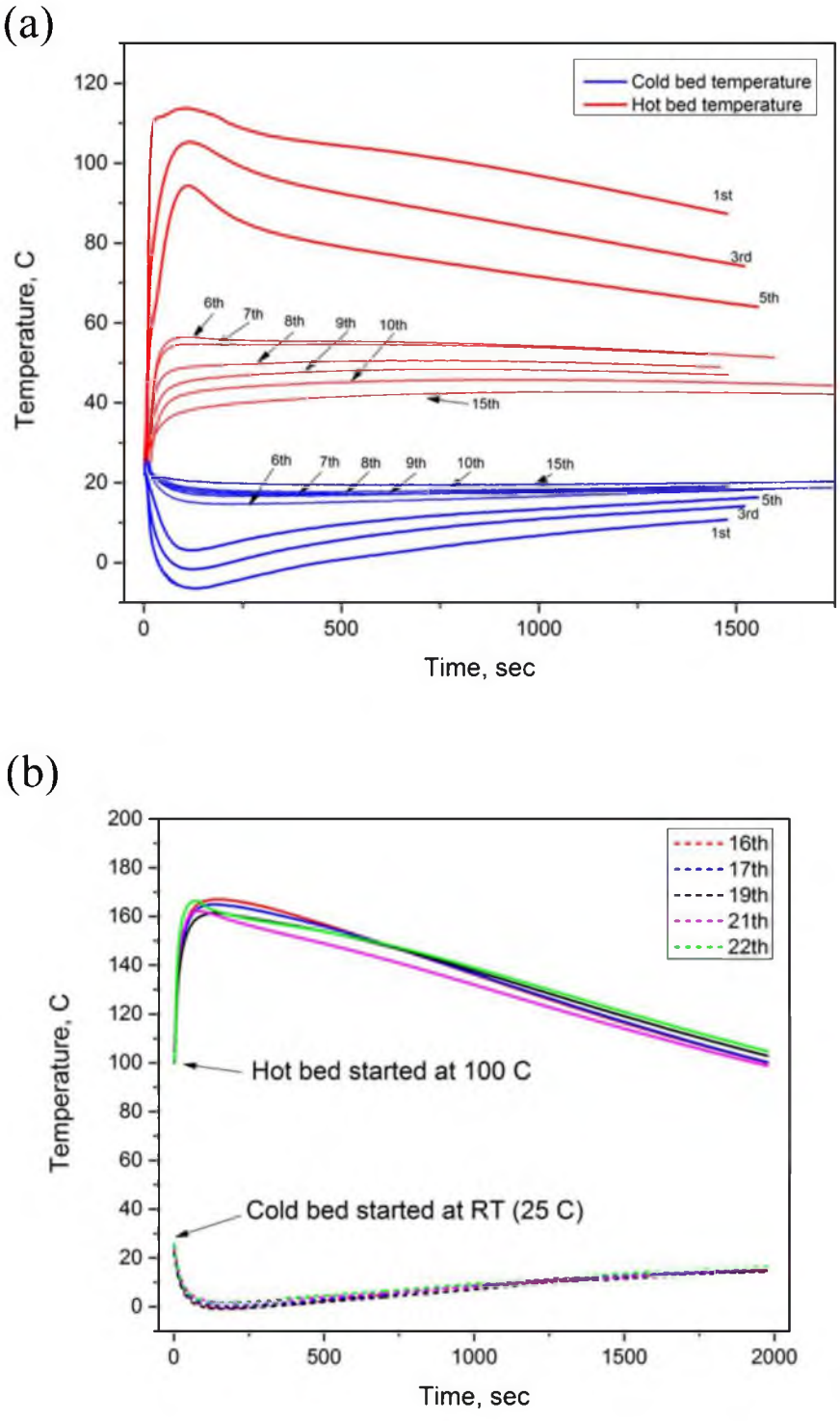

Figure 8-5. Cyclic discharge tests of Prototype-III. (a) The 1st to 15th cycles; (b) The 16th to 22nd cycles.

CHAPTER 9

CONCLUSIONS AND FUTURE WORKS

9.1 Conclusions

The research aim of this dissertation focused on the development of advanced magnesium-based hydride material as well as a metal hydride thermal battery system. In the first part of the study, a high-energy-high-pressure (HEHP) milling technique was employed for producing nanosized MgH_2-additive composites. The kinetics enhancement, thermodynamic destabilization, and cyclic stability of the magnesium-based hydride were analyzed and discussed. In the second part of this research, efforts were dedicated to develop and fabricate laboratory-scale prototypes to demonstrate the concept and the performance of the thermal battery.

The major conclusions of this study are as follows:

(1) The concept of a thermal battery based on advanced metal hydrides was introduced. A comprehensive survey of hydride materials showed that catalyzed MgH_2 is a suitable candidate of hot hydride material due to its high energy density. Hydride materials including $TiMn_2$, TiMnV, $LaNi_5$ were considered as candidates of cold hydride.

(2) A comprehensive additive survey for improving the kinetics of MgH_2 were performed based on the dehydrogenation temperature of MgH_2 through the use of TGA analysis. Additives with strong catalytic effects were found to be Ti-based, V-based metals,

hydride, as well as some intermetallic compounds.

(3) The Ti and V-based intermetallic alloys studied in this work had significant effects on improving the kinetics of dehydrogenation and hydrogenation of magnesium hydride. In particular, $TiMn_2$ doped MgH_2 exhibited drastically improved kinetics of hydrogenation at room temperature, significantly more effective than other catalytic materials as reported in the literature. Further mechanistic analysis indicated that an optimum catalyst should have both a high hydrogen solubility and diffusion coefficient.

(4) Formation of magnesium solid solution with elements such as In, Al, Ga, and Zn has been proved to be an effective route to destabilize MgH_2. PCT characterizations showed that all magnesium solid solutions had higher equilibrium hydrogen pressure than that of magnesium. *In situ* XRD analysis indicated that the solute element(s) and MgH_2 form a solid solution after dehydrogenation. Further, *ex situ* XRD results revealed that magnesium intermediate phases with MgH_2 appeared in the rehydrogenated-state solid solution.

(5) Cyclic stability of catalyzed MgH_2 was characterized and analyzed. Results showed that both the hydrogenation and dehydrogenation kinetics at high temperature were generally stable after 100 cycles. However, the low temperature (25 °C to 150 °C) hydrogenation kinetics suffered a severe degradation during cycling. Further experiments confirmed that the low temperature kinetic degradation can be mainly related to the extended cycling. TEM and high-resolution EDS revealed the evolution of microstructure of cycled materials, showing that an agglomeration of the catalyst occurred during cycling.

(6) Two laboratory prototypes of thermal batteries were designed, fabricated, and tested. The results successfully demonstrated the principles of the thermal battery using

advanced metal hydrides including the hot hydride, MgH_2, and the cold hydride, TiMnV, as a working pair with matching thermodynamic properties. The performance of the concept demonstration unit showed both high heating/cooling power and high energy densities.

(7) A metal hydride based hydrogen compressor was used to boost hydrogen pressure during the recharge of the thermal battery. The use of a metal hydride hydrogen compressor was proved to improve the performance of thermal battery. Results showed that no degradation occurred when the hot bed was preheated to 100 °C, although significant impacts were observed during room temperature operation.

9.2 Future Works

The suggested future works are listed as follows:

(1) The kinetics study in Chapter 4 suggested that criteria of a suitable catalyst are sufficient hydrogen solubility and a high diffusion coefficient. Future work to support this hypothesis can focus on collecting more data related to the diffusion of hydrogen of a catalyst candidate. Regarding the large amount of catalyst candidates to be examined, screening via theoretical calculation methods will be useful.

(2) The thermodynamic investigation in Chapter 5 demonstrated that the thermodynamics of MgH_2 is tunable. More Mg-based solid solution systems can be explored for further improvement on the thermodynamic properties of MgH_2.

(3) Concerning the cyclic stability of catalyzed MgH_2, new additives should be explored in order to improve the cyclic performance. More details should be clarified to support the mechanism that the degradation related to the agglomeration of catalyst.

(4) There will be a lot of work on optimization of thermal battery system. Regarding the scale-up thermal battery system, many issues need to be resolved.